

Investigation on the molecular factors driving the formation of distinct tau ‘strains’

Dissertation

to acquire the doctoral degree in mathematics and natural science

‘Doctor rerum naturalium’

at the Georg-August-Universität Göttingen

in the doctoral degree program of Biology

at the Georg-August University School of Science (GAUSS)

submitted by

Pijush Chakraborty

from Purulia, India

Göttingen 2021

Thesis Committee

Prof. Dr. Markus Zweckstetter

Translational Structural Biology in Dementia, German Center for Neurodegenerative Diseases, Göttingen

Structure Determination of Proteins using NMR, Max-Planck-Institute for Biophysical Chemistry, Göttingen

Dr. Sebastian Kügler

Department of Neurology, University Medical Center Göttingen

Dr. Alex Faesen

Biochemistry of Signal Dynamics, Max-Planck-Institute for Biophysical Chemistry, Göttingen

Members of the Examination Board

Reviewer: Prof. Dr. Markus Zweckstetter

Second Reviewer: Dr. Sebastian Kügler

Further members of the Examination Board

Dr. Alex Faesen

Biochemistry of Signal Dynamics, Max-Planck-Institute for Biophysical Chemistry, Göttingen

Prof. Dr. Henning Urlaub

Bioanalytical Mass Spectrometry, Max-Planck-Institute for Biophysical Chemistry, Göttingen

Dr. Johannes Söding

Quantitative and Computational Biology, Max-Planck-Institute for Biophysical Chemistry, Göttingen

Prof. Dr. Rubén Fernández-Busnadiego

Institute of Neuropathology, University Medical Center Göttingen

Date of oral examination: 7th December 2021

Affidavit

I hereby declare that the doctoral thesis entitled 'Investigation on the molecular factors driving the formation of distinct tau strains' has been written independently, with no other sources and aids than quoted.

.....
Pijush Chakraborty

Göttingen, October, 2021

Acknowledgements

First and foremost, I would like to thank Prof. Markus Zweckstetter for giving me a chance to join his cosmopolitan research group and allowing me to work on this exciting project. Thanks for his guidance, supervision, and continuous support and encouragement throughout these years. I couldn't have asked for a better supervisor who is always open to scientific discussions and shares the same excitement on the progress of the project.

I would also like to thank the members of the Thesis Advisory Committee, Dr. Sebastian Kügler, and Dr. Alex Faesen, for their support and scientific advice during the thesis committee meetings.

Thanks as well to the extended members of the examination board, Prof. Henning Urlaub, Dr. Johannes Söding, and Prof. Rubén Fernández-Busnadiego.

Many thanks to Dr. Loren Andreas for his help to set up the ssNMR experiments reported in this thesis. Also, thanks to Dr. Gwladys Rivière and Dr. Riza Dervişoğlu for acquiring some ssNMR experiments reported in this thesis.

Thanks to Prof. Ina Vorberg, Dr. Shu Liu, and Alina Hebestreit for performing the in-cell seeding assay of tau fibrils reported in this thesis.

I would like to express my deepest gratitude and appreciation to Dr. Alain Ibáñez de Opakua for his help and support in different stages of the project. Thanks for teaching me how to use different software and analyze the data as well as for the help in interpreting the results from various experiments. Thanks for your unconditional support and for being an amazing colleague.

A huge thanks to Maria-Sol Cima-Omori for the help in different stages of protein purification and mutant preparation. Thanks to Kerstin Overkamp for purifying the protein by reverse-phase chromatography and for acquiring mass spectra. Thanks as well to Leonie Kopecny, Gudrun Heim, and Dr. Dietmar Riedel from the electron-microscopy facility for the EM images. Thanks to Uwe Pleßmann from the mass spectrometry facility for the in-gel digestion of the tau fibrils.

A special thanks to Dr. Tae-Kyung Yu for teaching me how to perform NMR experiments and analyze data during my initial days in the group. Thanks as well to Dr. Garima Jaipuria for helping me with the administrative procedures during my initial days in Germany.

I was fortunate enough to work closely with brilliant colleagues from different parts of the world in the past years. I am grateful to all of you. Your constant support, recommendation, encouragement, and discussions helped me to overcome setbacks and remain focused. Thanks for creating an excellent work environment; it was such a pleasure to be at work every day. Especially, I would like to mention Tae-kyung, Garima, Sol, Conny, Timo, Javier, Yuniior, Susmitha, Adriana, Tina, Antonia, Alain, Matthew, Maria, Crhistian, Jeff, Zheng, Milan, Anton, Lisa, Gwladys, Reshma, Anna, Sàra, Franziska, Hessam, Gunnar, Kulice, and Jeremy. A special thanks to Marija, David, Filippo, and Irina for being such fantastic office mates.

I would also like to thank Prof. Christian Griesinger and the entire staff of NMRII for being supportive and providing help when needed.

I am also very grateful to my great friends in Göttingen. Thanks for always being there for me and helping me to manage stress in my personal and professional life. Living in Göttingen, so far from the family and friends in India, would have been much difficult without your presence. I would like to specially mention Sandeep, Anil, Jyoti, Somraj, Ashok, Samir, Saurabh, Atasi, Samaresh, Soumen, Subrata, and Samya.

My sincere gratitude to my two dear friends in India, Arka and Swarup. There aren't enough words to thank you guys. Thanks for your unconditional support. Thanks to Rolly for always being supportive and understanding and for sharing my ups and downs. Thanks for staying beside me.

Lastly, I would like to express my gratitude to my family; maa, baba, didi, and mama. None of this would have been possible without your love and understanding. Thanks for always supporting me and believing in me. Thanks for your understanding when I was too busy and couldn't talk for long or when I couldn't meet you for years. Thanks for always assuring me that I am not alone in this journey, and I know that I can always count on you.

Thank you!

Abstract

Pathological aggregation of the microtubule-binding protein tau into amyloid fibrils is a hallmark of different neurodegenerative diseases collectively termed tauopathies. To date, tau amyloid structures associated with different tauopathies (Alzheimer's disease, Chronic traumatic encephalopathy, Corticobasal degeneration, Progressive supranuclear palsy, Globular glial tauopathies, and Pick's disease) have been determined. Strikingly, structures are homogeneous within one disease, but differ significantly between different diseases, suggesting a critical interplay between the amyloid structure, the nature of the disease and its propagation. The distinct aggregate structures, termed amyloid "strains", can induce tau aggregation in cellulo and recapitulate pathological phenotypes when injected into animals. So far, the emergence of such tau amyloid strains remains elusive, and the factors that drive tau aggregation towards a well-defined strain are unknown.

Recombinant tau monomers can efficiently form fibrils in vitro but only in the presence of negatively charged co-factors such as heparin. However, the biological relevance of co-factor-induced fibrillization as an in vitro model of tau aggregation has been questioned. Indeed, cryo-electron microscopy (cryoEM) of heparin-induced fibrils of the longest isoform of tau demonstrated that the heparin-induced fibrils differ structurally from the tau filaments extracted from the human patient brain. Another major drawback of the heparin-based in vitro fibrilization assay is the high negative charge of the heparin: heparin-induced tau fibrillization has been extensively used to search for small molecules as tau aggregation inhibitors, potentially generating false positives due to electrostatic interactions between the small molecules and heparin.

Here we show that full-length tau protein can be aggregated in the absence of co-factors into seeding-competent amyloid fibrils that sequester RNA. Using a combination of solid-state NMR spectroscopy and biochemical experiments, we demonstrate that the co-factor-free amyloid fibrils of 4R tau and 3R tau have a rigid core that is similar in size and location to the rigid core of tau fibrils purified from the brain of patients with corticobasal degeneration and Pick's disease, respectively. In addition, we demonstrate that the N-terminal 30 residues of tau are immobilized during fibril formation, in agreement with the

presence of an N-terminal epitope that is specifically detected by antibodies in pathological tau. Experiments in vitro and in biosensor cells further established that co-factor-free tau fibrils efficiently seed tau aggregation, while binding studies with different RNAs show that the co-factor-free tau fibrils strongly sequester RNA.

Tau can be modified by numerous post-translational modifications (PTMs) in vivo. Based on the inception of tau pathology in a particular region of the brain, different brain regions can exert different PTMs that might influence tau filaments' structure in different tauopathies. Among all the PTMs, acetylation of lysine residues in tau is one of the critical PTMs observed in different tauopathies, and reducing the acetylated tau is neuroprotective in brain injuries. Here we show that acetylation can discriminate disease and isoform-specific tau by accelerating the aggregation of 3R tau and inhibiting the aggregation of 4R tau. Our data further reveal the critical role played by five lysine residues present in the R2 domain of tau, especially K298, in inhibiting 4R tau aggregation upon acetylation. Thus, our findings identify acetylation as a critical molecular factor to specifically deposit the 3R isoform of tau. Taken together, our work provides a critical advancement in revealing the molecular factors that guide aggregation towards disease-specific tau strains shedding light on the enigmatic emergence of 3R tauopathies.

Publications

Following publications appeared in peer-reviewed journals as a doctoral student including personal contributions as stated in the respective publications.

Oroz J., Chang B. J., Wysoczanski P., Lee C., Pérez-Lara Á., Chakraborty P., Hofele R. V., Baker J. D., Blair L. J., Biernat J., Urlaub H., Mandelkow E., Dickey C. A., & Zweckstetter, M. Structure and pro-toxic mechanism of the human Hsp90/PPIase/Tau complex. *Nat Commun* **9**, 4532 (2018)

Chakraborty P., Rivière G., Liu S., Ibáñez de Opakua A., Dervişođlu R., Hebestreit A., Andreas L. B., Vorberg I. M., & Zweckstetter M. Co-factor-free aggregation of tau into seeding-competent RNA-sequestering amyloid fibrils *Nat Commun* **12**, 4231 (2021)

A part of the work described in this thesis is published in the following peer-reviewed journal

Chakraborty P., Rivière G., Liu S., Ibáñez de Opakua A., Dervişođlu R., Hebestreit A., Andreas L. B., Vorberg I. M., & Zweckstetter M. Co-factor-free aggregation of tau into seeding-competent RNA-sequestering amyloid fibrils *Nat Commun* **12**, 4231 (2021)¹

Table of Contents

1. Introduction	1
1.1 <i>Neurodegenerative disorders</i>	1
1.2 <i>Tau</i>	3
1.2.1. Isoforms of tau in human brain.....	4
1.3 <i>Tauopathies</i>	6
1.3.1 Deposition of different isoforms of tau in different tauopathies.....	7
1.3.2 Alzheimer's disease (AD).....	8
1.3.3 Chronic traumatic encephalopathy (CTE).....	10
1.3.4 Corticobasal degeneration (CBD).....	11
1.3.5 Progressive supranuclear palsy (PSP).....	12
1.3.6 Globular glial tauopathies (GGTs).....	13
1.3.7 Pick's disease (PiD).....	14
1.4 <i>High-resolution structure of distinct 'strains' in different tauopathies</i>	15
1.4.1 Structure of tau filaments in 3R + 4R tauopathies.....	17
1.4.2 Structure of tau filaments in 4R tauopathies.....	19
1.4.3 Structure of tau filaments in 3R tauopathy.....	24
1.5 <i>In vitro aggregation of tau in presence of co-factors</i>	25
1.5.1 Structure of <i>in vitro</i> heparin-induced tau filaments.....	26
1.5.2 Drawbacks of <i>in vitro</i> heparin-induced aggregation protocol of tau.....	28
1.6 <i>Spreading of tau fibrils in brain</i>	28
1.7 <i>Post-translational modifications (PTMs) of tau</i>	29
1.7.1 Role of PTMs in determining different 'strains' of tau filament.....	33
1.7.2 Acetylation as an important PTM to determine distinct tau 'strains'.....	34
1.8 <i>Aims and outline</i>	35
2. Materials and methods	37
2.1 <i>Chemical reagents</i>	37
2.2 <i>Bacterial strains</i>	37
2.3 <i>Equipment</i>	38
2.4 <i>Software</i>	38
2.5 <i>Protein preparation</i>	38
2.5.1 Transformation in <i>E. coli</i>	39
2.5.2 Protein expression.....	39
2.5.3 Protein purification.....	41
2.6 <i>Preparation of different mutants of 2N4R tau</i>	43
2.7 <i>Aggregation assay of tau</i>	44
2.8 <i>Electron microscopy</i>	45
2.9 <i>Circular dichroism</i>	45

2.10	<i>Trypsin digestion</i>	46
2.11	<i>Pronase digestion</i>	46
2.12	<i>In-gel digestion and extraction of peptides for mass spectrometry</i>	46
2.13	<i>NMR spectroscopy</i>	48
2.13.1	<i>2D HSQC</i>	48
2.13.1.1	<i>HSQC spectra of full-length 4R and 3R tau</i>	48
2.13.1.2	<i>HSQC spectra of lysine labeled 4R and 3R tau (unmodified and acetylated)</i>	49
2.13.1.2.1	<i>Determination of extent of acetylation by analyzing the HSQC spectra</i>	49
2.13.2	<i>¹H-¹⁵N INEPT spectra of tau fibrils</i>	49
2.13.2.1	<i>Analysis of the INEPT spectra</i>	50
2.13.3	<i>2D ¹³C-¹³C RFDR spectra of tau fibrils</i>	50
2.13.4	<i>2D NCA/NCO spectra and 3D NCACX/NCOCX spectra of 2N4R tau fibrils</i>	51
2.13.5	<i>Dynamic Nuclear Polarization (DNP)</i>	51
2.13.5.1	<i>DNP-enhanced hCHHC and hNHHC spectra of 2N4R tau fibrils</i>	52
2.14	<i>Seeding of tau aggregation</i>	53
2.14.1	<i>In vitro seeding heparin-free 2N4R tau fibrils</i>	53
2.14.2	<i>Seeding of heparin-free/ heparin-induced 2N4R tau in cells</i>	53
2.14.3	<i>In vitro cross-seeding experiment</i>	54
2.15	<i>RNA binding assay</i>	54
2.16	<i>Bicinchoninic acid assay</i>	54
2.17	<i>Electrostatic surface potential</i>	55
2.18	<i>Microtubule polymerization</i>	55
2.19	<i>Acetylation of 4R and 3R isoform of tau</i>	55
2.20	<i>Synthesis of acetyl-lysine mimics of 4R tau</i>	56
3.	Results	59
3.1	<i>Full-length tau fibrillizes without co-factors</i>	59
3.2	<i>Protease-resistant core of heparin-free 2N4R tau fibrils</i>	61
3.3	<i>Rigidification of the N-terminal epitope of pathological tau</i>	64
3.4	<i>Solid state NMR of the core of 2N4R tau fibrils</i>	66
3.5	<i>Seeding of Tau fibrillization in-vitro and in-cell</i>	70
3.6	<i>Heparin-free Tau fibrils strongly bind RNA</i>	72
3.7	<i>Unmodified 3R tau forms amyloid fibrils in the absence of co-factors</i>	74
3.8	<i>P300/CBP selectively acetylate tau in repeats R2/R3</i>	77
3.9	<i>Acetylation accelerates 3R tau but blocks 4R tau fibrillization</i>	81
3.10	<i>K298 acetylation determines isoform-specific accumulation of tau</i>	83
3.11	<i>Acetylated 3R tau fibrils fail to seed acetylated 4R tau</i>	88
4.	Discussions	90

4.1	<i>Drastic difference in the molecular properties of co-factor-free tau fibrils and heparin-induced tau fibrils</i>	90
4.2	<i>Importance of the N-terminus of tau to pathological aggregation</i>	91
4.3	<i>RNA binding depends on the structure and surface electrostatic properties of tau conformers</i>	92
4.4	<i>Co-factor-free aggregation of 3R tau is essential to study the effect of PTMs on the emergence of 3R tauopathies</i>	93
4.5	<i>Acetylation – a critical pathogenic PTM associated with different tauopathies</i>	94
4.6	<i>Acetylation discriminates disease and isoform-specific tau – the emergence of 3R tauopathies</i>	95
4.7	<i>Towards therapeutic intervention in Pick’s disease</i>	100
4.8	<i>Lysine acetylation can direct the interaction of co-factors with monomeric tau leading to the formation of different 4R tau strains</i>	101
4.9	<i>The synergy between acetylation and other PTMs of lysine residues can lead to the formation of different tau conformers</i>	102
4.10	<i>Future outlook</i>	103
5.	Bibliography	106
6.	Appendix	117
6.1	<i>Human tau sequence</i>	117
6.1.1	<i>Sequence of human 2N4R tau</i>	117
6.1.2	<i>Sequence of human 0N3R tau</i>	118
6.2	<i>Preparation of 2N4R tau mutants</i>	118
6.2.1	<i>K280Q 2N4R tau</i>	118
6.2.2	<i>K281Q 2N4R tau</i>	119
6.2.3	<i>K290Q 2N4R tau</i>	120
6.2.4	<i>K294Q 2N4R tau</i>	120
6.2.5	<i>K298Q 2N4R tau</i>	121
6.2.6	<i>K298Q K311Q 2N4R tau</i>	122
6.2.7	<i>C291S 2N4R tau</i>	122
6.2.8	<i>C291S C322S 2N4R tau</i>	123
6.2.9	<i>C291S C322S K280C 2N4R tau</i>	124
6.2.10	<i>C291S C322S K294C 2N4R tau</i>	125
6.2.11	<i>C291S C322S K298C 2N4R tau</i>	125
6.2.12	<i>C291S C322S K311C 2N4R tau</i>	126
6.2.13	<i>C291S C322S K298C K311C 2N4R tau</i>	127
6.3	<i>Methods used to perform the aggregation assay</i>	129
6.4	<i>Pulse program for 2D ¹H-¹⁵N HSQC</i>	130
6.5	<i>Pulse program for 2D ¹H-¹⁵N INEPT experiments</i>	133
6.6	<i>Pulse program for 2D ¹³C-¹³C RFDR experiments</i>	140
6.7	<i>Pulse program for 2D NCA/NCO experiments</i>	147

6.8	<i>Pulse program for 3D NCACX/NCOCX experiments.....</i>	154
6.9	<i>Pulse program for hCHHC experiment.....</i>	163
6.10	<i>Pulse program for hNHHC experiments.....</i>	175
6.11	<i>Bicinchoninic acid assay of 2N4R tau</i>	181
6.12	<i>2D hCH spectra of specifically labeled heparin-free 2N4R tau fibrils.....</i>	182
6.13	<i>Electrostatic surface potential of heparin-induced 2N4R tau fibrils</i>	183

Table of figures

Figure 1-1 Antibody staining of protein deposits in different tauopathies.....	1
Figure 1-2 Prevalence of neurodegenerative diseases.....	2
Figure 1-3 Tau - a microtubule-associated protein.....	3
Figure 1-4 MAPT gene and the different isoforms of tau present in the human brain.....	5
Figure 1-5 Immunohistochemically staining of sections of brain (with AD) by AT8 antibody (detecting hyperphosphorylated tau).....	9
Figure 1-6 AT8 stained slices of cerebral cortex in 3 cases of CTE.....	10
Figure 1-7 Neuropathological features of CBD.....	11
Figure 1-8 Neuropathological features of PSP.....	12
Figure 1-9 Neuropathological features of GGTs.....	13
Figure 1-10 Neuropathological features of Pick's disease.....	15
Figure 1-11 Classification of tauopathies based on the structure of tau protofilament.....	16
Figure 1-12 Structure of PHFs and SFs in AD.....	18
Figure 1-13 Structure of tau filaments in CTE.....	19
Figure 1-14 Structure of tau filaments in CBD and AGD.....	21
Figure 1-15 Structure of tau filaments in PSP and GGT.....	22
Figure 1-16 Structure of tau filaments derived from a particular case of PSP-F termed as GGT-PSP tau.....	23
Figure 1-17 Structure of tau filaments in Pick's disease.....	24
Figure 1-18 Structure of <i>in vitro</i> heparin-induced tau filaments.....	27
Figure 1-19 Transneuronal spreading of tau pathology in the brain.....	29
Figure 1-20 Frequency of different post-translational modifications on 2N4R tau.....	30
Figure 1-21 Classifications of different chemical modifications of amyloid fibrils.....	34
Figure 2-1 Vector map of pNG2htau40.....	39
Figure 2-2 Purification of tau.....	43
Figure 2-3 The flow of magnetization in a ¹ H- ¹⁵ N HSQC experiment.....	48
Figure 2-4 Scheme of reaction to synthesize acetyl-lysine mimic ¹⁷⁴	57
Figure 2-5 Mass spectra of acetyl-lysine mimics of 2N4R tau.....	58
Figure 3-1 Amyloid fibrils of tau without co-factors.....	60
Figure 3-2 Heparin-free tau fibrils have an extended core and an immobile N-terminal antibody-binding epitope.....	62
Figure 3-3 Pronase-resistant core of heparin-free 2N4R tau fibrils.....	63
Figure 3-4 INEPT spectra of tau fibrils.....	65
Figure 3-5 Solid-state NMR of the core of heparin-free tau fibrils.....	67
Figure 3-6 Residue type-specific contacts within the core of heparin-free 2N4R tau fibrils.....	69
Figure 3-7 Seeding activity of heparin-free tau fibrils.....	71
Figure 3-8 Heparin-free tau fibrils strongly bind RNA.....	73
Figure 3-9 Co-factor-free aggregation of 3R tau.....	75
Figure 3-10 The rigid core of co-factor-free 3R tau fibrils.....	76
Figure 3-11 Acetylation of 4R tau at three lysines in repeat R2.....	78
Figure 3-12 Common tau acetylation patterns by p300 and CBP.....	80
Figure 3-13 Acetylation accelerates 3R tau but blocks 4R tau fibrillization.....	81
Figure 3-14 Impact of acetylation of repeat R2 on 4R tau fibrillization.....	84
Figure 3-15 Acetylation of K298 profoundly impacts fibrillization of 4R tau.....	85
Figure 3-16 Estimation of the amount of aggregated tau proteins.....	86
Figure 3-17 Fibrils of acetylated 3R tau fail to seed acetylated 4R tau.....	88
Figure 3-18 Fibrils of acetylated 3R tau cross-seed unmodified 4R tau monomer.....	89

Figure 4-1 Similar core of co-factor free 4R tau fibrils and brain-derived 4R tau fibrils.....	90
Figure 4-2 Structure of different RNAs	92
Figure 4-3 Distinct acetylation patterns in different tauopathies.....	97
Figure 4-4 Model for the emergence of 3R tauopathies.	99
Figure 4-5 Structure-based model of the influence of PTM on tau filament's structure.....	102
Figure 4-6 Distinct phosphorylation pattern in different tauopathies.....	104
Figure 6-1 Methods used to perform the aggregation assay.....	129
Figure 6-2 BCA assay of 2N4R tau.....	181
Figure 6-3 2D hCH spectra of heparin-free fibrils of ¹³ C _γ valine, 13C-ring phenylalanine-labeled 2N4R tau.....	182
Figure 6-4 Electrostatic surface potential of the heparin-induced 2N4R tau fibrils (snake form; PDB code: 6QJH).....	183

Abbreviations

AD	Alzheimer's disease
AGD	Argyrophilic grain disease
ARTAG	Aging-related tau astrogliopathy
A β	Amyloid- β
BCA	Bicinchoninic acid
CaMKII	Calmodulin-dependent protein kinase II
CBD	Corticobasal degeneration
CBP	CREB-binding protein
CD	Circular dichroism
Cdk5	Cyclin-dependent kinase 5
CK1	Casein kinase 1
CNS	Central nervous system
CP	Cross-polarization
Cryo-EM	Cryo-electron microscopy
CTE	Chronic traumatic encephalopathy
DNA	Deoxyribonucleic acid
DNP	Dynamic nuclear polarization
DTT	Dithiothreitol
EDTA	Ethylenediaminetetraacetic acid
EGTA	Ethylene glycol-bis(β -aminoethyl ether)-N,N,N',N'-tetraacetic acid
EPR	Electron paramagnetic resonance
FBD	Familial British dementia
FDD	Familial Danish dementia
FTD	Frontotemporal dementia
FTLD	Frontotemporal lobar degeneration
GAI	Globular astroglial inclusions
GCI	Glial cytoplasmic inclusions
GFP	Green fluorescent protein
GGT	Globular glial tauopathy
GOI	Globular oligodendroglial inclusions
GPT	GGT PSP tau
GSK3	Glycogen synthase kinase 3
GTP	Guanosine-5'-triphosphate
HAT	Histone acetyltransferase
HDAC	Histone deacetylase
HEK	Human embryonic kidney
HEPES	4-(2-hydroxyethyl)-1-piperazineethanesulfonic acid
HPLC	High-performance liquid chromatography
HSQC	Heteronuclear single quantum coherence
IDP	Intrinsically disordered protein
INEPT	Insensitive nuclei enhanced by polarization transfer
IPTG	sopropyl β -D-1-thiogalactopyranoside
LB	Lysogeny broth

MAPT	Microtubule-associated protein tau
MARK	Microtubule affinity-regulating kinases
MAS	Magic-angle spinning
MES	2-(N-morpholino)ethanesulfonic acid
MS	Mass spectrometry
MSA	Multiple system atrophy
MT	Microtubules
NAD	Nicotinamide adenine dinucleotide
NFT	Neurofibrillary tangles
NMR	Nuclear magnetic resonance
NPF	Narrow pick filament
OD	Optical density
PART	Primary age-related tauopathy
PDSD	Proton-driven spin diffusion
PHF	Paired helical filament
PiD	Pick's disease
PIPES	Piperazine-N,N'-bis(2-ethanesulfonic acid)
PMSF	Phenylmethylsulfonyl fluoride
PSP	Progressive supranuclear palsy
PTM	Post-translational modification
RF	Radio-frequency
RFDR	Radio frequency-driven recoupling
RNA	Ribonucleic acid
SDS-PAGE	Sodium dodecyl sulphate–polyacrylamide gel electrophoresis
SF	Straight filament
SN	Supernatant
TauRD	Repeat domain of tau
TCEP	Tris (2-carboxyethyl) phosphine
ThT	Thioflavin-T
WPF	Wide Pick filament

1. Introduction

1.1 Neurodegenerative disorders

Neurodegenerative diseases are primarily age-related² disorders characterized by the progressive loss of neurons leading to the degeneration of the structure and function of the nervous system³. Pathological aggregation of different proteins into insoluble aggregates is the hallmark of these disorders (Figure 1-1 and Table 1-1). The most common neurodegenerative diseases are tauopathies, amyloidosis, α -synucleinopathies, and transactivation response DNA binding protein 43 (TDP-43) proteinopathies³.

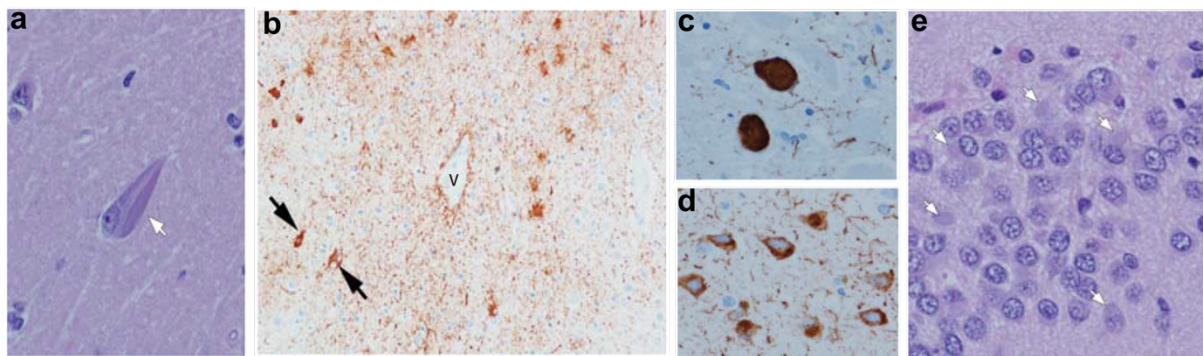


Figure 1-1 Antibody staining of protein deposits in different tauopathies.

a, Neurofibrillary tangles (NFT) in Alzheimer's disease (AD). **b**, Neuronal and astroglial tau deposits around blood vessels (v) in Chronic traumatic encephalopathy (CTE). **c**, 4R tau deposits in Progressive supranuclear palsy (PSP). **d**, Neuronal tau lesion in Corticobasal degeneration (CBD). **e**, Pick bodies composed of 3R tau in Pick's disease. Images adapted from Dugger et al.³

Neurodegenerative disorders	Protein aggregates
Alzheimer's disease ⁴	Amyloid β ⁵ and Tau ⁶
Creutzfeldt – Jakob disease ⁷	Prion protein ⁸
Parkinson's disease ⁹	α -synuclein ¹⁰
Multiple system atrophy ¹¹	α -synuclein
Lewy body dementia ¹²	α -synuclein ¹⁰
Amyotrophic lateral sclerosis ¹³	TDP-43 ¹⁴

Pick's disease ¹⁵	Tau ¹⁶
Corticobasal degeneration ¹⁷	Tau ¹⁶
Chronic traumatic encephalopathy ¹⁸	Tau ¹⁶
Progressive supranuclear palsy ¹⁹	Tau ¹⁶

Table 1-1. Selected neurodegenerative disorders and the proteins deposited in the brain

The neurodegenerative disorders are very diverse in their phenotype, and barring few exceptions, the cause of these disorders is essentially unknown. Several genetic and environmental risk factors are associated with different neurodegenerative diseases. Among all factors, aging is considered the most critical risk factor of neurodegeneration²(Figure 1-2). As average life expectancy has increased due to the improvement in the healthcare system, the elderly population is growing worldwide. According to a recent report, the population of people aged ≥ 65 in the United States will increase from 53 million in 2018 to 88 million in 2050²⁰, leading to an increased financial burden.

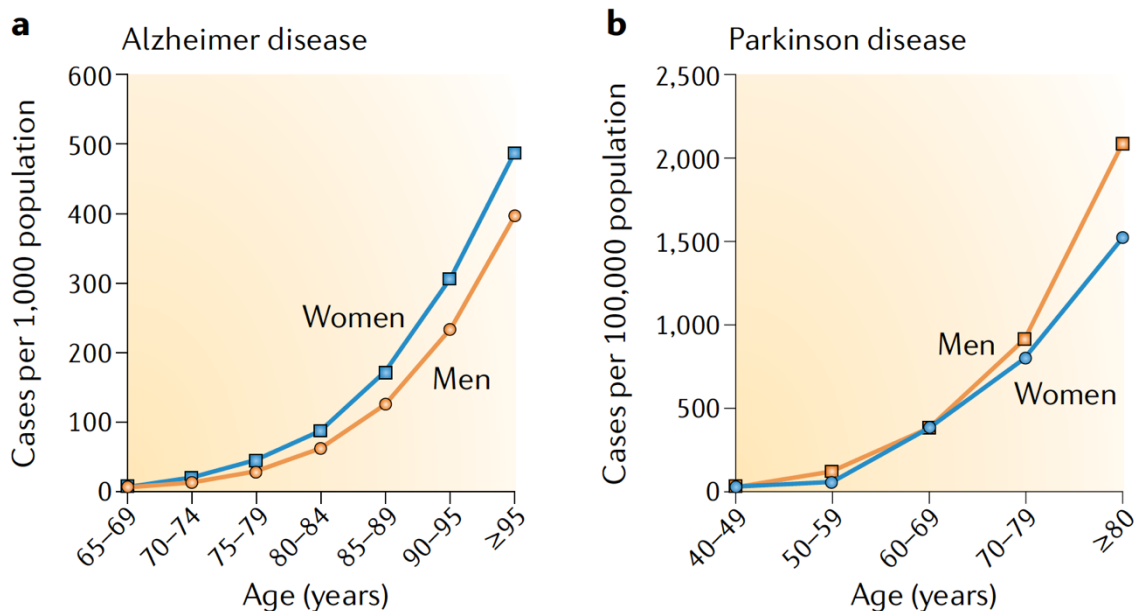


Figure 1-2 Prevalence of neurodegenerative diseases.

a, Prevalence of Alzheimer's disease per 1,000 men and women by age in USA²⁰⁻²². **b**, Prevalence of Parkinson's disease per 100,000 men and women by age in USA^{21,23}. Image is taken from Hou et al.²

Another recent report from Alzheimer's association revealed more than 16 million family members of Alzheimer's disease or other dementia patients spent 18.6 billion hours to take care with an estimated cost of \$244 billion²⁴. Over the last few decades, extensive research on multiple fronts advanced our understanding of different neurodegenerative diseases. Still, till now, there are no effective treatments available to cure these dreadful diseases. Effective therapeutic and preventive approaches are thus urgently needed.

1.2 Tau

Tau was first identified in 1975 as a heat-stable microtubule-associated protein that is essential for microtubule assembly²⁵. Tau is a hydrophilic, highly soluble, and natively unfolded protein²⁶. In the brain, tau is mainly found in the neuron and at low levels in glia²⁷. In adult neurons, tau is predominantly found in the axons where it interacts with the microtubule through its repeat domains, thereby regulating the properties of microtubules; in particular, it regulates the dynamic instability of the microtubules^{28,29} (Figure 1-3a). Tau binds at the interface between the tubulin heterodimers through a small group of residues, including the hexapeptide motifs (²⁷⁵VQIINK²⁸⁰ and ³⁰⁶VQIVYK³¹¹) essential for its aggregation³⁰.

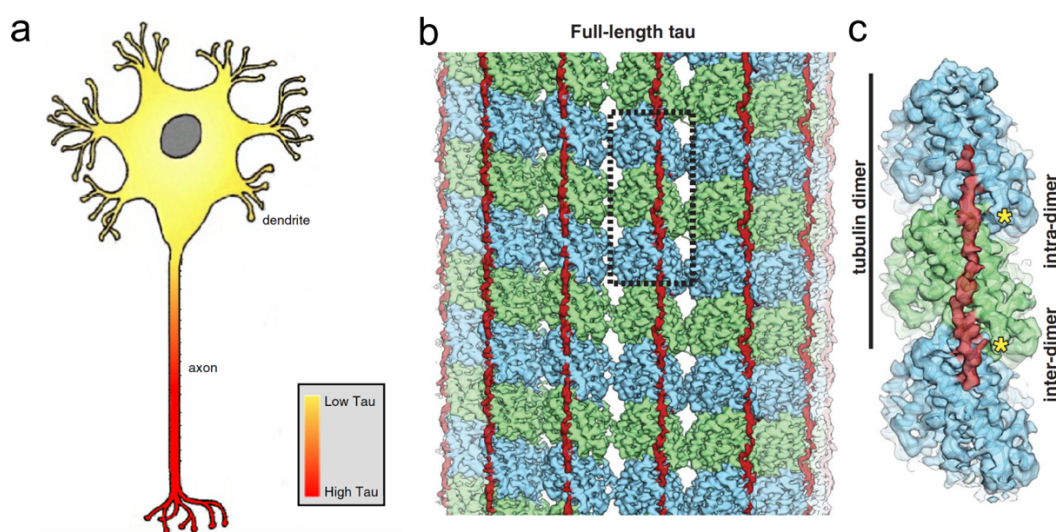


Figure 1-3 Tau - a microtubule-associated protein.

a, Differential tau expression levels in mature neurons showing a predominant localization in the axon. Image adapted from Scholz et al.³¹ **b**, Cryo-EM density map of full-length tau (red) bound to the microtubule. α -tubulin is shown in green, and β -tubulin is shown in blue. **c**, One repeat of tau spans over three tubulin monomers and binds across intra and interdimer interfaces of tubulin. (b) and (c) adapted from Kellogg et al.³²

A near-atomic model of tau bound to microtubule revealed that each tau repeat has an extended conformation spanning over both intra and interdimer interfaces of tubulin and connects three tubulin monomers³² (Figure 1-3b). Besides regulating the dynamics of microtubule, tau also regulates axonal transport via different mechanisms³³. Tau influences the function of motor proteins dynein and kinesin by competing with them for binding to the microtubules, thereby reducing the binding of these motor proteins leading to the slowdown of both anterograde (towards the presynaptic terminal) and retrograde transport (towards the cell body)^{34,35}. Some reports also suggest that tau, as a cargo, competes with other cargoes available for the motor proteins (dynein and kinesin), affecting axonal transport^{36,37}. However, overexpression or deletion of tau in mice has little influence on axonal transport, suggesting unknown *in vivo* mechanisms responsible for neutralizing the impact of tau on axonal transport³⁸. The physiological role of dendritic tau has not been well characterized to date; however, it might be involved in the regulation of synaptic plasticity³⁹.

1.2.1. Isoforms of tau in human brain

Human tau is encoded by the Microtubule-associated protein tau (MAPT) gene located on chromosome 17q21⁴⁰. The MAPT gene is comprised of 16 exons. The exons 0 and 14 are transcribed but not translated. In the adult human brain, six isoforms of tau (between 37-46 KDa) are generated due to the alternative splicing of exon 2, exon 3, and exon 10 (Figure 1-4). MAPT exons 2 and 3 encode an insert of 29 amino acids each at the amino terminus generating isoforms containing 0, 1, or 2 inserts known as 0N, 1N, and 2N, respectively. Exon 3 does not transcribe in the absence of exon 2, leading to the presence of only N1 insert in the case of 1N isoform. Tau's microtubule-binding domain comprises four highly conserved imperfect repeats of 30-31 amino acids at the carboxy terminus, encoded by exons 9-12.

Exon 10 encodes for the R2 repeat, and the alternative splicing of exon 10 generates two isoforms, either containing three repeats (3R tau - R1, R3, and R4) or four repeats (4R tau – R1, R2, R3, and R4). Accordingly, the six isoforms of tau are 2N4R, 1N4R, 0N4R, 2N3R, 1N3R, and 0N3R (Figure 1-4).

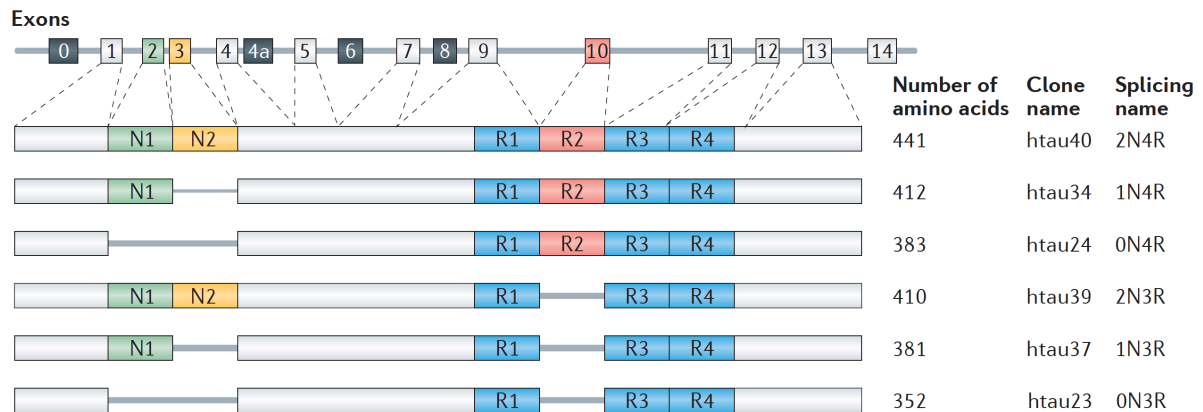


Figure 1-4 MAPT gene and the different isoforms of tau present in the human brain.

Image is taken from Wang et al.³³

Expression of tau is developmentally regulated. All six isoforms of tau are present in the adult human brain, whereas in the fetal brain, only the shortest isoform of tau, i.e., 0N3R tau, is expressed⁴¹. In the brain of healthy human adults, the expression of 3R and 4R tau is comparable. In contrast, the expression of the 2N isoform of tau is less than the 0N and 1N isoforms (human CNS comprises 54% 1N tau, 37% 0N tau, and 9% 2N tau)⁴².

Due to the presence of additional repeat R2, 4R tau can interact with microtubule with higher affinity than 3R tau leading to more efficient microtubule assembly⁴². However, the function of the N terminal inserts of tau still remains elusive. Being part of the projection domain of tau, the N terminal inserts might influence the spacing between microtubules^{43,44}. Apart from this, the N terminal inserts might affect the subcellular distribution of tau in neurons⁴⁵.

1.3 Tauopathies

Tauopathies are a collection of ≥ 25 distinct syndromes (Table 1-2) where extensive neurodegeneration occurs, and pathological accumulation of tau is detected in neurons and glia⁴⁶⁻⁴⁸. These diseases are clinically, biochemically, and morphologically heterogeneous in nature. Classically, tauopathies are categorized into two parts – primary tauopathies and secondary tauopathies. Primary tauopathies are the disorders where tau is believed to be the primary factor contributing to neurodegeneration. Some examples of primary tauopathies are Corticobasal degeneration, Frontotemporal dementia and Progressive supranuclear palsy. On the other hand, secondary tauopathies are diseases where other proteins also play a major role in neurodegeneration, or other driving forces trigger neurodegeneration⁴⁸. One example of a secondary tauopathy is Alzheimer's disease (AD). In AD, apart from tau pathology, insoluble deposits of amyloid- β ($A\beta$) form. Another example of a secondary tauopathy is Chronic traumatic encephalopathy (CTE), where tau protein aggregation is triggered by repetitive brain injury¹⁸. Pathological aspects of the most common tauopathies are described in sections 1.3.2 to 1.3.7.

- Aging-related tau astroglipathy
- Alzheimer's disease
- Amyotrophic lateral sclerosis
- Argyrophilic grain diseases
- Chronic traumatic encephalopathy
- Corticobasal degeneration
- Creutzfeldt-Jakob disease
- Dementia pugilistica
- Diffuse neurofibrillary tangles with calcification
- Down's syndrome
- Familial British dementia
- Familial Danish dementia
- Frontotemporal dementia with parkinsonism linked to chromosome 17

	Corticobasal degeneration (CBD)
	Globular glial tauopathy (GGT)
	Argyrophilic grain diseases (AGD)
	Aging-related tau astrogliopathy (ARTAG)
• 3R tauopathy	Pick's disease (PiD)
• (4R + 3R) tauopathy	Alzheimer's disease (AD)
	Primary age-related tauopathy (PART)
	Chronic traumatic encephalopathy (CTE)
	Familial British dementia (FBD)
	Familial Danish dementia (FDD)

Table 1-3. Classification of different tauopathies based on the deposition of either 3R, 4R, or both isoforms of tau

1.3.2 Alzheimer's disease (AD)

Alzheimer's disease is the most prevalent of the tauopathies and is a mixed proteinopathy that includes the presence of both tau inclusions in neurons (i.e., NFT) and amyloid- β deposits in the parenchyma as senile plaques. In AD, differential degeneration of frontal, temporal, and parietal lobes is observed, and in a subset of cases, the occipital lobe is also damaged. The degree of cortical atrophy relates to the distribution of tau pathology and clinical syndromes, but not with amyloid- β pathology^{54,55}.

Both 3R and 4R isoforms of tau are deposited in an equimolar ratio in AD, but immunostaining with 3R and 4R tau specific monoclonal antibodies has shown distinct regional differences⁵⁶. In 1991 Braak and Braak proposed that NFTs in AD progress in an anatomically hierarchical fashion in six stages⁵⁷ (Figure 1-5). Stage I begins in the transentorhinal cortex, followed by the entorhinal region in stage II, temporo-occipital gyrus in stage III, temporal cortex in stage IV, peristriatal cortex in stage V, and striatal cortex in stage VI⁵⁸. Although most AD cases

follow the Braak staging scheme, it does not fit in a subset of patients (~20 %). This includes limbic predominant AD as well as hippocampal-sparing AD⁵⁹. Although both NFTs and A β plaques are present in AD, some individuals have been diagnosed with only NFTs. This is referred to as Primary age-related tauopathy (PART), with most cases having Braak NFT stages I to IV⁶⁰.

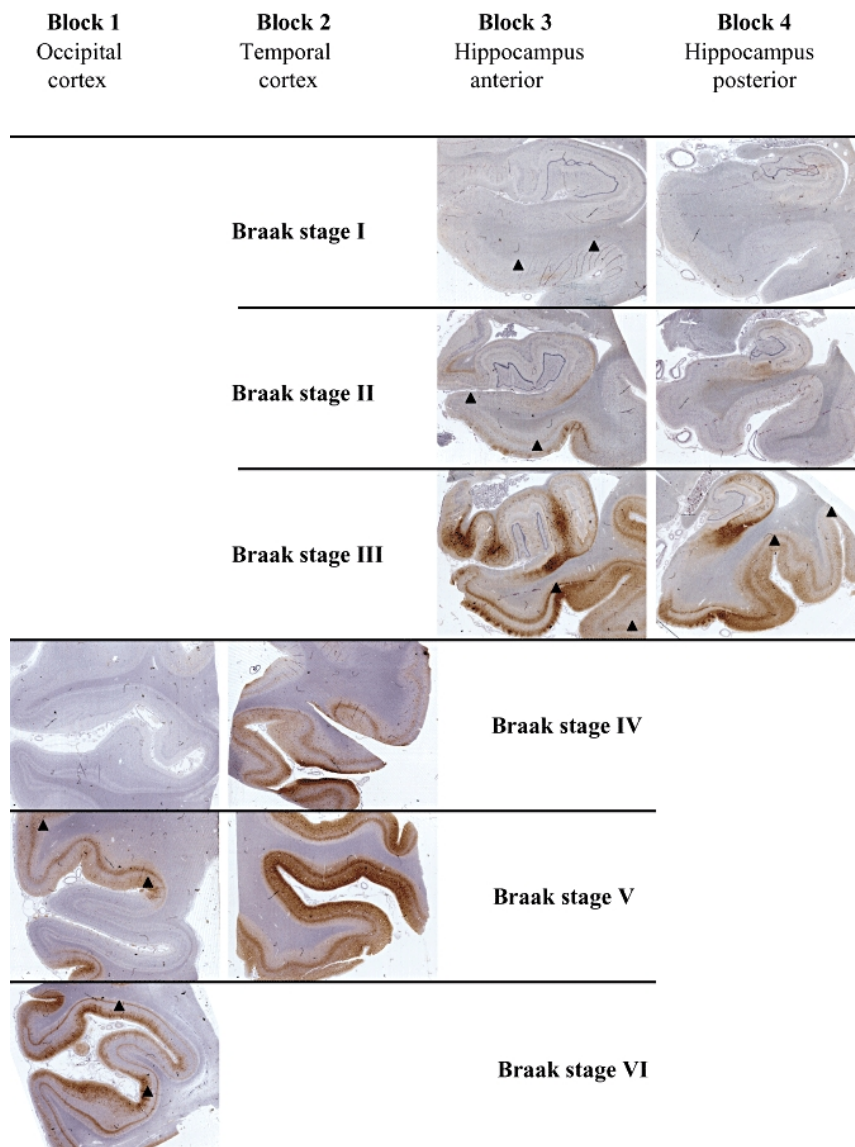


Figure 1-5 Immunohistochemically staining of sections of brain (with AD) by AT8 antibody (detecting hyperphosphorylated tau).

Sections were taken from the Occipital cortex, including calcarine fissure (Block 1), temporal cortex including middle temporal gyrus (Block 2), anterior hippocampus (Block 3), and posterior hippocampus (Block 4). The arrowheads indicate borders for the relevant neuroanatomical regions for each Braak stage. The image is taken from Alafuzoff et al.⁵⁸

1.3.3 Chronic traumatic encephalopathy (CTE)

Chronic traumatic encephalopathy (CTE) is a tauopathy associated with repetitive brain injury. It has been first reported in boxers and referred to as 'punch drunk syndrome' or 'dementia pugilistica'⁶¹. CTE has also been identified in athletes of other contact sports, such as American football⁶², ice hockey⁶³, baseball, rugby, wrestling, and military veterans exposed to blast⁶⁴.



Figure 1-6 AT8 stained slices of cerebral cortex in 3 cases of CTE.

Irregular patches of phosphorylated tau are observed with highest density at the depths of sulci. Image is taken from McKee et al.⁶⁵

In CTE, both 3R and 4R isoforms of tau are deposited in the NFTs, and varying degrees of cerebral atrophy in the frontal or temporal lobes are observed⁶⁶. In the early stage of CTE, neurofibrillary pathology is observed in the superficial cortical layers (often proximal to the blood vessels) followed by involvement of the temporal lobe at a later stage^{63,67}. Recently McKee et al. proposed a four-stage scheme of CTE neuropathology with tau pathology initially in discrete epicenters in the cerebral cortex (stage I and II) followed by involvement of cortical and medial temporal lobe (stage III) and at the end widespread in the cerebral cortex and subcortical structures (stage IV)⁶⁵. Although the defining lesion in CTE is the

characteristic distribution of neuronal tau pathology, astroglial tau pathology is also observed. Thus, CTE must be clearly differentiated from age-related tau astrogliopathy (ARTAG), a 4R tauopathy observed in normal elderly individuals⁶⁸.

1.3.4 Corticobasal degeneration (CBD)

Corticobasal degeneration (CBD) is a 4R tauopathy with asymmetric focal cortical atrophy and depigmentation of substantia nigra as macroscopic changes in the brain⁴⁸. In 1968, it was first recognized as 'cortico-dentato-nigral degeneration with neuronal achromasia⁶⁹', and later the term CBD was coined¹⁷. Initially, the neuropathological description of CBD was the presence of chromatolytic-like cortical neurons or 'ballooned neurons', and only later the importance of tau pathology was identified^{70,71}. Tau astrocytic lesions and astrocytic plaques in the affected cortices are characteristic of CBD. The most common neuronal lesion is 'pretangle', a cytoplasmic inclusion that is weakly stained with traditional histological methods for detecting NFTs in AD. Neuronal and glial lesions in CBD are immunoreactive for 4R tau and negative for 3R tau⁴⁷.

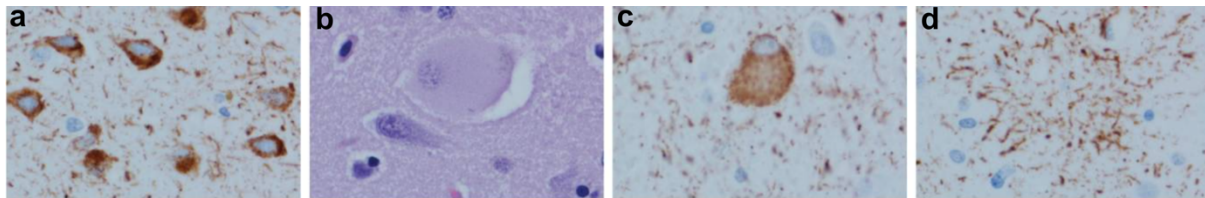


Figure 1-7 Neuropathological features of CBD.

a, Typical neuronal lesion 'pretangle' visible with tau immunohistochemistry. **b**, Cortical 'ballooned neurons' with Hematoxylin and Eosin (H&E) staining. **c**, Cortical 'ballooned neurons' detected with phospho-tau antibody. **d**, A typical astrocytic lesion, astrocytic plaques. Image is adapted from Dugger et al.³

Neuropathological criteria for CBD require neuronal and glial lesions, threads in the white and grey matter, coiled bodies, and astrocytic plaques⁷² (Figure 1-7). The antemortem diagnostic accuracy of CBD is abysmal due to the heterogeneity of cortical involvement that overlaps with other disorders⁷³. Also, patients with symmetrical cortical deficits in CBD are

clinically challenging to differentiate from PSP, but they can be characterized based on distinct tau pathologies⁷⁴. In general, mainly the forebrain in CBD and the hindbrain in PSP are affected due to neuronal tau pathology, and distinct astroglial tau pathology along with subcortical tangles are observed only in PSP⁷⁵.

1.3.5 Progressive supranuclear palsy (PSP)

Progressive supranuclear palsy (PSP) is a sporadic 4R tauopathy characterized by postural instability leading to falls and characteristic oculomotor signs leading to supranuclear gaze palsy⁷⁶. These symptoms are accompanied by atypical parkinsonism and behavioral changes. PSP was first identified in 1964 and is often referred to as Steele-Richardson-Olszewski syndrome⁷⁷. Clinically, typical PSP is referred to as Richardson's syndrome or PSP-RS. Pathologically PSP is characterized by deposition of abnormal tau in neurons and glia, which are immunoreactive for 4R tau and negative for 3R tau. Macroscopic changes in the PSP include atrophy in the frontal cortex, subthalamic nucleus, and the midbrain region, along with neuromelanin pigment loss in the substantia nigra. PSP is pathologically and clinically heterogeneous. Based on different motor phenotypes and phenotypes based on cortical manifestations, PSP can be divided as PSP- Parkinsonism (PSP-P), PSP- progressive gait freezing (PSP-PGF), PSP- Corticobasal syndrome (PSP-CBS), PSP with frontal lobe cognitive presentations (PSP-Fs), and PSP- speech/language disorder (PSP-SL)⁷⁸.

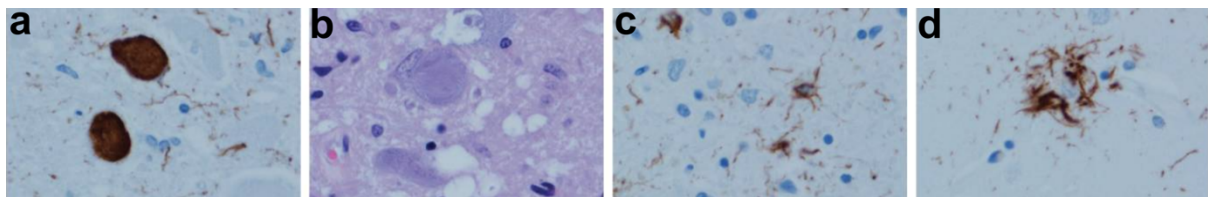


Figure 1-8 Neuropathological features of PSP.

a, Typical neuronal lesion 'globose NFT' visible with phospho-tau immunohistochemistry. **b**, 'Globose NFT' visible with Hematoxylin and Eosin (H&E) staining. **c**, Oligodendroglial 'coiled bodies' visible with tau immunohistochemistry **d**, Tufted astrocytes are visible with tau immunohistochemistry. Image is adapted from Dugger et al.³

Neuropathological criteria for PSP require globose Neurofibrillary tangles (NFTs) in subcortical nuclei, “coiled bodies” in the oligodendroglia, and tufted astrocytes (Figure 1-8). Tufted astrocytes are frequently observed in the motor cortex and neostriatum than other affected brain regions, and they are critical for differentiation of PSP from CBD. Neuronal loss in PSP is primarily observed in substantia nigra and subthalamic nucleus as well as in globus pallidus and cerebellar dentate nucleus, and it correlates with the vulnerability to neuronal, not astroglial, tau pathology³.

1.3.6 Globular glial tauopathies (GGTs)

Globular glial tauopathies are a class of 4R tauopathies which are characterized by argyrophilic and 4R-tau-immunoreactive globular oligodendroglial and non-argyrophilic, 4R-tau-immunoreactive globular astroglial inclusions⁷⁹. GGT was first identified in 1998 by Molina et al., where they observed ‘glial cytoplasmic inclusions’ (GCIs) in a temporal lobe biopsy obtained from a patient with moderate frontotemporal atrophy⁸⁰. These inclusions were described as ‘sickle or ring-shaped perinuclear inclusions’ with morphological similarities to the GCIs observed in multiple system atrophy (MSA) and strongly immunoreactive for phosphorylated tau (GCIs observed in MSA are negative for phosphorylated tau⁸¹ and positive for α -synuclein).

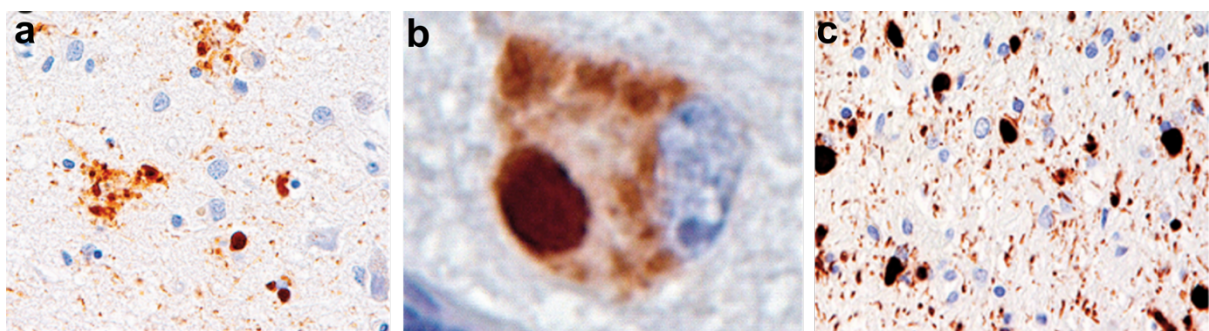


Figure 1-9 Neuropathological features of GGTs.

a, Globular astroglial inclusions (GAIs) visible with tau immunohistochemistry **b**, Spherical neuronal inclusions in frontal cortex visible with tau immunohistochemistry **c**, Globular oligodendroglial inclusions (GOIs) in white matter are visible with tau immunohistochemistry. Image is adapted from Rösler et al⁸².

Macroscopic changes in the GGTs include atrophy of the frontal and temporal lobes or precentral gyrus. Globular or small tangle-like inclusions represent neuronal tau pathology, and the anatomical distribution of tau pathology correlates with the clinical symptoms⁷⁹. GGTs have at least three subtypes; type I cases show predominant involvement of the frontotemporal lobe, and in white matter, prominent globular oligodendroglial inclusions (GOIs) are observed. Patients with restricted involvement of motor cortex and corticospinal tract along with the presence of globular oligodendroglial inclusions (GOIs) and globular astroglial inclusions (GAIs) are referred to as type II. Type III cases are characterized by the involvement of the frontotemporal lobe, motor cortex, and corticospinal tract and the abundance of globular astroglial inclusions (GAIs). According to some recent studies, some forms of GGTs may be observed in elderly individuals associated with AD-type pathology^{83,84}.

1.3.7 Pick's disease (PiD)

Pick's disease is a rare neurodegenerative 3R tauopathy characterized by the degeneration of the frontal and temporal lobes and detection of neuronal cytoplasmic Pick bodies that are immunoreactive to 3R tau and negative to 4R tau. It was first described by Pick in 1892 and neuropathologically by Alzheimer in 1911⁸⁵. Pick bodies are spherical inclusions that are clearly delimited from the cytoplasm, and they are predominantly found in the granule cells of the dentate gyrus, hippocampus, cortical areas, as well as in subcortical structures. Due to the asymmetrical distribution of the cortical atrophy, clinically, Pick's disease resembles focal cortical syndromes, such as progressive aphasia, behavioral variant frontotemporal dementia, or even corticobasal syndrome.

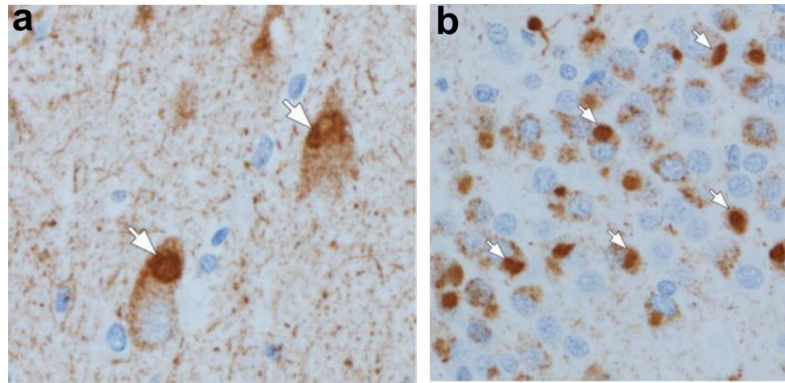


Figure 1-10 Neuropathological features of Pick's disease.

a, Pick bodies detected in pyramidal neurons of the hippocampus by phospho-tau immunohistochemistry. **b**, Pick bodies detected in granule neurons of the dentate fascia by phospho-tau immunohistochemistry. Immunohistochemistry was performed with CP13, whose epitope is near phosphoserine 202. Image is adapted from Dugger et al.³

The defining histological feature of Pick's disease is the presence of intraneuronal Pick body along with ballooned neurons ('Pick cells') which affects both pyramidal and granular-type neurons (Figure 1-10). Although the 3R isoform of tau is predominantly deposited in Pick's disease, some biochemical studies suggested a significant 4R tau pathology⁸⁶. However, the presence of 4R tau is most probably due to the associated argyrophilic grains as a secondary cause of neurodegeneration in the examined patients⁸⁷.

1.4 High-resolution structure of distinct 'strains' in different tauopathies

The structure of tau filaments from several tauopathies has been solved in recent times by cryo-electron microscopy (cryo-EM) using ex-vivo brain-derived fibrils from patients⁸⁸⁻⁹⁷. These structures can be categorized into three sections based on the pseudo-repeat domains of tau that form the filament's core (Figure 1-11). In addition, there is a correlation between the structure of the tau filaments and which isoform of tau is deposited in the diseases. For example, the structure of tau protofilaments in the tauopathies where both the 3R and 4R tau isoforms are deposited is the same/highly similar for AD, PART, FBD, and FDD with some minor differences in the case of CTE. On the other hand, the structures of the tau protofilaments in 4R tauopathies are different from the 3R+4R tauopathies, and they can be

classified into two parts, one with four-layered topology (CBD, AGD, ARTAG, cases with intronic +3/+16 mutations) and another one with elongated three-layered topology (PSP, GGT). Again, tau adopts a different filament structure in the case of the 3R tauopathy Pick's disease.

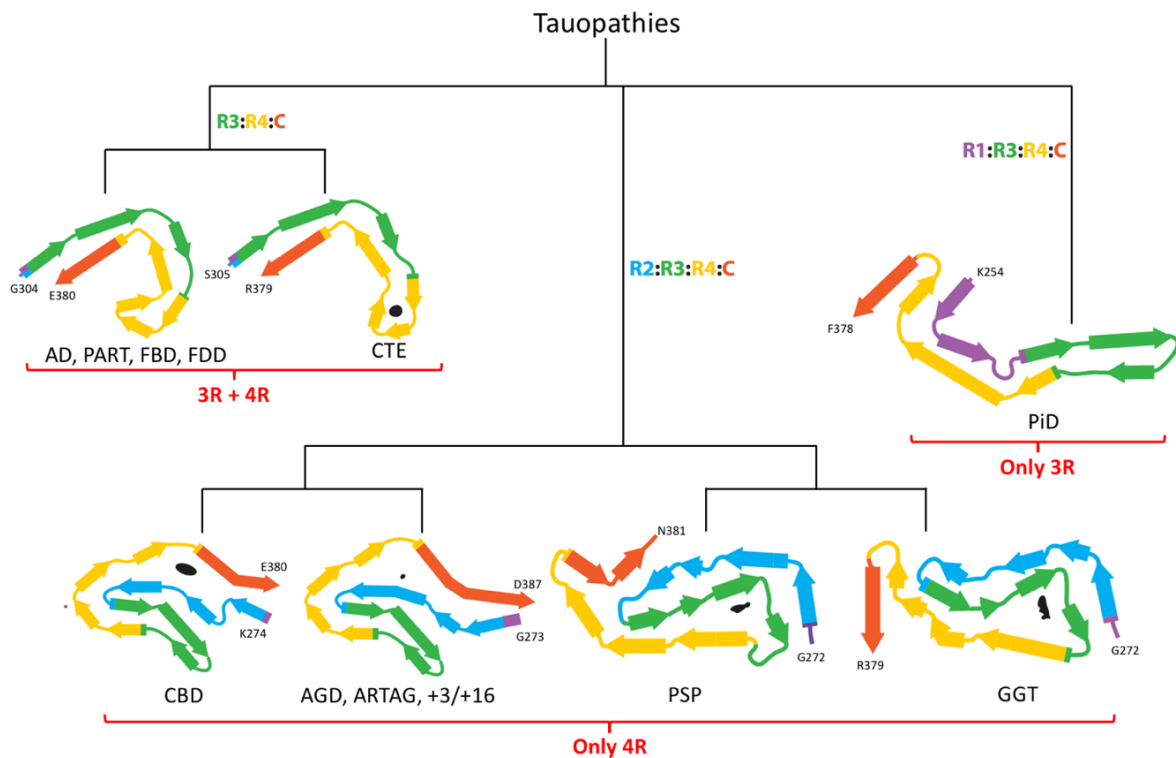


Figure 1-11 Classification of tauopathies based on the structure of tau protofilament.

Structure of tau protofilament in Alzheimer's disease (AD), Primary age-related tauopathy (PART), Familial British dementia (FBD), Familial Danish dementia (FDD), Chronic traumatic encephalopathy (CTE), Pick's disease (PiD), Corticobasal degeneration (CBD), Argyrophilic grain disease (AGD), Age-related tau astroglipathy (ARTAG), Frontotemporal lobar degeneration (FTLD) with MAPT intronic +3/+16 mutations, Progressive supranuclear palsy (PSP) and Globular glial tauopathies (GGTs) has been shown. Image is adapted from Shi, Zhang et al.^{88,97}

These distinct aggregate structures, termed amyloid "strains", can induce tau aggregation *in cellulo* and recapitulate pathological phenotypes when injected into animals⁹⁸. However, the molecular factors that lead to the formation of such well-defined amyloid strains are still mysterious.

1.4.1 Structure of tau filaments in 3R + 4R tauopathies

In 2017, Fitzpatrick et al. solved the structure of the tau filament in AD, which was the first available structure of tau fibrils in any tauopathies⁸⁹. Ultrastructurally, tau inclusions in AD are made of two different filaments, paired helical filaments (PHF) and straight filaments (SF) (Figure 1-12). Both the PHFs and SFs are composed of two C-shaped protofilament subunits, which are structurally identical and differ only at the inter-protofilament interphase. The ordered core of the protofilament is made of residues 306 to 378 comprising the complete R3, R4 repeat domain, as well as ten residues of the R' domain/C terminus domain of tau. The core is composed of eight beta sheets running along the length of the protofilament. In PHFs, two protofilaments pack symmetrically, and the interface is formed by anti-parallel stacking of residues ₃₃₂PGGGQ₃₃₆. In SFs, two protofilaments pack asymmetrically with the backbone nearest to each other between residues ₃₂₁KCGS₃₂₄ (in the first protofilament) and ₃₁₃VDLSK₃₁₇ (in the second protofilament). In addition to the ordered core, additional weaker densities have been observed at the filament's N and C terminus. These weaker densities arise from the more dynamic regions of tau. In addition to the densities at N and C terminus, additional densities around the side chains of K317, T319, and K321 have been observed in both the PHFs and SFs. This density was reported to be strongest in SFs near the protofilament interface. Currently, the details of the additional densities near lysine side chains are unknown. However, the authors speculated that this might correspond to the presence of some N-terminal residues (γ EFE γ) or some unknown co-factors⁸⁹. In another study, the structure of tau filaments from 17 cases (15 sporadic and 2 inherited) of AD have been reported to be identical, suggesting a critical interplay of the structure of tau filament with the progress of the disease⁹¹.

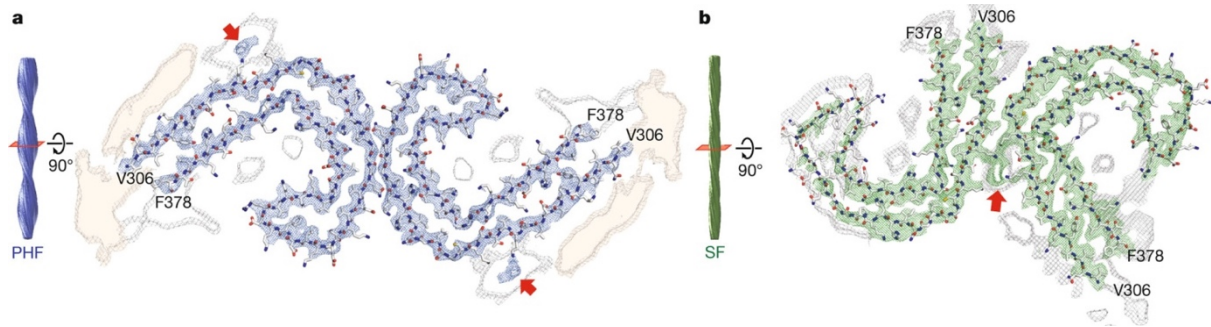


Figure 1-12 Structure of PHFs and SFs in AD.

a, Cryo-EM density and atomic model of PHFs **b**, Cryo-EM density and atomic model of SFs. Additional electron density both at the C and N-terminus is observed. Additional densities near the lysine residues are highlighted with red arrows. The image is taken from Fitzpatrick et al.⁸⁹

Tau inclusions in CTE are composed of two kinds of filaments, type I and type II. The type I and type II filaments are composed of precisely same protofilament core, but they differ in their inter-protofilament interface⁹⁰ (Figure 1-13). The ordered core of the protofilament is composed of residues 305 to 379, and the structure of the protofilament is very similar to the AD protofilament with minor differences near $\beta 4$, $\beta 5$, $\beta 6$ regions. Due to the minor difference in the structure, the CTE-protofilament adopts a more open conformation than the AD- protofilament. In CTE protofilament, an additional density (primarily hydrophobic) is observed, surrounded by the hydrophobic side chains of V339, L344, F346, V350, I354, and the hydroxyl group of S341, S352 residues. The signal from this additional density is as strong as of tau, suggesting a near stoichiometric occupancy. The additional density does not connect to the densities of tau, suggesting that the density interacts hydrophobically with the residues of tau. The minor difference between the structure of AD and CTE protofilament was suggested to be due to the presence of this additional hydrophobic molecule. Details about this additional hydrophobic density are currently unknown. However, it might arise due to the presence of some co-factors like non-polar sterols and sterol derivatives as well as fatty acids with short aliphatic chains.

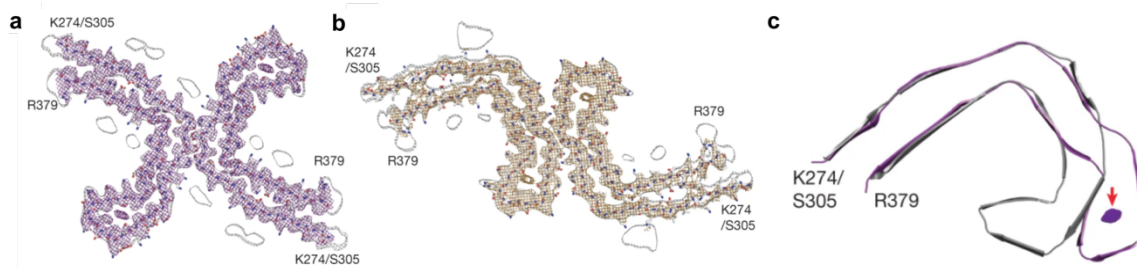


Figure 1-13 Structure of tau filaments in CTE.

a, Cryo-EM density and atomic model of type I CTE filament **b**, Cryo-EM density and atomic model of type II CTE filament. **c**, Comparison of the AD (in black) and CTE protofilament (in purple). Additional electron density in CTE protofilament is highlighted with a red arrow. The image is adapted from Falcon et al.⁹⁰

In PART (an AD-like tauopathy where only tau pathology is present), the structure of the tau filament is identical to tau filaments from AD. Like AD, both PHFs and SFs are present in PART. Only in one patient with PART, along with PHF and SF, the CTE type I (around 13 %) filament structure was also observed⁹².

The tau filaments from patients with FBD and FDD have the same structure as AD PHFs. Only in one case of FBD, AD SFs and CTE type I filaments were observed along with AD PHFs. The presence of CTE type I filaments is most probably a result of head trauma resulting from ataxia in that particular case^{88,97}.

1.4.2 Structure of tau filaments in 4R tauopathies

Tau inclusions in CBD are made of two types of filaments, type I and type II. Type I filaments are composed of a single protofilament, whereas type II filaments are made of two identical type I protofilaments⁹⁴ (Figure 1.14a). The protofilament adopts a four-layered fold and is composed of residues 274 to 380 comprising the last residue of R1, the complete repeats R2, R3, and R4, as well as 12 residues of the R' domain of tau. The ordered core of one protofilament comprises 11 β -strands, three from R2, three from R3, four from R4, and one from the sequence after R4. In type II filaments, two protofilaments are related by C2 symmetry, and the protofilament interface is formed by anti-parallel stacking of

³⁴³KLDFKDR³⁴⁹ residues. An additional density is observed within the hydrophilic cavity of the filament's core, with the side chains of K290, K294, and K370 pointing towards it. As the additional density is not connected to tau density, it probably does not represent post-translational modifications of lysine residues. The additional density is as strong as of tau, suggesting near stoichiometric occupancy. The additional density has a dimension of 9 Å by 4 Å, and the attempts to solve its structure have not been successful yet. As the density is present within a hydrophilic environment, it indicates the presence of a polyanionic molecule which is most likely incorporated during filament formation. Therefore, it can also be possible that this negatively charged molecule stabilizes the CBD fold during initial filament assembly.

The structure of tau filaments from another 4R tauopathy, AGD, has been recently determined^{188,97}. Three different filaments are present in AGD, type I (Figure 1-14b), type II (Figure 1-14c), and type III. All three filaments consist of a common protofilament core that adopts a four-layered structure similar to CBD. The type I filament comprises residues 273 to 387 and consists only of a single protofilament like CBD type I filaments. The type II filament is made of two protofilaments packed against each other with C2 symmetry, and each protofilament comprises residues 279 to 381. The structure of the type III filaments is not solved with sufficient resolution, but the low-resolution structure suggests an asymmetric packing of two protofilaments with similar folds. A large region of the AGD protofilament adopts the same conformation to the CBD protofilament with differences in the C-terminal segment. The C-terminal segment (residues 368 to 386) of the AGD protofilament interacts differently with R2 as it comprises seven more residues at the C-terminus compared to CBD. Like in CBD, an additional non-tau density is observed between K294 and K370 in AGD. However, the size of the additional density is smaller in comparison to CBD. Apart from these three types of filaments, both AD PHFs, SFs, as well as CTE type I filaments are observed in AGD. This is likely because AGD is commonly found together with other tau pathologies.

ARTAG is another 4R tauopathy where astroglial tau pathology is observed. Like AGD, ARTAG also coexists with other tau pathologies. The structures of tau filaments from ARTAG

are primarily identical to AGD type II and type III filaments. Apart from this, AD PHFs and SFs were also observed in ARTAG^{88,97}.

In MAPT, +3/+16 mutations in intron 10 give rise to a 4R tauopathy that belongs to Frontotemporal lobar degeneration (FTLD). The structure of tau filaments in this 4R tauopathy is similar to AGD type I and type II filaments^{88,97}.

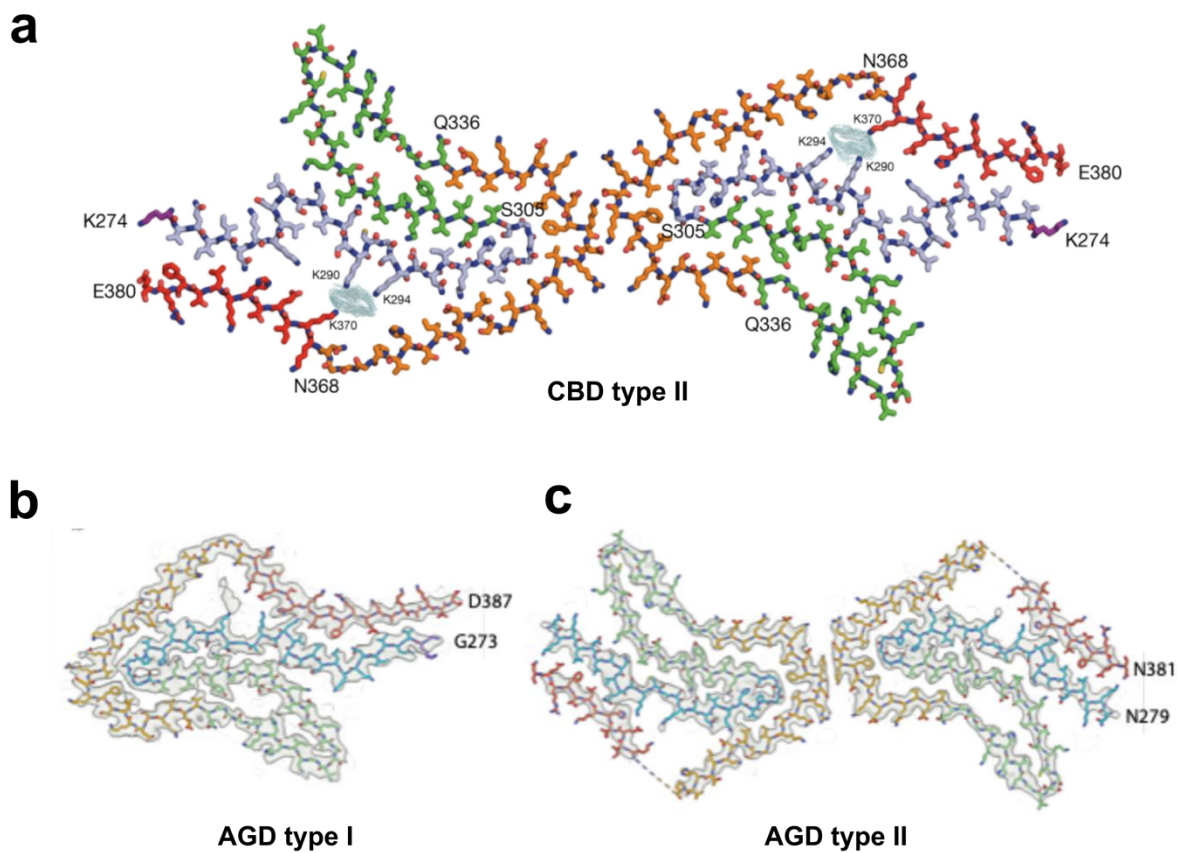


Figure 1-14 Structure of tau filaments in CBD and AGD.

a, Atomic model of type II CBD filament. Each protofilament is made of one type I filament. Extra electron density between K290, K294, and K370 is shown in light green. **b**, Cryo-EM density and atomic model of type I AGD filament. **c**, Cryo-EM density and atomic model of type II AGD filament. The image is adapted from Zhang et al.⁹⁴ and Shi, Zhang et al.^{88,97}

The structures of tau filaments from different subtypes of PSP (PSP-RS, PSP-CBS, PSP-P, and PSP-F case I) have also been solved^{88,97}. All PSP subtypes are composed of a single protofilament that adopts a significantly different three-layered structure when compared to CBD/AGD (Figure 1-15a). However, the core comprises a similar region (residue 272 to 381) of tau. In the PSP protofilament, the repeat domains R2, R3 and R4 form a three-layered structure with turns at the conserved PGGG motifs at the end of each repeat. In this three-layered structure, R3 forms the middle layer and R2 packs against R3. Two non-tau densities are observed at the interface between R2-R3; the first one is most probably a non-polar molecule present between residues N279 and G323. The second one is most likely a solvent molecule present next to the salt bridge between K294 and D314. At the R3-R4 interface, a larger cavity between K317, K321, and K340 exists that includes an additional non-tau electron density. This additional electron density has a similar dimension (9 Å by 4 Å) to the density observed in the case of CBD filament between K290, K294, and K370⁹⁶. Assuming that the additional density found in CBD and PSP are made of the same polyanionic molecule, the emergence of different molecular polymorphs (CBD and PSP protofilament) thus might be regulated by certain co-factors.

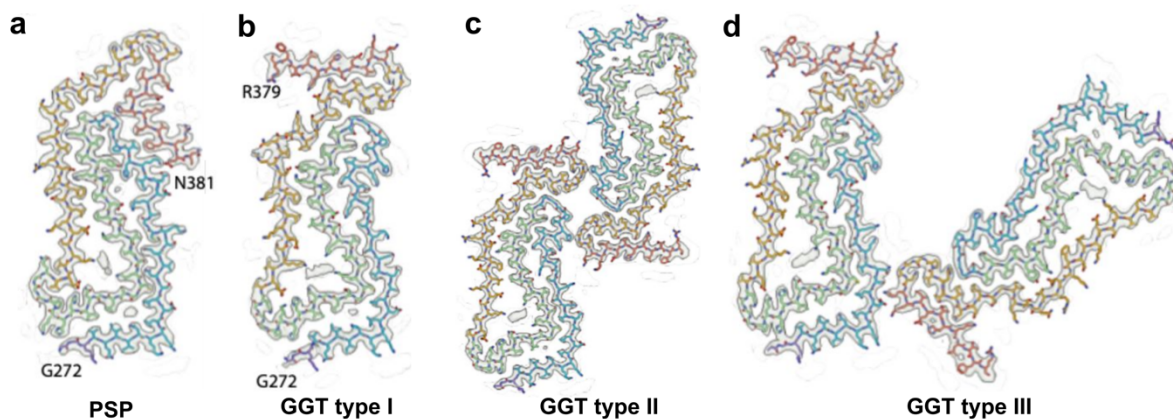


Figure 1-15 Structure of tau filaments in PSP and GGT.

a, Cryo-EM density and atomic model of PSP filament. **b**, Cryo-EM density and atomic model of type I GGT filament. **c**, Cryo-EM density and atomic model of type II GGT filament. **d**, Cryo-EM density and atomic model of type III GGT filament. The image is adapted from Shi, Zhang et al.^{88,97}

Tau filament structures from two different subtypes of GGTs, GGT-I (type I) and GGT-II (type II), have been solved^{88,97} (Figure 1-15b,c,d). Both GGT-I and GGT-II show a three-layered fold comparable to PSP-fold and composed of an ordered core comprising residues 272 to 379. Like in the case of PSP, each chain turns after the conserved PGGG motifs in the GGT protofilament, but the conformation of each turn is different in comparison to PSP. Also, the C-terminal segment in GGT points to the opposite direction in comparison to the PSP counterpart. In GGT-I, three different filaments (type I, type II, and type III) are observed. The type I filament is made of a single protofilament. The type II filament is made of two type I protofilaments with 21 screw symmetry, and the type III filament is made of two type I protofilaments packed asymmetrically. In GGT-II, only type II and type III filaments are observed.

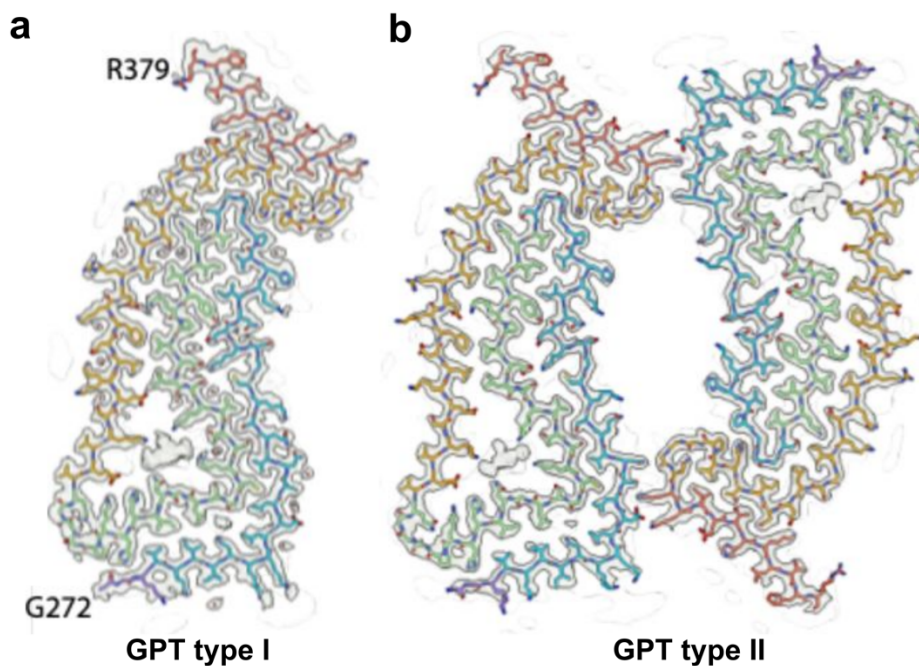


Figure 1-16 Structure of tau filaments derived from a particular case of PSP-F termed as GGT-PSP tau

a, Cryo-EM density and atomic model of type I GPT filament. **b**, Cryo-EM density and atomic model of type II GPT filament. The image is adapted from Shi, Zhang et al.^{88,97}

The same study, which reported the structure of PSP and GGT filaments, reported a different filament structure in one patient diagnosed with PSP-F (case 2, filament taken from frontal

cortex)^{88,97}. As the fold of the tau filament from this specific PSP-F case was found to be comparable with both the PSP and the GGT fold, the authors coined a new name for this fold, GGT-PSP-tau or GPT fold (Figure 1-16). The GPT fold also comprises a similar three-layered structure, and the C-terminal segment also turns in the same direction as in GGT (i.e., in the opposite direction compared to PSP) but with a different conformation. Two different filaments were reported to have the GPT fold in this particular PSP-F case. Type I GPT filaments comprise only a single protofilament, whereas type II GPT filaments are made of two protofilaments packed in an opposite direction.

1.4.3 Structure of tau filaments in 3R tauopathy

The structure of tau filaments from only one 3R tauopathy, Pick's disease, has been solved to date⁹³. Ultra-structurally, Pick-bodies are formed with two types of filaments, narrow pick filaments (NPFs) (around 93 % of total) and wide pick filaments (WPFs) (approximately 7 % of total) (Figure 1-17). NPFs are composed of a single protofilament with an elongated structure, while the WPFs are composed of two NPFs attached through their distal parts. The ordered core of the NPF is composed of residues 254 to 378 of 3R tau comprising a significant portion of R1, the complete R3 and R4 repeats, as well as ten residues after R4. A total of nine β -strands are present in the NFT, two from R1, three from R2 and R3 each, and one from the sequence after R4. Unlike the case of tau filaments from most 4R tauopathies (CBD, AGD, PSP, GGT), no additional electron densities were observed inside the filament's core of NFT. The structure of the WPFs could not be solved at high-resolution due to the lower abundance of these filaments.

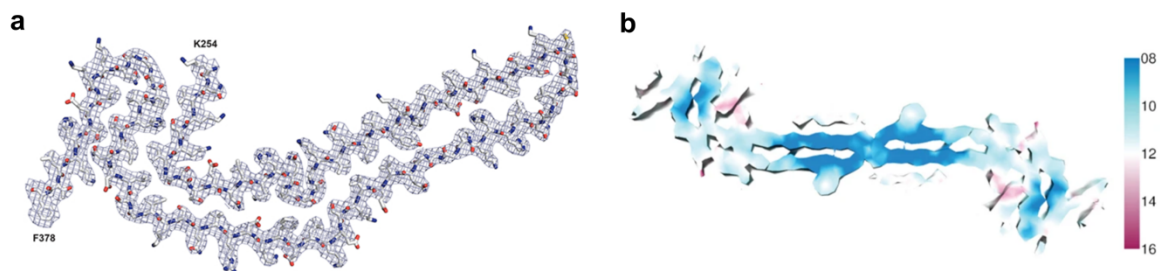


Figure 1-17 Structure of tau filaments in Pick's disease.

a, Cryo-EM density and atomic model of narrow pick filament (NPF). **b**, Cryo-EM density of wide pick filament (WPF). Local resolution estimation has been shown with a colour gradient. The image is adapted from Falcon et al.⁹³

1.5 *In vitro* aggregation of tau in presence of co-factors

Tau is presumed to be one of the most soluble proteins, and unlike other amyloidogenic proteins (prion protein, α -synuclein, amyloid- β), to date, self-aggregation of full-length tau protein is not reported under physiological conditions or even using extreme pH conditions. In the last decades, several methods were reported to aggregate the full-length isoforms of tau *in vitro*, mainly in the presence of polyanionic molecules such as RNA⁹⁹, fatty acids^{100,101}, polyglutamates¹⁰² or sulphated glycosaminoglycan such as heparin^{103,104}. These negatively charged co-factors induce tau aggregation by neutralizing the positively charged residues present in the repeat domain of tau, containing the hexapeptide motifs essential for aggregation, thereby increasing the intermolecular hydrophobic interactions leading to fibril formation.¹⁰⁵⁻¹⁰⁸ Among all of the negatively charged co-factors, heparin-induced aggregation of tau has been extensively used as an *in vitro* model system to identify novel small molecule inhibitors^{109,110} of tau aggregation as well as to investigate the effect of different mutations¹¹¹⁻¹¹³ and post-translational modifications¹¹⁴⁻¹¹⁷ on the aggregation of tau.

Low-resolution electron micrographs along with different biochemical experiments were used to suggest that the *in vitro* heparin-induced tau filaments are similar to the filaments derived from the brain of patients with different tauopathies. However, the relevance of the heparin-induced tau filaments has recently been questioned as outlined below. The seeding activity of heparin-induced 0N4R P301S tau was reported to be much lower than the seeding activity using sarkosyl-insoluble tau from the brain of transgenic mice expressing human 0N4R P301S tau¹¹⁸. Another study revealed differences between tau filaments seeded by heparin-induced *in vitro* fibrils and tau filaments seeded using brain-derived filaments from AD¹¹⁹. Finally, the atomic structures of heparin-induced tau filaments using recombinant 2N4R and 2N3R tau proteins were solved by cryo-EM, demonstrating that the heparin-induced filaments are polymorphic and structurally different from brain-derived tau filaments¹²⁰.

1.5.1 Structure of *in vitro* heparin-induced tau filaments

Heparin-induced aggregation of 2N4R tau leads to the formation of four polymorphs – snake filaments (~45 %), twister filaments (~30 %), hose filaments (~20 %), and jagged filaments (~5 %). All of the filaments adopt a completely different structure than tau filaments derived from different 4R or 4R+3R tauopathies (Figure 1-18). The ordered core of the snake filament is composed of residues 272 to 330 comprising the last three residues of R1, entire R2, and most of the R3 domain. A total of six β -strands are present in the ordered core with three beta strands from R2 and R3 each, and four of these strands pack against each other (β 1- β 5 and β 2- β 4), forming a cross β -sheet. A total of 12 positively charged residues (9 lysines and 3 histidines) and 3 negatively charged (all aspartates) residues are present inside the core of the snake filament, with all aspartate residues pointing inside the filament core (forming salt bridges), and most of the positively charged residues pointing outside the filament core. A large diffused external density is observed around the side chains of the positively charged residues. This diffused density most likely corresponds to the presence of heparin on the surface of the filament.

The twister filament is composed of a smaller ordered core compared to the snake filaments and comprises residues 274 to 321, i.e., the last residue of R1, entire R2, and half of the R3 repeat. Four β -strands are present in the core of the twister filament, two from each R2 and R3. In the ordered part of R3, the secondary structure of the twister is comparable to the snake filament. The secondary structure of the R2 ordered part in the twister is different than the snake resulting in a more polar interior and more hydrophobic exterior than that of snake filament. Due to the low electron density between residues 293 to 303 (which forms the hammerhead arc) in twister filament, no atomic model is available for this region.

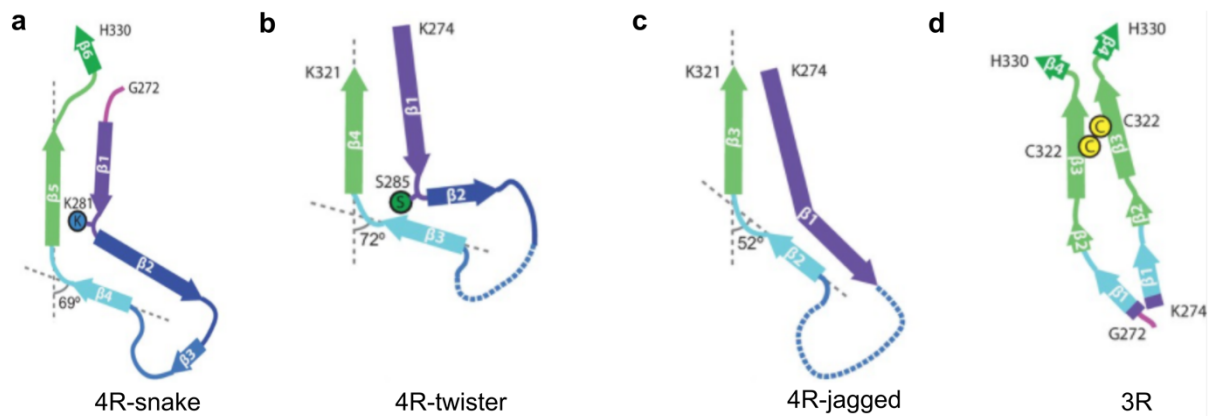


Figure 1-18 Structure of *in vitro* heparin-induced tau filaments.

a, Atomic model of heparin-induced 2N4R tau ‘snake’ filament. **b**, Atomic model of heparin-induced 2N4R tau ‘twister’ filament. **c**, Atomic model of heparin-induced 2N4R tau ‘jagged’ filament. **d**, Atomic model of heparin-induced 2N3R tau filament. The image is adapted from Zhang et al.¹²⁰

The ordered core of the jagged filament is similar to the twister filament comprising residues 274 to 321 and consists of three beta-strands. As in the other two filament types, the ordered part of R3 adopts a similar secondary structure. Also, no atomic model is available for the hammerhead arc region (residue 293 to 303) due to low electron density suggesting increased flexibility of this region in the case of all heparin-induced 4R tau fibrils.

Heparin-induced 2N3R tau filaments are less polymorphic (~ 98 % forms the same structure) than their 4R counterparts and form a different structure than those of the 2N4R tau filaments. Unlike the case of heparin-induced 2N4R tau filaments, heparin-induced 2N3R tau filaments contain two tau molecules in each rung arranged in a parallel cross- β packing. The ordered core of one tau molecule is composed of residues 274 to 330, and another molecule is composed of residues 272 to 330. The structure of this tau filament is also very different from the structure of tau filament in Pick’s disease.

Apart from the structural differences when compared to the brain-derived filaments, another striking observation for all heparin-induced tau filaments is the charge distribution of the residues facing outwards of the filament’s core. Unlike the case of brain-derived fibrils, where

both positively and negatively charged residues face outwards, mainly the positively charged residues face outwards in heparin-induced fibrils. This is due to the absence of the R4 domain in the core for heparin-induced fibrils, which contains the greatest number of negatively charged residues among the repeat domains. Thus, the *in vitro* structures, which formed by neutralizing the positive charges on the filament by the negatively charged heparin, cannot represent the brain-derived filament's structure, and most likely, these *in vitro* structures will not be stable in the brain¹²⁰.

1.5.2 Drawbacks of *in vitro* heparin-induced aggregation protocol of tau

As discussed in the sections before, the major drawback of the heparin-induced aggregation protocol of tau is the generation of *in vitro* tau filaments that are polymorphic, consist of much shorter cores than the brain-derived filaments, and adopt a significantly different fold when compared to all of the brain-derived filaments. Another drawback of the heparin-based *in vitro* fibrilization assay is the high negative charge of heparin: heparin-induced tau fibrillization has been extensively used to search for small molecules as tau aggregation inhibitors^{121,122}, potentially generating false hits due to electrostatic interactions between the small molecules and heparin. Due to the same reason, heparin-based fibrilization assays are not ideal for studying the effect of different post-translational modifications (for example – acetylation, phosphorylation, etc.) as the high negative charge of heparin can override the impact of PTMs. Thus, the development of a better *in vitro* protocol of tau aggregation is essential, especially a protocol where full-length tau can be assembled in the absence of co-factors.

1.6 Spreading of tau fibrils in brain

Tau pathology in the brain follows a 'prion-like' behavior with transneuronal propagation of tau aggregates from one brain region to another through connected neuronal networks⁹⁸. This process is called templated misfolding, and via this, pathological tau seeds can propagate from an affected cell to a healthy cell. Pathological tau spreads in the brain in an anatomically hierarchical manner and are categorized into six Braak stages⁵⁷ (Figure 1-5,

section 1.3.2). The inter-cell transmission of the tau seeds occurs in several steps (Figure 1-19). In the first step, both the physiological and pathological tau (seeds) get released to the extracellular space via synaptic vesicles¹²³, extracellular vesicles such as exosomes¹²⁴, or direct translocation across the membrane¹²⁵. In the following step, tau seeds are taken up from the extracellular space by healthy neurons via different mechanisms, such as bulk endocytosis¹²⁶, clathrin-mediated endocytosis¹²⁷, or via macropinocytosis by heparan sulphate proteoglycans¹²⁸. In the last step, these taken-up tau seeds damage the endocytic vesicle¹²⁹, get released to the cytoplasmic compartment of the healthy neuron, and then seed the physiological tau to fibrils, thereby spreading the pathology.

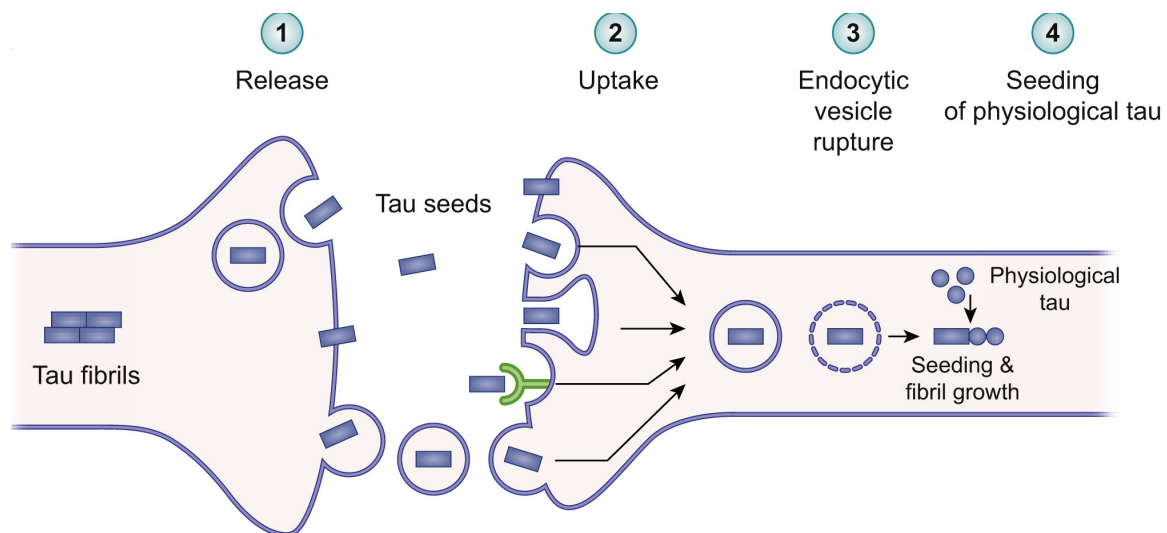


Figure 1-19 Transneuronal spreading of tau pathology in the brain.

The image is taken from Vogels et al.¹³⁰

1.7 Post-translational modifications (PTMs) of tau

Post-translational modification (PTM) refers to the covalent modification of specific amino acid residues of a protein generally by different enzymes after its translation by ribosomes. PTMs change the electrostatic properties of a protein, thereby influencing the structure of the protein, as well as protein-protein interactions and protein aggregation. Intrinsically disordered proteins (IDPs) do not have a well-defined structure, unlike structured proteins, thus making them more vulnerable to different PTMs.

Tau, a classic example of an intrinsically disordered protein, can be modified by countless PTMs¹³¹. Almost 35% of residues in tau (serine, threonine, tyrosine, lysine, arginine, asparagine, histidine, and cysteine) are susceptible to undergo different PTMs. In tau, serine (S), threonine (T), and tyrosine (Y) residues undergo phosphorylation; lysine (K) residues undergo acetylation, ubiquitination, SUMOylation, methylation, and glycation; arginine (R) residues undergo methylation. Attachment of sugar residues, like O-GlcNAcylation, N-glycosylation, and glycation is also observed in tau.

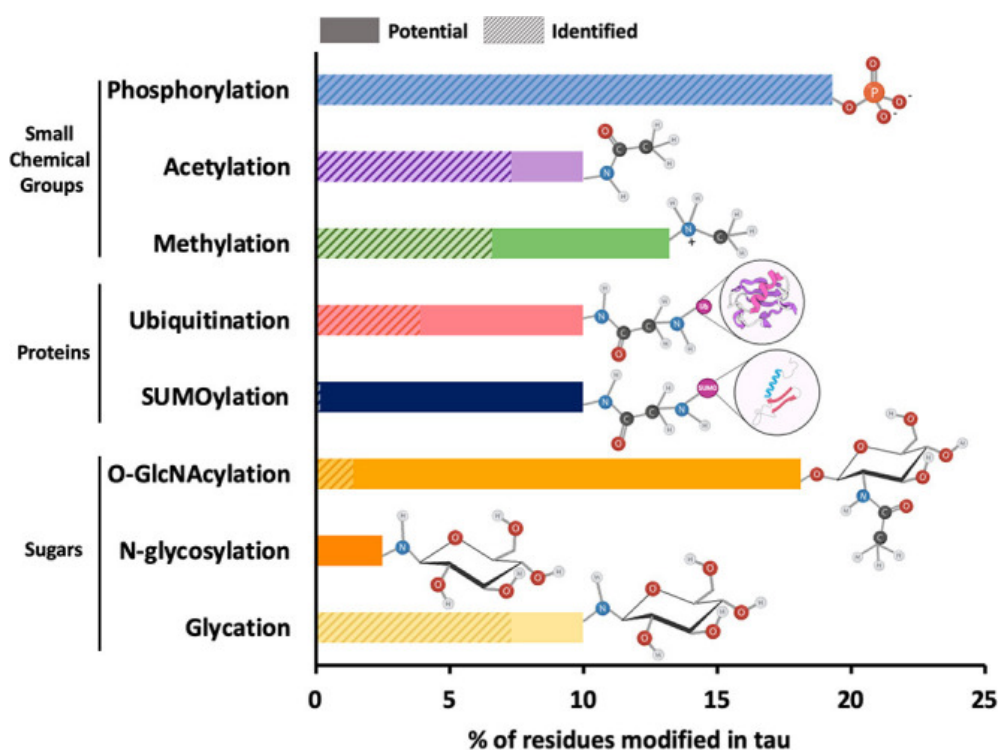


Figure 1-20 Frequency of different post-translational modifications on 2N4R tau.

Solid bar and shaded bars refer to potential and identified modifications of tau, respectively. The image is taken from Alquezar, Arya et al.¹³¹

Phosphorylation is the most abundant PTM observed in tau. The longest isoform of tau, 2N4R tau, has 85 potential sites for phosphorylation. Among these, around 20 sites have been found to undergo phosphorylation in healthy brain¹³². However, under pathological conditions, i.e., in the diseased brain, around 44 sites have been identified to undergo hyperphosphorylation¹³³. Several serine/threonine kinases are responsible for

phosphorylating tau in the brain. This includes glycogen synthase kinase 3 (GSK3), microtubule affinity-regulating kinases (MARK), cyclin-dependent kinase 5 (cdk5), calmodulin-dependent protein kinase II (CaMKII), casein kinase 1 (CK1) and cyclic AMP-dependent protein kinase (PKA). Furthermore, several tyrosine kinases, such as FYN, SYK and ABL, can phosphorylate tau's tyrosine residues. Phosphorylation of tau inside the microtubule-binding domain (e.g., S262, S214) has been reported to reduce the affinity towards the negatively charged microtubules leading to the destabilization of microtubule assembly^{134,135}. Hyperphosphorylation of several residues in the KXGS motifs of tau has been identified in NFTs of several tauopathies¹³³. Phosphorylation within these motifs impair the neurite outgrowth¹³⁶, deregulates the axonal transport¹³⁷ leading to synaptic dysfunction and neurodegeneration¹³⁸. Some of the residues outside the microtubule-binding domain (S396, S404, S422) have been identified to be abnormally hyperphosphorylated in the diseased brain¹³⁹. However, phosphorylation of these residues does not affect the microtubule binding but can influence tau aggregation¹⁴⁰. Several reports suggested that tau phosphorylation might lead to the development of tauopathies; however, the exact mechanism behind how phosphorylation regulates the function and aggregation of tau *in vivo* remains elusive.

Acetylation of lysine residues in tau has emerged as one of the critical PTM observed in different tauopathies. The longest isoform of tau, 2N4R tau, consists of 44 lysine residues distributed throughout the tau sequence. Two histone acetyltransferases (HATs), p300, and its close homolog CREB-binding protein (CBP) can efficiently acetylate tau *in vitro*^{141,142}, and histone deacetylase 6 (HDAC6) and NAD⁺-dependent sirtuin 1 (SIRT1) are the major deacetylases of tau^{142,143}. Disease-specific dysregulation of HATs and HDACs involved in tau acetylation has been observed in different tauopathies.^{144,145} For example, increased activity of p300/CBP was reported in FTLD-tau patient's brains, whereas both the activity and levels of p300/CBP were found to be lower in the brain of AD patients^{145,146}. Also in AD brain, the expression of SIRT1 is reduced while the expression of HDAC6 increases suggesting an opposite effect of these deacetylases on tau function and dysfunctions^{143,147}. Also, SIRT1 deacetylation has been found to be protective against tau accumulation in a tauopathy

mouse model; on the other hand, HDAC6 deacetylation of tau increases tau phosphorylation, thereby inducing tau aggregation *in vitro*^{115,148}. The acetylation of a specific lysine residue present in the microtubule-binding domain (K280) of tau was reported to decrease the affinity towards microtubules, thereby destabilizing the microtubule network and inducing tau aggregation¹¹⁴. Also, acetylation of a specific lysine residue (K174) outside the microtubule-binding domain of tau was found to induce tau aggregation¹⁴⁴. In contrast to these reports, HDAC6-regulated tau acetylation at KXGS motifs reduces tau phosphorylation and aggregation¹⁴⁹. In this regard, the acetylation of four lysine residues (K259, K290, K321, and K353) present in the KXGS motifs was found to be reduced in tauopathy brains¹⁴⁹. A recent report suggested the inhibition of chaperone-mediated autophagy by acetylated tau resulting in the propagation of tauopathy in mice¹⁵⁰. It has also been shown that reducing acetylated tau by p300 inhibition is neuroprotective in brain injury¹⁵¹.

Several groups have studied the effect of lysine acetylation on tau aggregation; however, the results from these studies are contradictory. Cohen et al. reported an enhanced aggregation of the K18 fragment of tau (comprising the microtubule-binding domain) upon acetylation in the presence of CREB-binding protein (CBP)¹¹⁴. On the other hand, another study from Cook et al. reported inhibition of aggregation upon acetylation of ON4R tau in the presence of p300 acetyltransferase¹⁵². The same study also reported a complete reversal of acetylation and aggregation inhibition upon the addition of deacetylase HDAC6. Both of these studies used heparin-induced aggregation of tau to study the effect of acetylation on tau aggregation, which is not ideal due to the high negative charge of heparin. Moreover, these contradictory results might arise due to the presence of full-length tau (ON4R) in one case and only the microtubule-binding repeat domain (K18) of tau in the other case. Another study reported that tau can undergo acetylation in the absence of acetyltransferases attributing to a previously unknown role of tau as an acetyltransferase¹⁵³. Two cysteine residues of tau (C291 and C322) were identified as the catalytic residues responsible for the unique function of tau.

1.7.1 Role of PTMs in determining different 'strains' of tau filament

Tau forms distinct fibril structures in different diseases, which are often referred to as 'strains'. However, the molecular factors that drive the formation of distinct disease-specific tau strains are largely unknown. One of the potential factors that lead to the emergence of distinct strains is post-translational modification (PTM). Based on the inception of tau pathology in a particular region of the brain, different brain regions might exert different PTMs that then could influence tau filament structure in different tauopathies. Depending on the location and role of modifications in fibril formation, Li *et al.* categorized the modifications in four classes – class I to IV¹⁵⁴ (Figure 1-21). Class I modifications refer to the modification in the interior of the fibril core. These kinds of modifications arise due to the PTMs of different tau residues pointing towards the interior of the filament or the presence of co-factors at the interior of filament, which can play a crucial role in establishing tau protofilament folds. One classic example of a Class I modification found in the filaments from different tauopathies is the presence of the hydrophobic co-factor in CTE (discussed in section 1.4.1) and the hydrophilic co-factor in CBD and PSP (discussed in section 1.4.2). Class II and III modifications refer to those on the exterior of the fibril core. These kinds of modifications can preferably select a particular fold of the protofilament (Class II) or the inter-protofilament interface (Class III). In the cryo-EM maps of all brain-derived tau filaments, extra density around the fibril surface is present. These extra densities might correspond to the PTMs of the residues pointing outwards the filaments' core, thus selecting only some allowed conformations of the protofilament and the inter-protofilament interface.

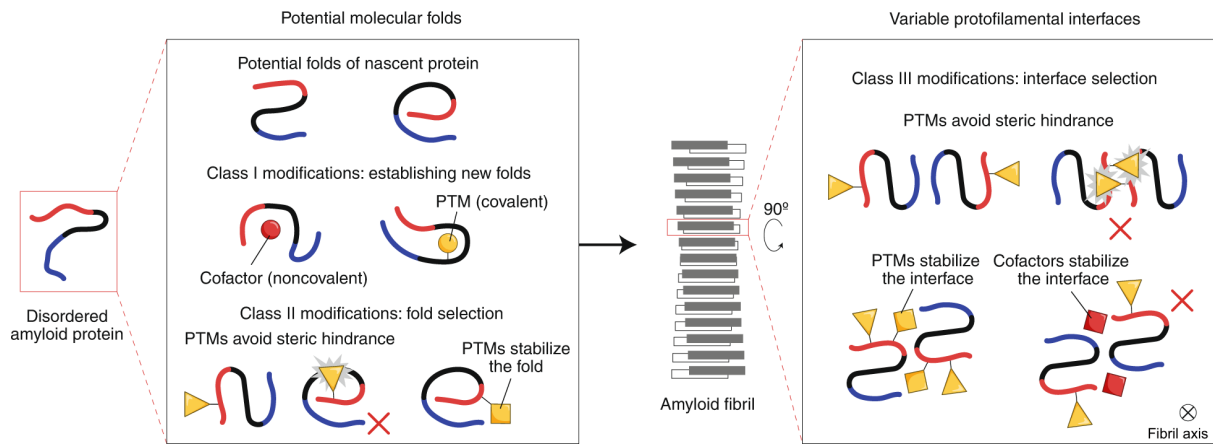


Figure 1-21 Classifications of different chemical modifications of amyloid fibrils.

The image is taken from Li et al.¹⁵⁴

The last class of modifications, i.e. Class IV, are the modifications of the residues not involved in the filament core. As only ~30% of tau residues form the core of the fibril (considering the longest isoform 2N4R tau) in different tauopathies, the remaining ~70% of the dynamic region (fuzzy coat) of tau are subjected to extensive PTMs. However, the influence of PTMs of the residues present in the fuzzy coat on the structure of the rigid core of different tau filaments is currently unknown.

1.7.2 Acetylation as an important PTM to determine distinct tau 'strains'

Lysine acetylation is one of the crucial PTMs of tau that plays a significant role in the pathogenic progression of different tauopathies^{142,155,156}. Lysine residues are distributed throughout the sequence of tau, and acetylation of the lysine residues present within the core of the tau filament can influence both the fold of the protofilament (Class I and II according to the classification of Li et al.¹⁵⁴) and the inter-protofilament interface (Class III). The selection of a specific protofilament fold and inter-protofilament interface might depend more on the PTMs of lysine residues when compared to other residues because the side chain of the lysine is long, which gets bulkier upon modifications and thus can exert severe steric hindrance in the vicinity. The lysine residues undergoing acetylation in different tauopathies have been reported in recent studies^{95,157}. Also, the acetylated lysine residues have been precisely mapped on the cryo-EM structures of tau filaments in AD and CBD⁹⁵. Notably, different

tauopathies are associated with distinct patterns of acetylation, suggesting a critical role played by acetylation on the emergence of distinct tau strains.

1.8 Aims and outline

The aggregation of tau protein into insoluble amyloid fibrils is a pathological hallmark of different neurodegenerative disorders, referred to as tauopathies. However, the emergence of distinct tau aggregate structures termed 'strains' in different diseases remains mysterious. Increasing evidence implies that the tau fibrils' structure varies between distinct tauopathies. This advocates that tau fibril structure-based molecular pathology might not only assist in stratifying patient groups but also in designing personalized medicines to treat these deadly diseases. Concurrently, we do not know the reason behind the emergence of different structures of tau fibrils in different diseases, as well as the molecular factors that drive tau into distinct amyloid strains. Insights into these questions would be critical in designing and developing therapeutic interventions in different tauopathies.

A prime hurdle towards this goal was the high solubility of tau. Thus, a crucial advancement was the finding that negatively charged co-factors can efficiently fibrillize tau *in vitro*^{102,103}. Among all the co-factors, heparin is a remarkably effective one and thus has been extensively used to investigate the molecular mechanisms of tau aggregation. The shorter constructs of tau comprising the repeat domains have been shown to further accelerate aggregation when potentially combined with different genetic mutations^{108,158,159}. However, the comparison of the structure of tau filaments derived from the brain and heparin-induced tau fibrils revealed that the heparin-induced tau filaments differ drastically from those derived from patients. This questioned the findings of an enormous number of studies that used heparin-induced aggregation to gain insight into the molecular factors that drive the aggregation of tau into amyloid fibrils. In addition, we are still in a situation where we know about the existence of distinct tau strains, but do not know the causes behind the formation of these strains.

The work of this thesis aims to unravel the molecular factors that drive the formation of distinct tau strains in different tauopathies. To this end, the following strategy was taken:

1. Development of an *in vitro* method to aggregate full-length tau protein in the absence of co-factors.
2. Characterization of co-factor-free tau fibrils with different biochemical and biophysical methods and structural characterization using solid-state NMR spectroscopy.
3. *In vitro* and in cell (through collaboration) seeding of co-factor-free tau fibrils.
4. To study the interaction of co-factor-free tau fibrils with different RNAs and compare it with the heparin-induced tau fibrils.
5. To investigate the effect of acetylation on the co-factor-free aggregation of 4R and 3R tau.

2. Materials and methods

The sections 2.12, 2.13.4, 2.13.5.1, 2.14.1, 2.14.2, 2.15, 2.16, 2.17 are taken from the following article –

Chakraborty P., Rivière G., Liu S., Ibáñez de Opakua A., Dervişoğlu R., Hebestreit A., Andreas L. B., Vorberg I. M., & Zweckstetter M.

Co-factor-free aggregation of tau into seeding-competent RNA-sequestering amyloid fibrils *Nat Commun* **12**, 4231 (2021)¹

The sections 2.5.2, 2.5.3, 2.7, 2.8, 2.9, 2.10, 2.11, 2.13.2.1, 2.13.3 are partially taken from the following article –

Chakraborty P., Rivière G., Liu S., Ibáñez de Opakua A., Dervişoğlu R., Hebestreit A., Andreas L. B., Vorberg I. M., & Zweckstetter M.

Co-factor-free aggregation of tau into seeding-competent RNA-sequestering amyloid fibrils *Nat Commun* **12**, 4231 (2021)¹

2.1 Chemical reagents

¹⁵NH₄Cl (299251, Sigma-Aldrich), D-Glucose-¹³C₆ (389374, Sigma-Aldrich), L-phenylalanine (ring-¹³C₆, 99 %) (CLM-1055, Cambridge Isotope Laboratories), L- valine (dimethyl-¹³C₂, 99%) (CLM-9217-PK, Cambridge Isotope Laboratories), L-histidine (¹⁵N₃, 98 %) (NLM-1513 Cambridge Isotope Laboratories), Streptomycin sulphate (Carl Roth GmbH), L-Lysine-2-¹⁵N-dihydrochloride (Sigma-aldrich), Thioflavin-T (T3516, Sigma-Aldrich), Heparin sodium salt (Carl Roth GmbH), TEMTriPol-1 (Synthetic Chemistry facility of the MPIBPC Göttingen), 2,5-dibromopentanoic acid methyl ester (sc-481713, Chemcruz), N-acetylcysteamine (363340, Sigma-Aldrich)

2.2 Bacterial strains

Competent BL21(DE3) cells from Invitrogen (44-0048), Invitrogen Subcloning Efficiency DH5α Competent cells, XL2-(Blue) Ultracompetent cells (Agilent)

2.3 Equipment

Bruker NMR spectrometer (600 – 950 MHz), IKA KS 4000i incubator, INFPRS HT Multitron incubator, Bandelin sonuplus sonicator, AVESTIN EmulsiFlex C3 French press, Beckman Coulter Avanti JXN-26 centrifuge, Beckman Coulter JLA-8.1 rotor, Beckman Coulter OPTIMA XPN-80 ultracentrifuge, Beckman Coulter 45Ti rotor, Beckman Coulter OPTIMA MAX-XP ultracentrifuge, Beckman Coulter JA-25 rotor, Eppendorf centrifuge 5810R, Eppendorf centrifuge 5424R, GFL water bath, Bandelin Sonorex Digitec ultrasonic bath, Zirbus VaCO-2-II Lyophilizer, GE Äkta pure, Mono S 10/100 GL (GE Healthcare), GE Superdex 75 26/600 GL column, C4 column (Vydac 214 TP, 5 µm, 8 x 250 mm), Eppendorf Thermomixer comfort, SensoQuest Labcycler, Tecan spark plate reader, Tecan spark 20M plate reader, CM 120 transmission electron microscope (FEI, Eindhoven, The Netherlands), Chirascan-plus qCD spectrometer (Applied Photophysics, UK), BioRad GelDoc XR+, Orbitrap Fusion Tribrid Mass spectrometer (Thermo Fischer Scientific), Confocal microscope (CellVoyager 6000), Nanodrop 2000 spectrophotometer (Thermo Fischer Scientific), Eppendorf Biospectrometer.

2.4 Software

Topspin 3.6.1 (Bruker), Sparkcontrol v2.2 (TECAN), CCPNMR 2.4.2¹⁶⁰, Graphpad PRISM 9.0, Pro-Data Chirascan, Inkscape 1.1, Endnote X9, Word v16 (Microsoft), Chemdraw (PerkinElmer), UCSF Chimera¹⁶¹ (v 1.14.0), PyMOL v2.2.0, Fiji (ImageJ).¹⁶²

2.5 Protein preparation

The plasmids carrying 2N4R tau/htau40 (schematic representation Figure 1-4) and 0N3R tau/htau23 (schematic representation Figure 1-4) were kindly provided by the laboratory of Prof. Dr. Eckhard Mandelkow. Both the htau40 and htau23 constructs are cloned in the pNG2 vector (a derivative of pET-3a, Merck-Novagen, Darmstadt). The vector map with the htau40 sequence is shown in Figure 2-1. All the other mutants of 2N4R tau were generated by site-directed mutagenesis using unmodified 2N4R tau as a template. Mrs. Maria-Sol Cima-Omori (Translational structural biology in dementia, DZNE, Göttingen) helped during different

stages of purification. Mrs. Kerstin Overkamp (NMRII, MPIBPC, Göttingen) performed the reverse-phase chromatography along with mass spectrometry.

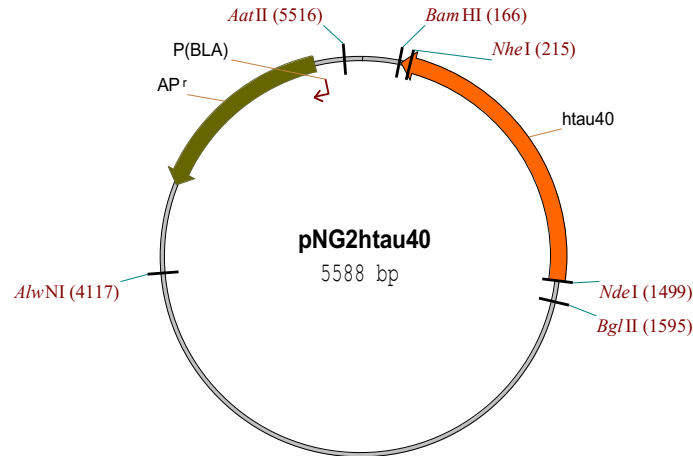


Figure 2-1 Vector map of pNG2htau40.

The htau40 construct is cloned between Bam H1 and NdeI restriction sites.

2.5.1 Transformation in *E. coli*

BL21TMDE3 competent cells were used to transform the constructs of tau (htau40, htau23, and the htau40 mutants). 25 μ l of competent cells stored in -80 °C were thawed in ice for 15 mins followed by the addition of 1 μ l of DNA plasmid. The plasmid-cell mixture was incubated in ice for 20 minutes. The heat-shock transformation was performed at 42 °C in an Eppendorf thermomixer for 45 seconds; afterwards, cells were put back in ice for 2 minutes. Cells were incubated at 37 °C with 550 r.p.m shaking in an Eppendorf thermomixer after the addition of 250 μ l of LB medium. Afterwards, 100 μ l of the cells were streaked onto LB-agar plates supplemented with 100 μ g/mL Ampicillin antibiotic. Plates were incubated overnight at 37 °C.

2.5.2 Protein expression

To prepare unlabeled protein, a single colony from the LB-agar plate was taken and grown overnight in 50 mL LB medium supplemented with 100 μ g/mL Ampicillin at 37 °C. 22 mL of

the overnight culture was transferred to 1L LB medium supplemented with 100 µg/mL Ampicillin and allowed to grow until OD₆₀₀ of 0.8-0.9 was reached. Afterwards, the cells were induced with 0.5 mM IPTG (in case of WT/mutant 2N4R tau) or 1 mM IPTG (in case of 0N3R tau) and expressed for 1 hour.

To obtain uniformly ¹³C/¹⁵N-labeled proteins, cells were grown in 8 L LB until an OD₆₀₀ of 0.6-0.8 was reached, then centrifuged at low speed (4,000 g), washed with 1X M9 salts, and resuspended in 2 L M9 minimal medium* supplemented with 1 g/L ¹⁵NH₄Cl as the only nitrogen source, 4 g/L ¹³C Glucose as carbon source. After 1 hour, the cells were induced with 0.5 mM IPTG (for 2N4R tau) or 1 mM IPTG (for 0N3R tau) and expressed overnight at 37 °C.

To obtain specifically lysine labeled proteins, cells were grown in 4 L LB until an OD₆₀₀ of 0.6-0.8 was reached, then centrifuged at low speed (4,000 g), washed with 1X M9 salts, resuspended in 1 L M9 minimal medium*. After 30 minutes, 150 mg/L of L-Lysine-2-¹⁵N-dihydrochloride (Sigma-Aldrich) was added, and after another 30 minutes, cells were induced with 0.5 mM IPTG (for 2N4R tau) or 1 mM IPTG (for 0N3R tau) and expressed overnight at 37 °C.

To obtain specifically (¹³C_γ valine, ¹³C-ring phenylalanine, ¹⁵N histidine) labeled 2N4R tau, cells were grown in LB until an OD₆₀₀ of 0.6-0.8 was reached, then centrifuged at low speed (4,000 g), washed with M9 salts and resuspended in M9 minimal medium supplemented with 0.125 g/L of L-phenylalanine (ring-¹³C₆, 99 %) (CLM-1055, Cambridge Isotope Laboratories), 0.15 g/L of L- valine (dimethyl-¹³C₂, 99%) (CLM-9217-PK, Cambridge Isotope Laboratories), 0.125 g/L of L-histidine (¹⁵N₃, 98 %) (NLM-1513 Cambridge Isotope Laboratories). To minimize scrambling, all other amino acid types were added in unlabeled form: 0.50 g/L alanine, 0.40 g/L arginine, 0.40 g/L aspartic acid, 0.05 g/L cystine, 0.40 g/L glutamine, 0.65 g/L glutamic acid, 0.55 g/L glycine, 0.23 g/L isoleucine, 0.23 g/L leucine, 0.42 g/L lysine hydrochloride, 0.25 g/L methionine, 0.10 g/L proline, 2.10 g/L serine, 0.23 g/L threonine and 0.17 g/L tyrosine,), as well as 0.50 g/L adenine, 0.65 g/L guanosine, 0.20 g/L thymine, 0.50 g/L uracil*

and 0.20 g/L cytosine ¹⁶³. After 1 hour, the cells were induced with 0.5 mM IPTG and expressed overnight at 37 °C.

After the expression, the bacterial cells were harvested by centrifugation at 7500 rpm using a JLA 8.1000 rotor in a Beckman Coulter Avanti centrifuge for 40 minutes.

*

Minimal medium (1L)

100 mL 10x M9 salts

10 mL 100x trace elements

1 mL 1000x vitamins

1 mM MgSO₄

0.3 mM CaCl₂

100 µg/mL Ampicillin

Stock solutions

10x M9 salts (1L):

60 g Na₂HPO₄, 30 g KH₂PO₄, 5 g NaCl

100x trace elements (1L):

5 g EDTA, 0.8 g FeCl₃, 0.05 g ZnCl₂, 0.01 g CuCl₂, 0.01 g CoCl₂, 0.01 g H₃BO₃, 1.6 mg MnCl₂

1000x vitamins (500 mL):

0.5 g riboflavin, 0.5 g niacinamide, 0.5 g pyridoxine monohydrate, 0.5 g thiamine

2.5.3 Protein purification

The cell pellets were resuspended in lysis buffer (20 mM MES pH 6.8, 1 mM EGTA, 2 mM DTT) complemented with protease inhibitor mixture, 0.2 mM MgCl₂, lysozyme, and DNase I. *Subsequently, cells were disrupted with a French pressure cell press (in ice-cold conditions to avoid protein degradation). In the next step, NaCl was added to a final concentration of 500 mM, and lysates were boiled for 20 minutes. Denatured proteins were removed by ultracentrifugation with 127,000 g at 4 °C for 30 minutes. To precipitate the DNA, 20 mg/mL*

streptomycin sulfate was added to the supernatant and incubated for 15 minutes at 4 °C followed by centrifugation at 15,000 g for 30 minutes. The pellet was discarded, and tau protein was precipitated by adding 0.361 g/mL ammonium sulfate to the supernatant, followed by centrifugation at 15,000 g for 30 minutes. The pellet containing tau protein was resuspended in buffer A (20 mM MES pH 6.8, 1 mM EDTA, 2 mM DTT, 0.1 mM PMSF, 50 mM NaCl) and dialyzed against the same buffer (buffer A) to remove excess salt. *The following day, the sample was filtered and applied onto an equilibrated ion-exchange chromatography column (Mono S 10/100 GL, GE Healthcare), and the weakly bound proteins were washed out with buffer A. Tau protein was eluted with a linear gradient of 60 % final concentration of buffer B (20 mM MES pH 6.8, 1 M NaCl, 1 mM EDTA, 2 mM DTT, 0.1 mM PMSF). Protein samples were concentrated by ultrafiltration (5 kDa Vivaspin, Sartorius) and further purified by reverse phase chromatography using a preparative C4 column (Vydac 214 TP, 5 µm, 8 x 250 mm) in an HPLC system coupled with ESI mass spectrometer. The purity of the proteins was confirmed from the mass, and the purified protein was lyophilized and re-dissolved in the buffer of interest.*

A representative ion-exchange chromatogram of 2N4R tau and the mass of purified unlabeled 2N4R and 0N3R tau are shown in Figure 2-2.

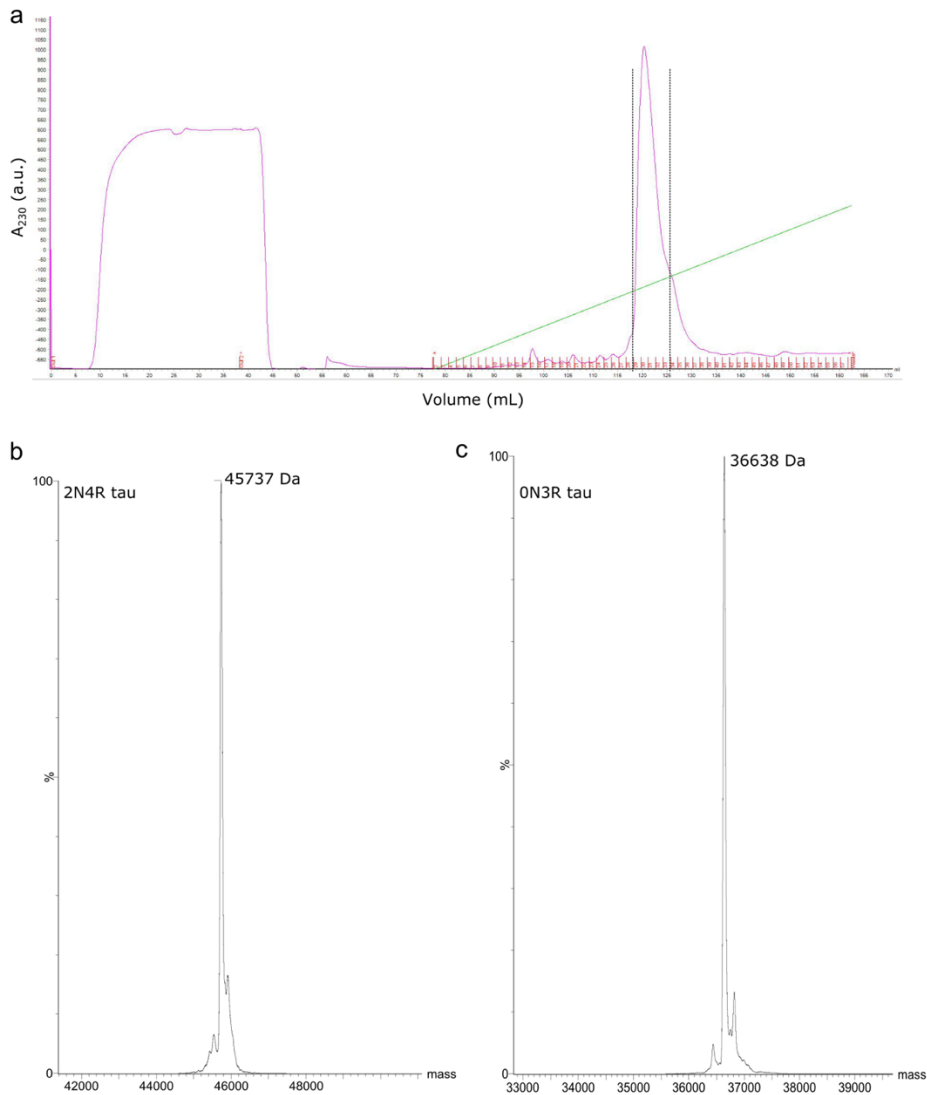


Figure 2-2 Purification of tau.

a, Ion-exchange chromatogram of 2N4R tau using a Mono-S column. The vertical lines show the fractions collected for further purification. **b**, Mass of 2N4R tau after purification by reverse-phase chromatography. **c**, Mass of 0N3R tau after purification by reverse-phase chromatography.

2.6 Preparation of different mutants of 2N4R tau

All 2N4R tau mutants were generated using site-directed mutagenesis protocol using a thermocycler (SensoQuest Labcycler). Phusion high-fidelity PCR master mix (Thermofisher) was used to perform all the PCR reactions. The detailed protocol to generate each mutant is discussed in the Appendix section 6.2.

After the PCR reaction, to digest the template plasmid, 0.5 μ L of DpnI enzyme was added to 50 μ L of DNA and incubated for one hour at 37 °C. After one hour, the DNA was transformed using subcloning efficiency DH5 α Competent cells (Invitrogen).

2.7 Aggregation assay of tau

Aggregation of 25 μ M 2N4R tau was performed in 25 mM HEPES, 10 mM KCl, 5 mM MgCl₂, 3 mM TCEP, 0.01% NaN₃, pH 7.2 buffer (aggregation assay buffer)¹. One tablet of protease inhibitor (complete, EDTA-free, Sigma Aldrich) was added to 100 mL aggregation assay buffer. The buffer was filtered through a 0.2 μ m filter to remove bacterial contamination. Thioflavin T (ThT) was added to the protein at a final concentration of 50 μ M to monitor aggregation kinetics. 100 μ L of 25 μ M 2N4R tau protein with 50 μ M ThT was pipetted in a well of 96 well plate (Greiner Bio-one, microplate, 96 well, PS, F-bottom, Chimney well, μ Clear, black, non-binding, item no – 655906) with 3 polytetrafluoroethylene beads of 2.45 mm per well (Kugelfertigung Hoch GmbH & Co. KG). The aggregation assay was performed at 37 °C in a Tecan spark 20M/ Tecan spark plate reader with double orbital shaking (shaking duration – 1 minute, shaking amplitude – 6 mm, shaking frequency –54 rpm) at an interval of 10 minutes. An excitation monochromator at a wavelength of 440 nm with an excitation bandwidth of 10 nm (in Tecan spark 20M) or an excitation filter at a wavelength of 430 nm with an excitation bandwidth of 35 nm (Tecan spark) was used to excite ThT. The emission wavelength was set to 482 nm with a bandwidth of 10 nm (manual gain – 60, number of flashes –30, integration time – 40 μ s) in Tecan spark 20M plate reader or to 485 nm with a bandwidth of 20 nm (manual gain – 40, number of flashes –30, integration time –40 μ s) in Tecan spark plate reader (Figure 6-1). The Z-position was calibrated using an empty well before starting each experiment. ThT fluorescence data were collected using Tecan Spark control software (v 2.2). The analysis of the aggregation data was performed using Graphpad PRISM (v 9) software.

The aggregation of all mutants of 2N4R tau, unmodified ON3R tau, acetylated 2N4R/ON3R tau, as well as acetyl-lysine mimics of 2N4R tau was performed using the same protocol as described above.

The heparin-induced aggregation of 25 μ M 2N4R tau was performed using the same protocol as described above, but 6.25 μ M heparin was added to 25 μ M protein.

2.8 Electron microscopy

40 μ L of 25 μ M unmodified 2N4R tau fibril or unmodified/acetylated ON3R tau fibril was pelleted down by centrifugation at 20,000 g using Eppendorf centrifuge 5424. The supernatant was discarded, and the pellet was redissolved in 30 μ L 25 mM HEPES, 500 mM KCl, 10 mM MgCl₂, 3 mM TCEP, 0.01% NaN₃, pH 7.2 buffer. *The heparin-induced 2N4R tau fibril sample was directly imaged by transmission electron microscopy (TEM) after the aggregation. Aggregated samples were stained by 1% uranyl acetate solution after adsorbing onto carbon-coated copper grids. The images were taken with a Tietz F416 CMOS camera (TVIPS, Gauting, Germany) using a CM 120 transmission electron microscope (FEI, Eindhoven, The Netherlands). The negative stain electron microscopy images were taken by Mrs. Gudrun Heim, Ms. Leonie Kopecny from the electron microscopy facility at the Max Planck Institute for Biophysical Chemistry (MPIBPC) Göttingen.*

2.9 Circular dichroism

10 μ L of 25 μ M 2N4R fibril/ ON3R tau fibril/ acetylated-ON3R tau fibril were centrifuged at 20,000g for 15 minutes in an Eppendorf centrifuge 5424. *The supernatant was removed, and the pellet was resuspended in 50 μ L of distilled water. The 2N4R tau monomer was also diluted to a final concentration of 5 μ M in 50 μ L of distilled water. Also, the acetylated 2N4R tau was diluted to a final concentration of 5 μ M after five days of aggregation. The fibril and the monomer samples were transferred to a 0.02 cm pathlength cuvette, and CD data were collected from 190 to 280 nm using a Chirascan-plus qCD spectrometer (Applied Photophysics, UK) at 25 °C, 1.5 seconds per point in 1 nm steps. The datasets were averaged*

from 10 repeated measurements. Spectra were baseline-corrected and smoothed with a window size of 6. CDNN software v 2 (Chirascan, Applied Photophysics, UK) was used to analyze the CD spectrum of the heparin-free 2N4R tau fibrils.

2.10 Trypsin digestion

50 μ L of 0.9 mg/mL 2N4R fibril (aggregated in either the absence or presence of heparin) and 0.45 mg/mL of trypsin (T8003, Sigma-Aldrich) or 0.8 mg/mL unmodified 0N3R tau fibrils and 0.4 mg/mL of trypsin (T8003, Sigma-Aldrich) were incubated in the aggregation assay buffer for 30 minutes with 1400 rpm shaking in an Eppendorf thermomixer at 37 °C. The trypsin-resistant material was pelleted down by ultracentrifugation at 160,000 g for 30 minutes at 4 °C using a Beckman Coulter Optima MAX-UP ultracentrifuge. The supernatant was removed, and the pellet was redissolved in 10 μ L of aggregation assay buffer and loaded in a 15% SDS-PAGE gel.

2.11 Pronase digestion

50 μ L of 0.8 mg/mL unmodified 2N4R tau fibrils or unmodified/acetylated 0N3R tau fibrils and 0.4 mg/mL of pronase (53702, Merck-millipore) were incubated in the aggregation assay buffer for 30 minutes with 1400 rpm shaking in an Eppendorf thermomixer at 37 °C. The pronase-resistant material was pelleted down by ultracentrifugation at 160,000 g for 30 minutes at 4 °C using a Beckman Coulter Optima MAX-UP ultracentrifuge. The supernatant was removed, and the pellet was redissolved in 10 μ L of aggregation assay buffer and loaded in a 15% SDS-PAGE gel.

2.12 In-gel digestion and extraction of peptides for mass spectrometry

The respective bands from the SDS-PAGE gels were carefully cut and kept in an Eppendorf tube. To wash the gel pieces, 150 μ L of water was added and incubated for 5 minutes at 26 °C with 1050 rpm shaking in a thermomixer. The gel pieces were spun down, and the liquid was removed using thin tips (the same washing protocol was used in all subsequent steps with different solvents). The gel pieces were rewashed with 150 μ L acetonitrile. After washing,

the gel pieces were dried for 5 minutes using a SpeedVacc vacuum centrifuge. To reduce disulfide bridges, 100 μ L of 10 mM DTT was added to the gel pieces and incubated for 50 minutes at 56 °C, followed by centrifugation and removal of liquid. The gel pieces were washed again with 150 μ L of acetonitrile. To alkylate reduced cysteine residues, 100 μ L of 55 mM iodoacetamide were added and incubated for 20 minutes at 26 °C with 1050 rpm shaking followed by centrifugation and removal of liquid. Subsequently, the gel pieces were washed with 150 μ L of 100 mM NH_4HCO_3 and then twice with 150 μ L of acetonitrile and dried for 10 minutes in a vacuum centrifuge. The gel pieces were rehydrated at 4 °C for 45 minutes by the addition of small amounts (2-5 μ L) of digestion buffer 1 (12.5 μ g/mL trypsin, 42 mM NH_4HCO_3 , 4 mM CaCl_2). The samples were checked every 15 minutes, and more buffer was added if the liquid was completely absorbed by the gel pieces. 20 μ L of digestion buffer 2 (42 mM NH_4HCO_3 , 4 mM CaCl_2) were added to cover the gel pieces and incubated overnight at 37 °C.

To extract the peptides, 15 μ L water was added to the digest and incubated for 15 minutes at 37 °C with 1050 rpm shaking followed by spinning down the gel pieces. 50 μ L acetonitrile was added to the entire mixture and incubated for 15 minutes at 37 °C with 1050 rpm shaking. The gel pieces were spun down, and the supernatant (SN1) containing the extracted peptides was collected. 30 μ L of 5 % (v/v) formic acid was added to the gel pieces and incubated for 15 minutes at 37 °C with 1050 rpm shaking followed by spinning down. Again 50 μ L acetonitrile were added to the entire mixture and incubated for 15 minutes at 37 °C with 1050 rpm shaking. The gel pieces were spun down, and the supernatant (SN2) containing the extracted peptides was collected. Both supernatants (SN1 & SN2) containing the extracted peptides were pooled together and evaporated in the SpeedVacc vacuum centrifuge. The dried peptides were resuspended in 5 % acetonitrile and 0.1 % formic acid and analyzed using an Orbitrap Fusion Tribrid (Thermo Fischer Scientific) instrument. The in-gel digestion and extraction of peptides experiments were performed by Mr. Uwe Pleßmann from the mass spectrometry facility at the Max Planck Institute for Biophysical Chemistry (MPIBPC) Göttingen.

2.13 NMR spectroscopy

2.13.1 2D HSQC

The two-dimensional Heteronuclear Single Quantum Coherence (HSQC) experiment¹⁶⁴ is the most standard NMR experiment performed with a protein sample. The HSQC experiment gives rise to a fingerprint spectrum of a protein sample showing all the H-N correlations. These correlations are mainly between the backbone amide groups, but the tryptophan/arginine side chain $N\epsilon$ - $H\epsilon$, asparagine side chain $N\delta$ - $H\delta$, and the glutamine side chain $N\epsilon$ - $H\epsilon$ are also observed.

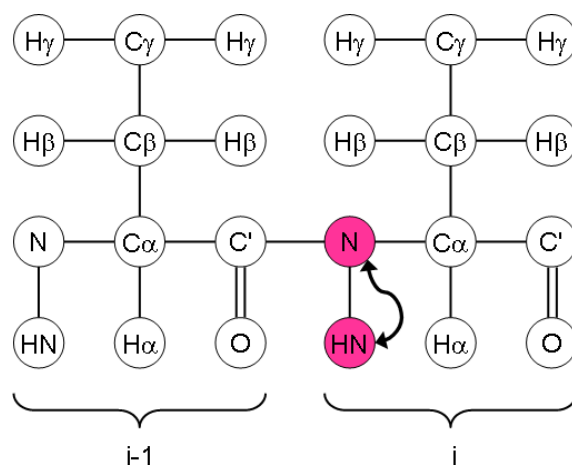


Figure 2-3 The flow of magnetization in a 1H - ^{15}N HSQC experiment.

The nuclei involved are shown in red. The image is taken from the Protein-NMR webpage (www.protein-nmr.org.uk/solution-nmr/spectrum-descriptions/1h-15n-hs qc/).

In this experiment, the magnetization is transferred from 1H to the attached ^{15}N nuclei via J-coupling followed by the evolution of the chemical shift on nitrogen. Then, the magnetization is transferred back to the amide proton for detection.

2.13.1.1 HSQC spectra of full-length 4R and 3R tau

The 1H - ^{15}N HSQC spectrum of 25 μM 2N4R tau monomer or 25 μM ^{13}C / ^{15}N labeled 0N3R tau monomer in the aggregation assay buffer was acquired at 278 K on an Avance III 900 MHz spectrometer (Bruker) using a 5 mM HCN Cryoprobe. Both spectra were collected with 40 scans per point (ns), and indirect acquisition times $td1 = 9$ ms and $td2 = 12$ ms. The chemical

shift assignments of 2N4R tau had been previously established¹⁶⁵. The chemical shift assignment of 0N3R tau was performed by transferring the assignment of 2N4R tau. The pulse program used to perform the experiment is attached in section 6.4.

2.13.1.2 HSQC spectra of lysine labeled 4R and 3R tau (unmodified and acetylated)

The ¹H-¹⁵N HSQC spectra of 50 μM ¹⁵N-lysine-labeled unmodified/acetylated 2N4R/0N3R tau proteins were collected at 278 K in 50 mM NaP, 10 mM NaCl, 1 mM TCEP, pH 6.8 buffer on an Avance III 900 MHz spectrometer (Bruker) equipped with a 5 mm HCN cryoprobe and an Avance neo 800 MHz spectrometer (Bruker) equipped with a 3 mm HCN cryoprobe. Spectra were collected with 24 scans per point (ns), and indirect acquisition times td1 = 9 ms and td2 = 9.8 ms. The pulse program used to perform the experiment is attached in section 6.4.

2.13.1.2.1 Determination of extent of acetylation by analyzing the HSQC spectra

The signals in the ¹H-¹⁵N HSQC spectra of ¹⁵N-lysine-labeled unmodified 2N4R/0N3R tau were assigned by transferring the assignment from the ¹H-¹⁵N HSQC spectra of uniformly ¹⁵N labeled 2N4R/0N3R tau. Some peaks of the acetylated 2N4R tau were assigned from the previously published literature¹⁴¹. The acetylation level of individual lysine residues was determined using the following equation –

$$\text{Acetylation level (\%)} = \left\{ 1 - \frac{\text{Intensity of unacetylated lysine (in the acetylated sample)}}{\text{Intensity of unmodified lysine (in the non - acetylated sample)}} \right\} \times 100$$

2.13.2 ¹H-¹⁵N INEPT spectra of tau fibrils

Insensitive nuclei enhanced by polarization transfer¹⁶⁶ (INEPT) experiments use scalar coupling for polarization transfer, thereby detecting only the highly dynamic residues in solid samples, i.e., the fuzzy coat in the case of tau fibrils. To record the ¹H-¹⁵N INEPT spectra, ¹³C/¹⁵N labeled 2N4R tau/ 0N3R tau was aggregated without ThT using the protocol described above, and ~ 30 mg of fibrils were packed into a 3.2 mm MAS rotor. The ¹H-¹⁵N INEPT spectra of both heparin-free and heparin-induced 2N4R tau fibrils were acquired at 265 K and 17 kHz MAS on an Avance-III 850 MHz spectrometer (Bruker) using a 3.2 mm HCN probe with 32 scans per point (ns), and indirect acquisition times td1 = 48 ms, td2 = 50 ms.

The ^1H - ^{15}N INEPT spectra of 0N3R tau fibrils were acquired at 265 K and 17 kHz MAS on an Avance III 950 MHz spectrometer (Bruker) using a 3.2 mm HCN probe with 32 scans per point (ns), and indirect acquisition times $\text{td1} = 36$ ms, $\text{td2} = 40$ ms. The ^1H - ^{15}N INEPT spectra of 0N3R tau fibril was recorded by Dr. Gwladys Rivière (Translational structural biology in dementia, DZNE, Göttingen). The pulse program used to perform the experiment is attached in section 6.5.

2.13.2.1 Analysis of the INEPT spectra

Signals in the ^1H - ^{15}N INEPT spectra of heparin-free/heparin-induced 2N4R tau fibrils or 0N3R tau fibrils were assigned by transferring the resonance assignment of the 2N4R tau / 0N3R tau monomer. *Intensity ratios were calculated by dividing the intensity of each residue in the ^1H - ^{15}N INEPT spectrum of the fibril sample by the intensity observed in the ^1H - ^{15}N HSQC spectrum of the monomeric protein. The residue with the highest intensity was normalized to 1, and the average line was calculated by smoothening using a 2nd order polynomial function with window size four.*

2.13.3 2D ^{13}C - ^{13}C RFDR spectra of tau fibrils

In solution-state NMR, the spectra consist of sharp lines due to the averaging of anisotropic NMR interactions by rapid molecular tumbling. By contrast, in solid-state NMR the spectra exhibit broader linewidths due to the presence of orientation-dependent interactions (anisotropy). These anisotropic interactions are suppressed by spinning the sample at a magic angle ($\theta = 54.74^\circ$) with respect to the magnetic field. The magic angle spinning (MAS) also attenuates the homo- and hetero-dipolar couplings; however, most critical information is present in the dipolar couplings (the dipolar interactions contain the term $3\cos^2\theta - 1$, and it gives a 0 value when $\theta = 54.74^\circ$)¹⁶⁷. Thus, in order to reintroduce the dipolar couplings, rotor synchronized radio frequency (rf) pulses are introduced.

A common 2D experiment, which is recorded on solid-like protein samples, is the ^{13}C - ^{13}C Proton-Driven Spin Diffusion (PDSD) experiment. However, PDSD experiments can be

inefficient as no radio-frequency (rf) irradiations are used in this experiment. In contrast, ^{13}C - ^{13}C dipolar couplings are reintroduced by applying rf pulses in experiments such as Radio Frequency-Driven Recoupling (RFDR). The RFDR experiments are very efficient in observing the correlation between directly bonded atoms using a shorter mixing time.

^{13}C - ^{13}C Radio Frequency-Driven Recoupling (RFDR) experiments of both heparin-free and heparin-induced 2N4R tau fibrils were recorded at 265 K and 17 kHz MAS on an Avance-III 850 MHz spectrometer (Bruker) using a 3.2 mm HCN probe with $ns = 64$, $td1 = 21.5$ ms, $td2 = 15$ ms, $T_{mix} = 1.882$ ms. The final ^{13}C - ^{13}C RFDR spectra are the sum of 11 data sets. The ^{13}C - ^{13}C RFDR spectra of heparin-induced 2N4R tau fibril was recorded by Dr. Gwladys Rivière (Translational structural biology in dementia, DZNE, Göttingen). The pulse program used to perform the experiments is attached in section 6.6.

2.13.4 2D NCA/NCO spectra and 3D NCACX/NCOCX spectra of 2N4R tau fibrils

The 2D NCA/NCO and 3D NCACX and NCOCX of heparin-free 2N4R tau fibril were recorded at 265K and 17 kHz MAS on an Avance-III 850 MHz spectrometer (Bruker) using a 3.2 mm HCN probe. The 2D NCA/NCO experiment of the heparin-free 2N4R fibrils was recorded using a TEDOR sequence with $ns = 64$, $td1 = 21.5$ ms, $td2 = 75.5$ ms. 3D NCACX and NCOCX spectra of heparin-free 2N4R fibrils were recorded using a TEDOR pulse sequence with $ns = 8$, $td1 = 21.7$ ms, $td2 = 4.72$ ms, $td3 = 5.9$ ms. The final 3D NCACX and NCOCX spectra used for analysis are the sums of 9 experiments each. Spectra were processed using the Topspin 3.6.2 (Bruker) and analyzed using CCPNMR 2.4.2 ¹⁶⁰. The pulse program used to perform the experiments are attached in section 6.7 and 6.8.

2.13.5 Dynamic Nuclear Polarization (DNP)

Dynamic Nuclear Polarization (DNP) is a phenomenon to enhance the difference between nuclear energy levels, thereby dramatically increasing the NMR signal. Briefly, in MAS solid-state NMR, DNP is observed by the addition of different biradicals to the solid sample. The EPR spectrum of the biradical is irradiated with microwaves. The microwave excites one

electron present in the biradical, which then excites the other dipolar coupled electron. If the difference between the Larmor frequencies of two electrons matches the nuclear Larmor frequency, then the nuclear spin is also excited, leading to cross-effect DNP.

2.13.5.1 DNP-enhanced hCHHC and hNHHC spectra of 2N4R tau fibrils

DNP-enhanced solid-state NMR spectra were recorded for heparin-free fibrils of 2N4R labeled with $^{13}\text{C}_2$ (methyl) Val, and $^{13}\text{C}_6$ (ring) Phe and $^{15}\text{N}_3$ His using a commercial Bruker DNP spectrometer system with a sweepable cryo-magnet of $14.1 \pm 0.1\text{T}$ ($\sim 600 \pm 5$ MHz ^1H frequency) and 395 GHz gyrotron for the microwaves, operating at 100K with the Bruker 3.2mm LT-MAS HCN probe and an Avance III HD spectrometer. 2N4R tau sample was prepared for MAS DNP NMR as follows: the 2N4R tau fibril pellet was mixed with 10 μL of the stock 10 mM TEMTriPol-1^{168,169} in DNP juice (60:30:10 by volume ^{12}C -glycerol- d_8 : D_2O : H_2O). The excess solution was removed by ultra-centrifugation at 24,000 rpm for 1 hour with a Beckman Coulter SW32-Ti rotor (k-Factor 204). After removal of the excess solution, the sample was homogenized with a non-stick stainless steel needle tool. The TEMTriPol-1 final concentration was estimated at 3 mM. The sample was packed into a 3.2 mm Bruker zirconia MAS rotor with a vespel drive cap and spun at a frequency of 12.5 kHz. The 90° hard pulses were, respectively, 2.5 μs , 3.5 μs and 6 μs for ^1H , ^{13}C and ^{15}N . The ^1H - ^{13}C and ^{13}C - ^1H cross-polarization (CP) conditions were met with 75kHz for ^{13}C and a ramp from 90 to 100kHz for ^1H and a duration of 700 μs (^1H to ^{13}C CP) or 350 μs (^{13}C to ^1H CP). The ^1H - ^{15}N and ^{15}N - ^1H CP conditions were met with 30 kHz ^{15}N radiofrequency (rf) and 46 to 45 kHz linear ramp for ^1H RF with a duration of 350 μs (^1H - ^{15}N) and 370 μs (^{15}N - ^1H). The interscan delay was 2.5 s. The magnetic field was calibrated to an internal standard, the ^{13}C resonance of the silicone plug (polydimethylsiloxane) used for DNP sample packing, which was set to be at 1.6 ppm on the TMS scale¹⁷⁰. With these NMR settings, 2D hCHHC at 200 μs and 400 μs H-H mixing times were acquired for 2 days, and hNHHC at 200 μs H-H mixing time for 3 days¹⁷¹. The DNP-enhanced hCHHC and hNHHC spectra of heparin-free 2N4R tau fibrils were recorded by Dr. Riza Dervişoğlu, NMRII, MPIBPC, Göttingen. The pulse programs used to perform the experiments are attached in section 6.9 and 6.10.

2.14 Seeding of tau aggregation

2.14.1 *In vitro* seeding heparin-free 2N4R tau fibrils

To perform the in-vitro seeding experiments, 2N4R tau fibrils, which had been generated in the absence of heparin according to the protocol described above, were used as seed. 1 % (w/w) and 5 % (w/w) seeds were added to 25 μ M monomeric 2N4R tau in the aggregation assay buffer. Prior to the addition, the seeds were sonicated for 2 minutes at 37 °C in a water bath. The same protocol was used for aggregation, as described above. The in vitro measurements were performed with three independently prepared samples.

2.14.2 Seeding of heparin-free/ heparin-induced 2N4R tau in cells

Biosensor cell line HEK293T TauRD-GFP was generated to assess the seeding activity of fibrils in cellula. These cells were engineered to stably express the human tau repeat domain (RD; amino acids 243 to 375) with point mutations P301L/V337M and a carboxyterminal GFP-tag connected through an 18-amino acid flexible linker (EFCSRRYRGPGIHRSPATA) (thereafter termed TauRD-GFP)¹⁷². HEK293T TauRD-GFP cells were seeded on 384 well plates. Next day, tau fibrils were mixed with lipofectamine 2,000 and added to the cells at different concentrations. Prior to the addition, the fibrils were sonicated for 6 minutes at 10 % power. After three days, cells were fixed, and nuclei were stained with Hoechst. Images were taken with an automated confocal microscope (CellVoyager 6000), and automated image analysis was performed to calculate total Tau-GFP cell numbers and cells containing Tau-GFP aggregates as previously described¹⁷³. Please note that automatic image analysis of aggregates takes into account local fluorescence intensity increase, resulting in low background levels of positives due to condensed cell bodies. Cell measurements were performed with three independent transfections at different concentrations per fibril type. The in-cell seeding experiments were performed by Dr. Shu Liu, Ms. Alina Hebestreit from the laboratory of Prof. Ina Vorberg at DZNE Bonn.

2.14.3 *In vitro* cross-seeding experiment

To perform *in vitro* cross-seeding experiments, acetylated ON3R tau fibrils were used as seeds. Prior to aggregation, the ON3R tau was acetylated in the presence of both CREB-binding protein (CBP) and p300 using the protocol described in section 2.19. One percent (w/w) seeds were added to 25 μ M unmodified/acetylated 2N4R tau monomer in the aggregation assay buffer. The acetylated 2N4R tau monomer was also created by acetylation in the presence of both CBP and p300. The seeds were sonicated for 4 minutes before addition. The same protocol described above was used for the aggregation. The measurements were performed with three independently prepared samples.

2.15 RNA binding assay

10 μ g/mL of yeast tRNA (AM7119, Thermo Fischer Scientific) poly(A) (P9403, Sigma-Aldrich) or polyU (P9528, Sigma-Aldrich) were added to 100 μ L of 5 μ M 2N4R fibrils either in the aggregation assay buffer (10 mM KCl, 25 mM HEPES, 5 mM MgCl₂, 3mM TCEP, pH 7.2) or in the same buffer but at increased ionic strength (100 mM KCl, 25 mM HEPES, 5 mM MgCl₂, 3 mM TCEP, pH 7.2). The fibril/RNA-mixture was incubated at 37 °C with 550 rpm shaking for 1.5 hours in a Thermomixer (Eppendorf, Thermomixer comfort). After the incubation, the fibril/RNA-mixture was centrifuged at 160,000g at 37 °C for 30 minutes in an ultracentrifuge (Optima MAX-XP, Beckman Coulter). The supernatant was removed, and the pellet was resuspended in 100 μ L of aggregation assay buffer with 2 % SDS. The concentration of RNA in the supernatant and the pellet (resuspended) was calculated using a Nanodrop 2000 spectrophotometer (Thermo Fischer Scientific). Spectra were baseline corrected using the buffer as reference. The concentrations of polyU, polyA, and tRNA were calculated from a sample of 10 μ g/mL RNA in 100 μ L of buffer. Measurements were performed with three independently prepared samples in each case.

2.16 Bicinchoninic acid assay

The concentration of 2N4R tau in the supernatant after aggregation (in the absence of heparin) was determined using the micro-bicinchoninic acid (BCA) assay kit (23235, Thermo

Fischer Scientific). The microplate procedure (linear working range of 2-40 $\mu\text{g/mL}$) as described in the instruction manual provided by the manufacturer was used to perform the experiment.

2.17 Electrostatic surface potential

The electrostatic surface potential of the tau filament (type 1) extracted from the brain of a patient with CBD (PDB code: 6TJO) and the heparin-induced 2N4R tau fibrils (snake form; PDB code: 6QJH) was displayed using the coulombic surface coloring tool in UCSF Chimera¹⁶¹ (v 1.14.0). The dielectric constant of water ($\epsilon = 78.4$) was used; the distance from the surface (d) was set to 1.4 \AA . The minimum value for the number of colors was set to -0.5 kcal/mol*e and the maximum value was set to 0.5 kcal/mol*e.

2.18 Microtubule polymerization

To polymerize tubulin into microtubules, 25 μM tubulin in BRB80 buffer (100 mM PIPES, 1 mM MgSO_4 , 1 mM EGTA, 1 mM DTT, pH 6.9) and 1 mM GTP were incubated at 37 $^\circ\text{C}$ at 350 rpm shaking for 30 minutes in an Eppendorf thermomixer. After 30 minutes, 25 μM paclitaxel (Sigma Aldrich) were added to the mixture and further incubated for another 30 minutes at 37 $^\circ\text{C}$ with 350 rpm shaking. The suspensions of the sample were fractionated by ultracentrifugation at 40,000 rpm for 45 minutes. The microtubule pellet was resuspended with 25 μM ¹⁵N-lysine-labeled 4R tau in the aggregation assay buffer.

2.19 Acetylation of 4R and 3R isoform of tau

To acetylate tau, 200 μM of 2N4R tau/0N3R tau/¹⁵N-lysine-labeled 2N4R tau/ ¹⁵N-lysine-labeled 0N3R tau were incubated at 30 $^\circ\text{C}$ for 12 hours in an Eppendorf thermomixer with 300 rpm shaking in the presence of either 0.028 mg/mL CBP (BML-SE452, Enzo), or 0.028 mg/mL p300 (BML-SE451, Enzo), or both and 20 mM acetyl-coA (Sigma-Aldrich), 1 mM PMSF, 1 mM EGTA. After 12 hours of reaction, the sample was boiled at 98 $^\circ\text{C}$ for 20 minutes to precipitate the acetyltransferases, followed by centrifugation at 20,000 g in an Eppendorf centrifuge 5424. Next, the pellet was discarded, and the supernatant containing acetylated

tau was dialyzed against the aggregation assay buffer or NMR buffer (50 mM NaP, 10 mM NaCl, 1 mM TCEP, pH 6.8).

The acetylation reaction of 25 μ M microtubule-bound 15 N-lysine-labeled tau was performed by incubation at 30 °C for 2 hours with 300 rpm shaking in the presence of 0.0035 mg/mL p300 (BML-SE451, Enzo), 0.0035 mg/mL CBP (BML-SE452, Enzo), 2.5 mM acetyl-coA (Sigma-Aldrich), 1 mM PMSF, 1 mM EGTA. After two hours, 1 M NaCl was added to the solution to break the interaction between microtubule and tau, followed by boiling at 98 °C for 20 minutes. The precipitated microtubules and enzymes were separated by ultracentrifugation at 55,000 rpm for 30 minutes. Next, the pellet was discarded, and the supernatant containing acetylated tau was dialyzed against the NMR buffer (50 mM NaP, 10 mM NaCl, 1 mM TCEP, pH 6.8).

2.20 Synthesis of acetyl-lysine mimics of 4R tau

The acetyl-lysine mimics were created using a previously published protocol¹⁷⁴. First, 200 μ M of Cys-free* K280C 2N4R tau/ Cys-free* K294C 2N4R tau/ Cys-free* K298C 2N4R tau/ Cys-free* K311C 2N4R tau were mixed with 20 mM 2,5-dibromopentanoic acid methyl ester (sc-481713, Chemcrux) in 20 mM NaP, pH 8.0 buffer and incubated at 37 °C for 12 hours in an Eppendorf thermomixer with 500 rpm shaking. After the reaction, excess 2,5-dibromopentanoic acid methyl ester was removed by passing the solution three times through a spin desalting column with 7KDa MW cut-off (Thermo fisher).

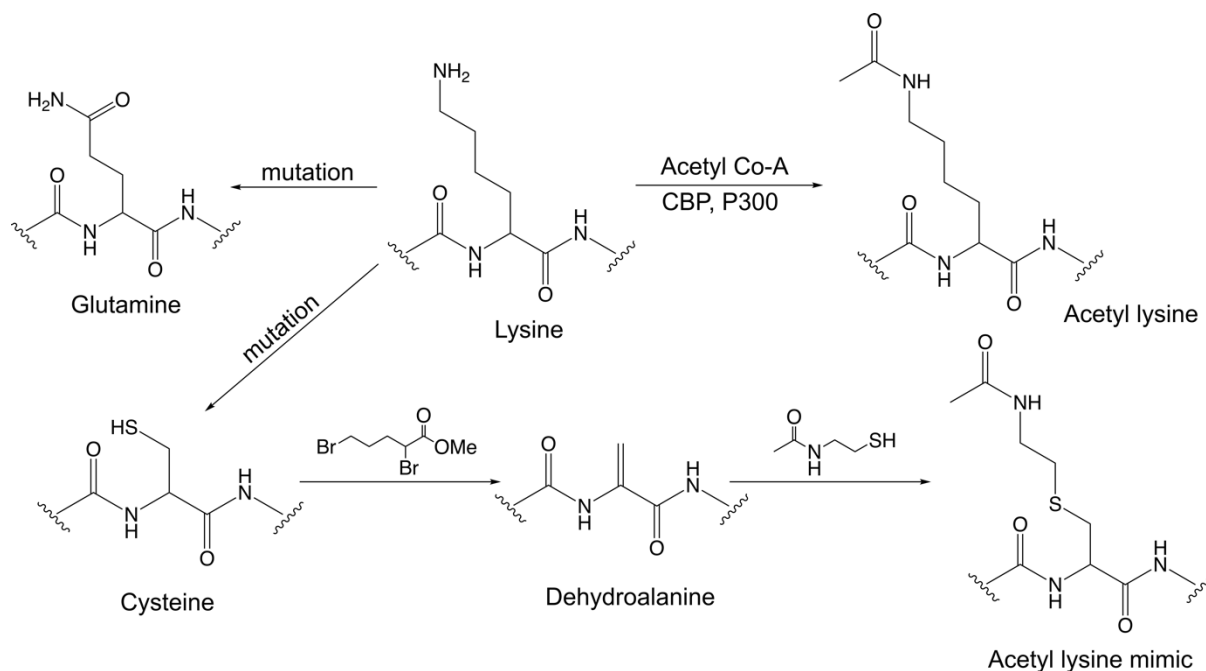


Figure 2-4 Scheme of reaction to synthesize acetyl-lysine mimic¹⁷⁴.

The traditional approach of mimicking lysine acetylation by mutating lysine residue to glutamine is also shown.

Next, N-acetylcysteamine (363340, Sigma-Aldrich) was added to the solution to a final concentration of 200 mM, and the mixture was incubated at 37 °C for 12 hours in an Eppendorf thermomixer with 500 rpm shaking. After 12 hours, the excess N-acetylcysteamine was removed by passing the solution three times through a spin desalting column with 7KDa MW cut-off (Thermo fisher) followed by dialysis against the aggregation assay buffer. The increase in mass by 85 Da confirmed the formation of the acetyl-lysine mimics (Figure 2-5).

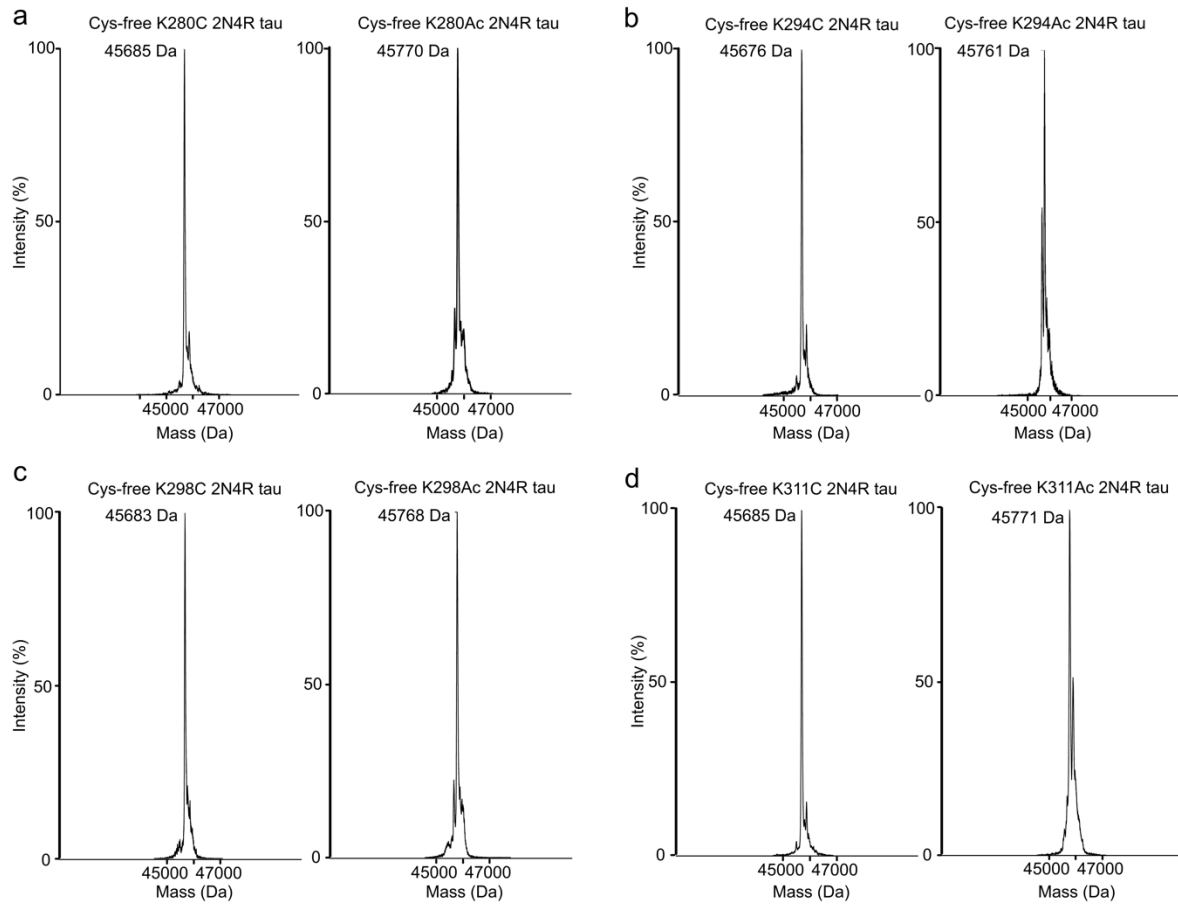


Figure 2-5 Mass spectra of acetyl-lysine mimics of 2N4R tau.

a, Mass spectra of Cys-free* K280C 2N4R tau before and after acetyl-lysine mimic formation. **b**, Mass spectra of Cys-free* K294C 2N4R tau before and after acetyl-lysine mimic formation. **c**, Mass spectra of Cys-free* K298C 2N4R tau before and after acetyl-lysine mimic formation. **d**, Mass spectra of Cys-free* K311C 2N4R tau before and after acetyl-lysine mimic formation.

* Cys-free refers that the endogenous cysteine residues of tau (C291, C322) are mutated to serine (S).

3. Results

The sections 3.1 to 3.6 are taken from the following article –

Chakraborty P., Rivière G., Liu S., Ibáñez de Opakua A., Derviçoğlu R., Hebestreit A., Andreas L. B., Vorberg I. M., & Zweckstetter M.

Co-factor-free aggregation of tau into seeding-competent RNA-sequestering amyloid fibrils
Nat Commun **12**, 4231 (2021)¹

3.1 Full-length tau fibrillizes without co-factors

To achieve tau fibrillization in the absence of co-factors, we incubated 25 μM 2N4R tau at 37 °C in 25 mM HEPES, 10 mM KCl, 5 mM MgCl₂, 3 mM TCEP, 0.01% NaN₃, pH 7.2, buffer with polytetrafluoroethylene beads. To trigger aggregation, double orbital shaking at an interval of every 10 minutes was applied. Thioflavin-T was used to monitor the aggregation kinetics. 2N4R tau started aggregating after 3 days in the absence of heparin as compared to very rapid aggregation in presence of heparin (Figure 3-1d). After about six days the ThT fluorescence saturated in the absence of heparin, indicating that heparin-free fibrillization of 2N4R was complete (Figure 3-1d). The time-dependent ThT fluorescence of heparin-free tau aggregation displayed the typical sigmoidal kinetics of nucleation-dependent protein aggregation (Figure 3-1d). By measuring the concentration of the monomeric protein left after reaching ThT saturation, we found that ~80 % of 2N4R tau was aggregated (Appendix section 6.11).

To gain first insights into the structure of the aggregated 2N4R tau, we recorded circular dichroism (CD) spectra and negative-stain electron microscopy (EM) images. According to CD, monomeric tau prior to aggregation displays a spectrum (Figure 3-1e), which is characteristic for intrinsically disordered proteins such as tau^{25,165}. In contrast, the CD spectrum of the heparin-free 2N4R tau fibrils obtained after six days of aggregation (Figure 3-1e) is typical for amyloid fibrils comprised of a β-structure-rich core and flexible tails. Quantification of the CD spectrum estimated the β-structure content as ~39 %.

In the case of heparin-induced tau aggregation, it is known that this results in long tau fibrils that form an almost net-like arrangement on EM grids (Figure 3-1g)^{175,176}. In contrast, the 2N4R tau fibrils formed in the absence of heparin (but otherwise using the identical protocol,

i.e. the same buffer, the same polytetrafluoroethylene beads and the same shaking procedure) are short and do not display an extended network on the EM grid (Figure 3-1f). The overall morphological properties of tau fibrils obtained without and with heparin are thus very different (Figure 3-1f,g).

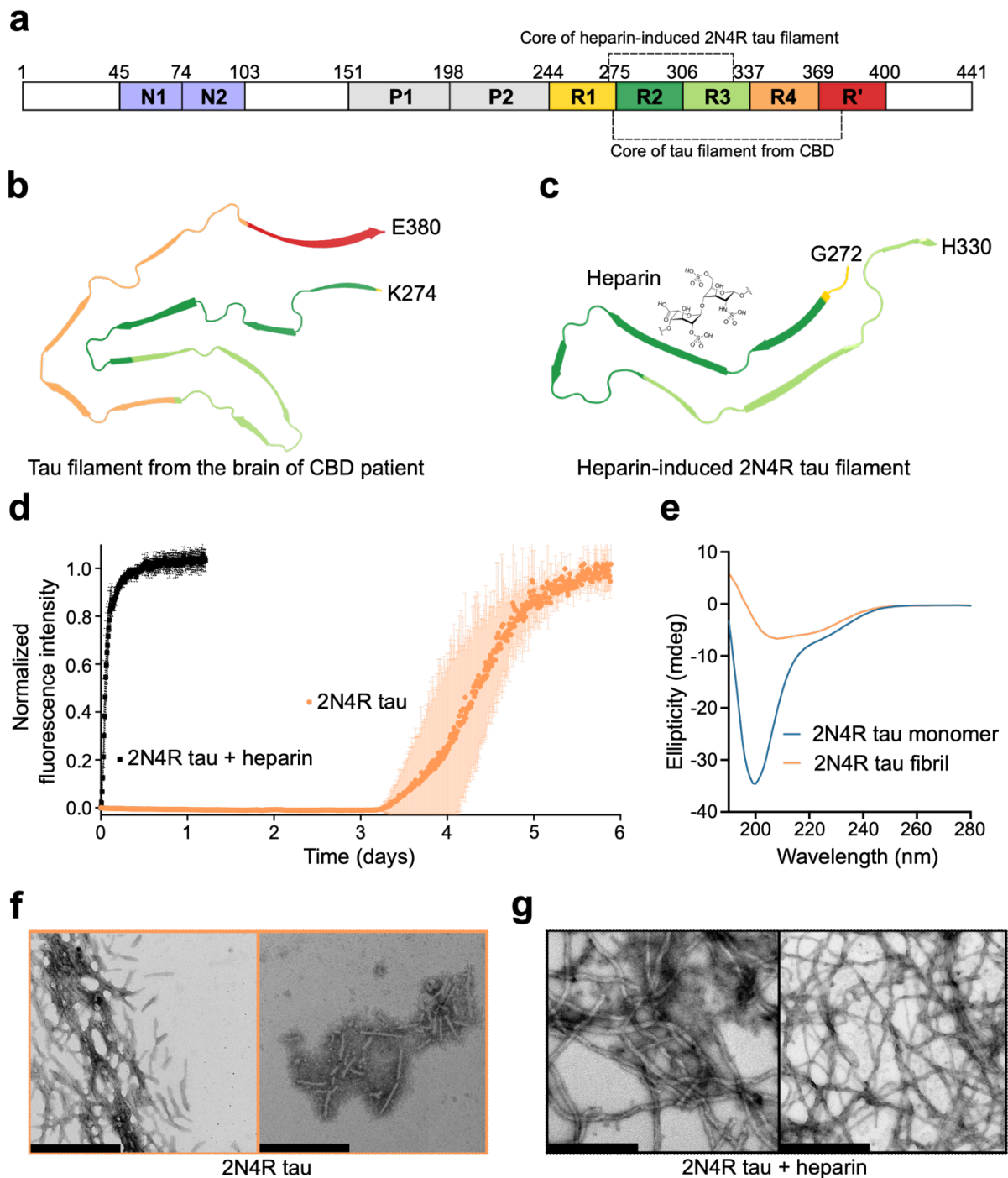


Figure 3-1 Amyloid fibrils of tau without co-factors.

a, Schematic representation of the domain organization of 2N4R tau. N1 and N2 are two inserts subject to alternative splicing, P1 and P2 mark the proline-rich regions, and R1-R' are pseudo-repeats that bind to microtubules. Tau fibril cores from CBD-brain and heparin-induced 2N4R fibrils are marked by dashed lines (see also (b,c)). **b**, CryoEM structure of tau filament (type 1) extracted from the brain of a patient with CBD (PDB code: 6TJO). **c**, CryoEM structure of heparin-induced 2N4R tau fibrils (snake form; PDB code: 6QJH). A molecule of heparin is displayed to illustrate that these fibrils are formed in the presence of heparin. **d**, Aggregation kinetics of 25 μ M 2N4R tau with (black) and without (orange) heparin. Data are presented as mean values \pm standard deviation of $n=3$ independent samples. **e**, Circular dichroism spectra of 2N4R tau monomer and heparin-free fibrils. **f, g** Negative-stain electron micrographs of 2N4R fibrils aggregated without heparin (f) or with heparin (g). Scale bar, 500 nm. Similar micrographs have been observed for both 2N4R fibrils aggregated in presence/absence of heparin with 10 independently aggregated samples.

3.2 Protease-resistant core of heparin-free 2N4R tau fibrils

To obtain direct information about the fibrillar core, 2N4R fibrils were digested by trypsin to remove the fuzzy coat (Figure 3-2a), followed by pelleting down the protease-resistant material through ultracentrifugation. SDS-PAGE gel analysis indicated a much longer core for 2N4R tau fibrils as compared to heparin-induced fibrils (Figure 3-2b). The short trypsin-resistant core of heparin-induced fibrils is in agreement with previous data¹⁷⁶.

To further analyze the rigid core of the fibrils, we determined the sequence of the tau bands observed in SDS-PAGE by mass spectrometry. For heparin-induced fibrils, we detected a large number of peptides from residues ~260 to ~340 (Figure 3-2c; black), consistent with structural analysis by cryoEM (Figure 3-1c)¹²⁰. For 2N4R fibrils, we detected a large number of peptides from residue ~280 to ~400 (Figure 3-2c, orange). In addition, a few peptides for the C-terminal tail were detected, most probably because trypsin cuts the protein carboxy-terminally of K/R residues and there are only a few target residues (K395, R406, K438) for trypsin in this region.

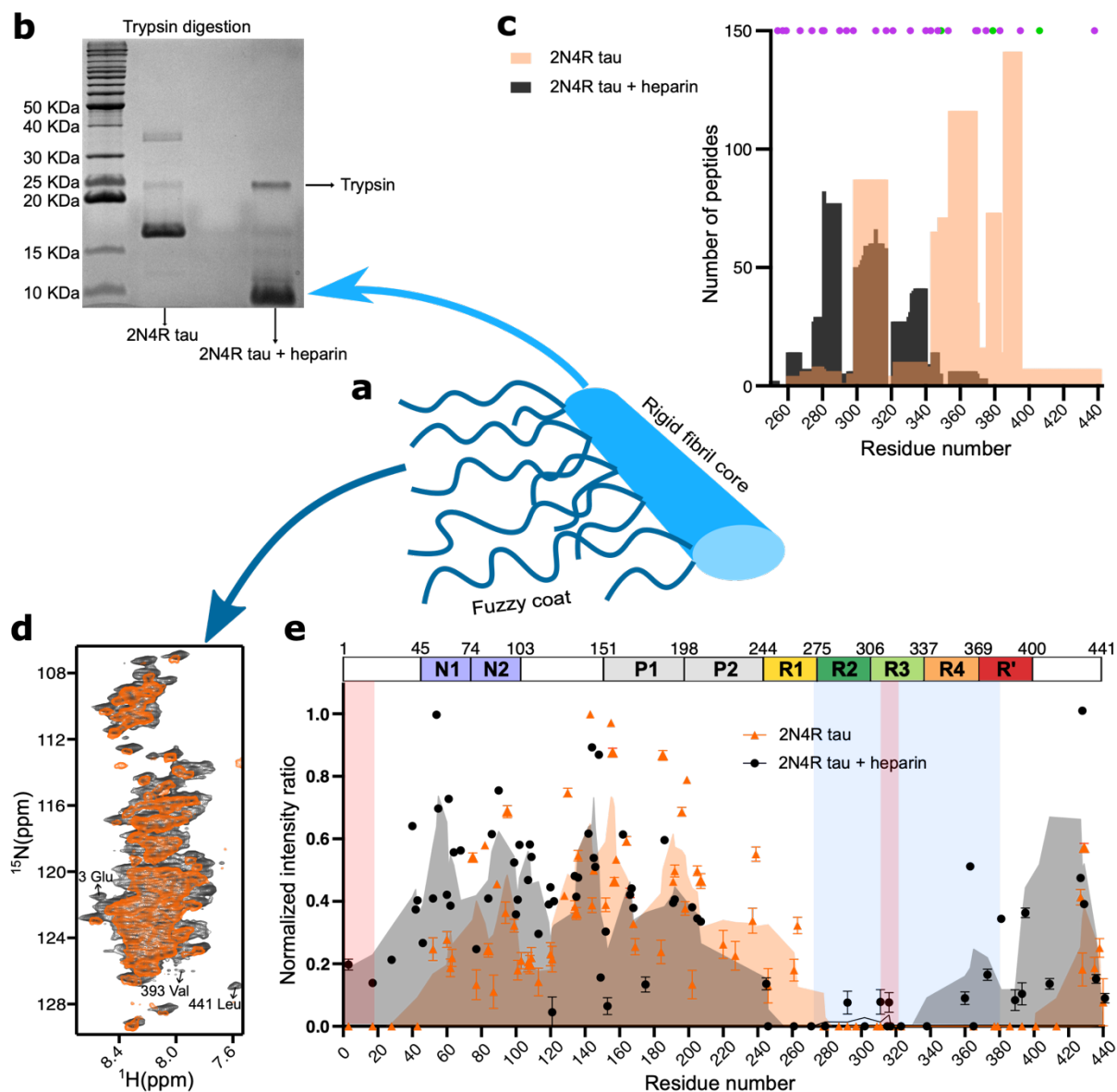


Figure 3-2 Heparin-free tau fibrils have an extended core and an immobile N-terminal antibody-binding epitope.

a, Cartoon representation of the rigid core and dynamic (termed fuzzy) coat of tau fibrils. **b**, SDS-PAGE gel of trypsin-digested tau fibrils formed in the absence or presence of heparin. The trypsin band is indicated. The result was reproducible for three independently performed experiments. **c**, Number of peptides detected from the enzymatic digestion of the tau bands observed in SDS-PAGE in (a). The position of lysine and arginine residues of 2N4R tau are marked with purple and green dots, respectively. **d**, Superposition of ^1H - ^{15}N INEPT spectra of 2N4R tau fibrils aggregated in the absence (orange) and presence (black) of heparin. **e**, Intensity ratio plot of 2N4R tau fibrils aggregated in the absence (orange) and presence (black) of heparin. The intensity ratio was calculated by dividing the

signal intensity of each residue in the fibril state by the monomeric state. The error of the intensity ratio for each residue was calculated from the signal-to-noise ratio of the cross peaks in the spectra. The rigid cross- β -sheet core of the tau fibril extracted from a CBD patient brain (PDB code: 6TJO) is marked in light blue. The two discontinuous epitopes (residues 1–18 and residues 313–322) of antibodies that specifically detect pathological tau¹⁷⁷ are marked by red boxes.

To get more precise information about the protease-resistant core of the heparin-free 2N4R fibrils, especially to get more resolution at the C-terminus, we repeated the experiments with pronase. Pronase is a mixture of several endo- and exoproteases that can digest a protein into individual amino acids. 2N4R fibrils were digested by pronase and the resistant fibril core was pelleted down by ultracentrifugation. After excising the pronase-resistant band with trypsin, we detected peptides up to residue 379 (Figure 3-3).

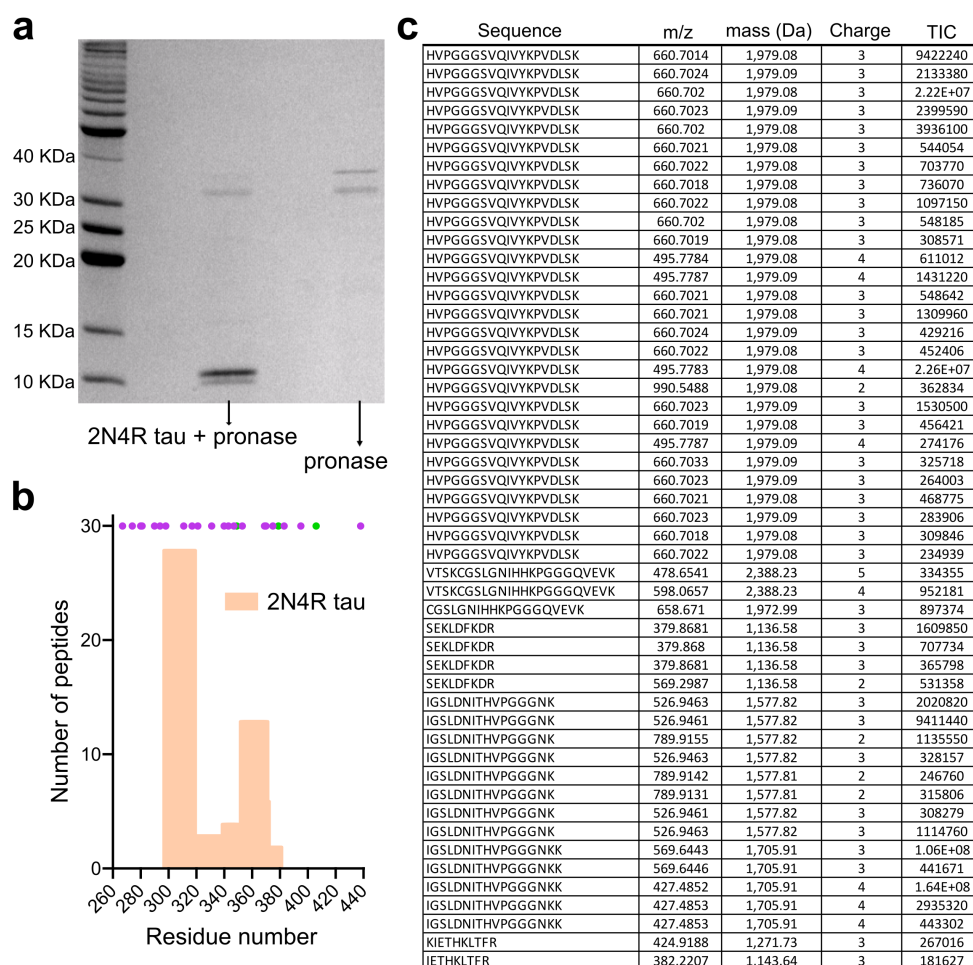


Figure 3-3 Pronase-resistant core of heparin-free 2N4R tau fibrils.

a, SDS-PAGE gel of pronase-digested tau fibrils formed in the absence of heparin. The pronase band is indicated in a separate lane. The result was reproducible for three independently performed experiments. **b**, Number of peptides detected from the enzymatic digestion of the tau band observed in SDS-PAGE in (a). The position of lysine and arginine residues in 2N4R tau are marked with purple and green dots, respectively. **c**, Details of the peptides detected as shown in (b).

3.3 Rigidification of the N-terminal epitope of pathological tau

Next, we aggregated uniformly $^{13}\text{C}/^{15}\text{N}$ -labeled 2N4R tau both in the absence and presence of heparin and recorded ^1H - ^{15}N insensitive nuclei enhanced by polarization transfer (INEPT) spectra under conditions of magic angle spinning (Figure 3-2d and Figure 3-4). INEPT experiments use scalar coupling for polarization transfer, thereby detecting only the highly dynamic residues in solid samples, i.e. the fuzzy coat in the case of tau fibrils (Figure 3-2a,d). Residue-specific analysis of the INEPT spectra revealed a complete loss of signal from residues ~270 to ~400 in the case of 2N4R fibrils (Figure 3-2e), in agreement with mass spectrometry analysis (Figure 3-2c). In the case of heparin-induced fibrils, no INEPT signals were detected for residues ~260 to ~330. Because cryoEM resolves only the very rigid residues in cross- β -structure at high resolution and has reported additional unidentified electron density in tau fibrils, the analysis suggests that in vitro-generated 2N4R fibrils, but not heparin-induced fibrils, have a similar core length as tau fibrils purified from CBD patient brain (residues ~274 to ~380 were resolved at high resolution; PDB code: 6TJO; marked in light blue in Figure 3-2e).

The NMR analysis, however, provided further insights into the key regions of tau aggregation. Not only residues ~270 to ~400 were broadened beyond detection in the case of the heparin-free 2N4R tau fibrils, but also the amino-terminal 30 residues (Figure 3-2e; marked in pink). This is most likely because of a dynamic interaction of the N-terminus of tau with the cross- β -structure core¹⁷⁸. The immobilization of the N-terminal 30 residues provides a structural basis for the specificity of antibodies that specifically detect pathological tau¹⁷⁷ and require two discontinuous epitopes located in the repeat region (residues 313–322) and at the N-terminus (residues 1–18)¹⁷⁷.

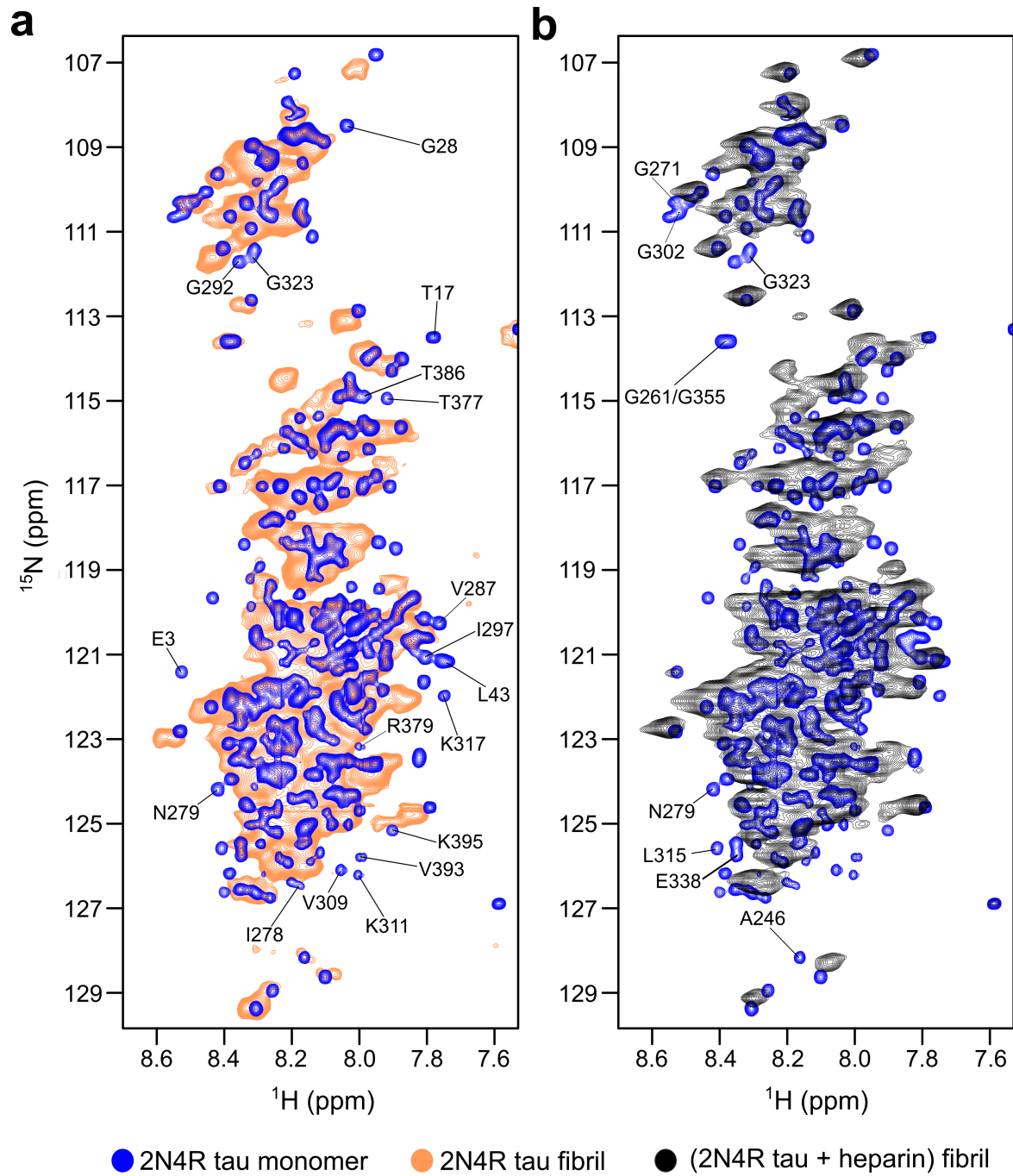


Figure 3-4 INEPT spectra of tau fibrils

Superposition of the ^1H - ^{15}N HSQC spectrum of monomeric 2N4R tau (blue) with ^1H - ^{15}N INEPT spectra of heparin-free 2N4R fibrils (orange; left) and heparin-induced fibrils of 2N4R tau (black; right).

3.4 Solid state NMR of the core of 2N4R tau fibrils

Next, we probed the rigid core of the 2N4R tau fibrils. To this end, ^{13}C - ^{13}C correlations were recorded using cross-polarization solid-state NMR experiments (Figure 3-5a). In agreement with mass spectrometry and the INEPT-based NMR analysis (Figure 3-2), the ^{13}C - ^{13}C spectrum of 2N4R fibrils contained many more signals when compared to the spectrum of heparin-induced fibrils (Figure 3-5a). This was particularly evident from the C_β region of serine and threonine residues (Figure 3-5a), indicating that more serine and threonine residues are located in the core of 2N4R fibrils (Figure 3-5b,c). In addition, only one broad cross peak was observed in the threonine C_γ region of the heparin-induced fibrils, while about six cross-peaks were present in the case of the 2N4R fibrils (Figure 3-5a, selected zoom). Because only rigid residues are detected in the cross-polarization NMR experiments, the number of observed threonine cross peaks is consistent with the fibrillar core of 2N4R fibrils derived from mass spectrometry and INEPT-based NMR experiments (Figure 3-5b,c).

To further characterize the 2N4R fibrils, we recorded 2D NCA as well as 3D NCACX and 3D NCOCX experiments. Due to strong signal overlap, however, only a few residues in the fibril core could be identified (Figure 3-5d,e,f). This included the residue stretch from G303 to V306 (Figure 3-5d,e,f) that is part of the cross- β -structure core of tau fibrils purified from a CBD patient (Figure 3-1b). Isolated peaks in the 2D RFDR and 2D NCA spectra of the heparin-free 2N4R tau fibrils show ^{13}C and ^{15}N line widths of 0.6 to 0.8 ppm and 0.9 to 1.1 ppm, respectively, indicating structural homogeneity of the rigid core.

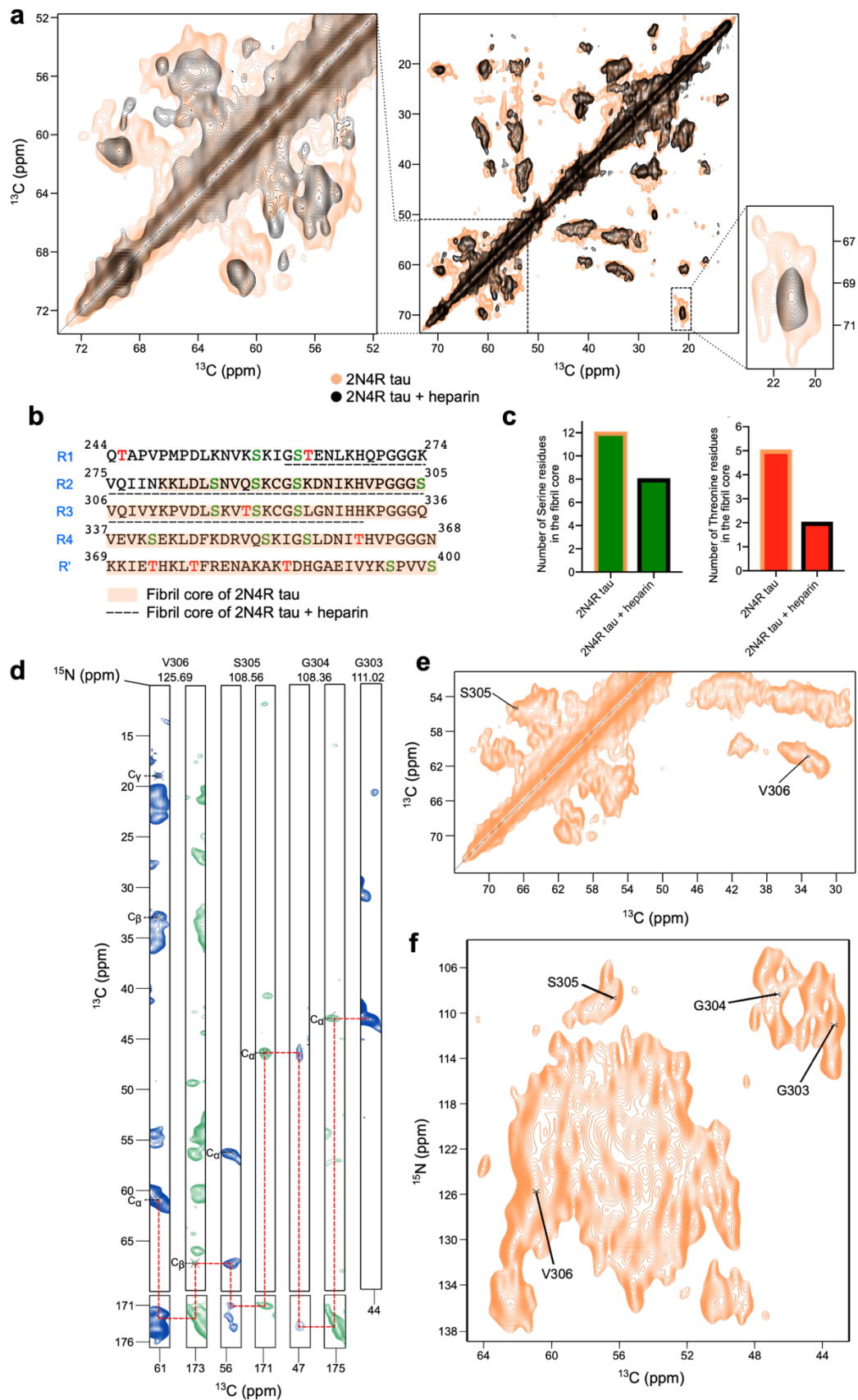


Figure 3-5 Solid-state NMR of the core of heparin-free tau fibrils.

a, ^{13}C - ^{13}C RFDR spectra of 2N4R tau fibrils (middle panel), which were aggregated without (orange) or with heparin (black). The C_{β} region of serine and threonine residues is highlighted on the left, the C_{γ} region of threonine to the right. **b**, Amino acid sequence of the repeat region of 2N4R tau. Serine residues are colored in green, threonine residues in red. The core of heparin-free 2N4R tau fibrils is highlighted in orange. The fibrillar core of heparin-induced 2N4R tau fibrils is underlined with black dashed lines. **c**, Number of serine and threonine residues in the core of 2N4R tau fibrils that were formed in the absence or presence of heparin (according to (b)). **d**, Strips from 3D NCACX (blue) and 3D NCOCX (green) spectra of heparin-free 2N4R tau fibrils, illustrating the sequential assignment of residues. **e**, Selected region of the ^{13}C - ^{13}C RFDR spectrum of heparin-free 2N4R tau fibrils, indicating the assignment of the cross peaks of residues S305 and V306. **f**, 2D NCA spectrum of heparin-free 2N4R tau fibrils, indicating the assignment of the cross peaks of residues 303-306 (based on (d)).

To gain further insight into the structural properties of 2N4R tau fibrils, we aggregated selectively labeled ($^{13}\text{C}_{\gamma}$ valine, ^{13}C -ring phenylalanine, ^{15}N histidine) 2N4R tau in the absence of heparin. 2D hCH and 2D hNH cross-polarization spectra demonstrated that the protein is ^{13}C labeled only at the C_{γ} of valine and the ring carbons of phenylalanine, and ^{15}N labeled at the backbone and side chain of histidine residues (Figure 3-6a; Appendix section 6-12). We then recorded Dynamic Nuclear Polarization (DNP)-enhanced solid-state NMR spectra in order to achieve maximum sensitivity. We used TEMTriPol-1^{168,169} and observed a 12-fold DNP enhancement of the signal (Figure 3-6b).

Next, DNP-enhanced 2D hCHHC spectra with 200 μs and 400 μs mixing were measured. The chosen mixing times will result in cross-peaks between two ^{13}C atoms that are about ≤ 4 Å and ≤ 6 Å apart, respectively¹⁷¹. In the spectra displayed in Figure 3-6c, two cross peaks between the C_{γ} of valine and the ring carbons of phenylalanine are present. The cross peaks are detected both below and above the diagonal (Figure 3-6c), in agreement with the expected symmetric magnetization transfer. The presence of the two cross peaks suggests that the side chains of one or two valine residues are in close spatial proximity to the side chain of a phenylalanine residue. We also recorded DNP-enhanced 2D hNHHC spectra with 200 μs mixing and observed a cross peak between the ^{15}N -ring of histidine and $^{13}\text{C}_{\gamma}$ of valine (Figure 3-6d), indicating that the aromatic ring of a histidine is in proximity (~ 4 Å) to the side chain of a valine residue in the structure of 2N4R fibrils.

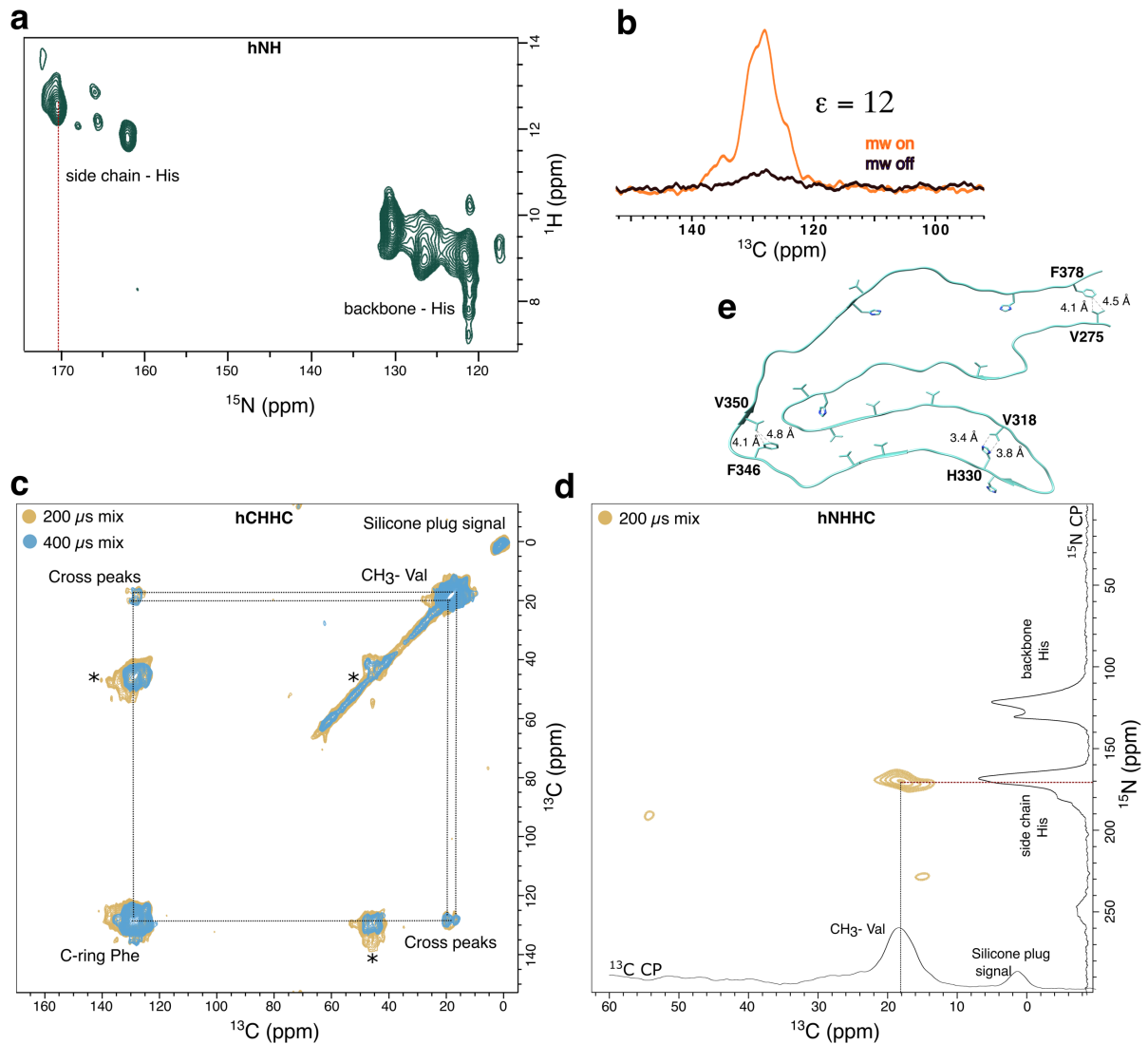


Figure 3-6 Residue type-specific contacts within the core of heparin-free 2N4R tau fibrils.

a, Proton-detected ^1H - ^{15}N correlation solid-state NMR spectrum of heparin-free fibrils of 2N4R tau selectively labeled with ^{15}N Histidine (and at the $^{13}\text{C}_\gamma$ of valine and the ^{13}C -ring of phenylalanine). The spectrum was recorded at room temperature at a NMR spectrometer with 850 MHz ^1H frequency using 55 kHz magic angle spinning (MAS) frequency. **b**, Comparison of the ^{13}C NMR signal of phenylalanine (ring carbons) when the microwave is turned on (orange) or off (black). The signal enhancement (ϵ) is displayed. Spectra shown in (b-d) were recorded at a temperature of 100 K at a NMR spectrometer with 600 MHz ^1H frequency using 12.5 kHz MAS spinning. **c**, Superposition of DNP-enhanced 2D hCHHC spectra of selectively labeled ($^{13}\text{C}_\gamma$ valine, ^{13}C -ring phenylalanine, ^{15}N histidine) heparin-free 2N4R tau fibrils with 200 μs (yellow) and 400 μs (sky blue) mixing time. Spinning side bands are labeled with *. **d**, DNP-enhanced 2D hNHHC spectrum of selectively labeled ($^{13}\text{C}_\gamma$ valine, ^{13}C -ring

phenylalanine, ^{15}N histidine) heparin-free 2N4R tau fibrils. **e**, Location of valine, phenylalanine and histidine residues within the core structure of the tau filament (type 1) extracted from the brain of a patient with CBD (PDB code: 6TJO). Short-range distances between valine and phenylalanine, and histidine and valine are marked.

The 2N4R tau sequence contains three phenylalanine residues, but only two (F346 and F378) are located in the rigid/semi-rigid core of 2N4R tau fibrils, which comprises residues ~270 to ~380 (Figure 3-2). In the cryoEM structure of ex vivo CBD fibrils, F346 contacts V350, and F378 contacts V275 (Figure 3-6e). The two phenylalanine-valine cross peaks observed in the spectra of 2N4R fibrils might thus arise from these structure-specific contacts. In addition, there is only a single close contact between the aromatic ring of a histidine (H330) and the C_γ of valine (V318) in the structure of CBD fibrils (Figure 3-6e). This could correspond to the observed $\text{His}^{(15}\text{N-ring})/\text{V}^{(13}\text{C}_\gamma)$ cross peak in 2N4R fibrils (Figure 3-6d).

3.5 Seeding of Tau fibrillization *in-vitro* and *in-cell*

Tau pathology in the brain follows a “prion-like” behavior with transneuronal propagation of tau aggregates from one brain region to another⁹⁸. A critical process in tau spreading is the ability of tau aggregates to seed fibrillization of monomeric tau. In order to study the *in vitro* seeding efficiency of 2N4R fibrils, 1 % and 5 % seeds (w/w) of 2N4R fibrils were added to the monomeric protein. The addition of seeds decreased the half time of aggregation four times (Figure 3-7a, b), confirming the seeding activity of 2N4R fibrils.

Next, we performed an *in-cell* seeding experiment using tau biosensor cells (Figure 3-7c)¹⁷⁹. Four different concentrations (0.1, 0.2, 0.4, and 0.8 μM) of seeds of 2N4R fibrils, as well as heparin-induced fibrils, were used to induce aggregation. The 2N4R fibril seeds efficiently induced TauRD-GFP puncta in a concentration-dependent manner (Figure 3-7d, e).

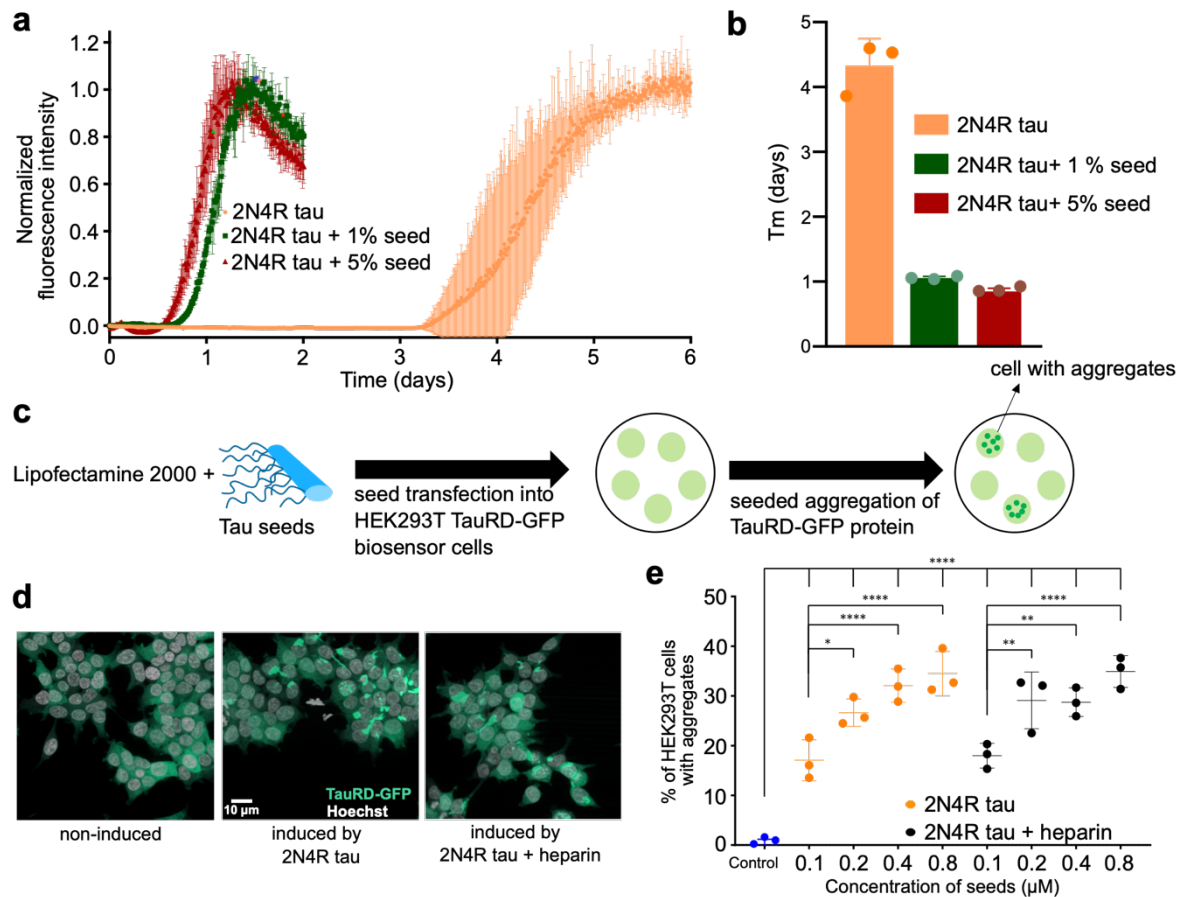


Figure 3-7 Seeding activity of heparin-free tau fibrils.

a, Aggregation kinetics of 25 μM 2N4R tau in the absence (orange) and presence of 1% (green) and 5% (red) tau seeds generated without heparin. Data are presented as mean values \pm standard deviation of $n=3$ independent samples. **b**, Half-time (T_m) of aggregation of 2N4R tau in the absence (orange) and presence of 1% (green), 5% (red) tau seeds (see (a)). Data are presented as mean values \pm standard deviation of $n=3$ independent samples. **c**, Schematic representation of the process of seeding of tau aggregation in biosensor cells. **d**, TauRD-GFP puncta in HEK293T biosensor cells^{172,179}, expressing the tau repeat domain carrying the mutations P301L and V337M, induced by 2N4R tau seeds, which were formed either in the absence (left) or presence of heparin (right). The result was reproducible for three independently performed experiments. **e**, Comparison of the efficiency of 2N4R tau seeding in tau biosensor cells. Fibrils were generated by aggregating 2N4R tau in the absence (orange) or presence (black) of heparin. Different concentrations of seeds (0.1 to 0.8 μM) were used to induce TauRD-GFP puncta. The statistical analysis between the % of HEK293T cells with puncta induced by each concentration of seeds in the absence/presence of heparin was performed by one-way ANOVA analysis. Fibrils of different concentrations were independently transfected $n=3$ times.

Error bars represent the standard deviation of three independent experiments. Four stars represent p value < 0.0001 , two stars represents p value = <0.0021 , one star represents p value = 0.0296 .

3.6 Heparin-free Tau fibrils strongly bind RNA

Tau aggregates in human patient brains are extensively decorated with RNA¹⁸⁰, consistent with the positively charged surface seen in the cryoEM structure of CBD fibrils (Figure 3-8a). To investigate the interaction of 2N4R fibrils with RNA, we added polyU, polyA or tRNA to the fibrils and incubated the samples for 1.5 hours in the aggregation assay buffer (10 mM KCl, 25 mM HEPES, 5 mM MgCl₂, 3 mM TCEP, pH 7.2) followed by centrifugation to separate the pellet and supernatant (Figure 3-8b). In these conditions, 2N4R tau fibrils were found to interact strongly with all three RNAs as detected by the presence of ~82 % polyU, ~80 % polyA and ~93 % tRNA in the pellet (Figure 3-8c). In contrast, only ~18 % polyU, ~15 % polyA and ~7 % tRNA were found in the pellets of the heparin-induced fibrils (Figure 3-8c) suggesting very weak affinity of all three RNAs to the heparin-induced fibrils in the aggregation assay buffer.

In order to investigate the fibril interaction of the three RNAs at higher ionic strength, we repeated the experiments in a buffer with increased KCl concentration (100 mM KCl). At this higher ionic strength, the 2N4R tau fibrils, which were aggregated in the absence of heparin, interacted with all three RNAs (Figure 3-8c). Comparison of the amount of RNA in the pellets further suggested that polyU binds most efficiently to the fibrils (Figure 3-8c). In the case of the heparin-induced 2N4R tau fibrils, ~90 % polyU, ~35 % polyA and ~6 % tRNA was detected in the pellet. The heparin-induced fibrils thus bind to polyU in 100 mM KCl, but hardly interact in this condition with tRNA (Figure 3-8c).

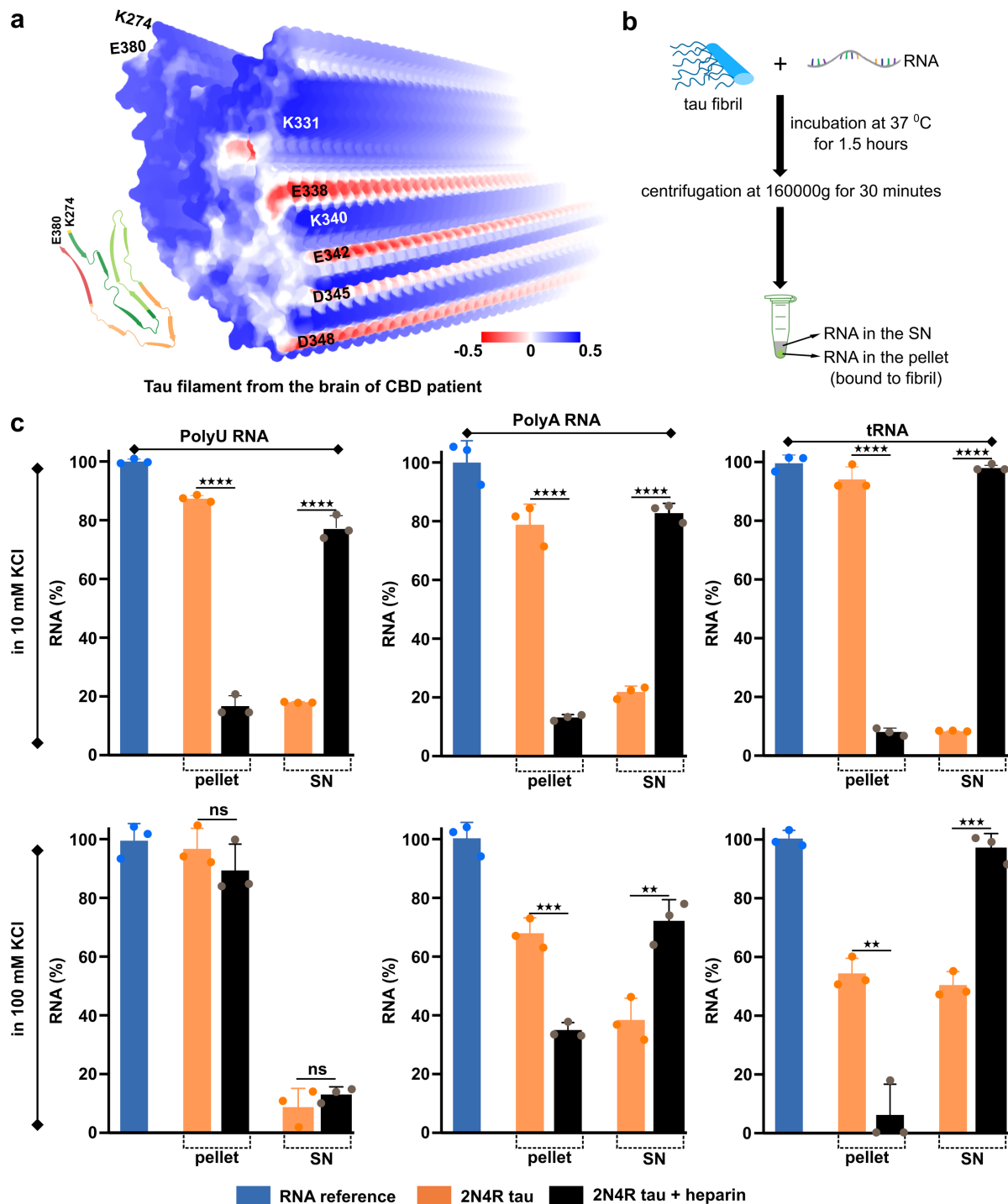


Figure 3-8 Heparin-free tau fibrils strongly bind RNA.

a, Electrostatic surface potential of the tau filament extracted from a CBD patient (PDB code: 6TJO). Positively and negatively charged residues are shown in blue and red, respectively. **b**, Schematic representation of the protocol to determine the binding of RNA to tau fibrils. **c**, Quantitative analysis of the binding of polyU, polyA and tRNA to tau fibrils aggregated without (orange) or with heparin

(black) in the aggregation assay buffer (10 mM KCl, 25 mM HEPES, 5 mM MgCl₂, 3 mM TCEP, pH 7.2) or at increased ionic strength (100 mM KCl, 25 mM HEPES, 5 mM MgCl₂, 3 mM TCEP, pH 7.2). The amount of RNA in the pellet represents the % of RNA bound to the fibril and the amount of RNA in the supernatant (SN) represents the % of unbound RNA. The statistical analysis between the % of RNA bound to heparin-free and heparin-induced tau fibrils was performed by Welch's t test. Four stars represent p value < 0.0001, three stars represents p value < 0.0002, two stars represents p value < 0.0021. Data are represented as mean values of n=3 independent experiments. Error bars represent the standard deviation of three independent experiments.

3.7 Unmodified 3R tau forms amyloid fibrils in the absence of co-factors

To gain insight into the molecular factors that determine the formation of disease-specific tau aggregate structures, we focused on 3R tau fibrils because they are specific pathological hallmarks of the 3R tauopathy Pick's disease⁸⁵ (Figure 3-9a). We aggregated 3R tau *in vitro* in the absence of heparin or other co-factors following the assay previously established for 4R tau¹ (Section 3.1). 3R tau started to form fibrils after two days according to the increase in ThT fluorescence intensity (Figure 3-9c). At the end of the incubation period, the samples displayed CD spectra typical for amyloid fibrils with a minimum at ~220 nm (Figure 3-9d). Negative-stain EM confirmed the presence of fibrils (Figure 3-9e).

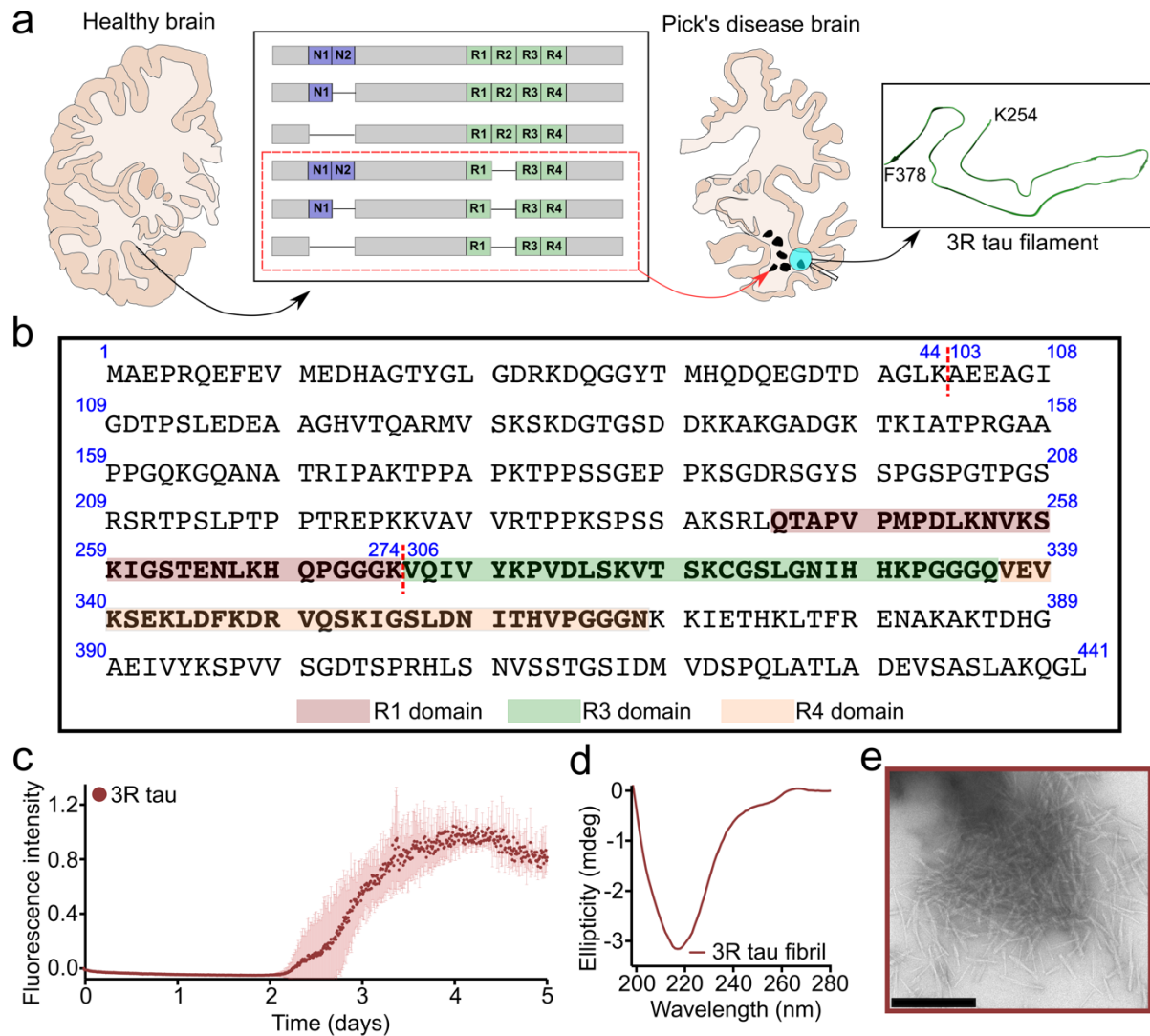


Figure 3-9 Co-factor-free aggregation of 3R tau.

a, Cartoon representation of the specific deposition of 3R tau in 3R tauopathy, Pick's disease. The structure of tau filament derived from the brain of Pick's disease patient (PDB code: 6GX5) is shown. **b**, Amino acid sequence of 0N3R tau. The amino acids are numbered based on the sequence of the full-length tau (2N4R tau). The pseudo-repeat domains R1, R3, and R4 are highlighted with red, green, and orange, respectively. **c**, Aggregation kinetics of 3R tau (25 μ M) in the absence of co-factors. Error bars represent std of three independent samples. **d,e**, CD spectra (b) and negative-stain electron micrographs (c) of 3R tau fibrils. Scale bar, 500 nm.

To determine the rigid core of the co-factor-free 3R tau fibrils, we aggregated uniformly $^{13}\text{C}/^{15}\text{N}$ -labeled protein and recorded ^1H - ^{15}N Inensitive nuclei enhanced by polarization

transfer (INEPT) spectra with magic angle spinning (Figure 3-10a). INEPT experiments selectively detect highly dynamic residues. Sequence-specific analysis identified residues upstream of residue ~260 and downstream of residue ~380 (Figure 3-10a,b). Cross peaks for residues in between were not observed (Figure 3-10b), indicating that the rigid core of the 3R tau fibrils comprises approximately residues 260-380. In addition to residues in the central part of tau, ~30-40 residues at the N-terminus were broadened beyond detection in the fibril spectrum. This residue stretch contains the epitope for recognition of pathologically aggregated tau by conformation-specific monoclonal antibodies¹⁸¹. In the cryoEM structure of tau fibrils extracted from the brain of patients with Pick's disease, residues 254-378 were resolved⁹³.

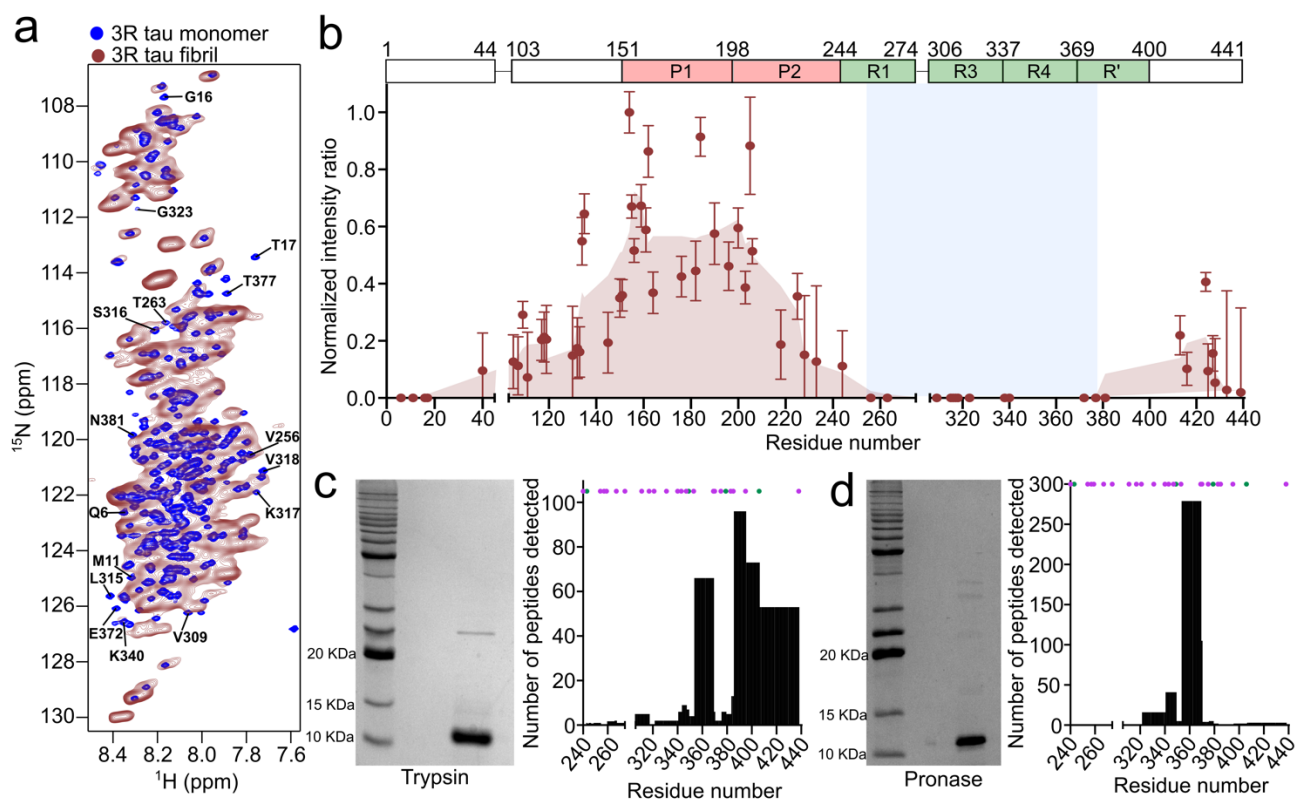


Figure 3-10 The rigid core of co-factor-free 3R tau fibrils

a,b, NMR analysis of the rigid core of 3R tau fibrils. Superposition of the ^1H - ^{15}N HSQC spectrum of monomeric 3R tau (blue, a) with ^1H - ^{15}N INEPT MAS spectra of 3R tau fibrils (red, a). Assignments of residues broadened beyond detection in the fibrils are displayed. Residue-specific intensity ratios

derived from (a) are shown in (b). Errors in intensity ratios were calculated from the signal-to-noise ratio of the cross-peaks in the respective spectra. Residues resolved in the cryoEM structure of tau fibrils extracted from the brain of a patient with Pick's disease (PDB code: 6GX5) are marked in light blue. **c,d**, Protease digestion of 3R tau fibrils. SDS-PAGE gel of trypsin (c) and pronase (d) -digested 3R tau fibrils. Numbers of detected peptides are shown to the right. The position of lysines and arginines are marked with purple and green dots, respectively.

To confirm the findings from NMR, 3R tau fibrils were digested by trypsin to remove the fuzzy coat, followed by pelleting down the trypsin-resistant material and loading it in an SDS-PAGE gel. We analyzed the trypsin-resistant band observed in the SDS-PAGE gel by mass spectrometry and detected peptides from residues ~250 to 438 (Figure 3-10c). The detection of peptides for the C-terminal residues (after residue 380) is due to the scarcity of trypsin-target residues (K395, R406, K438). To get further resolution at the C-terminus, we repeated the digestion experiment in the presence of the more promiscuous protease pronase. We detected peptides up to residue 380 upon analyzing the pronase resistant band by mass spectrometry (Figure 3-10d). The combined data show that 3R tau efficiently aggregates *in vitro* into amyloid fibrils that have a rigid core similar to fibrils extracted from Pick's disease patient brain.

3.8 P300/CBP selectively acetylate tau in repeats R2/R3

Amyloid fibrils purified from Pick's disease patient brain contain predominantly 3R tau⁸⁵. Brain-derived 3R tau fibrils are acetylated at multiple lysine residues¹⁵⁷. In addition, monomeric tau can be efficiently acetylated *in vitro* by the acetyltransferases p300 and CBP^{141,142}, and reducing acetylated tau by p300 inhibition is neuroprotective in brain injury¹⁵¹. To determine the sites of p300/CBP-mediated acetylation of 3R tau with single-residue resolution and quantify their degree of acetylation with high accuracy, we performed *in vitro* acetylation of ¹⁵N-lysine labeled monomeric 3R tau in the presence of either p300 or CBP, or both enzymes together. The acetylation levels of individual lysine residues were determined from the intensity ratios of the cross peaks of the unacetylated lysine (in the acetylated sample) and unmodified lysine in 2D ¹H-¹⁵N HSQC NMR spectra (Figure 3-11b).

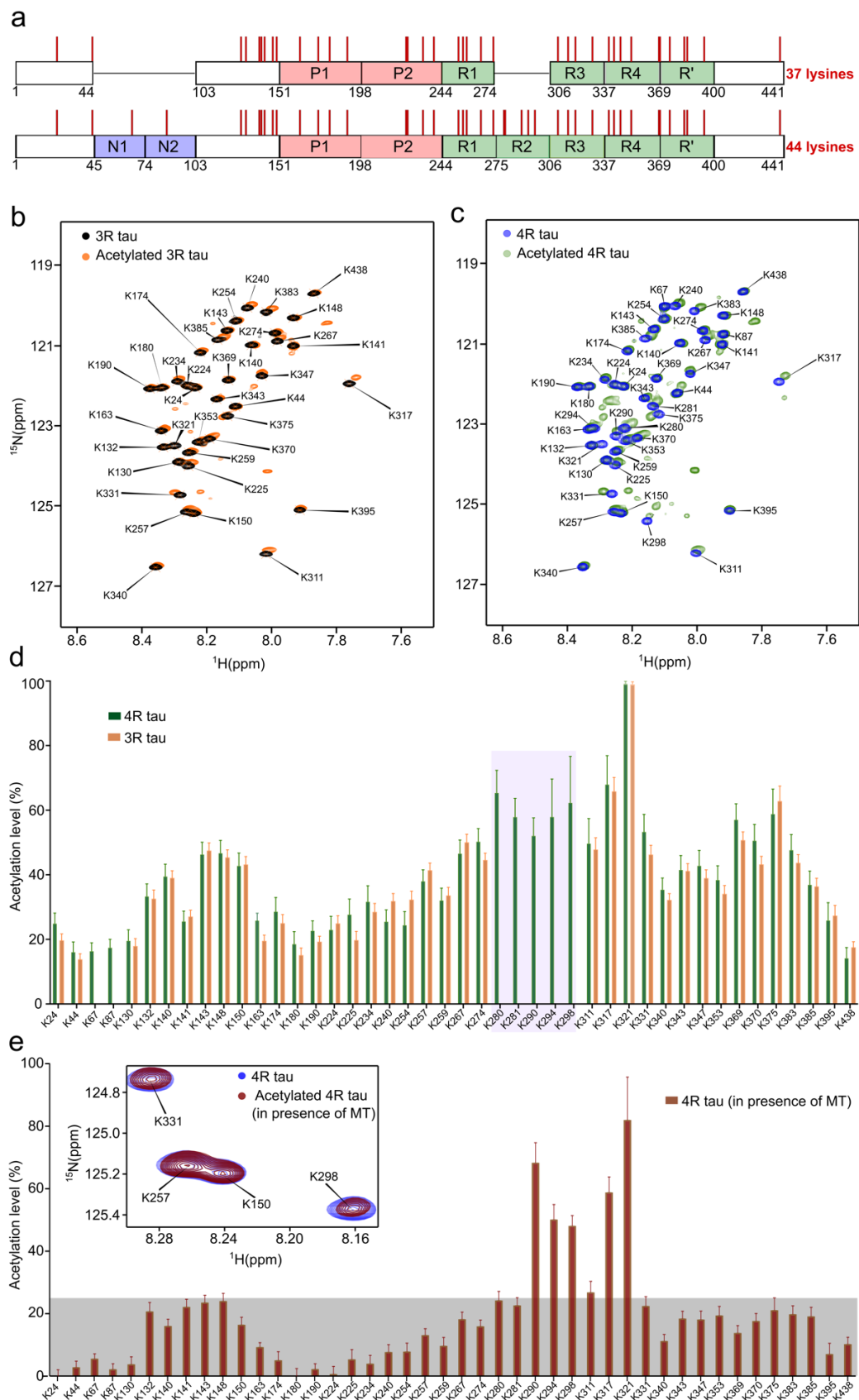


Figure 3-11 Acetylation of 4R tau at three lysines in repeat R2.

a, Domain diagram of 3R and 4R tau. Lysines are indicated with red bars. The total numbers of lysine residues present in 0N3R tau and 2N4R tau are indicated. **b,c** Superposition of the ^1H - ^{15}N HSQC spectra of unmodified lysine-labeled 3R tau (**b**; 50 μM ; black) or 4R tau (**c**; 50 μM ; blue) and the corresponding acetylated proteins (**b**: orange; **c**: green). Acetylation was performed by incubation with both p300 and CBP for twelve hours. **d**, Analysis of acetylation levels of individual lysine residues derived from (**b**) and (**c**). Errors in acetylation levels were calculated from the signal-to-noise ratio of the cross-peaks in the NMR spectra. The strongly acetylated five lysine residues in R2 repeat of 4R tau are highlighted by a purple box. **e**, Analysis of acetylation levels of individual lysine residues of 4R tau after acetylating with both p300 and CBP for two hours in the presence of microtubules. Errors in acetylation levels were calculated from the signal-to-noise ratio of the cross-peaks in the NMR spectra. The grey box represents a 25 % cut-off for weakly acetylated lysine residues. Superposition of the selected region of the ^1H - ^{15}N HSQC spectra of unmodified lysine-labeled 4R tau (blue) and acetylated 4R tau (in presence of MT) (brown) is shown in the inset.

The analysis revealed that p300 and CBP can broadly acetylate lysine residues in 3R tau (Figure 3-11b,d), and tau acetylation is similar when the enzymes are used individually or together (Figure 3-12). However, the degree of acetylation strongly varies from ~20-70 % between different lysine residues (Figure 3-11d, 3-12). K317 and K321 in repeat R3 were acetylated most strongly after twelve hours of the acetylation reaction, i.e. in conditions of hyper-acetylation (Figure 3-11d).

To test if acetylation is isoform-specific, we acetylated 4R tau (Figure 3-11c). Residue-specific analysis showed that the levels of hyper-acetylation at individual lysines are highly similar in 3R and 4R tau with K317 and K321 being most strongly acetylated (Figure 3-11d, 3-12). In addition, however, the five lysine residues (K280, K281, K290, K294, K298) of repeat R2 - the repeat that is missing in 3R tau isoforms - were strongly acetylated by p300/CBP in 4R tau (Figure 3-11d).

Physiological tau is predominantly bound to microtubules²⁵. We therefore repeated the acetylation reaction of ^{15}N -lysine-labeled 4R tau in the presence of a two-fold excess of microtubules over tau, matching the molar stoichiometry of the tau:tubulin interaction.¹⁸² In

addition, we decreased the time of acetylation from twelve hours to two hours, in order to acetylate predominantly the most reactive lysines in tau. In these conditions, only three lysine residues in repeat R2 (K290, K294, K298) and two lysine residues in repeat R3 (K317, K321) were efficiently acetylated (< 25%) (Figure 3-11e). In contrast, K280 and K281, which are part of the heptapeptide motif in R2 that localizes to the intra-dimer interface of microtubules,³² only reached low levels of acetylation (Figure 3-11e). The combined data reveal highly selective acetylation of a total of five lysine residues in tau, with three of them (K290, K294 and K298 in repeat R2) unique to 4R tau.

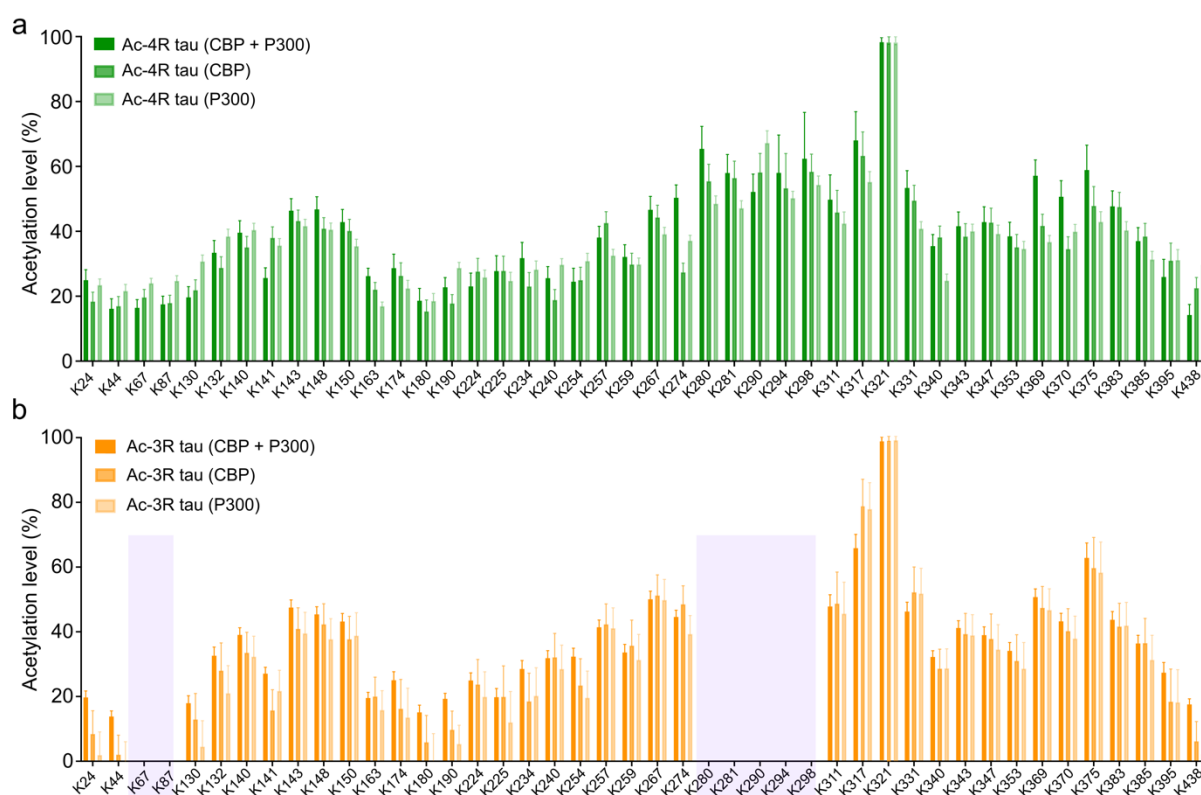


Figure 3-12 Common tau acetylation patterns by p300 and CBP.

a,b Comparison of acetylation levels of individual lysine residues present in 2N4R tau (a) or 0N3R tau (b) upon acetylation with either p300 or CBP, or both acetyltransferases. The acetylation level of the lysine residues was determined from the signal intensity ratio of the unacetylated lysine (in the acetylated sample) and unmodified lysine. Error in intensity ratios were calculated from the signal-to-noise ratio of the cross-peaks in the NMR spectra. Lysine residues only present in 2N4R tau are marked by purple boxes.

3.9 Acetylation accelerates 3R tau but blocks 4R tau fibrillization

All five lysine residues that are efficiently acetylated by p300/CBP are part of repeat R2 and R3, which play an important role in the pathogenic aggregation of tau^{155,156,183}. Tau acetylation thus might have a strong impact on both the protein's aggregation kinetics and the amyloid fibril structure. To gain insight into the influence of acetylation on tau fibrillization, we performed aggregation assays of unmodified as well as p300/CBP-acetylated 3R and 4R tau. Unmodified 3R tau starts to fibrillize after ~2-2.5 days (Figure 3-13a, black). In contrast, acetylated 3R tau forms fibrils already after ~1.5 days (Figure 3-13a, orange), demonstrating that acetylation strongly accelerates the fibrillization of 3R tau.

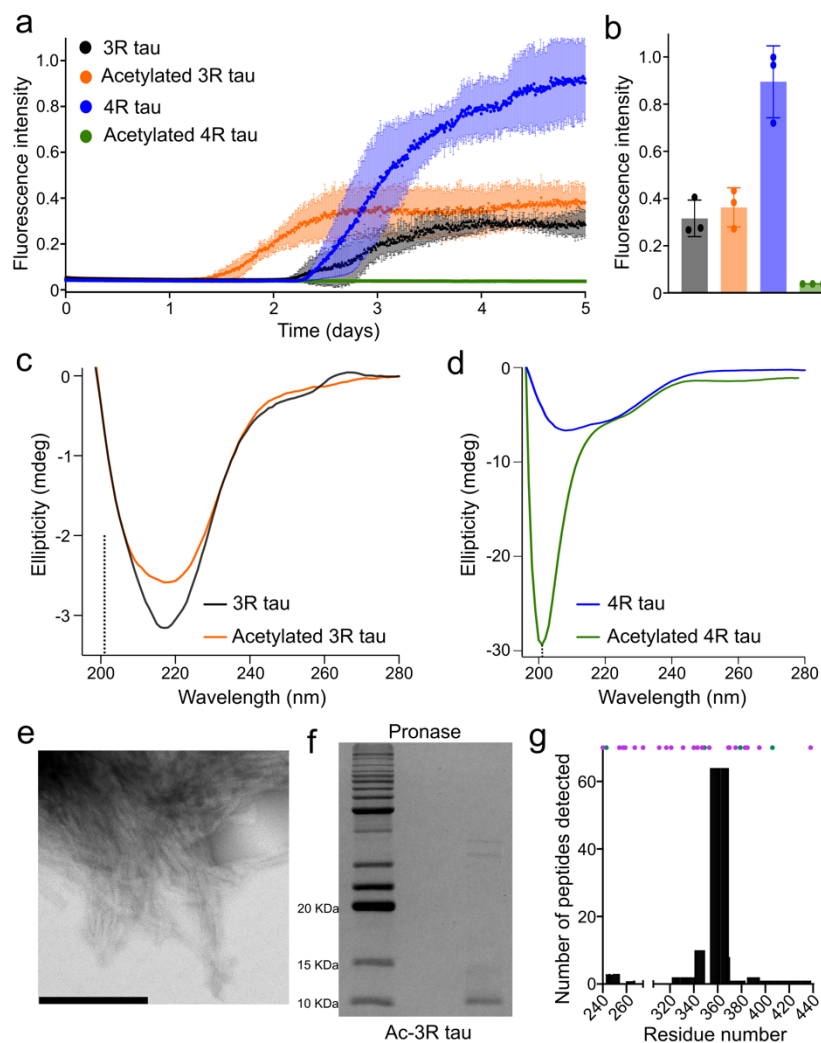


Figure 3-13 Acetylation accelerates 3R tau but blocks 4R tau fibrillization.

a, Fibrillization kinetics of unmodified 3R (black) and 4R (blue) tau, as well as p300/CBP-acetylated 3R (orange) and 4R (green) tau followed by ThT fluorescence. Protein concentrations were 25 μ M. Error bars represent std of three independent samples. **b**, Final ThT intensity of unmodified 3R (black) and 4R (blue) tau, as well as p300/CBP-acetylated 3R (orange) and 4R (green) tau after five days of aggregation. **c**, CD spectra of unmodified (black) and acetylated (orange) 3R tau after five days of aggregation. The location of the minimum expected for random coil structure is marked by a dotted line. **d**, CD spectra of unmodified (blue) and acetylated (green) 4R tau after five days of aggregation. **e**, Negative-stain EM of acetylated 3R tau fibrils. Scale bar, 200 nm. **f**, SDS-PAGE gel of pronase-digested acetylated 3R tau fibrils. **g**, Number of peptides detected from the enzymatic digestion of the tau band observed in (f). Lysine and arginine residues are marked with purple and green dots, respectively.

According to the time-dependent ThT increase, the fibrillization kinetics of unmodified 4R tau are very similar to those of unmodified 3R tau (Figure 3-13a). The absence or presence of repeat R2 thus has no strong influence when tau is unmodified. However, the situation drastically changes when tau is acetylated: acetylated 4R tau did not display an increase in ThT fluorescence intensity when incubated for even five days (Figure 3-13a,b; green).

To confirm the findings from the aggregation assay, we recorded CD spectra of both the unmodified and acetylated 3R and 4R tau after five days of aggregation. Both the unmodified and acetylated 3R tau displayed a typical spectrum for amyloid fibrils with a minimum at \sim 220 nm (Figure 3-13c). Electron microscopy confirmed the presence of fibrils (Figure 3-13e). We also observed a typical β -structure CD spectrum for the aggregated unmodified 4R tau (Figure 3-13d). In contrast, a random coil CD spectrum with a minimum at \sim 200 nm was seen for the acetylated 4R protein, confirming that acetylated 4R tau does not form amyloid fibrils even after long periods of incubation (Figure 3-13c, green).

To further characterize the amyloid fibrils of acetylated 3R tau, we performed protease-digestion in the presence of pronase and pelleted down the pronase-resistant core. The analysis of the pronase-resistant band from the SDS-PAGE gel by mass spectrometry (Figure

3-13f,g) revealed that the acetylated 3R tau fibrils have a similar rigid core as unmodified 3R tau fibrils (Figure 3-10d). The location of the pronase-resistant core of the *in vitro* aggregated fibrils of acetylated 3R tau is also similar to that of tau fibrils purified from the brain of patients with the 3R tauopathy Pick's disease⁹³.

3.10 K298 acetylation determines isoform-specific accumulation of tau

The above data reveal that acetylation strongly accelerates fibril formation of 3R tau while at the same time blocking 4R tau aggregation (Figure 3-13). We can rationalize the faster aggregation of 3R tau upon acetylation when considering the importance of electrostatic interactions in tau aggregation: acetylation of lysines removes positive charges thus decreasing electrostatic repulsion and favoring intermolecular interactions in the repeat region during tau aggregation. However, simple changes in electrostatics would also predict faster aggregation of acetylated 4R tau, in striking contrast to the observed inhibition of 4R tau aggregation by acetylation (Figure 3-13a). Notably, the only detectable difference in p300/CBP-acetylation between 3R and 4R tau is the acetylation of the five lysine residues in repeat R2 of 4R tau (Figure 3-11). We thus hypothesize that the acetylation of lysine residues in R2, the repeat that is unique to 4R tau, is a critical determinant in isoform-specific tau accumulation.

To study the role of acetylation of individual lysine residues in discriminating between 3R and 4R tau aggregation, we created several lysine to glutamine mutants of 4R tau. We individually mutated all five lysine residues (K280Q, K281Q, K290Q, K294Q, K298Q) of repeat R2 (Figure 3-14a, 3-15a). In addition, we created the double mutant K298Q/K311Q. We then aggregated the six mutant proteins along with wild-type 4R tau (Figure 3-14a).

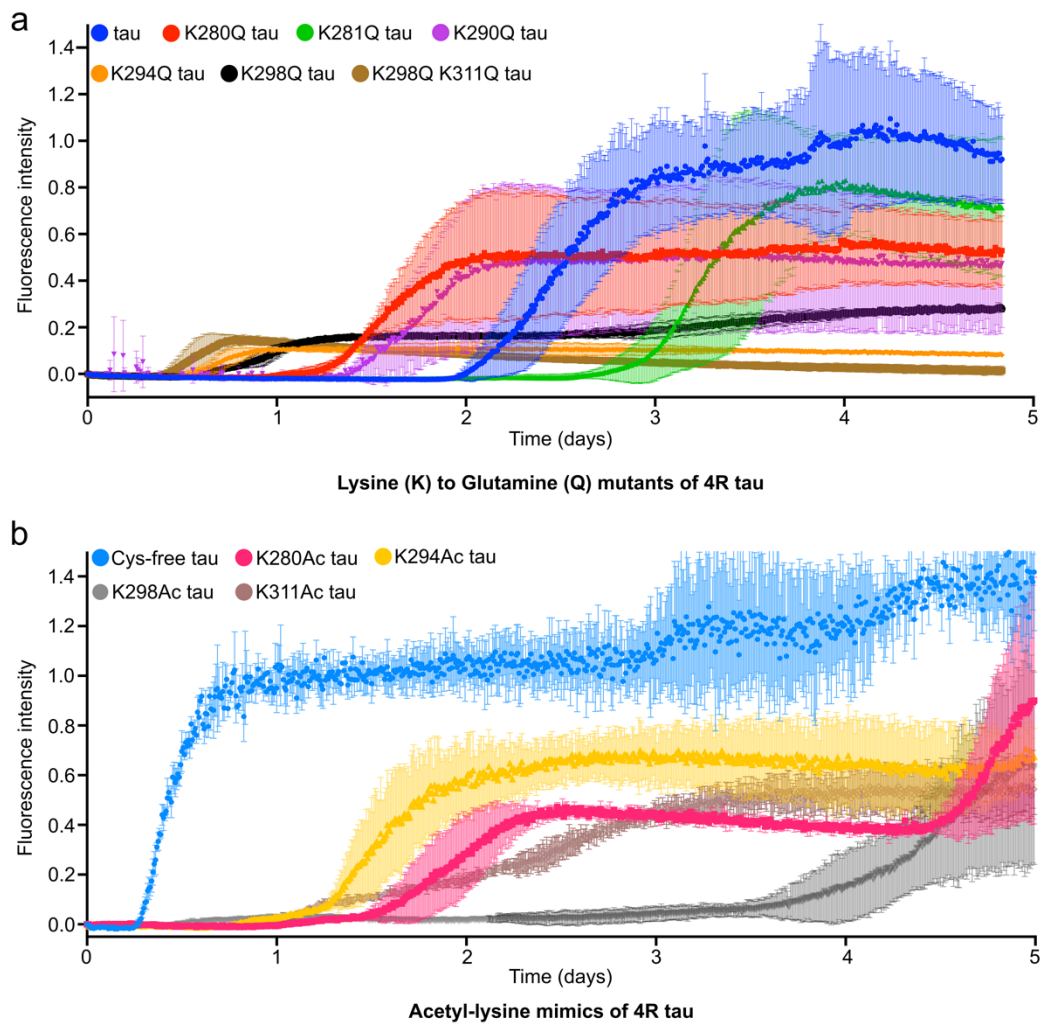


Figure 3-14 Impact of acetylation of repeat R2 on 4R tau fibrillization.

a, Lysine-to-glutamine mutations in repeat R2 modulate the fibrillization kinetics of 4R tau (25 μ M). **b**, Acetyl-lysine mimics of individual lysine residues delay aggregation of C291S/C322S-4R tau (25 μ M). Unmodified C291S/C322S-4R tau is named "Cys-free" 4R tau. Error bars in (a) and (b) represent the standard deviation of three independently aggregated samples.

Analysis of the aggregation kinetics showed that five out of the six K-to-Q mutant proteins aggregated faster than wild-type 4R tau (Figure 3-15b). Only in the case of K281Q tau, the half time of fibrillization was increased while maintaining a similar maximum ThT intensity (Figure 3-15b; green). The enhanced aggregation kinetics, which we observed for the five K-to-Q tau mutants (K280Q, K290Q, K294Q, K298Q, K298Q/K311Q), can again be rationalized on the basis of a change in electrostatics: the mutation-associated decrease in positive charge

in the repeat region lowers the electrostatic repulsion between R2 repeats during the aggregation of 4R tau.

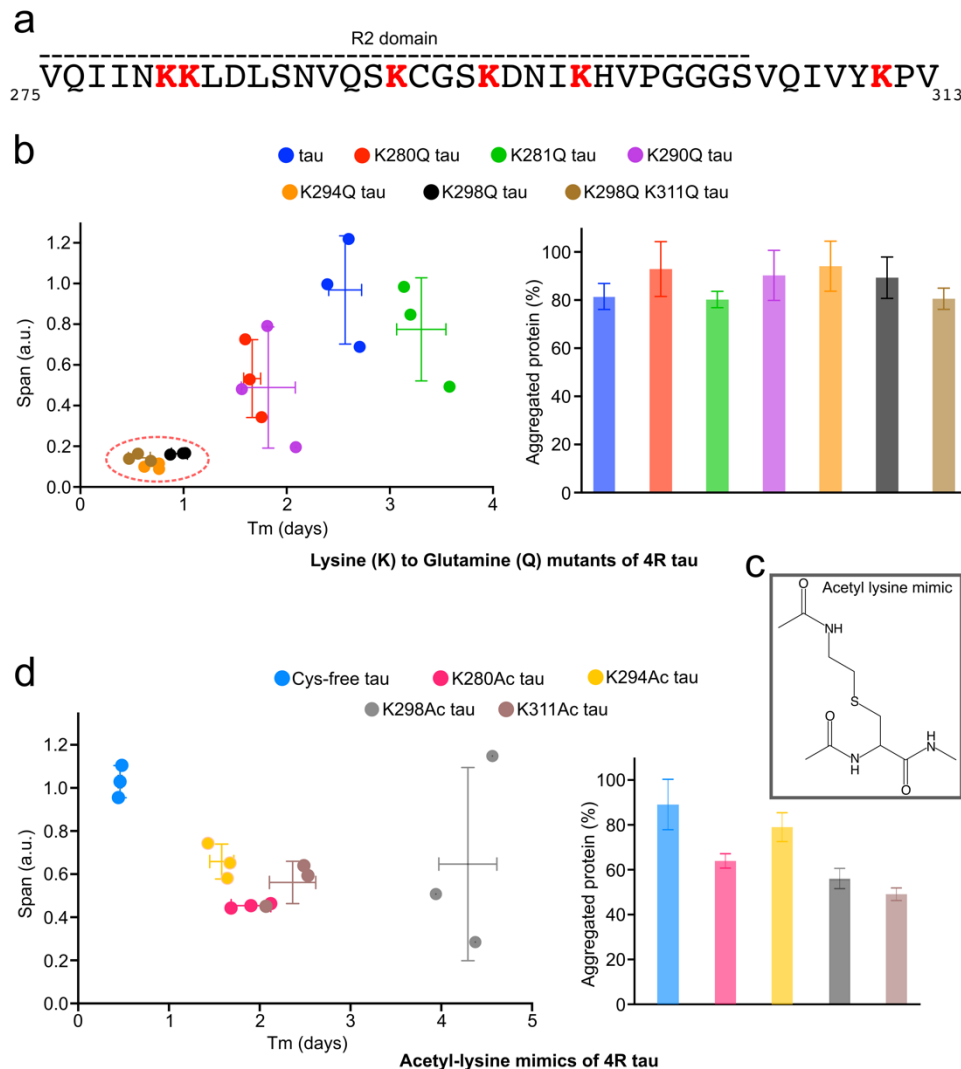


Figure 3-15 Acetylation of K298 profoundly impacts fibrillization of 4R tau.

a, Amino acid sequence of the R2 repeat domain and the beginning of R3 repeat domain of tau. Lysine residues present in the sequence are shown in red colour. **b**, Impact of lysine-to-glutamine mutation in repeat R2/R3 on fibrillization of 4R tau. (left) Span vs. half time of aggregation (T_m). Error bars represent std of three independently aggregated samples. (right) Percentage of protein aggregated. **c**, Acetyl-lysine mimic. The acetylation mimic differs only by the presence of a sulphur atom in place of the C_γ of lysine **d**, Impact of acetyl-lysine mimic in repeat R2/R3 on fibrillization of 4R tau. (left) Span vs. half time of aggregation. Error bars represent std of three independently aggregated samples.

(right) Percentage of protein aggregated. Error bars were calculated from the signal-to-noise ratio of the bands in the SDS-PAGE gel.

In addition to the changes in aggregation kinetics, we observed a strong decrease in the maximum ThT intensity reached by the three tau mutants K294Q, K298Q and K298Q/K311Q (Figure 3-14a, 3-15b). To evaluate if the lower ThT intensity is due to attenuated aggregation, we centrifuged all samples at the end of the incubation period. The supernatants were loaded into a SDS-PAGE gel and the amount of residual soluble protein was analyzed (Figure 3-16a). Comparison of the intensity of the supernatant to the monomeric unaggregated protein, however, showed that comparable protein amounts were aggregated for the wild-type 4R tau and the K-to-Q mutant proteins (Figure 3-15b, right panel). This suggests that the much lower ThT intensity detected for the three mutants K294Q, K298Q and K298Q/K311Q is not a result of aggregation inhibition, but might arise from differences in tau fibril structure induced by the mutations.

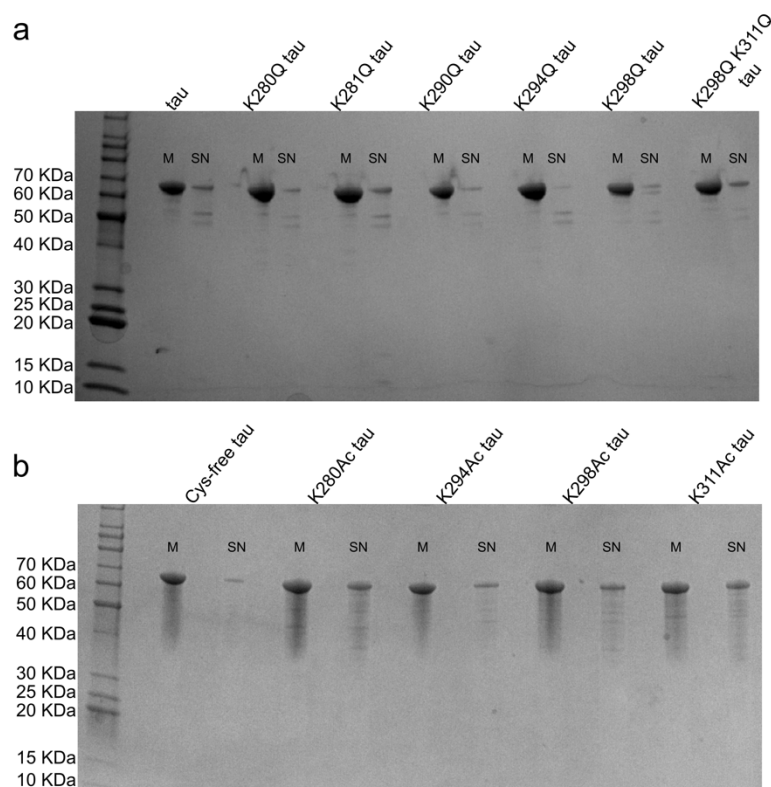


Figure 3-16 Estimation of the amount of aggregated tau proteins.

a, SDS-PAGE gel of soluble/monomeric (M) and supernatant (SN) after fibril pelleting of aggregated samples of unmodified and different K-to-Q mutants of 4R tau. Fibril samples were taken after five days of aggregation, shown in Figure 3-14a. **b**, SDS-PAGE gel of soluble/monomeric (M) and supernatant (SN) (after pelleting down the fibrils) of C291S/C322S tau ("Cys-free") and several single-site acetylation mimics of 4R tau. Fibril samples were taken after five days of aggregation, shown in Figure 3-14b.

K-to-Q mutation is widely used to mimic acetylation of proteins in cell and animal studies^{184,185}. The mutation captures the acetylation-associated removal of the positive charge of lysine, but fails to represent the size of the acetylated lysine side chain (Figure 2-4). We therefore created four single-site acetylation mimics (K280Ac, K294Ac, K298Ac, K311Ac) of 4R tau by mutating individual lysine residues in R2 to cysteine, followed by converting the cysteine residue to dehydroalanine, which enables the access of N-acetylcysteamine (Fig 2-4)¹⁷⁴. K281 and K290 were not included, because they showed the smallest impact on aggregation in the analysis of the K-to-Q mutations (Figure 3-15b). Prior to introduction of the lysine-to-cysteine mutations, the two endogenous cysteine residues (C291, C322) were changed to serine. The acetylation mimics created using this protocol are similar to the acetyl-lysine and differ only by the presence of a sulphur atom in place of the C γ of lysine (Figure 3-15c). The formation of the acetylation mimics was confirmed by mass spectrometry (Figure 2-5).

We then aggregated the 4R tau proteins containing the acetylation mimics, as well as the cysteine-free 4R tau as reference (Figure 3-14b). In agreement with previous studies, we observe that removal of the cysteines strongly accelerates 4R tau aggregation (Cys-free tau in Figure 3-14b when compared to wild-type tau in Figure 3-14a), because intermolecular disulphide bonds no longer interfere with aggregation.¹⁸⁶ Further analysis showed that all four acetylation mimics strongly delay the fibrillization of 4R tau (Figure 3-14b, 3-15d). The delay in fibril formation was strongest for the K298Ac mimic, increasing the duration of the lag phase of fibrillization by ~8 fold (Figure 3-15d). The other three acetylation mimics (K280Ac, K294Ac, K311Ac) delayed the onset of fibrillization by a factor of ~3-5 (Figure 3-

15d), i.e., were intermediate between the cysteine-free tau and K298Ac tau. In addition, all four acetylation mimics had lower maximum ThT intensity and less aggregated protein at the end of the aggregation period (Figure 3-15d, 3-16b). The combined data show that the lysine residues in repeat R2 critically influence aggregation of 4R Tau. While acetylation of a single lysine in repeat R2 is not sufficient to fully block aggregation of 4R Tau, we demonstrate that acetylation of K298 is a particularly important modification for discriminating isoform-specific tau aggregation.

3.11 Acetylated 3R tau fibrils fail to seed acetylated 4R tau

Transneuronal propagation of tau pathology follows a process called ‘templated misfolding’, in which pathological tau seeds propagate from an affected to a healthy cell and seed monomeric tau to aggregate into fibrils (Figure 3-17a)⁹⁸. In the adult human brain both 4R and 3R isoforms of tau are abundant and both can undergo acetylation by acetyltransferases. However, only 3R tau forms insoluble deposits/amyloid fibrils in 3R tauopathies such as Pick’s disease. While the above data showed that acetylation of lysine residues in repeat R2 blocks aggregation of 4R tau, seeding might overcome this barrier. We therefore asked if fibrils of acetylated 3R tau can seed aggregation of acetylated 4R tau.

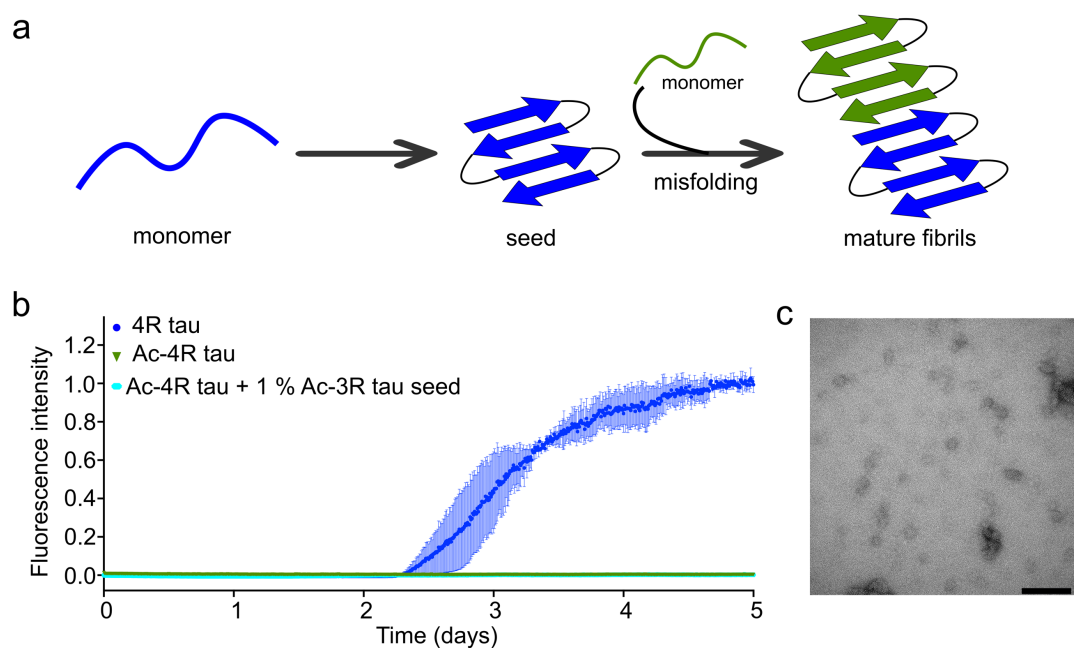


Figure 3-17 Fibrils of acetylated 3R tau fail to seed acetylated 4R tau.

a, Cartoon representation of 'templated misfolding' of monomeric tau by fibril seeds. b, Aggregation kinetics of 25 μM unmodified 4R tau (blue), acetylated 4R tau (green), and acetylated 4R tau in the presence of 1% fibril seeds (w/w) of acetylated 3R tau (cyan). Error bars represent std of three independent samples. c, Negative-stain EM of acetylated 4R tau monomer in presence of acetylated 3R tau seeds after five days of aggregation. Scale bar, 100 nm.

To study the cross-seeding efficiency of acetylated 3R tau fibrils, 1% (w/w) preformed fibrils of acetylated 3R tau were added to acetylated 4R tau monomer. Even in the presence of these seeds, however, acetylated 4R tau did not form fibrils as evidenced by very low ThT intensity during five days of incubation (Figure 3-17b). Electron microscopy confirmed the absence of fibrils (Figure 3-17c). In contrast, we observed efficient *in vitro* seeding of unmodified 4R tau by acetylated 3R tau fibrils (Figure 3-18). The combined data show that amyloid fibrils of acetylated 3R tau fail to seed acetylated 4R tau monomer.

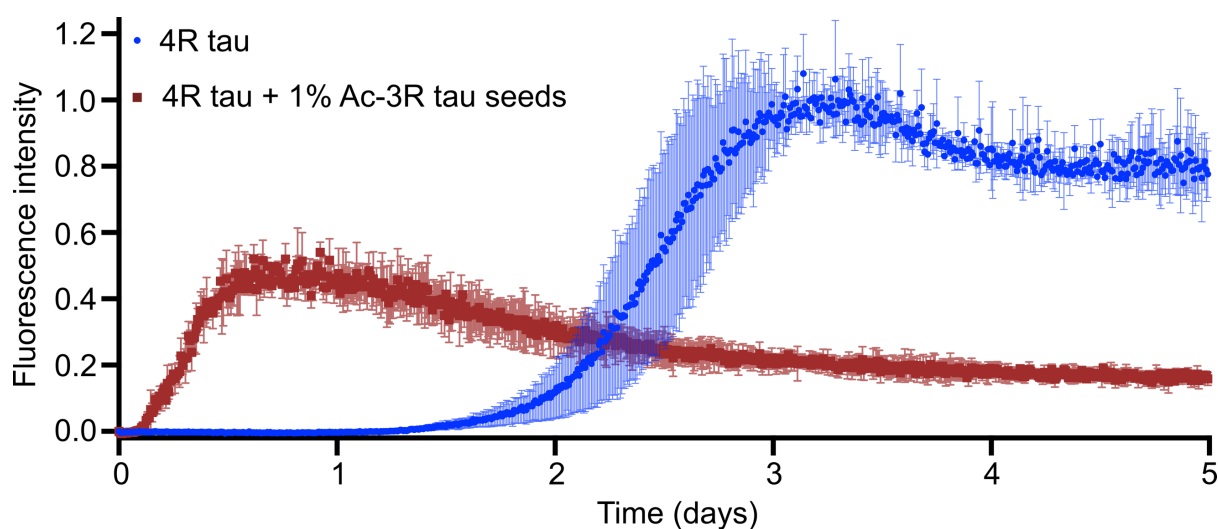


Figure 3-18 Fibrils of acetylated 3R tau cross-seed unmodified 4R tau monomer.

Aggregation kinetics of 25 μM 4R tau in the absence (blue) and presence (maroon) of 1% (w/w) acetylated-3R tau seeds. Error bars represent the std of three independently aggregated samples.

4. Discussions

The sections 4.1 to 4.3 are taken from the following article –

Chakraborty P., Rivière G., Liu S., Ibáñez de Opakua A., Dervişoğlu R., Hebestreit A., Andreas L. B., Vorberg I. M., & Zweckstetter M.

Co-factor-free aggregation of tau into seeding-competent RNA-sequestering amyloid fibrils
Nat Commun **12**, 4231 (2021)¹

4.1 Drastic difference in the molecular properties of co-factor-free tau fibrils and heparin-induced tau fibrils

In this thesis, we made an important advance towards a better understanding of the molecular factors that drive tau aggregation: we showed that the full-length tau protein can be aggregated into amyloid fibrils in the absence of heparin or other co-factors (Figure 3-1). We further showed that the co-factor-free tau fibrils differ drastically in their structure and molecular properties from heparin-induced fibrils. Solid-state NMR spectroscopy in combination with biochemical experiments revealed that the rigid/semi-rigid core of the heparin-free 4R tau fibrils is formed by the tau residues ~270 to ~380, i.e. a similar size and location of the fibril core region as in tau fibrils purified from a CBD patient brain (Figure 4-1).

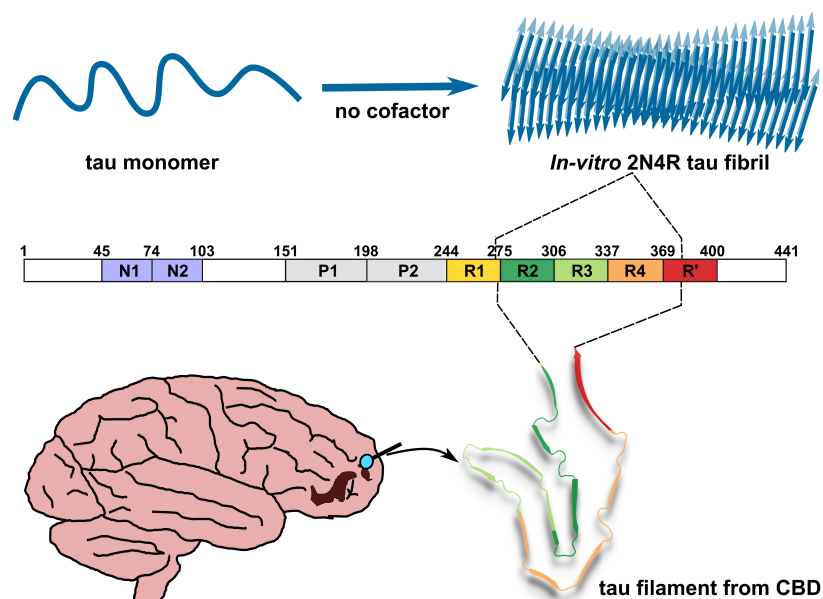


Figure 4-1 Similar core of co-factor free 4R tau fibrils and brain-derived 4R tau fibrils

However, the similarity in the size and location of the fibril core region does not guarantee that the heparin-free 2N4R tau fibrils prepared *in vitro* and the tau fibrils purified from CBD patient brain have an identical structure. *In vivo* tau exists in an environment rich in co-factors and also undergoes post-translational modifications including phosphorylation, ubiquitination and acetylation^{154,187}. The structure of the *in vitro* aggregated 2N4R tau fibrils therefore might differ in the presence of co-factors (e.g. RNA, polyphosphate) in the aggregation reaction or when post-translationally modified tau is used. Consistent with this hypothesis, the fibrillar cores of tau filaments from AD and CBD display distinct patterns of acetylation, phosphorylation, trimethylation and ubiquitination⁹⁵. Using the protocol of *in vitro* self-aggregation of tau, the effect of different post-translational modifications and co-factors can now be studied. In contrast, heparin is likely to largely override the impact of PTMs and other co-factors (especially when these co-factors are used at low concentrations) due to its very high negative charge.

4.2 Importance of the N-terminus of tau to pathological aggregation

Our study further provides single-residue evidence for the contribution of the N-terminal region of tau to pathological aggregation. The broadening of the NMR signals of the N-terminal 30 residues indicates that the corresponding residues lose their mobility during aggregation (Figure 3-2). Taking further into account that conformation-specific antibodies such as Alz50 and MC1 specifically detect pathological tau in brain tissue, but require two discontinuous epitopes, one located in the repeat region (residues 313–322) and the other at the N-terminus (residues 1–18)¹⁷⁷, suggests that the N-terminal residues of tau bind to the cross- β -structure of the fibrils and thereby generates the pathology-specific recognition motif. Currently, we do not know if part of the N-terminal epitope folds into β -structure as part of this process. The interaction, however, might be more transient when compared to the interactions that stabilize the fibrillar core, because the N-terminal region of tau was so far not detected in cryo-EM studies of tau fibrils (despite its importance for antibody binding).

4.3 RNA binding depends on the structure and surface electrostatic properties of tau conformers

A potential mechanism for the connection between tau fibril structure and specific diseases could be related to differences in the interactions that each tau fibril structure has with proteins and nucleic acids. In this study, we probed the interaction of the heparin-free 2N4R fibrils with three different RNAs (polyU, polyA, tRNA) (Figure 3-8). PolyU is mainly disordered and it's able to engage in both hydrophobic (through the nitrogen bases) and electrostatic interactions (through the negatively charged phosphate backbone) (Figure 4-2). PolyA is known to have partial secondary structure in the presence of Mg^{2+} ¹⁸⁸(Figure 4-2). PolyA can thus engage in some hydrophobic interactions but less efficiently than polyU. tRNA, on the other hand, has a distinct secondary structure and is unable to engage in hydrophobic interactions through its bases, because the bases are hidden inside the structure (Figure 4-2). tRNA thus mainly interacts electrostatically through its negatively charged phosphate backbone.

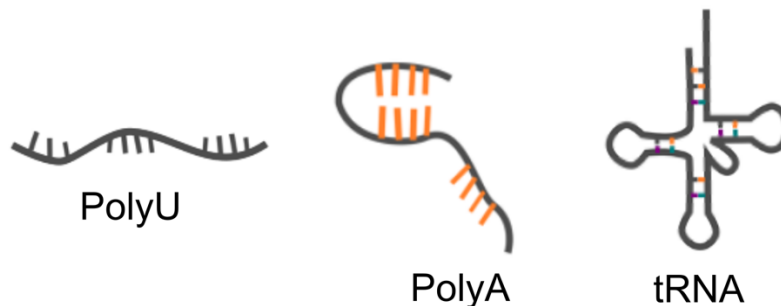


Figure 4-2 Structure of different RNAs

We observed that at low ionic strength, the heparin-free 2N4R fibrils strongly interact with all three RNAs (polyU, polyA and tRNA) (Figure 3-8c). At increased ionic strength, the interaction gradually weakens from polyU to polyA and to tRNA (Figure 3-8c). In contrast the heparin-induced 2N4R tau fibrils were found to interact very weakly with the three RNAs at low ionic strength, but strongly bound to polyU at higher ionic strength (Figure 3-8c). In addition, a weaker interaction of the heparin-induced 2N4R tau fibrils was observed with polyA, and very little interaction with tRNA at higher ionic strength (Figure 3-8c). These results can be

attributed to differences in the surface charge of the two fibril types and differences in the dominating interactions at low and high ionic strength: at low ionic strength electrostatic interactions dominate, while at higher ionic strength hydrophobic interactions come into play.

The surface of the heparin-free 2N4R fibril is mostly positively charged (Figure 3-8a) with some patches of uncharged hydrophobic residues (shown in white, Figure 3-8a) giving it the possibility to interact both electrostatically and hydrophobically with different RNAs. At low ionic strength, all three RNAs (polyU, polyA and tRNA) electrostatically interact with the heparin-free 2N4R tau fibrils resulting in comparable amounts of bound RNA (Figure 3-8c). At higher ionic strength, hydrophobic interactions play a bigger role and the amount of bound RNA gradually decreases from polyU to polyA and to tRNA (hydrophobic interaction strength of polyU > polyA > tRNA). In contrast, heparin-induced tau fibrils (Appendix sec. 6-13) show weak affinity for RNA at low ionic strength where electrostatic repulsion between negatively charged RNA and the negatively charged heparin is strong. At higher ionic strength, this repulsion is attenuated and hydrophobic interactions between polyU and the surface of the fibrils result in binding of polyU, but not tRNA, to the heparin-induced fibrils. The combined data suggest that the binding of RNAs depends both on the structure of the RNA and the surface electrostatic properties of different tau conformers.

4.4 Co-factor-free aggregation of 3R tau is essential to study the effect of PTMs on the emergence of 3R tauopathies

The microtubule-associated protein tau adopts distinct conformations of insoluble aggregates in different neurodegenerative diseases, collectively referred to as tauopathies. These distinct fibril conformations (or strains) are also associated with the deposition of varying tau isoforms consisting of only 4R tau, 3R tau, or both. Pick's disease, a classic example of primary tauopathies is associated with the selective deposition of 3R tau in the brain⁸⁵. The 3R tau adopts a unique fold in Pick's disease, which is very different from tau filaments' structure from other primary or secondary tauopathies⁹³. However, the molecular

factors that drive the formation of the distinct tau fold in Pick's disease are enigmatic. Even the reason behind the specific deposition of 3R tau in Pick's disease is still unknown.

Tau can be modified by countless post-translational modifications (PTMs) *in vivo*. Based on the inception of tau pathology in a particular region of the brain, different brain regions may exert different PTMs that might influence tau filament structure in different tauopathies. In order to study the effect of different PTMs on the aggregation of the 3R isoform of tau, it is essential to aggregate the protein in the absence of negatively charged co-factors, such as heparin, as the presence of negative charges can override the effect of PTMs. In the first part of the thesis, we made an important advancement by establishing an *in vitro* method of self-aggregation of 2N4R tau, which is crucial to study the effect of different PTMs on the aggregation of 4R tau¹. We then showed that 3R tau can be aggregated *in vitro* using the same protocol (Figure 3-9). Next, by solid-state NMR spectroscopy and protease digestion, we confirmed that the core of the *in vitro* generated co-factor-free 3R tau fibrils is similar to the core of tau filaments derived from the brain of patients with the 3R tauopathy Pick's disease (Figure 3-10). This sets the basis for investigating the effect of PTMs on the aggregation of 3R tau.

4.5 Acetylation – a critical pathogenic PTM associated with different tauopathies

Acetylation of lysine residues has emerged as a critical pathogenic PTM of tau in brains from AD^{155,156} and other tauopathies^{47,142,155}. Among the lysine residues detected to be acetylated in tauopathies, K174, K274, K280, and K281 have been most intensively studied¹⁸⁹. Acetylation of K280 is detected in the diseased brain (NFTs in AD, neuronal and glial inclusions in AGD, CDB, PSP, FTDP-17) but not in the brain of healthy individuals^{114,155,156}. It decreases the binding affinity of tau to microtubules, which might enhance the aggregation of tau into paired helical filaments (PHFs)¹⁵⁵. In addition, overexpression of the K280Q acetylation mimic of human tau in transgenic *Drosophila* models enhanced total tau levels and increased tau phosphorylation at T212, S214, and S262, potentially caused by increased oligomerization or disparate protein degradation¹⁸⁴. Acetylation of K274 and K281 has been

identified in AD brains and was reported to disrupt synaptic plasticity by reducing the Kidney/Brain protein (KIBRA). Consistent with synaptic toxicity of K274/K281-acetylated tau, the expression of human tau with lysine to glutamine mutation at K274 and K281 in transgenic mice leads to impaired hippocampal long-term potentiation and AD-related memory deficits¹⁹⁰. Another study reported that acetylation of K274 and K281 destabilizes the axon initial segment (AIS) and promotes the mislocalization of tau into the somatodendritic compartment initiating an early event of neurodegeneration¹⁹¹. Lastly, acetylation of K174 has been identified as an early modification in the soluble fraction from AD patients¹⁴⁴, and the expression of pseudo-acetylated tau at K174 (K174Q) in transgenic mice attenuated tau clearance leading to the accumulation of acetylated tau¹⁴⁴. Notably, acetylated tau can promote tau pathology in mice by inhibiting chaperone-mediated autophagy (CMA)¹⁵⁰. These reports support the critical role of acetylation of individual lysine residues in the pathogenic progression of different tauopathies. However, little is known about the influence of lysine acetylation on the emergence of distinct tau strains. Regarding this, the K311 has been reported to undergo acetylation exclusively in the 3R tauopathy (Pick's disease) brain but not in the 4R tauopathies (CBD, PSP), indicating a potential role played by this lysine in influencing the formation of different tau strains^{157,183}.

4.6 Acetylation discriminates disease and isoform-specific tau – the emergence of 3R tauopathies

In this thesis, we probed the effect of acetylation on the aggregation of 3R and 4R isoforms of tau. Despite the similar site-specific acetylation identified in both 3R and 4R, we observed an inhibition of aggregation of 4R tau and accelerated aggregation of 3R tau upon acetylation (Figure 3-13). This suggested that acetylation of the lysine residues in repeat R2, which is lacking in 3R tau, plays a critical role in inhibiting the aggregation of acetylated 4R tau. We also demonstrated that in more physiologically conditions, i.e., when tau is bound to microtubules, at least three (K290, K294, and K298) of the five lysine residues in repeat R2 are specifically acetylated (Figure 3-12e). We then created single-site acetylation mimics of K294 and K298 in repeat R2. We also prepared tau proteins in which K280 (repeat R2) and

K311 (repeat R3) have acetylation mimics, because acetylated K280 and K311 have been linked to tau pathology^{155,156,183}. K290 was omitted because it showed a negligible impact on aggregation in the analysis of the K-to-Q mutations (Figure 3-15b).

Aggregation of each of the four (K280Ac, K294Ac, K298Ac, and K311Ac) pseudo-acetylated proteins was slower than the unmodified 4R tau (Figure 3-15d). At the same time, none of the single site acetylation mimics was sufficient to completely inhibit the aggregation of 4R tau, in contrast to our observations when acetylating 4R tau by p300/CBP (Figure 3-15d). This suggests that simultaneous acetylation of multiple lysine residues in R2 is needed to abrogate aggregation of 4R tau. This might further be tested by introducing acetyl-lysine at more than one lysine residue. However, in our hands the presence of multiple cysteine residues, which are required in order to chemically attach the acetyl group, created unwanted intramolecular disulphide bonds and thereby prevented the formation of dehydroalanine, i.e., the preparation of tau proteins with acetylation-mimics present simultaneously at two lysine residues.

Pseudo-acetylation of K298 delayed fibrillization most dramatically increasing the lag phase by eight-fold (Figure 3-15d). Inspection of the 3D structure of tau filaments purified from the 4R tauopathy CBD provides a rationale for the importance of K298 acetylation in discriminating 4R and 3R tauopathies (Figure 4-3d). In the tau CBD structure, the side chain of K298 points inside the core of the tau fibrils and forms a salt bridge with D358. When K298 is acetylated the salt bridge can no longer form. In addition, the increased bulkiness of the side chain of K298 upon acetylation will generate a steric clash, i.e., 4R tau will be unable to form the CBD structure when K298 is acetylated. The impact of acetylation at K294 on 4R tau aggregation can further be rationalized on the basis of the structure of tau fibrils purified from the 4R tauopathy PSP (Figure 4-3e): K294 forms a salt bridge with D314/S316 in the core of the tau PSP structure. Thus, the substantial delay observed in the aggregation of 4R tau upon specifically acetylating K298 or K294 likely arises from the increase in steric crowding in the

vicinity of these residues upon acetylation. Thus, acetylation of specific lysine residues in repeat R2 favors the accumulation of only one kind of isoform (3R/4R) of tau in the brain.

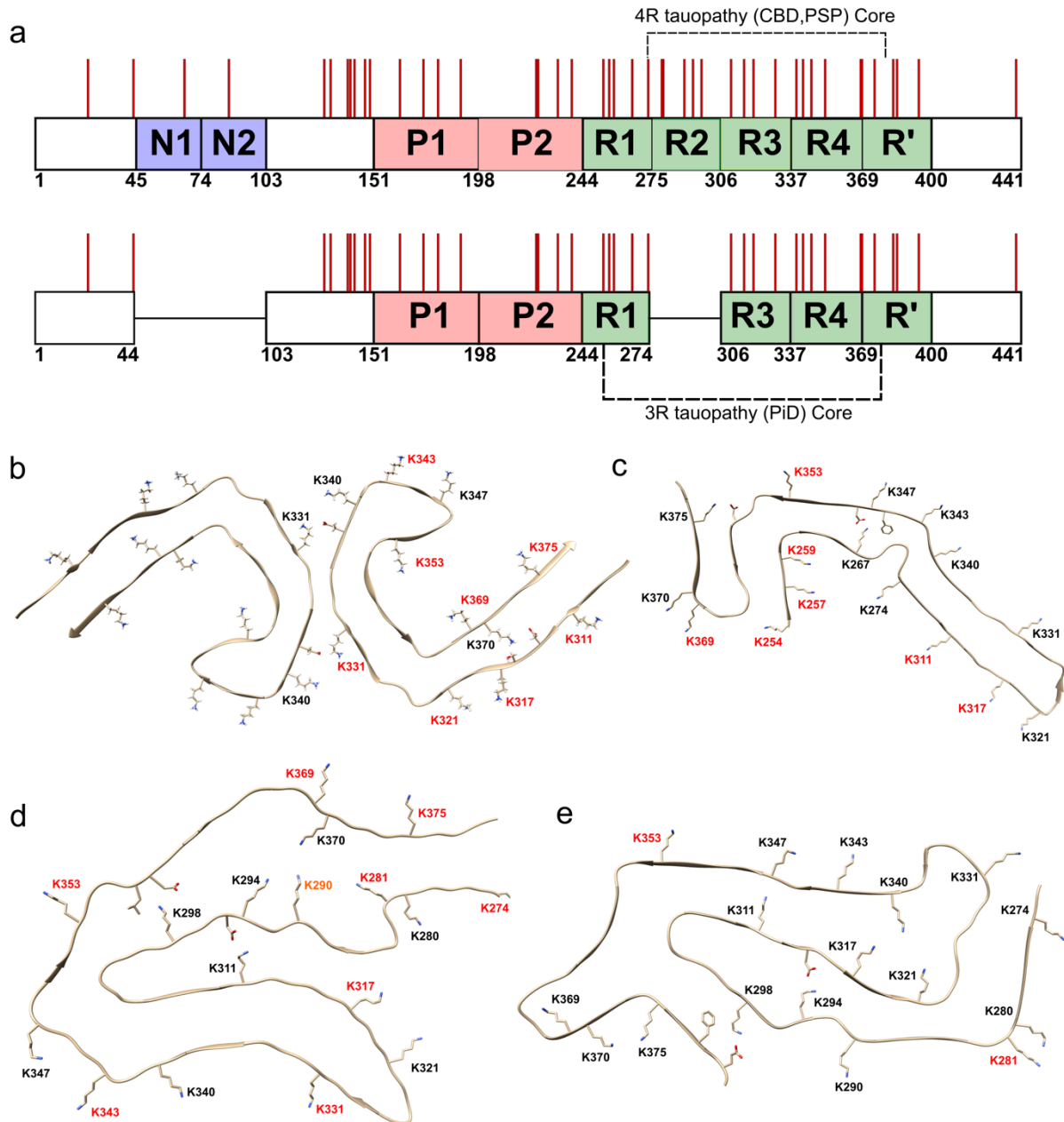


Figure 4-3 Distinct acetylation patterns in different tauopathies

a, Domain organization of 2N4R tau and 0N3R tau. Lysine residues are marked with red bars. The filament cores of 3R (PiD) and 4R tauopathies (CBD, PSP) are marked with dashed lines. **b**, Atomic structure of PHFs derived from the brain of AD patients (PDB code – 5O3L). **c**, Atomic structure of tau filaments derived from the brain of a PiD patient (PDB code – 6GX5). **d**, Atomic structure of tau filament derived from the brain of a CBD patient (PDB code – 6TJO). **e**, Atomic structure of tau filaments derived

from the brain of PSP patients (PDB code – 7P65). Unmodified lysine residues present in the filament core of each disease are shown in black; acetylated lysine residues in red. Very weakly acetylated K290 in CBD is shown in orange. The data of acetylated lysine residues in different tauopathies were taken from kametani et al.¹⁵⁷ and Zhang et al.⁹⁴

Besides the acetylation of the lysine residues in repeat R2, acetylation at other sites might further contribute to isoform-specific tau deposition in tauopathies¹⁵⁷. For example, K311 is acetylated in the 3R tauopathy PiD, whereas it is not acetylated in the case of the 4R tauopathies CBD and PSP^{157,183}. In the structure of PiD tau fibrils, K311 points away from the filament core (Figure 4-3c). Acetylation of K311 thus will not interfere with the structure of the tau fibril core in PiD. In contrast, K311 forms a salt bridge with H299 in the CBD tau structure (Figure 4-3d), and is located in a compact region of the PSP tau structure (Figure 4-3e). Selective acetylation of K311 in PiD is thus likely because acetylation of K311 interferes with the formation of CBD/PSP tau fibril structures due to severe steric hindrance. In agreement with this hypothesis, we observed a strong delay in the aggregation of 4R tau along with a decrease in aggregated protein upon selectively acetylating K311 (Figure 3-15d). In addition, selective acetylation of K311 in PiD will be favored by its solvent accessible location in the structure of PiD tau fibrils, whereas the K311 side chain is not accessible in the structure of tau fibrils in CBD and PSP (Figure 4-3c-e).

The combined data establish a model that rationalizes the selective deposition of 3R tau in 3R tauopathies (Figure 4-4). In the adult human brain, both 3R and 4R isoforms of tau are present. However, during the disease both isoforms become acetylated. This accelerates pathogenic accumulation of 3R tau, while at the same time blocking aggregation of 4R tau. Thus, insoluble deposits of only 3R tau build up in the brain of patients with PiD. The selective deposition of insoluble 3R tau is further supported by the inability of tau fibrils of acetylated 3R tau to seed aggregation of acetylated 4R tau monomers (Figure 3-17). Thus, even if tau aggregates of acetylated 3R tau are transferred from one cell to another cell – during disease progression and the spreading of tau to different brain regions – they will only seed the pathogenic accumulation of 3R tau in the host cells.

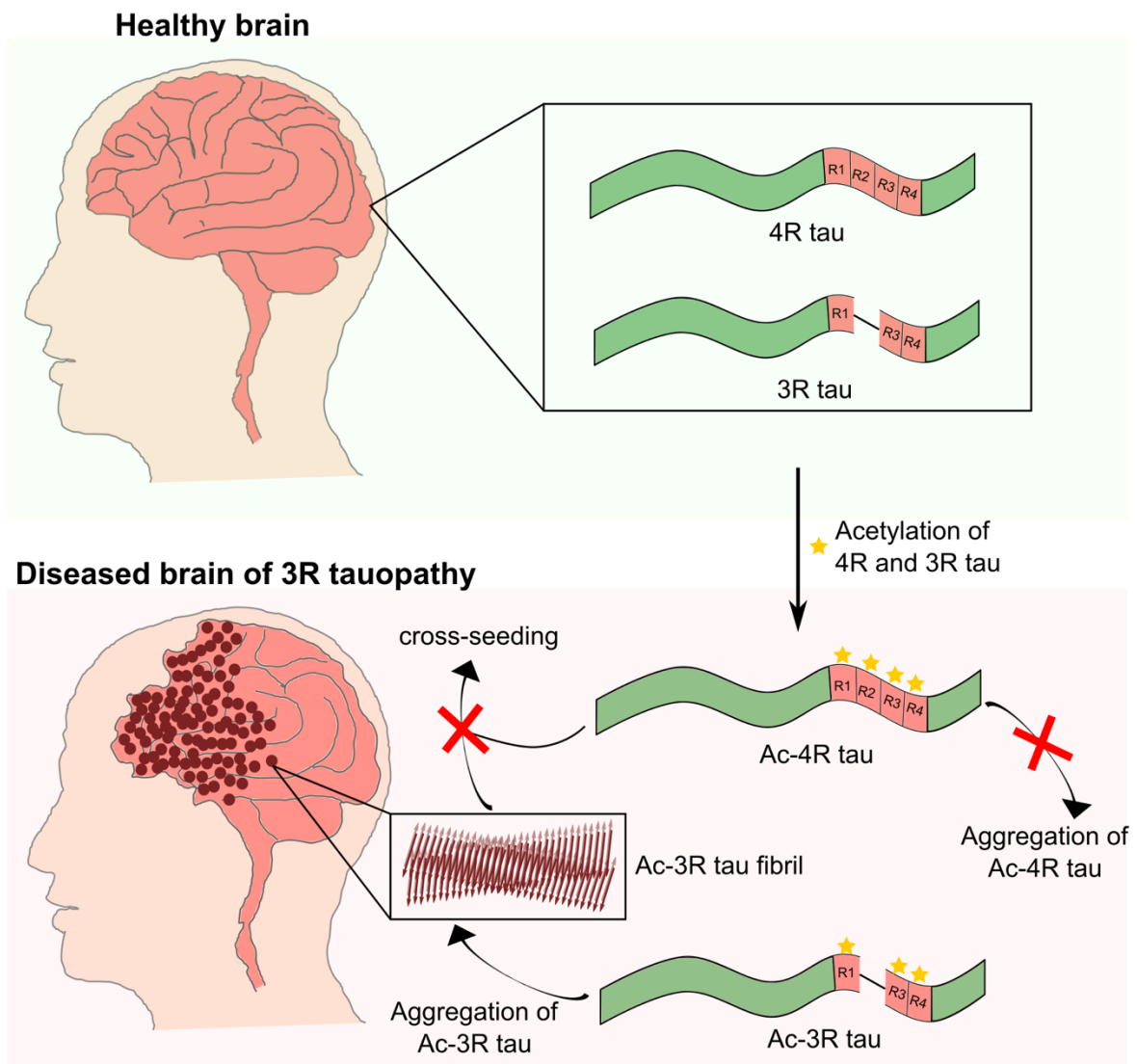


Figure 4-4 Model for the emergence of 3R tauopathies.

Selective deposition of acetylated 3R tau leads to the emergence of 3R tauopathies.

The results from our study identify K298 as a critical residue in the development of 3R tauopathy, Pick's disease. Acetylation of K298 residue, along with acetylation of other lysine residues in the R2 domain, can inhibit the accumulation of 4R tau in the Pick's disease brain leading to the selective deposition of 3R tau. However, to this date, nothing is known about the post-translational modifications of the soluble 4R tau in the Pick's disease brain. Due to the strong aggregation-inhibition effect observed in our *in vitro* experiments after acetylation of 4R tau, we speculate that the 4R tau in the brain of Pick's disease might be hyperacetylated in the R2 domain. However, a detailed analysis of the PTMs of the 4R tau from the Pick's

disease brain would be essential to further identify crucial modifications leading to the selective deposition of the 3R tau. This will also unravel the potential role of other modifications (ubiquitination of lysine residues, phosphorylation of serine/threonine/tyrosine residues) of both 4R and 3R tau in the emergence of 3R tauopathies.

4.7 Towards therapeutic intervention in Pick's disease

Our work suggests a critical role of acetylation of lysine residues in the emergence of 3R tauopathies. As described in section 4.5, the impact of acetylating the first two lysine residues in repeat R2 (K280 and K281) has been extensively studied both *in vitro* and *in vivo*.^{155,156,190} However, no information is so far available on the role of the acetylation of K290, K294 and K298 in modulating tau toxicity and pathology *in vivo*. Investigating the effect of acetylation of these three lysine residues, especially K298, in animal models of tauopathies is therefore of utmost importance and will critically enhance our understating of the disease progression and pathology in tauopathies. The importance of studying in particular the acetylation of K298 is further supported by the identification of a novel MAPT mutation of tau, K298E, in the brain of an FTDP-17 patient¹⁹². Biophysical analysis showed that the K298E mutation reduced the ability of tau to promote microtubule assembly and affected alternative splicing of mRNA, leading to the elevation of 4R tau levels in the brain¹⁹². We note, however, that our work also highlights the difficulties of studying the impact of acetylation in animal models of disease. We demonstrated that mutation of lysine to glutamine in repeat R2 to mimic acetylation has the opposite effect (i.e., enhanced 4R tau aggregation), when compared to pseudo-acetylation by acetyl-lysine, which much more closely represents tau acetylation and strongly delays fibrillization of 4R tau (Figure 3-15). Thus, results obtained from animal models that are based on overexpression/replacement of wild-type 4R Tau by tau mutants carrying lysine-to-glutamine substitutions have to be critically evaluated.

Our work also raises the question whether reducing tau acetylation levels by administrating inhibitors of acetyl-transferases can be a potential treatment for PiD. Consistent with this hypothesis, reduction of acetylated tau by inhibiting p300/CBP acetyltransferase activity has been shown to be neuroprotective in traumatic brain injury (TBI)¹⁵¹. Notably, levels of

acetylated tau are increased in AD patients with a history of TBI. The results reported in this thesis indicate that both the 3R tau deposits and the 4R tau monomers are acetylated in the brain of PiD patients (Figure 4-4). Our data further suggest the possibility of hyperacetylation in the R2 repeat of 4R tau in PiD. Although the hyperacetylation of R2 inhibits the fibrillization of 4R tau, it might contribute to neurotoxicity in PiD by influencing the formation and properties of soluble oligomeric species of 4R tau. Thus, reducing acetylation of tau might be a promising therapeutic intervention in PiD.

4.8 Lysine acetylation can direct the interaction of co-factors with monomeric tau leading to the formation of different 4R tau strains

The structures of tau filaments from two 4R tauopathies, CBD and PSP, were reported to be different despite the involvement of the same core region in both cases, and the potential reason behind this difference is the interaction of different lysine residues with the same acidic co-factor in both cases⁹⁶. In CBD, the acidic co-factor (9 Å x 4 Å in dimension) interacts with the side chains of K290, K294, and K370, whereas the same co-factor interacts with K317 in PSP. Considering the interaction between the lysine residues and the co-factor to be electrostatically driven and occurring at the monomeric level (the co-factor is present within the core of the filament, which is only possible if the interaction occurs at the monomeric level, i.e., before the fibrillization), the selectivity towards a specific group of lysine residues in CBD and a different lysine residue in PSP can only be justified if one/multiple residues in PSP/CBD are unable to interact with the co-factor. The inability of a lysine residue to interact electrostatically with the co-factor might occur due to its acetylation as it removes the positive charge of the lysine. Thus, acetylation of different lysine residues in PSP and CBD might direct the interaction of the same co-factor with discrete lysine residues in each case, leading to distinct filament structures.

4.9 The synergy between acetylation and other PTMs of lysine residues can lead to the formation of different tau conformers

The role of lysine modifications in determining the structure of tau filaments in CBD and AD has recently been discussed⁹⁵. Four lysine residues (K321, K343, K353, and K369) in the CBD type I filaments (singlet) and two lysine residues (K321 and K353) in the CBD type II (doublet) filaments were reported to undergo ubiquitination. The strong electron density of the terminal ⁷⁶GG⁷⁵ residues of ubiquitin attached to these lysine residues revealed a near-stoichiometric occupancy, with the rest of the ubiquitin not visible due to being highly dynamic. In the CBD doublet fibrils, the ubiquitination at K353 was suggested to further stabilize the inter-protofilament interface of two singlet filaments made by the antiparallel stacking of the tau segment ³⁴³KLDFKDR³⁴⁹. Based on the site of ubiquitination and acetylation, the authors proposed a structure-based model (Figure 4-5) of CBD filament formation with Ub-K353 and Ac-K343 favoring the formation of CBD type II (doublet) filaments and Ub-343 and Ac-K353 favoring the formation of CBD type I (singlet) filaments.

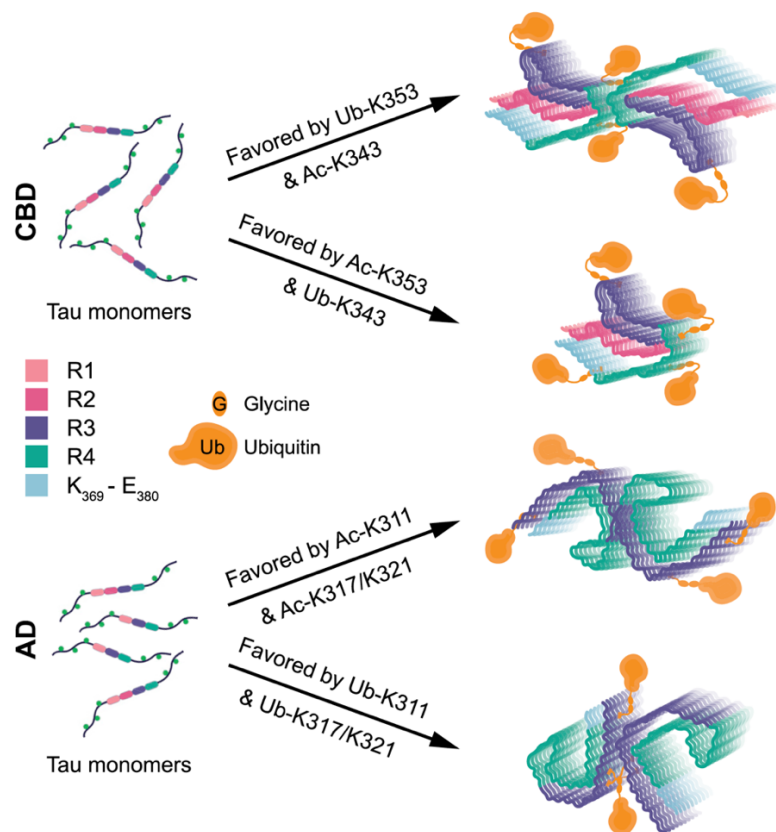


Figure 4-5 Structure-based model of the influence of PTM on tau filament's structure

The image is taken from Arakhamia et al.⁹⁵

The same study also reported the ubiquitination of K317 and K321 in AD. It further suggested the vital role of Ub-K317 and Ub-K321 residues in stabilizing the structure of straight filaments (SF) in AD. The SF in AD is formed by the asymmetric packing of two protofilaments mediated by a region with additional density connected to K317/K321. As the SF in AD doesn't have any salt bridges, hydrophobic packing, or hydrogen bonds holding the two protofilaments together, the author suggested the stabilization of the inter-protofilament interface is driven by the ubiquitination of K317 and K321 residues. On the other hand, they further proposed that acetylation of K317/K321 can lead to the formation of paired helical filaments (PHFs) in AD (Figure 4.5). Notably, we observed a high degree of acetylation of K317 and K321 residues in both 3R and 4R tau (Figure 3-11). As in AD, both 3R and 4R isoforms of tau are deposited, *in vitro* aggregation of a mixture of acetylated 3R and 4R tau can potentially lead to the formation of tau filament structure similar to AD PHFs. The successful *in vitro* recapitulation of AD PHF will be extremely important to develop potential therapeutic agents for the treatment of AD.

4.10 Future outlook

The work described in this thesis provides an essential step to reveal the connection between tau fibril structure, tau pathology and neurodegenerative disease. It identifies acetylation as a crucial factor in the emergence of 3R tauopathies. The result from our study further confirms a similar rigid core of *in vitro* acetylated 3R tau fibrils and brain-derived tau fibrils from the 3R tauopathy Pick's disease. However, future work is needed to determine the 3D structure of the *in vitro* acetylated 3R tau fibrils at high resolution by cryo-electron microscopy or solid-state NMR spectroscopy. The similarity between the structures of *in vitro* acetylated 3R tau fibrils and brain-derived fibrils from Pick's disease will open new avenues for developing appropriate diagnostic and therapeutic agents targeting 3R tauopathies.

Additional studies are also required to identify the molecular factors that determine the formation of distinct tau strains in 4R tauopathies, as well as in AD and other tauopathies

where both 3R and 4R tau accumulate into insoluble deposits. The specific deposition of 4R tau in some cases of 4R tauopathies might be due to an increase in the levels of 4R tau in the brain. For example, some mutations detected in the 5' splice site of exon 10 of the MAPT gene in FTDP-17 patients alter the alternative splicing of this exon by destabilizing a potential stem-loop structure of the RNA⁵². This leads to more frequent usage of the 5' site leading to an increased proportion of tau mRNA that includes exon 10. The increase in exon 10 containing mRNA increase the proportion of the 4R tau isoform in the brain leading to an increased risk of selective deposition of 4R tau.

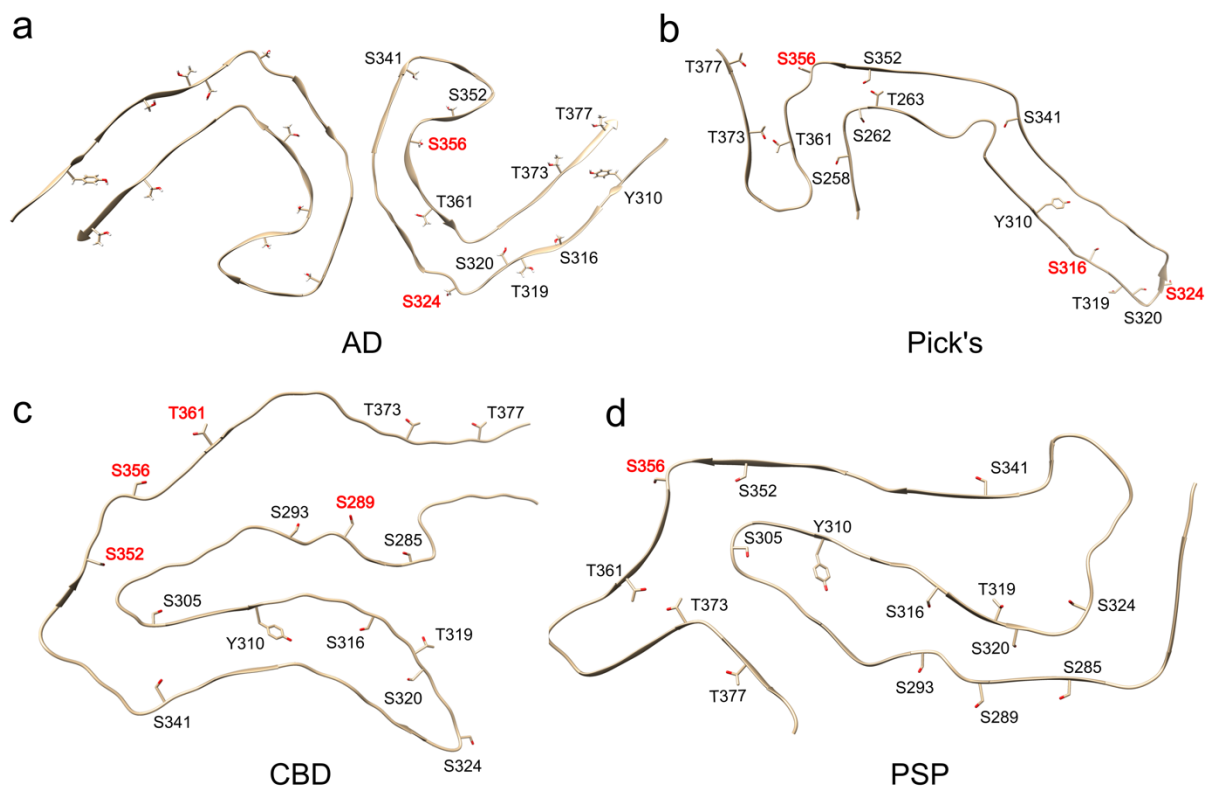


Figure 4-6 Distinct phosphorylation pattern in different tauopathies.

a, Atomic model of PHF derived from the brain of AD patient (PDB code – 5O3L). **b**, Atomic model of tau filament derived from the brain of PiD patient (PDB code – 6GX5). **c**, Atomic model of tau filament derived from the brain of CBD patient (PDB code – 6TJO). **d**, Atomic model of tau filament derived from the brain of PSP patient (PDB code – 7P65). The unmodified serine/threonine/tyrosine residues present in the filament core of each disease are shown in black, and the phosphorylated residues (in each disease) are shown in red. The data of phosphorylated residues in different tauopathies are taken from kametani et al.¹⁵⁷ and Zhang et al.⁹⁴

In addition, PTMs other than lysine acetylation such as ubiquitination/methylation/glycation of the lysine residues or phosphorylation of serine/threonine/tyrosine residues might influence the selective deposition of 4R tau in 4R tauopathies. Among all the other PTMs which were not studied in this thesis, phosphorylation is the far-reaching modification needed to be studied in detail as it is the most abundant PTM observed in tau. Similar to acetylation, different tau 'strains' are also associated with distinct phosphorylation patterns^{94,157} as shown in Figure 4-6. The distinctive phosphorylation pattern observed in these tauopathies might be recapitulated *in vitro* by phosphorylating 3R/4R tau using different kinases, or a mixture of kinases, acetyltransferases and other PTM-attaching enzymes. Future studies investigating the effect of these different PTMs, potentially in the presence of different co-factors, on the aggregation of 4R tau can thus potentially unravel the emergence of different 4R tau strains, a mystery still unsolved.

5. Bibliography

1. Chakraborty, P. et al. Co-factor-free aggregation of tau into seeding-competent RNA-sequestering amyloid fibrils. *Nat Commun* **12**, 4231 (2021).
2. Hou, Y. et al. Ageing as a risk factor for neurodegenerative disease. *Nat Rev Neurol* **15**, 565-581 (2019).
3. Dugger, B.N. & Dickson, D.W. Pathology of Neurodegenerative Diseases. *Cold Spring Harb Perspect Biol* **9**(2017).
4. Alzheimer, A., Stelzmann, R.A., Schnitzlein, H.N. & Murtagh, F.R. An English translation of Alzheimer's 1907 paper, "Uber eine eigenartige Erkrankung der Hirnrinde". *Clin Anat* **8**, 429-31 (1995).
5. Hardy, J. & Allsop, D. Amyloid deposition as the central event in the aetiology of Alzheimer's disease. *Trends Pharmacol Sci* **12**, 383-8 (1991).
6. Morishima-Kawashima, M. et al. Hyperphosphorylation of tau in PHF. *Neurobiol Aging* **16**, 365-71; discussion 371-80 (1995).
7. Stengel, E. & Wilson, W.E. Jakob-Creutzfeldt disease. *J Ment Sci* **92**, 370-8 (1946).
8. Prusiner, S.B. Novel proteinaceous infectious particles cause scrapie. *Science* **216**, 136-44 (1982).
9. Parkinson, J. An essay on the shaking palsy. 1817. *J Neuropsychiatry Clin Neurosci* **14**, 223-36; discussion 222 (2002).
10. Spillantini, M.G., Crowther, R.A., Jakes, R., Hasegawa, M. & Goedert, M. alpha-Synuclein in filamentous inclusions of Lewy bodies from Parkinson's disease and dementia with lewy bodies. *Proc Natl Acad Sci U S A* **95**, 6469-73 (1998).
11. Wenning, G.K., Colosimo, C., Geser, F. & Poewe, W. Multiple system atrophy. *Lancet Neurol* **3**, 93-103 (2004).
12. Armstrong, M.J. Lewy Body Dementias. *Continuum (Minneap Minn)* **25**, 128-146 (2019).
13. Wijesekera, L.C. & Leigh, P.N. Amyotrophic lateral sclerosis. *Orphanet J Rare Dis* **4**, 3 (2009).
14. Hardiman, O. et al. Amyotrophic lateral sclerosis. *Nat Rev Dis Primers* **3**, 17071 (2017).
15. Karenberg, A. [Early history of Pick's disease]. *Fortschr Neurol Psychiatr* **69**, 545-50 (2001).
16. Kovacs, G.G. Tauopathies. *Handb Clin Neurol* **145**, 355-368 (2017).
17. Gibb, W.R., Luthert, P.J. & Marsden, C.D. Corticobasal degeneration. *Brain* **112** (Pt 5), 1171-92 (1989).
18. Sabharwal, R.K., Sanchette, P.C., Sethi, P.K. & Dhamija, R.M. Chronic traumatic encephalopathy in boxers. *J Assoc Physicians India* **35**, 571-3 (1987).
19. Steele, J.C. Progressive supranuclear palsy. *Brain* **95**, 693-704 (1972).
20. 2018 Alzheimer's disease facts and figures. *Alzheimer's & Dementia* **14**, 367-429 (2018).
21. Nussbaum, R.L. & Ellis, C.E. Alzheimer's disease and Parkinson's disease. *N Engl J Med* **348**, 1356-64 (2003).

22. Hy, L.X. & Keller, D.M. Prevalence of AD among whites: a summary by levels of severity. *Neurology* **55**, 198-204 (2000).
23. Poewe, W. et al. Parkinson disease. *Nat Rev Dis Primers* **3**, 17013 (2017).
24. 2020 Alzheimer's disease facts and figures. *Alzheimers Dement* (2020).
25. Weingarten, M.D., Lockwood, A.H., Hwo, S.Y. & Kirschner, M.W. A protein factor essential for microtubule assembly. *Proc Natl Acad Sci U S A* **72**, 1858-62 (1975).
26. Jeganathan, S., von Bergen, M., Mandelkow, E.M. & Mandelkow, E. The natively unfolded character of tau and its aggregation to Alzheimer-like paired helical filaments. *Biochemistry* **47**, 10526-39 (2008).
27. LoPresti, P., Szuchet, S., Papasozomenos, S.C., Zinkowski, R.P. & Binder, L.I. Functional implications for the microtubule-associated protein tau: localization in oligodendrocytes. *Proc Natl Acad Sci U S A* **92**, 10369-73 (1995).
28. Feinstein, S.C. & Wilson, L. Inability of tau to properly regulate neuronal microtubule dynamics: a loss-of-function mechanism by which tau might mediate neuronal cell death. *Biochim Biophys Acta* **1739**, 268-79 (2005).
29. Mandelkow, E.M. & Mandelkow, E. Biochemistry and cell biology of tau protein in neurofibrillary degeneration. *Cold Spring Harb Perspect Med* **2**, a006247 (2012).
30. Kadavath, H. et al. Tau stabilizes microtubules by binding at the interface between tubulin heterodimers. *Proc Natl Acad Sci U S A* **112**, 7501-6 (2015).
31. Scholz, T. & Mandelkow, E. Transport and diffusion of Tau protein in neurons. *Cellular and Molecular Life Sciences* **71**, 3139-3150 (2014).
32. Kellogg, E.H. et al. Near-atomic model of microtubule-tau interactions. *Science* **360**, 1242-1246 (2018).
33. Wang, Y. & Mandelkow, E. Tau in physiology and pathology. *Nat Rev Neurosci* **17**, 5-21 (2016).
34. Stamer, K., Vogel, R., Thies, E., Mandelkow, E. & Mandelkow, E.M. Tau blocks traffic of organelles, neurofilaments, and APP vesicles in neurons and enhances oxidative stress. *J Cell Biol* **156**, 1051-63 (2002).
35. Dixit, R., Ross, J.L., Goldman, Y.E. & Holzbaur, E.L. Differential regulation of dynein and kinesin motor proteins by tau. *Science* **319**, 1086-9 (2008).
36. Konzack, S., Thies, E., Marx, A., Mandelkow, E.M. & Mandelkow, E. Swimming against the tide: mobility of the microtubule-associated protein tau in neurons. *J Neurosci* **27**, 9916-27 (2007).
37. Utton, M.A., Noble, W.J., Hill, J.E., Anderton, B.H. & Hanger, D.P. Molecular motors implicated in the axonal transport of tau and alpha-synuclein. *J Cell Sci* **118**, 4645-54 (2005).
38. Yuan, A., Kumar, A., Peterhoff, C., Duff, K. & Nixon, R.A. Axonal transport rates in vivo are unaffected by tau deletion or overexpression in mice. *J Neurosci* **28**, 1682-7 (2008).
39. Frandemiche, M.L. et al. Activity-dependent tau protein translocation to excitatory synapse is disrupted by exposure to amyloid-beta oligomers. *J Neurosci* **34**, 6084-97 (2014).
40. Andreadis, A. Misregulation of tau alternative splicing in neurodegeneration and dementia. *Prog Mol Subcell Biol* **44**, 89-107 (2006).

41. Goedert, M., Spillantini, M.G., Jakes, R., Rutherford, D. & Crowther, R.A. Multiple isoforms of human microtubule-associated protein tau: sequences and localization in neurofibrillary tangles of Alzheimer's disease. *Neuron* **3**, 519-26 (1989).
42. Goedert, M. & Jakes, R. Expression of separate isoforms of human tau protein: correlation with the tau pattern in brain and effects on tubulin polymerization. *EMBO J* **9**, 4225-30 (1990).
43. Chen, J., Kanai, Y., Cowan, N.J. & Hirokawa, N. Projection domains of MAP2 and tau determine spacings between microtubules in dendrites and axons. *Nature* **360**, 674-7 (1992).
44. Frappier, T.F., Georgieff, I.S., Brown, K. & Shelanski, M.L. tau Regulation of microtubule-microtubule spacing and bundling. *J Neurochem* **63**, 2288-94 (1994).
45. Liu, C. & Gotz, J. Profiling murine tau with 0N, 1N and 2N isoform-specific antibodies in brain and peripheral organs reveals distinct subcellular localization, with the 1N isoform being enriched in the nucleus. *PLoS One* **8**, e84849 (2013).
46. Lee, V.M., Goedert, M. & Trojanowski, J.Q. Neurodegenerative tauopathies. *Annu Rev Neurosci* **24**, 1121-59 (2001).
47. Spillantini, M.G. & Goedert, M. Tau pathology and neurodegeneration. *Lancet Neurol* **12**, 609-22 (2013).
48. Kovacs, G.G. Invited review: Neuropathology of tauopathies: principles and practice. *Neuropathol Appl Neurobiol* **41**, 3-23 (2015).
49. Baker, M. et al. Association of an extended haplotype in the tau gene with progressive supranuclear palsy. *Hum Mol Genet* **8**, 711-5 (1999).
50. Kovacs, G.G. et al. White matter tauopathy with globular glial inclusions: a distinct sporadic frontotemporal lobar degeneration. *J Neuropathol Exp Neurol* **67**, 963-75 (2008).
51. Ghetti, B. et al. Invited review: Frontotemporal dementia caused by microtubule-associated protein tau gene (MAPT) mutations: a chameleon for neuropathology and neuroimaging. *Neuropathol Appl Neurobiol* **41**, 24-46 (2015).
52. Hutton, M. et al. Association of missense and 5'-splice-site mutations in tau with the inherited dementia FTDP-17. *Nature* **393**, 702-5 (1998).
53. Spillantini, M.G. et al. Mutation in the tau gene in familial multiple system tauopathy with presenile dementia. *Proc Natl Acad Sci U S A* **95**, 7737-41 (1998).
54. Josephs, K.A. et al. Beta-amyloid burden is not associated with rates of brain atrophy. *Ann Neurol* **63**, 204-12 (2008).
55. Whitwell, J.L. et al. MRI correlates of neurofibrillary tangle pathology at autopsy: a voxel-based morphometry study. *Neurology* **71**, 743-9 (2008).
56. Espinoza, M., de Silva, R., Dickson, D.W. & Davies, P. Differential incorporation of tau isoforms in Alzheimer's disease. *J Alzheimers Dis* **14**, 1-16 (2008).
57. Braak, H. & Braak, E. Neuropathological staging of Alzheimer-related changes. *Acta Neuropathol* **82**, 239-59 (1991).
58. Alafuzoff, I. et al. Staging of neurofibrillary pathology in Alzheimer's disease: a study of the BrainNet Europe Consortium. *Brain Pathol* **18**, 484-96 (2008).
59. Murray, M.E. et al. Neuropathologically defined subtypes of Alzheimer's disease with distinct clinical characteristics: a retrospective study. *Lancet Neurol* **10**, 785-96 (2011).

60. Crary, J.F. et al. Primary age-related tauopathy (PART): a common pathology associated with human aging. *Acta Neuropathol* **128**, 755-66 (2014).
61. Roberts, G.W. Immunocytochemistry of neurofibrillary tangles in dementia pugilistica and Alzheimer's disease: evidence for common genesis. *Lancet* **2**, 1456-8 (1988).
62. Omalu, B.I. et al. Chronic traumatic encephalopathy in a National Football League player. *Neurosurgery* **57**, 128-34; discussion 128-34 (2005).
63. McKee, A.C. et al. The spectrum of disease in chronic traumatic encephalopathy. *Brain* **136**, 43-64 (2013).
64. McKee, A.C., Abdolmohammadi, B. & Stein, T.D. The neuropathology of chronic traumatic encephalopathy. *Handb Clin Neurol* **158**, 297-307 (2018).
65. McKee, A.C. et al. The first NINDS/NIBIB consensus meeting to define neuropathological criteria for the diagnosis of chronic traumatic encephalopathy. *Acta Neuropathol* **131**, 75-86 (2016).
66. Schmidt, M.L., Zhukareva, V., Newell, K.L., Lee, V.M. & Trojanowski, J.Q. Tau isoform profile and phosphorylation state in dementia pugilistica recapitulate Alzheimer's disease. *Acta Neuropathol* **101**, 518-24 (2001).
67. Hof, P.R. et al. Differential distribution of neurofibrillary tangles in the cerebral cortex of dementia pugilistica and Alzheimer's disease cases. *Acta Neuropathol* **85**, 23-30 (1992).
68. Kovacs, G.G. et al. Aging-related tau astroglialopathy (ARTAG): harmonized evaluation strategy. *Acta Neuropathol* **131**, 87-102 (2016).
69. Rebeiz, J.J., Kolodny, E.H. & Richardson, E.P., Jr. Corticodentatonigral degeneration with neuronal achromasia. *Arch Neurol* **18**, 20-33 (1968).
70. Ikeda, K. et al. Argyrophilic thread-like structure in corticobasal degeneration and supranuclear palsy. *Neurosci Lett* **174**, 157-9 (1994).
71. Feany, M.B. & Dickson, D.W. Widespread cytoskeletal pathology characterizes corticobasal degeneration. *Am J Pathol* **146**, 1388-96 (1995).
72. Dickson, D.W. et al. Office of Rare Diseases neuropathologic criteria for corticobasal degeneration. *J Neuropathol Exp Neurol* **61**, 935-46 (2002).
73. Armstrong, M.J. et al. Criteria for the diagnosis of corticobasal degeneration. *Neurology* **80**, 496-503 (2013).
74. Kouri, N., Whitwell, J.L., Josephs, K.A., Rademakers, R. & Dickson, D.W. Corticobasal degeneration: a pathologically distinct 4R tauopathy. *Nat Rev Neurol* **7**, 263-72 (2011).
75. Dickson, D.W. Neuropathologic differentiation of progressive supranuclear palsy and corticobasal degeneration. *J Neurol* **246 Suppl 2**, I16-15 (1999).
76. Boxer, A.L. et al. Advances in progressive supranuclear palsy: new diagnostic criteria, biomarkers, and therapeutic approaches. *Lancet Neurol* **16**, 552-563 (2017).
77. Steele, J.C., Richardson, J.C. & Olszewski, J. Progressive Supranuclear Palsy. A Heterogeneous Degeneration Involving the Brain Stem, Basal Ganglia and Cerebellum with Vertical Gaze and Pseudobulbar Palsy, Nuchal Dystonia and Dementia. *Arch Neurol* **10**, 333-59 (1964).
78. Giagkou, N., Hoglinger, G.U. & Stamelou, M. Progressive supranuclear palsy. *Int Rev Neurobiol* **149**, 49-86 (2019).

-
79. Ahmed, Z. et al. Globular glial tauopathies (GGT): consensus recommendations. *Acta Neuropathol* **126**, 537-544 (2013).
 80. Molina, J.A. et al. Primary progressive aphasia with glial cytoplasmic inclusions. *Eur Neurol* **40**, 71-7 (1998).
 81. Cairns, N.J. et al. Tau protein in the glial cytoplasmic inclusions of multiple system atrophy can be distinguished from abnormal tau in Alzheimer's disease. *Neurosci Lett* **230**, 49-52 (1997).
 82. Rosler, T.W. et al. Four-repeat tauopathies. *Prog Neurobiol* **180**, 101644 (2019).
 83. Kovacs, G.G. et al. Non-Alzheimer neurodegenerative pathologies and their combinations are more frequent than commonly believed in the elderly brain: a community-based autopsy series. *Acta Neuropathol* **126**, 365-84 (2013).
 84. Gelpi, E., Culler, F., Navarro-Otano, J. & Llado, A. Globular glial-like inclusions in a patient with advanced Alzheimer's disease. *Acta Neuropathol* **126**, 155-7 (2013).
 85. Constantinidis, J., Richard, J. & Tissot, R. Pick's disease. Histological and clinical correlations. *Eur Neurol* **11**, 208-17 (1974).
 86. Zhukareva, V. et al. Sporadic Pick's disease: a tauopathy characterized by a spectrum of pathological tau isoforms in gray and white matter. *Ann Neurol* **51**, 730-9 (2002).
 87. Kovacs, G.G. et al. Neuropathology of the hippocampus in FTLD-Tau with Pick bodies: a study of the BrainNet Europe Consortium. *Neuropathol Appl Neurobiol* **39**, 166-78 (2013).
 88. Shi, Y. et al. Structure-based Classification of Tauopathies. *bioRxiv*, 2021.05.28.446130 (2021).
 89. Fitzpatrick, A.W.P. et al. Cryo-EM structures of tau filaments from Alzheimer's disease. *Nature* **547**, 185-190 (2017).
 90. Falcon, B. et al. Novel tau filament fold in chronic traumatic encephalopathy encloses hydrophobic molecules. *Nature* **568**, 420-423 (2019).
 91. Falcon, B. et al. Tau filaments from multiple cases of sporadic and inherited Alzheimer's disease adopt a common fold. *Acta Neuropathol* **136**, 699-708 (2018).
 92. Shi, Y. et al. Cryo-EM structures of tau filaments from Alzheimer's disease with PET ligand APN-1607. *Acta Neuropathol* **141**, 697-708 (2021).
 93. Falcon, B. et al. Structures of filaments from Pick's disease reveal a novel tau protein fold. *Nature* **561**, 137-140 (2018).
 94. Zhang, W. et al. Novel tau filament fold in corticobasal degeneration. *Nature* **580**, 283-287 (2020).
 95. Arakhamia, T. et al. Posttranslational Modifications Mediate the Structural Diversity of Tauopathy Strains. *Cell* **180**, 633-644 e12 (2020).
 96. Xiang, X. et al. Role of molecular polymorphism in defining tau filament structures in neurodegenerative diseases. *bioRxiv*, 2021.05.24.445353 (2021).
 97. Shi, Y. et al. Structure-based classification of tauopathies. *Nature* **598**, 359-363 (2021).
 98. Clavaguera, F., Tolnay, M. & Goedert, M. The Prion-Like Behavior of Assembled Tau in Transgenic Mice. *Cold Spring Harb Perspect Med* **7**(2017).
 99. Kampers, T., Friedhoff, P., Biernat, J., Mandelkow, E.M. & Mandelkow, E. RNA stimulates aggregation of microtubule-associated protein tau into Alzheimer-like paired helical filaments. *FEBS Lett* **399**, 344-9 (1996).

-
100. Wilson, D.M. & Binder, L.I. Free fatty acids stimulate the polymerization of tau and amyloid beta peptides. In vitro evidence for a common effector of pathogenesis in Alzheimer's disease. *Am J Pathol* **150**, 2181-95 (1997).
 101. Chirita, C.N., Necula, M. & Kuret, J. Anionic micelles and vesicles induce tau fibrillization in vitro. *J Biol Chem* **278**, 25644-50 (2003).
 102. Friedhoff, P., Schneider, A., Mandelkow, E.M. & Mandelkow, E. Rapid assembly of Alzheimer-like paired helical filaments from microtubule-associated protein tau monitored by fluorescence in solution. *Biochemistry* **37**, 10223-30 (1998).
 103. Goedert, M. et al. Assembly of microtubule-associated protein tau into Alzheimer-like filaments induced by sulphated glycosaminoglycans. *Nature* **383**, 550-3 (1996).
 104. Perez, M., Valpuesta, J.M., Medina, M., Montejo de Garcini, E. & Avila, J. Polymerization of tau into filaments in the presence of heparin: the minimal sequence required for tau-tau interaction. *J Neurochem* **67**, 1183-90 (1996).
 105. Berriman, J. et al. Tau filaments from human brain and from in vitro assembly of recombinant protein show cross-beta structure. *Proc Natl Acad Sci U S A* **100**, 9034-8 (2003).
 106. Hasegawa, M., Crowther, R.A., Jakes, R. & Goedert, M. Alzheimer-like changes in microtubule-associated protein Tau induced by sulfated glycosaminoglycans. Inhibition of microtubule binding, stimulation of phosphorylation, and filament assembly depend on the degree of sulfation. *J Biol Chem* **272**, 33118-24 (1997).
 107. von Bergen, M. et al. Assembly of tau protein into Alzheimer paired helical filaments depends on a local sequence motif ((306)VQIVYK(311)) forming beta structure. *Proc Natl Acad Sci U S A* **97**, 5129-34 (2000).
 108. von Bergen, M. et al. Mutations of tau protein in frontotemporal dementia promote aggregation of paired helical filaments by enhancing local beta-structure. *J Biol Chem* **276**, 48165-74 (2001).
 109. Pickhardt, M. et al. Anthraquinones inhibit tau aggregation and dissolve Alzheimer's paired helical filaments in vitro and in cells. *J Biol Chem* **280**, 3628-35 (2005).
 110. Taniguchi, S. et al. Inhibition of heparin-induced tau filament formation by phenothiazines, polyphenols, and porphyrins. *J Biol Chem* **280**, 7614-23 (2005).
 111. Nacharaju, P. et al. Accelerated filament formation from tau protein with specific FTDP-17 missense mutations. *FEBS Lett* **447**, 195-9 (1999).
 112. Arrasate, M., Perez, M., Armas-Portela, R. & Avila, J. Polymerization of tau peptides into fibrillar structures. The effect of FTDP-17 mutations. *FEBS Lett* **446**, 199-202 (1999).
 113. Goedert, M., Jakes, R. & Crowther, R.A. Effects of frontotemporal dementia FTDP-17 mutations on heparin-induced assembly of tau filaments. *FEBS Lett* **450**, 306-11 (1999).
 114. Cohen, T.J. et al. The acetylation of tau inhibits its function and promotes pathological tau aggregation. *Nat Commun* **2**, 252 (2011).
 115. Carlomagno, Y. et al. An acetylation-phosphorylation switch that regulates tau aggregation propensity and function. *J Biol Chem* **292**, 15277-15286 (2017).
 116. Sui, D., Liu, M. & Kuo, M.H. In vitro aggregation assays using hyperphosphorylated tau protein. *J Vis Exp*, e51537 (2015).

-
117. Xia, Y. et al. Tau Ser208 phosphorylation promotes aggregation and reveals neuropathologic diversity in Alzheimer's disease and other tauopathies. *Acta Neuropathol Commun* **8**, 88 (2020).
 118. Falcon, B. et al. Conformation determines the seeding potencies of native and recombinant Tau aggregates. *J Biol Chem* **290**, 1049-65 (2015).
 119. Morozova, O.A., March, Z.M., Robinson, A.S. & Colby, D.W. Conformational features of tau fibrils from Alzheimer's disease brain are faithfully propagated by unmodified recombinant protein. *Biochemistry* **52**, 6960-7 (2013).
 120. Zhang, W. et al. Heparin-induced tau filaments are polymorphic and differ from those in Alzheimer's and Pick's diseases. *Elife* **8**(2019).
 121. Lo Cascio, F. et al. Modulating Disease-Relevant Tau Oligomeric Strains by Small Molecules. *J Biol Chem* (2020).
 122. Bulic, B. et al. Development of tau aggregation inhibitors for Alzheimer's disease. *Angew Chem Int Ed Engl* **48**, 1740-52 (2009).
 123. Pooler, A.M., Phillips, E.C., Lau, D.H., Noble, W. & Hanger, D.P. Physiological release of endogenous tau is stimulated by neuronal activity. *EMBO Rep* **14**, 389-94 (2013).
 124. Saman, S. et al. Exosome-associated tau is secreted in tauopathy models and is selectively phosphorylated in cerebrospinal fluid in early Alzheimer disease. *J Biol Chem* **287**, 3842-9 (2012).
 125. Katsinelos, T. et al. Unconventional Secretion Mediates the Trans-cellular Spreading of Tau. *Cell Rep* **23**, 2039-2055 (2018).
 126. Wu, J.W. et al. Small misfolded Tau species are internalized via bulk endocytosis and anterogradely and retrogradely transported in neurons. *J Biol Chem* **288**, 1856-70 (2013).
 127. Evans, L.D. et al. Extracellular Monomeric and Aggregated Tau Efficiently Enter Human Neurons through Overlapping but Distinct Pathways. *Cell Rep* **22**, 3612-3624 (2018).
 128. Holmes, B.B. et al. Heparan sulfate proteoglycans mediate internalization and propagation of specific proteopathic seeds. *Proc Natl Acad Sci U S A* **110**, E3138-47 (2013).
 129. Flavin, W.P. et al. Endocytic vesicle rupture is a conserved mechanism of cellular invasion by amyloid proteins. *Acta Neuropathol* **134**, 629-653 (2017).
 130. Vogels, T. et al. Propagation of Tau Pathology: Integrating Insights From Postmortem and In Vivo Studies. *Biol Psychiatry* **87**, 808-818 (2020).
 131. Alquezar, C., Arya, S. & Kao, A.W. Tau Post-translational Modifications: Dynamic Transformers of Tau Function, Degradation, and Aggregation. *Front Neurol* **11**, 595532 (2020).
 132. Morishima-Kawashima, M. et al. Proline-directed and non-proline-directed phosphorylation of PHF-tau. *J Biol Chem* **270**, 823-9 (1995).
 133. Hanger, D.P., Anderton, B.H. & Noble, W. Tau phosphorylation: the therapeutic challenge for neurodegenerative disease. *Trends Mol Med* **15**, 112-9 (2009).
 134. Biernat, J. & Mandelkow, E.M. The development of cell processes induced by tau protein requires phosphorylation of serine 262 and 356 in the repeat domain and is

- inhibited by phosphorylation in the proline-rich domains. *Mol Biol Cell* **10**, 727-40 (1999).
135. Biernat, J., Gustke, N., Drewes, G., Mandelkow, E.M. & Mandelkow, E. Phosphorylation of Ser262 strongly reduces binding of tau to microtubules: distinction between PHF-like immunoreactivity and microtubule binding. *Neuron* **11**, 153-63 (1993).
 136. Dawson, H.N. et al. Inhibition of neuronal maturation in primary hippocampal neurons from tau deficient mice. *J Cell Sci* **114**, 1179-87 (2001).
 137. Spittaels, K. et al. Glycogen synthase kinase-3beta phosphorylates protein tau and rescues the axonopathy in the central nervous system of human four-repeat tau transgenic mice. *J Biol Chem* **275**, 41340-9 (2000).
 138. Hoover, B.R. et al. Tau mislocalization to dendritic spines mediates synaptic dysfunction independently of neurodegeneration. *Neuron* **68**, 1067-81 (2010).
 139. Hasegawa, M. et al. Characterization of mAb AP422, a novel phosphorylation-dependent monoclonal antibody against tau protein. *FEBS Lett* **384**, 25-30 (1996).
 140. Haase, C., Stieler, J.T., Arendt, T. & Holzer, M. Pseudophosphorylation of tau protein alters its ability for self-aggregation. *J Neurochem* **88**, 1509-20 (2004).
 141. Kamah, A. et al. Nuclear magnetic resonance analysis of the acetylation pattern of the neuronal Tau protein. *Biochemistry* **53**, 3020-32 (2014).
 142. Min, S.W. et al. Acetylation of tau inhibits its degradation and contributes to tauopathy. *Neuron* **67**, 953-66 (2010).
 143. Ding, H., Dolan, P.J. & Johnson, G.V. Histone deacetylase 6 interacts with the microtubule-associated protein tau. *J Neurochem* **106**, 2119-30 (2008).
 144. Min, S.W. et al. Critical role of acetylation in tau-mediated neurodegeneration and cognitive deficits. *Nat Med* **21**, 1154-62 (2015).
 145. Chen, X. et al. Promoting tau secretion and propagation by hyperactive p300/CBP via autophagy-lysosomal pathway in tauopathy. *Mol Neurodegener* **15**, 2 (2020).
 146. Schueller, E. et al. Dysregulation of histone acetylation pathways in hippocampus and frontal cortex of Alzheimer's disease patients. *Eur Neuropsychopharmacol* **33**, 101-116 (2020).
 147. Julien, C. et al. Sirtuin 1 reduction parallels the accumulation of tau in Alzheimer disease. *J Neuropathol Exp Neurol* **68**, 48-58 (2009).
 148. Min, S.W. et al. SIRT1 Deacetylates Tau and Reduces Pathogenic Tau Spread in a Mouse Model of Tauopathy. *J Neurosci* **38**, 3680-3688 (2018).
 149. Cook, C., Stankowski, J.N., Carlomagno, Y., Stetler, C. & Petrucelli, L. Acetylation: a new key to unlock tau's role in neurodegeneration. *Alzheimers Res Ther* **6**, 29 (2014).
 150. Caballero, B. et al. Acetylated tau inhibits chaperone-mediated autophagy and promotes tau pathology propagation in mice. *Nat Commun* **12**, 2238 (2021).
 151. Shin, M.K. et al. Reducing acetylated tau is neuroprotective in brain injury. *Cell* **184**, 2715-2732 e23 (2021).
 152. Cook, C. et al. Acetylation of the KXGS motifs in tau is a critical determinant in modulation of tau aggregation and clearance. *Hum Mol Genet* **23**, 104-16 (2014).

-
153. Cohen, T.J., Friedmann, D., Hwang, A.W., Marmorstein, R. & Lee, V.M. The microtubule-associated tau protein has intrinsic acetyltransferase activity. *Nat Struct Mol Biol* **20**, 756-62 (2013).
 154. Li, D. & Liu, C. Hierarchical chemical determination of amyloid polymorphs in neurodegenerative disease. *Nat Chem Biol* **17**, 237-245 (2021).
 155. Irwin, D.J. et al. Acetylated tau, a novel pathological signature in Alzheimer's disease and other tauopathies. *Brain* **135**, 807-18 (2012).
 156. Irwin, D.J. et al. Acetylated tau neuropathology in sporadic and hereditary tauopathies. *Am J Pathol* **183**, 344-51 (2013).
 157. Kametani, F. et al. Comparison of Common and Disease-Specific Post-translational Modifications of Pathological Tau Associated With a Wide Range of Tauopathies. *Front Neurosci* **14**, 581936 (2020).
 158. Xiang, S. et al. A Two-Component Adhesive: Tau Fibrils Arise from a Combination of a Well-Defined Motif and Conformationally Flexible Interactions. *J Am Chem Soc* **139**, 2639-2646 (2017).
 159. Daebel, V. et al. beta-Sheet core of tau paired helical filaments revealed by solid-state NMR. *J Am Chem Soc* **134**, 13982-9 (2012).
 160. Vranken, W.F. et al. The CCPN data model for NMR spectroscopy: development of a software pipeline. *Proteins* **59**, 687-96 (2005).
 161. Pettersen, E.F. et al. UCSF Chimera--a visualization system for exploratory research and analysis. *J Comput Chem* **25**, 1605-12 (2004).
 162. Schindelin, J. et al. Fiji: an open-source platform for biological-image analysis. *Nature Methods* **9**, 676-682 (2012).
 163. Muchmore, D.C., McIntosh, L.P., Russell, C.B., Anderson, D.E. & Dahlquist, F.W. Expression and nitrogen-15 labeling of proteins for proton and nitrogen-15 nuclear magnetic resonance. *Methods Enzymol* **177**, 44-73 (1989).
 164. Sattler, M. Heteronuclear multidimensional NMR experiments for the structure determination of proteins in solution employing pulsed field gradients. *Prog. Nucl. Magn. Reson. Spectrosc.* **34**, 93-158 (1999).
 165. Mukrasch, M.D. et al. Structural polymorphism of 441-residue tau at single residue resolution. *PLoS Biol* **7**, e34 (2009).
 166. Morris, G.A. & Freeman, R. Enhancement of nuclear magnetic resonance signals by polarization transfer. *Journal of the American Chemical Society* **101**, 760-762 (1979).
 167. Griffin, R.G. Dipolar recoupling in MAS spectra of biological solids. *Nat Struct Biol* **5 Suppl**, 508-12 (1998).
 168. Mentink-Vigier, F. et al. Efficient cross-effect dynamic nuclear polarization without depolarization in high-resolution MAS NMR. *Chem. Sci.* (2017).
 169. Mathies, G. et al. Efficient Dynamic Nuclear Polarization at 800 MHz/527 GHz with Trityl-Nitroxide Biradicals. *Angewandte Chemie International Edition* **54**, 11770-11774 (2015).
 170. Birkefeld, A.B., Bertermann, R., Eckert, H. & Pfeleiderer, B. Liquid- and solid-state high-resolution NMR methods for the investigation of aging processes of silicone breast implants. *Biomaterials* **24**, 35-46 (2003).

-
171. Lange, A., Luca, S. & Baldus, M. Structural Constraints from Proton-Mediated Rare-Spin Correlation Spectroscopy in Rotating Solids. *Journal of the American Chemical Society* **124**, 9704-9705 (2002).
 172. Woerman, A.L. et al. Tau prions from Alzheimer's disease and chronic traumatic encephalopathy patients propagate in cultured cells. *Proc Natl Acad Sci U S A* **113**, E8187-E8196 (2016).
 173. Liu, S. et al. Highly efficient intercellular spreading of protein misfolding mediated by viral ligand - receptor interactions. *bioRxiv*, 2020.06.26.173070 (2020).
 174. Chalker, J.M., Lercher, L., Rose, N.R., Schofield, C.J. & Davis, B.G. Conversion of cysteine into dehydroalanine enables access to synthetic histones bearing diverse post-translational modifications. *Angew Chem Int Ed Engl* **51**, 1835-9 (2012).
 175. Xu, S., Brunden, K.R., Trojanowski, J.Q. & Lee, V.M. Characterization of tau fibrillization in vitro. *Alzheimers Dement* **6**, 110-7 (2010).
 176. Dregni, A.J. et al. In vitro 0N4R tau fibrils contain a monomorphic beta-sheet core enclosed by dynamically heterogeneous fuzzy coat segments. *Proc Natl Acad Sci U S A* **116**, 16357-16366 (2019).
 177. Jicha, G.A., Bowser, R., Kazam, I.G. & Davies, P. Alz-50 and MC-1, a new monoclonal antibody raised to paired helical filaments, recognize conformational epitopes on recombinant tau. *J Neurosci Res* **48**, 128-132 (1997).
 178. Bibow, S. et al. The dynamic structure of filamentous tau. *Angew Chem Int Ed Engl* **50**, 11520-4 (2011).
 179. Holmes, B.B. et al. Proteopathic tau seeding predicts tauopathy in vivo. *Proc Natl Acad Sci U S A* **111**, E4376-85 (2014).
 180. Ginsberg, S.D., Crino, P.B., Lee, V.M., Eberwine, J.H. & Trojanowski, J.Q. Sequestration of RNA in Alzheimer's disease neurofibrillary tangles and senile plaques. *Ann Neurol* **41**, 200-9 (1997).
 181. Jicha, G.A., Bowser, R., Kazam, I.G. & Davies, P. Alz-50 and MC-1, a new monoclonal antibody raised to paired helical filaments, recognize conformational epitopes on recombinant tau. *J Neurosci Res* **48**, 128-32 (1997).
 182. Gustke, N., Trinczek, B., Biernat, J., Mandelkow, E.M. & Mandelkow, E. Domains of tau protein and interactions with microtubules. *Biochemistry* **33**, 9511-22 (1994).
 183. Trzeciakiewicz, H. et al. An HDAC6-dependent surveillance mechanism suppresses tau-mediated neurodegeneration and cognitive decline. *Nat Commun* **11**, 5522 (2020).
 184. Gorsky, M.K., Burnouf, S., Dols, J., Mandelkow, E. & Partridge, L. Acetylation mimic of lysine 280 exacerbates human Tau neurotoxicity in vivo. *Sci Rep* **6**, 22685 (2016).
 185. Fujimoto, H. et al. A possible overestimation of the effect of acetylation on lysine residues in KQ mutant analysis. *J Comput Chem* **33**, 239-46 (2012).
 186. Bhattacharya, K., Rank, K.B., Evans, D.B. & Sharma, S.K. Role of cysteine-291 and cysteine-322 in the polymerization of human tau into Alzheimer-like filaments. *Biochem Biophys Res Commun* **285**, 20-6 (2001).
 187. Wickramasinghe, S.P. et al. Polyphosphate Initiates Tau Aggregation through Intra- and Intermolecular Scaffolding. *Biophys J* **117**, 717-728 (2019).

188. Tang, T.T.L. & Passmore, L.A. Recognition of Poly(A) RNA through Its Intrinsic Helical Structure. *Cold Spring Harb Symp Quant Biol* **84**, 21-30 (2019).
189. Kontaxi, C., Piccardo, P. & Gill, A.C. Lysine-Directed Post-translational Modifications of Tau Protein in Alzheimer's Disease and Related Tauopathies. *Front Mol Biosci* **4**, 56 (2017).
190. Tracy, T.E. et al. Acetylated Tau Obstructs KIBRA-Mediated Signaling in Synaptic Plasticity and Promotes Tauopathy-Related Memory Loss. *Neuron* **90**, 245-60 (2016).
191. Sohn, P.D. et al. Acetylated tau destabilizes the cytoskeleton in the axon initial segment and is mislocalized to the somatodendritic compartment. *Mol Neurodegener* **11**, 47 (2016).
192. Iovino, M. et al. The novel MAPT mutation K298E: mechanisms of mutant tau toxicity, brain pathology and tau expression in induced fibroblast-derived neurons. *Acta Neuropathol* **127**, 283-95 (2014).
193. US Food and Drug Administration. Manufacturer data sheet 9676203, Dolobid (Diflunisal). Merck & Co, l.h.w.a.f.g. & [drugsatfda_docs/label/2007/018445s058lbl.pdf](https://www.accessdata.fda.gov/drugsatfda_docs/label/2007/018445s058lbl.pdf).

6. Appendix

6.1 Human tau sequence

6.1.1 Sequence of human 2N4R tau

10 20 30 40 50 60
 MAEPRQEFEV MEDHAGTYGL GDRKDQGGYT MHQDQEGDTD AGLKESPLQT PTEDGSEEPG

70 80 90 100 110 120
 SETSDAKSTP TAEDVTAPLV DEGAPGKQAA AQPHTTEIPEG TTAEAEAGIGD TPSLEDEAAG

130 140 150 160 170 180
 HVTQARMVSK SKDGTGSDDK KAKGADGKTK IATPRGAAPP GQKGQANATR IPAKTTPAPK

190 200 210 220 230 240
 TPPSSGEPPK SGDRSGYSSP GSPGTPGSR S RTPSLPTPPT REPKKVAVVR TPPKSPSSAK

250 260 270 280 290 300
 SRLQTAPVPM PDLKNVSKI GSTENLKHQP GGGKVQIINK KLDLSNVQSK CGSKDNIKHV

310 320 330 340 350 360
 PGGGSVQIVY KPVDSLKVTS KCGSLGNIHH KPGGGQVEVK SEKLDFKDRV QSKIGSLDNI

370 380 390 400 410 420
 THVPGGNKK IETHKLTFR E NAKAKTDHGA EIVYKSPVVS GDTSPRHLSN VSSTGSIDMV

430 440
 DSPQLATLAD EVSASLAKQG L

Number of amino acids: 441

Molecular weight: 45849.91 Da

Theoretical pI: 8.24

6.1.2 Sequence of human ON3R tau

10 20 30 40 50 60
 MAEPRQEFEV MEDHAGTYGL GDRKDQGGYT MHQDQEGDTD AGLKAE EAGI GDTPSLEDEA

 70 80 90 100 110 120
 AGHVTQARMV SKSKDGTGSD DKKAKGADGK TKIATPRGAA PPGQKGQANA TRIPAKTPPA

 130 140 150 160 170 180
 PKTPPSSGEP PKSGDRSGYS SPGSPGTPGS RSRTPSLPTP PTREPKKVAV VRTPPKSPSS

 190 200 210 220 230 240
 AKSRLQTAPV PMPDLKNVKS KIGSTENLKH QPGGGKVQIV YKPVDLSKVT SKCGSLGNIH

 250 260 270 280 290 300
 HKPGGGQVEV KSEKLDKFKDR VQSKIGSLDN ITHVPGGGNK KIETHKLTFR ENAKAKTDHG

 310 320 330 340 350
 AEIVYKSPVV SGGTSPRHLS NVSSTGSIDM VDSPQLATLA DEVSASLAKQ GL

Number of amino acids: 352

Molecular weight: 36760.07 Da

Theoretical pI: 9.39

6.2 Preparation of 2N4R tau mutants

6.2.1 K280Q 2N4R tau

The following PCR protocol was used to generate the K280Q 2N4R tau construct:

Step	Time	Temp	Number of cycles
Heat Lid → On			
Initial denaturation	60sec	98 °C	
Denaturation	10 sec	98 °C	}30 cycles
Annealing	30 sec	72 °C	}30 cycles
Extension	180 sec	72 °C	}30 cycles
Final extension	10 min	72 °C	
Heat Lid → Off			
	Hold	4 °C	

Sample details:

2x Phusion master mix – 25 µL

Forward primer – 2.5 μ L (10 μ M stock)

Reverse primer - 2.5 μ L (10 μ M stock)

Template DNA – 1 μ L

DMSO (100 %) – 1.5 μ L

H₂O – 17.5 μ L

Forward primer: 5' GGTGCAGATAATTAATCAGAAGCTGGATCTTAGC 3'

Reverse primer: 5' GCTAAGATCCAGCTTCTGATTAATTATCTGCACC 3'

Template DNA – 2N4R tau

6.2.2 K281Q 2N4R tau

The following PCR protocol was used to generate the K281Q 2N4R tau construct:

Step	Time	Temp	Number of cycles
Heat Lid → On			
Initial denaturation	60sec	98 °C	
Denaturation	10 sec	98 °C	}30 cycles
Annealing	30 sec	66.4 °C	}30 cycles
Extension	180 sec	72 °C	}30 cycles
Final extension	10 min	72 °C	
Heat Lid → Off			
	Hold	4 °C	

Sample details:

2x Phusion master mix – 25 μ L

Forward primer – 2.5 μ L (10 μ M stock)

Reverse primer - 2.5 μ L (10 μ M stock)

Template DNA – 1 μ L

DMSO (100 %) – 2 μ L

H₂O – 17 μ L

Forward primer: 5' GTGCAGATAATTAATAAGCAGCTGGATCTTAGCAACG 3'

Reverse primer: 5' CGTTGCTAAGATCCAGCTGCTTATTAATTATCTGCAC 3'

Template DNA – 2N4R tau

6.2.3 K290Q 2N4R tau

The following PCR protocol was used to generate the K290Q 2N4R tau construct:

Step	Time	Temp	Number of cycles
Heat Lid → On			
Initial denaturation	60sec	98 °C	
Denaturation	10 sec	98 °C	}30 cycles
Annealing	30 sec	68 °C	}30 cycles
Extension	180 sec	72 °C	}30 cycles
Final extension	10 min	72 °C	
Heat Lid → Off			
	Hold	4 °C	

Sample details:

2x Phusion master mix – 25 µL

Forward primer – 2.5 µL (10 µM stock)

Reverse primer - 2.5 µL (10 µM stock)

Template DNA – 1 µL

DMSO (100 %) – 1.5 µL

H₂O – 17.5 µL

Forward primer: 5' CAACGTCCAGTCCCAGTGTGGCTCAAAG 3'

Reverse primer: 5' CTTTGAGCCCACTGGGACTGGACGTTG 3'

Template DNA – 2N4R tau

6.2.4 K294Q 2N4R tau

The following PCR protocol was used to generate the K294Q 2N4R tau construct:

Step	Time	Temp	Number of cycles
Heat Lid → On			
Initial denaturation	60sec	98 °C	
Denaturation	10 sec	98 °C	}30 cycles
Annealing	30 sec	69.3 °C	}30 cycles
Extension	180 sec	72 °C	}30 cycles
Final extension	10 min	72 °C	

Heat Lid → Off			
	Hold	4 °C	

Sample details:

2x Phusion master mix – 25 µL

Forward primer – 2.5 µL (10 µM stock)

Reverse primer - 2.5 µL (10 µM stock)

Template DNA – 1 µL

DMSO (100 %) – 1.5 µL

H₂O – 17.5 µL

Forward primer: 5' GTCCAAGTGTGGCTCACAGGATAATATCAAAC 3'

Reverse primer: 5' GTTTGATATTATCCTGTGAGCCACACTTGGAC 3'

Template DNA – 2N4R tau

6.2.5 K298Q 2N4R tau

The following PCR protocol was used to generate the K298Q 2N4R tau construct:

Step	Time	Temp	Number of cycles
Heat Lid → On			
Initial denaturation	60sec	98 °C	
Denaturation	10 sec	98 °C	}30 cycles
Annealing	30 sec	66.3 °C	}30 cycles
Extension	180 sec	72 °C	}30 cycles
Final extension	10 min	72 °C	
Heat Lid → Off			
	Hold	4 °C	

Sample details:

2x Phusion master mix – 25 µL

Forward primer – 2.5 µL (10 µM stock)

Reverse primer - 2.5 µL (10 µM stock)

Template DNA – 1 µL

DMSO (100 %) – 1.5 µL

H₂O – 17.5 µL

Forward primer: 5' CAAAGGATAATATCCAACACGTCCCGGG 3'

Reverse primer: 5' CCCGGGACGTGTTGGATATTATCCTTTG 3'

Template DNA – 2N4R tau

6.2.6 K298Q K311Q 2N4R tau

The following PCR protocol was used to generate the K298Q K311Q 2N4R tau construct:

Step	Time	Temp	Number of cycles
Heat Lid → On			
Initial denaturation	60sec	98 °C	
Denaturation	10 sec	98 °C	}30 cycles
Annealing	30 sec	67.2 °C	}30 cycles
Extension	180 sec	72 °C	}30 cycles
Final extension	10 min	72 °C	
Heat Lid → Off			
	Hold	4 °C	

Sample details:

2x Phusion master mix – 25 µL

Forward primer – 2.5 µL (10 µM stock)

Reverse primer - 2.5 µL (10 µM stock)

Template DNA – 1 µL

H₂O – 19 µL

Forward primer: 5' GTGCAAATAGTCTACCAACCAGTTGACCTG 3'

Reverse primer: 5' CAGGTCAACTGGTTGGTAGACTATTTGCAC 3'

Template DNA: K298Q 2N4R tau

6.2.7 C291S 2N4R tau

The following PCR protocol was used to generate the C291S 2N4R tau construct:

Step	Time	Temp	Number of cycles
Heat Lid → On			
Initial denaturation	60sec	98 °C	
Denaturation	10 sec	98 °C	}30 cycles

Annealing	30 sec	64 °C	}30 cycles
Extension	180 sec	72 °C	}30 cycles
Final extension	10 min	72 °C	
Heat Lid → Off			
	Hold	4 °C	

Sample details:

2x Phusion master mix – 25 µL

Forward primer – 2.5 µL (10 µM stock)

Reverse primer - 2.5 µL (10 µM stock)

Template DNA – 1 µL

DMSO (100 %) – 1.5 µL

H₂O – 17.5 µL

Forward primer: 5' CAACGTCCAGTCCAAGTCAGGCTCAAAGGATAATATC 3'

Reverse primer: 5' GATATTATCCTTTGAGCCTGACTTGGACTGGACGTTG 3'

Template DNA: 2N4R tau

6.2.8 C291S C322S 2N4R tau

The following PCR protocol was used to generate the C291S C322S 2N4R tau construct:

Step	Time	Temp	Number of cycles
Heat Lid → On			
Initial denaturation	60sec	98 °C	
Denaturation	10 sec	98 °C	}30 cycles
Annealing	30 sec	71.1 °C	}30 cycles
Extension	180 sec	72 °C	}30 cycles
Final extension	10 min	72 °C	
Heat Lid → Off			
	Hold	4 °C	

Sample details:

2x Phusion master mix – 25 µL

Forward primer – 2.5 µL (10 µM stock)

Reverse primer - 2.5 µL (10 µM stock)

Template DNA – 1 μ L

H₂O – 19 μ L

Forward primer: 5' GTGACCTCCAAGTCTGGCTCATTAGGC 3'

Reverse primer: 5' GCCTAATGAGCCAGACTTGGAGGTCAC 3'

Template DNA: C291S 2N4R tau

6.2.9 C291S C322S K280C 2N4R tau

The following PCR protocol was used to generate the C291S C322S K280C 2N4R tau construct:

Step	Time	Temp	Number of cycles
Heat Lid → On			
Initial denaturation	60sec	98 °C	
Denaturation	10 sec	98 °C	}30 cycles
Annealing	30 sec	72 °C	}30 cycles
Extension	180 sec	72 °C	}30 cycles
Final extension	10 min	72 °C	
Heat Lid → Off			
	Hold	4 °C	

Sample details:

2x Phusion master mix – 25 μ L

Forward primer – 2.5 μ L (10 μ M stock)

Reverse primer - 2.5 μ L (10 μ M stock)

Template DNA – 1 μ L

DMSO (100 %) – 1.5 μ L

H₂O – 17.5 μ L

Forward primer: 5' GGTGCAGATAATTAATTGCAAGCTGGATCTTAGC 3'

Reverse primer: 5' GCTAAGATCCAGCTTGCAATTAATTATCTGCACC 3'

Template DNA: C291S C322S 2N4R tau

6.2.10 C291S C322S K294C 2N4R tau

The following PCR protocol was used to generate the C291S C322S K294C 2N4R tau construct:

Step	Time	Temp	Number of cycles
Heat Lid → On			
Initial denaturation	60sec	98 °C	
Denaturation	10 sec	98 °C	}30 cycles
Annealing	30 sec	72 °C	}30 cycles
Extension	180 sec	72 °C	}30 cycles
Final extension	10 min	72 °C	
Heat Lid → Off			
	Hold	4 °C	

Sample details:

2x Phusion master mix – 25 µL

Forward primer – 2.5 µL (10 µM stock)

Reverse primer - 2.5 µL (10 µM stock)

Template DNA – 1 µL

DMSO (100 %) – 5 µL

H₂O – 14 µL

Forward primer: 5' CCAGTCCAAGTCAGGCTCATGTGATAATATCAAACACGTC 3'

Reverse primer: 5' GACGTGTTTGATATTATCACATGAGCCTGACTTGGACTGG 3'

Template DNA: C291S C322S 2N4R tau

6.2.11 C291S C322S K298C 2N4R tau

The PCR reaction was performed by Mrs. Maria-Sol Cima-Omori (Translational structural biology in dementia, DZNE, Göttingen). The following PCR protocol was used to generate C291S C322S K298C 2N4R tau construct:

Step	Time	Temp	Number of cycles
------	------	------	------------------

Heat Lid → On			
Initial denaturation	60sec	98 °C	
Denaturation	10 sec	98 °C	}30 cycles
Annealing	30 sec	64.5 °C	}30 cycles
Extension	180 sec	72 °C	}30 cycles
Final extension	10 min	72 °C	
Heat Lid → Off			
	Hold	4 °C	

Sample details:

2x Phusion master mix – 25 µL

Forward primer – 2.5 µL (10 µM stock)

Reverse primer - 2.5 µL (10 µM stock)

Template DNA – 1 µL

DMSO (100 %) – 1.5 µL

H₂O – 17.5 µL

Forward primer: 5' CAAAGGATAATATCTGTCACGTCCCGGGAGGC 3'

Reverse primer: 5' GCCTCCCGGGACGTGACAGATATTATCCTTTG 3'

Template DNA: C291S C322S 2N4R tau

6.2.12 C291S C322S K311C 2N4R tau

The following PCR protocol was used to generate the C291S C322S K311C 2N4R tau construct:

Step	Time	Temp	Number of cycles
Heat Lid → On			
Initial denaturation	60sec	98 °C	
Denaturation	10 sec	98 °C	}30 cycles
Annealing	30 sec	71.8 °C	}30 cycles
Extension	180 sec	72 °C	}30 cycles
Final extension	10 min	72 °C	
Heat Lid → Off			

	Hold	4 °C	
--	------	------	--

Sample details:

2x Phusion master mix – 25 µL

Forward primer – 2.5 µL (10 µM stock)

Reverse primer - 2.5 µL (10 µM stock)

Template DNA – 1 µL

DMSO (100 %) – 3 µL

H₂O – 16 µL

Forward primer: 5' GTGTGCAAATAGTCTACTGTCCAGTTGACCTGAGCAAG 3'

Reverse primer: 5' CTTGCTCAGGTCAACTGGACAGTAGACTATTTGCACAC 3'

Template DNA: C291S C322S 2N4R tau

6.2.13 C291S C322S K298C K311C 2N4R tau

The PCR reaction was performed by Mrs. Maria-Sol Cima-Omori (Translational structural biology in dementia, DZNE, Göttingen). The following PCR protocol was used to generate C291S C322S K298C K311C 2N4R tau construct:

Step	Time	Temp	Number of cycles
Heat Lid → On			
Initial denaturation	60sec	98 °C	
Denaturation	10 sec	98 °C	}30 cycles
Annealing	30 sec	71.8 °C	}30 cycles
Extension	180 sec	72 °C	}30 cycles
Final extension	10 min	72 °C	
Heat Lid → Off			
	Hold	4 °C	

Sample details:

2x Phusion master mix – 25 µL

Forward primer – 2.5 µL (10 µM stock)

Reverse primer - 2.5 μ L (10 μ M stock)

Template DNA – 1 μ L

DMSO (100 %) – 3 μ L

H₂O – 16 μ L

Forward primer: 5' GTGTGCAAATAGTCTACTGTCCAGTTGACCTGAGCAAG 3'

Reverse primer: 5' CTTGCTCAGGTCAACTGGACAGTAGACTATTTGCACAC 3'

Template DNA: C291S C322S K298C 2N4R tau

6.3 Methods used to perform the aggregation assay

a

K Kinetic Loop

Loop type: Number of cycles (1000)

Interval type: Fixed (00:10:00)

A Shaking

Duration: Time [sec] (60) At position: Current

Mode: Double orbital

Amplitude [mm]: 6

Frequency [rpm]: 54

Show ventilation settings

D Fluorescence Intensity

Name: Alain ThT

Mode: Top Bottom

Fluorophore: Other

Excitation wavelength [nm]: Monochromator (440) Bandwidth: 10,0

Emission wavelength [nm]: Monochromator (482) Bandwidth: 10,0

Hide advanced settings

Flashes: 30

Gain: Manual (60) Use gain regulation

Mirror: AUTOMATIC

Z-Position [µm]: Manual (25841)

Settle time [ms]: 0

Multiple reads per well: Not defined

b

K Kinetic Loop

Loop type: Number of cycles (1000)

Interval type: Fixed (00:10:00)

A Shaking

Duration: Time [sec] (60) At position: Current

Mode: Double orbital

Amplitude [mm]: 6

Frequency [rpm]: 54

D Fluorescence Intensity

Name: ThT

Mode: Top Bottom

Fluorophore: Other

Excitation wavelength [nm]: 430 (35)

Emission wavelength [nm]: 485 (20)

Hide advanced settings

Flashes: 30

Gain: Manual (40) Use gain regulation

Mirror: AUTOMATIC

Z-Position [µm]: Manual (24574)

Settle time [ms]: 0

Multiple reads per well: Not defined

Figure 6-1 Methods used to perform the aggregation assay

a, Method used to perform the aggregation assay using a Tecan spark 20M plate reader equipped with an excitation monochromator. b, Method used to perform the aggregation assay using a Tecan spark plate reader equipped with an excitation filter.

6.4 Pulse program for 2D ^1H - ^{15}N HSQC

```
# 1 "/opt/topspin3.2/exp/stan/nmr/lists/pp/user/hsqc15N.dl"  
;hsqc15N.new  
;D. Lee, Nov. 2002
```

```
;15N-1H HSQC correlations without water saturation  
;The delay for 3-9-19 watergate (d5) should be matched  
;with 1/d;d=distance of next null point (in Hz).
```

```
# 9 "/opt/topspin3.2/exp/stan/nmr/lists/pp/user/hsqc15N.dl"  
;S. Mori et al, JMR B108, 94-98 (1995)
```

```
;p1 : power for 1H  
;p2 : power for 13C  
;p3 : power for 15N  
;p13 : power for 15N waltz16 decoupling
```

```
;p1 : 90 degree hard pulse 1H  
;p3 : 90 degree hard pulse 13C  
;p4 : 180 degree hard 13C pulse (225d for 5/600)  
;p5 : 90 degree hard pulse 15N  
;pcpd3 : 90 deg cpd-pulse15N(waltz16,160u)
```

```
# 22 "/opt/topspin3.2/exp/stan/nmr/lists/pp/user/hsqc15N.dl"  
;d1 : relaxation delay  
;d2 : INEPT delay (~2.7m)  
;d5 : delay for 3-9-19=1/(Hz between nulls)  
;in0 : 1/(2 SW) (Hz)
```

```
;p21 : 500u (Gradient in first INEPT)  
;p22 : 500u (Gradient for z-filter)  
;p23 : 1m (Gradient for second INEPT)  
;gpz1 : 19%  
;gpz2 : 30%  
;gpz3 : 65%
```

```
# 1 "/opt/topspin3.2/exp/stan/nmr/lists/pp/user/Avance_dl.incl" 1
```

```
-----  
;Avance3.incl  
; for AVi  
;  
;avance-version (07/08/22)  
;  
;$CLASS=HighRes Incl  
;$COMMENT=  
  
# 157 "/opt/topspin3.2/exp/stan/nmr/lists/pp/user/Avance_dl.incl"  
;$Id: Avance3.incl,v 1.6.2.1 2007/09/14 16:17:35 ber Exp $  
# 35 "/opt/topspin3.2/exp/stan/nmr/lists/pp/user/hsqc15N.dl" 2  
  
define delay INEPT_W  
define delay INEPT_D  
# 44 "/opt/topspin3.2/exp/stan/nmr/lists/pp/user/hsqc15N.dl"  
"p2=2*p1"  
"p6=2*p5"  
"in0=inf1/2"  
"d0=in0/2-p5*2/3.14159"  
"d3=d5/2-p5"  
"INEPT_D=d2-p21-210u"  
"INEPT_W=d2-(p23+210u+p1*2.3846+d5*2.5)"  
  
"acqt0=0"  
baseopt_echo  
  
# 1 "mc_line 56 file /opt/topspin3.2/exp/stan/nmr/lists/pp/user/hsqc15N.dl exp. def. part of  
mc cmd. before ze"  
define delay MCWRK  
define delay MCREST  
define loopcounter ST1CNT  
"ST1CNT = td1 / 2"  
"MCREST = 1m - 1m"  
"MCWRK = 0.333333*1m"  
  
dcorr  
# 56 "/opt/topspin3.2/exp/stan/nmr/lists/pp/user/hsqc15N.dl"  
# 56 "/opt/topspin3.2/exp/stan/nmr/lists/pp/user/hsqc15N.dl"  
1 10u ze  
# 1 "mc_line 56 file /opt/topspin3.2/exp/stan/nmr/lists/pp/user/hsqc15N.dl exp. def. of mc  
cmd. after ze"  
# 57 "/opt/topspin3.2/exp/stan/nmr/lists/pp/user/hsqc15N.dl"
```

```
-----  
# 1 "mc_line 57 file /opt/topspin3.2/exp/stan/nmr/lists/pp/user/hsqc15N.dl exp. start label  
for mc cmd."  
2 MCWRK do:f3  
LBLSTS1, MCWRK  
LBLF1, MCWRK  
MCREST  
# 58 "/opt/topspin3.2/exp/stan/nmr/lists/pp/user/hsqc15N.dl"  
d1 pl1:f1  
20u pl3:f3  
20u setnmr3l0 setnmr0l34l32l33 ctrlgrad 0  
;-----first INEPT  
(p1 ph20):f1  
10u p21:gp1 200u  
INEPT_D  
(center(p2 ph21):f1 (p6 ph1):f3)  
10u p21:gp1 200u  
INEPT_D  
(p1 ph21):f1  
10u p22:gp2 200u  
;-----15N evolution  
; (p5 ph1):f3  
(refalign (p5 ph1 d0 d0 p5 ph20):f3 center (p3 ph23 1.5u p4 ph20 1.5u p3 ph23):f2  
center(p2 ph23):f1)  
; (p5 ph20):f3  
10u p22:gp2 200u  
;-----second INEPT  
(p1 ph22):f1  
10u p23:gp3 200u  
INEPT_W  
(p1*0.2308 ph21 d5 p1*0.6923 ph21 d5 p1*1.4615 ph21):f1  
(d3 p6 ph1 d3):f3  
(p1*1.4615 ph23 d5 p1*0.6923 ph23 d5 p1*0.2308 ph23):f1  
10u p23:gp3 200u  
INEPT_W pl13:f3 setnmr3^0 setnmr0^34^32^33 ctrlgrad 7  
;-----acquisition  
go=2 ph31 cpd3:f3  
# 1 "mc_line 86 file /opt/topspin3.2/exp/stan/nmr/lists/pp/user/hsqc15N.dl exp. mc cmd. in  
line"  
MCWRK do:f3 wr #0 if #0 zd ip1  
lo to LBLSTS1 times 2  
MCWRK id0  
lo to LBLF1 times ST1CNT  
MCWRK  
# 87 "/opt/topspin3.2/exp/stan/nmr/lists/pp/user/hsqc15N.dl"
```

```

10u do:f1
10u do:f2
10u do:f3
10u setnmr3^0 setnmr0^34^32^33 ctrlgrad 7
exit

ph1 =0 2
ph31=2 0

ph20=0
ph21=1
ph22=2
ph23=3
# 101 "/opt/topspin3.2/exp/stan/nmr/lists/pp/user/hsqc15N.dl"
;##/($P[1],$PL[1])= &SetPulse(f1,HP,90);
;##/($P[5],$PL[3])= &SetPulse(f3,HP,90);
;##/($P[3],$PL[2])= &SetPulse(f2,HP,90);
;##/if ($BF1>650) {$P[4]=2.*$P[3]} else {$P[4]=2.5*$P[3]}
;##/$D[5]=&round(1/(10*$BF1),.00001);
;##/($PCPD[3],$PL[13])= &SetPulse(f3,0.000160,90);

```

6.5 Pulse program for 2D ^1H - ^{15}N INEPT experiments

```

1 "/ssnmrpulprogs/hNHj.mpibpc"
;hsqc.sat.ajpalwgp
;avance-version (07/04/04)
;HSQC
;2D H-1/X correlation via double inept transfer
;phase sensitive
;with decoupling during acquisition
;
;Pell, Webber, Pintacuda (le chef)
;
;$CLASS=HighRes
;$DIM=2D
;$TYPE=
;$SUBTYPE=
;$COMMENT=

# 1 "/opt/topspin3.5pl7/exp/stan/nmr/lists/pp/Avance.incl" 1
;Avance3.incl
; for AV III

```

```
-----  
;  
;avance-version (13/06/17)  
;  
;$CLASS=HighRes Incl  
;$COMMENT=  
# 169 "/opt/topspin3.5pl7/exp/stan/nmr/lists/pp/Avance.incl"  
;$Id: Avance3.incl,v 1.10.2.2 2013/08/30 09:43:33 ber Exp $  
# 17 "/ssnmrpulprogs/hNHj.mpibpc" 2  
  
# 1 "/opt/topspin3.5pl7/exp/stan/nmr/lists/pp/Delay.incl" 1  
;Delay.incl - include file for commonly used delays  
;  
;version (13/08/07)  
;  
;$CLASS=HighRes Incl  
;$COMMENT=  
  
# 9 "/opt/topspin3.5pl7/exp/stan/nmr/lists/pp/Delay.incl"  
;general delays  
  
define delay DELTA  
define delay DELTA1  
define delay DELTA2  
define delay DELTA3  
define delay DELTA4  
define delay DELTA5  
define delay DELTA6  
define delay DELTA7  
define delay DELTA8  
define delay DELTA9  
define delay DELTA10  
define delay DELTA11  
define delay DELTA12  
define delay DELTA13  
define delay DELTA14  
define delay DELTA15  
define delay DELTA16  
  
define delay TAU  
define delay TAU1  
define delay TAU2  
define delay TAU3  
define delay TAU4  
define delay TAU5
```

```
define delay TAU6
define delay TAU7
define delay TAU8
define delay TAU9
# 40 "/opt/topspin3.5pl7/exp/stan/nmr/lists/pp/Delay.incl"
define delay INCR1
define delay INCR2
define delay INCR3
define delay INCR4
define delay INCR5
define delay INCR6
```

```
;delays for centering pulses
# 50 "/opt/topspin3.5pl7/exp/stan/nmr/lists/pp/Delay.incl"
define delay CEN_HN1
define delay CEN_HN2
define delay CEN_HN3
define delay CEN_HC1
define delay CEN_HC2
define delay CEN_HC3
define delay CEN_HC4
define delay CEN_HP1
define delay CEN_HP2
define delay CEN_CN1
define delay CEN_CN2
define delay CEN_CN3
define delay CEN_CN4
define delay CEN_CP1
define delay CEN_CP2
```

```
;loop counters
# 69 "/opt/topspin3.5pl7/exp/stan/nmr/lists/pp/Delay.incl"
define loopcounter COUNTER
define loopcounter SCALEF
define loopcounter FACTOR1
define loopcounter FACTOR2
define loopcounter FACTOR3
define loopcounter FACTOR4
define loopcounter FACTOR5
define loopcounter FACTOR6
```

```
-----  
  
# 80 "/opt/topspin3.5pl7/exp/stan/nmr/lists/pp/Delay.incl"  
;$ld: Delay.incl,v 1.14.2.1 2013/08/30 09:43:33 ber Exp $  
# 18 "/ssnmrpulprogs/hNHj.mpibpc" 2  
  
# 21 "/ssnmrpulprogs/hNHj.mpibpc"  
"p2=p1*2"  
"p4=p3*2"  
;"d4=1s/(cnst2*4)"  
"d0=-1u"  
;"d10=vd/2"  
"d11=30m"  
  
"in0=inf1"  
"in10=inf2/2"  
# 32 "/ssnmrpulprogs/hNHj.mpibpc"  
"DELTA=d0*2+p2"  
  
aqseq 321  
  
# 1 "mc_line 37 file /ssnmrpulprogs/hNHj.mpibpc exp. def. part of mc cmd. before ze"  
; dimension 2D; AQ_mode (F1) States-TPPI  
define delay MCWRK  
define delay MCREST  
define delay d0orig  
"d0orig=d0"  
define loopcounter t1loop  
"t1loop=0"  
define loopcounter ph1loop  
"ph1loop=0"  
define loopcounter ST1CNT  
"ST1CNT = td1 / 2"  
"MCREST = d1 - d1"  
"MCWRK = 0.200000*d1"  
  
dcorr  
# 37 "/ssnmrpulprogs/hNHj.mpibpc"  
# 37 "/ssnmrpulprogs/hNHj.mpibpc"  
1 ze  
# 1 "mc_line 37 file /ssnmrpulprogs/hNHj.mpibpc exp. def. of mc cmd. after ze"  
LBLAV, MCWRK  
"d0=d0orig + t1loop * in0 "  
"phval10 = (ph1loop % 4) * -90"
```

```
MCWRK ip10 + phval10
# 38 "/ssnmpulprogs/hNHj.mpibpc"
  d11 ;pl12:f2
# 1 "mc_line 39 file /ssnmpulprogs/hNHj.mpibpc exp. start label for mc cmd."
2 MCWRK * 2 do:f2 do:f3
LBLF1, MCWRK * 2
LBLST1, MCWRK
  MCREST
# 40 "/ssnmpulprogs/hNHj.mpibpc"

; -----1H to XY plane-----
3 (p1 pl1 ph14):f1

; -----1H to 15N INEPT transfer-----
  d4 ;pl2:f2
  (center (p1*2 pl1 ph2):f1 (p7*2 pl7 ph9):f2)
  d4
  (center (p1 pl1 ph3):f1 (p7 pl7 ph6):f2)
# 50 "/ssnmpulprogs/hNHj.mpibpc"
; (center (d0) (p2 pl1 ph8):f1)

  d14
  (center (p1*2 pl1 ph2):f1 (p7*2 pl7 ph5):f2)
  d14 ;pl12:f2

; -----15N CS evolution-----
# 58 "/ssnmpulprogs/hNHj.mpibpc"
if "d0<0" goto 4
  0.5u cpds1:f1
  (center (d0) (p3*2 pl11 ph0):f3)
  0.5u do:f1

; -----Hahn echo for T2 measurement-----

;4 vd
; (p7*2 pl7 ph13):f2
; vd
;0.5u do:f1
# 70 "/ssnmpulprogs/hNHj.mpibpc"
; -----15N to z axis for water suppression-----
4 (p7 pl7 ph10):f2

  1u pl13:f1
  p30*0.25 ph0
```

```
p30*0.25 ph1
p30*0.25 ph0
p30*0.25 ph1

# 80 "/ssnmrpulprogs/hNHj.mpibpc"
; -----15N to XY plane after water suppression-----
(p7 pl7 ph11):f2

; -----15N to 1H INEPT transfer-----
d14
(center (p1*2 pl1 ph2):f1 (p7*2 pl7 ph5):f2 )
d14 ;pl12:f2
(center (p1 pl1 ph4):f1 (p7 pl7 ph7):f2)
d4
(center (p1*2 pl1 ph2):f1 (p7*2 pl7 ph5):f2 )
d4 ;pl12:f2

; -----detection-----
go=2 ph31 cpds2:f2 cpds3:f3
# 1 "mc_line 94 file /ssnmrpulprogs/hNHj.mpibpc exp. mc cmd. in line "
MCWRK do:f2 do:f3 wr #0 if #0 zd

"ph1loop+=1"
"d0=d0orig + t1loop * in0 "
"phval10 = (ph1loop % 4) * -90"
MCWRK ip10 + phval10
lo to LBLF1 times 2
MCWRK

"t1loop+=1"
"d0=d0orig + t1loop * in0 "
"phval10 = (ph1loop % 4) * -90"
MCWRK ip10 + phval10
lo to LBLST1 times ST1CNT
MCWRK
"t1loop=0"
"ph1loop=0"
MCWRK rf #0
lo to LBLAV times tdav
# 96 "/ssnmrpulprogs/hNHj.mpibpc"
exit

ph0=0
ph1=1
```

```

ph2=0
ph3=1
ph4=0
ph5=0
ph6=0 0 0 0 2 2 2 2 ;0 0 0 0 2 2 2 2 2 2 2
ph7=0 2;0 2 2
ph8=0
ph9=0
ph10=1
ph11=3
ph12=0
;ph13=0 1
ph14=0 0 2 2 ;0 0 2 2 2 2
ph31=0 2 2 0 2 0 0 2
      ;2 0 0 2 0 2 2 0
# 117 "/ssnmrpulprogs/hNHj.mpibpc"
;p11 : f1 channel - power level for pulse (default)
;p12 : f2 channel - power level for pulse (default)
;p12: f2 channel - power level for CPD/BB decoupling
;p13: water suppression
;p30 : total water suppression.
;p1 : f1 channel - 90 degree high power pulse
;p2 : f1 channel - 180 degree high power pulse
;p3 : f2 channel - 90 degree high power pulse
;p4 : f2 channel - 180 degree high power pulse
;d0 : incremented delay (2D) [3 usec]
;d1 : relaxation delay; 1-5 * T1
;d4 : 1/(4J)XH
;d11: delay for disk I/O [30 msec]
;cnst2: = J(XH)
;inf1: 1/SW(X) = 2 * DW(X)
;in0: 1/(2 * SW(X)) = DW(X)
;nd0: 2
;NS: 4 * n
;DS: 16
;td1: number of experiments
;FnMODE: States-TPPI, TPPI, States or QSEQ
;cpd2: decoupling according to sequence defined by cpdprg2
;pcpd2: f2 channel - 90 degree pulse for decoupling sequence

# 143 "/ssnmrpulprogs/hNHj.mpibpc"
;$ld: hsqcph,v 1.4 2007/04/11 13:34:30 ber Exp $

```

6.6 Pulse program for 2D ^{13}C - ^{13}C RFDR experiments

```
# 1 "/opt/topspin3.5pl7/exp/stan/nmr/lists/pp/user/cpXpdsd_2D.moha"
; cpXpdsd_2D.suva
; modified by land dec 2017
; written on 120627

; First implemented on 850
; 2D CC correlations with single pulse and PDSD mixing
; proton decoupling during acquisition

; =====
; Variables introduction
; =====
# 13 "/opt/topspin3.5pl7/exp/stan/nmr/lists/pp/user/cpXpdsd_2D.moha"
; pl2 H 90 pulse power
; p2 H 90 pulse length
; P15 CP build up time
; pl5 (=sp1) CP power on X
; sp1 (=pl5) shape power o X
; pl6 (=sp0) CP power on H
; sp0 (=pl6) shape power o H
; l31 (=1) ramp on H (=2) ramp on X
; cnst10 CP offset on X
; cnst20 CP offset on H
; pl1 X 90 pulse power
; p1 X 90 pulse length
; pl12 H decoupling during acquisition
; cpd2 decoupling program
; pcpd2 decoupling pulse length
; d11 PDSD mixing time
; cpds4 1 decoupling (100 kHz)

; =====
; Set variables
; =====

"d0 = 0.2u"
"in0 = inf1"
# 38 "/opt/topspin3.5pl7/exp/stan/nmr/lists/pp/user/cpXpdsd_2D.moha"
"l31 = 1"
;"sp0 = pl6"
;"sp1 = pl5"
```

```
;"cnst63 = pl12"

"d5 = 0.5s/cnst5 - p10/2"
"acqt0=0"

define delay mix
"mix = (1s/cnst5)*11 "
;=====
; Include file for Protection
;=====
# 1 "/opt/topspin3.5pl7/exp/stan/nmr/lists/pp/Avance.incl" 1
;Avance3.incl
; for AV III
;
;avance-version (13/06/17)
;
;$CLASS=HighRes Incl
;$COMMENT=

# 169 "/opt/topspin3.5pl7/exp/stan/nmr/lists/pp/Avance.incl"
;$Id: Avance3.incl,v 1.10.2.2 2013/08/30 09:43:33 ber Exp $
# 52 "/opt/topspin3.5pl7/exp/stan/nmr/lists/pp/user/cpXpdsd_2D.moha" 2

# 1 "/opt/topspin3.5pl7/exp/stan/nmr/lists/pp/Delay.incl" 1
;Delay.incl - include file for commonly used delays
;
;version (13/08/07)
;
;$CLASS=HighRes Incl
;$COMMENT=

# 9 "/opt/topspin3.5pl7/exp/stan/nmr/lists/pp/Delay.incl"
;general delays

define delay DELTA
define delay DELTA1
define delay DELTA2
define delay DELTA3
define delay DELTA4
define delay DELTA5
define delay DELTA6
define delay DELTA7
define delay DELTA8
```

```
define delay DELTA9
define delay DELTA10
define delay DELTA11
define delay DELTA12
define delay DELTA13
define delay DELTA14
define delay DELTA15
define delay DELTA16
```

```
define delay TAU
define delay TAU1
define delay TAU2
define delay TAU3
define delay TAU4
define delay TAU5
define delay TAU6
define delay TAU7
define delay TAU8
define delay TAU9
# 40 "/opt/topspin3.5pl7/exp/stan/nmr/lists/pp/Delay.incl"
define delay INCR1
define delay INCR2
define delay INCR3
define delay INCR4
define delay INCR5
define delay INCR6
```

```
;delays for centering pulses
# 50 "/opt/topspin3.5pl7/exp/stan/nmr/lists/pp/Delay.incl"
define delay CEN_HN1
define delay CEN_HN2
define delay CEN_HN3
define delay CEN_HC1
define delay CEN_HC2
define delay CEN_HC3
define delay CEN_HC4
define delay CEN_HP1
define delay CEN_HP2
define delay CEN_CN1
define delay CEN_CN2
define delay CEN_CN3
define delay CEN_CN4
define delay CEN_CP1
```

```
define delay CEN_CP2

;loop counters
# 69 "/opt/topspin3.5pl7/exp/stan/nmr/lists/pp/Delay.incl"
define loopcounter COUNTER
define loopcounter SCALEF
define loopcounter FACTOR1
define loopcounter FACTOR2
define loopcounter FACTOR3
define loopcounter FACTOR4
define loopcounter FACTOR5
define loopcounter FACTOR6

# 80 "/opt/topspin3.5pl7/exp/stan/nmr/lists/pp/Delay.incl"
;$Id: Delay.incl,v 1.14.2.1 2013/08/30 09:43:33 ber Exp $
# 53 "/opt/topspin3.5pl7/exp/stan/nmr/lists/pp/user/cpXpdsd_2D.moha" 2

1m
if "p1 > 100" goto Problem
if "p2 > 100" goto Problem
if "p15 > 5100" goto Problem
if "aq > 25m" goto Problem
; if "in0 > 50u" goto Problem
if "d11 > 401m" goto Problem
if "cnst63 < 1.0" goto Problem
if "d1 < 1.0s" goto Problem
if "mix > 20m" goto Problem
goto PassParams
Problem, 1m
print "Parameters not accepted, ending."
goto HaltAcqu
PassParams, 1m
# 71 "/opt/topspin3.5pl7/exp/stan/nmr/lists/pp/user/cpXpdsd_2D.moha"
;=====
; Begin Pulse program
;=====
mix
# 1 "mc_line 75 file /opt/topspin3.5pl7/exp/stan/nmr/lists/pp/user/cpXpdsd_2D.moha exp.
def. part of mc cmd. before ze"
; dimension 2D; AQ_mode (F1) States-TPPI
define delay MCWRK
```

```

define delay MCREST
define delay d0orig
"d0orig=d0"
define loopcounter t1loop
"t1loop=0"
define loopcounter ph1loop
"ph1loop=0"
define loopcounter ST1CNT
"ST1CNT = td1 / 2"
"MCREST = d1 - d1"
"MCWRK = 0.200000*d1"

    dccorr
# 75 "/opt/topspin3.5pl7/exp/stan/nmr/lists/pp/user/cpXpdsd_2D.moha"
1 ze
# 1 "mc_line 75 file /opt/topspin3.5pl7/exp/stan/nmr/lists/pp/user/cpXpdsd_2D.moha exp.
def. of mc cmd. after ze"
LBLAV, MCWRK
    "d0=d0orig + t1loop * in0 "
    "phval2 = (ph1loop % 4) * 90"
    MCWRK ip2 + phval2
# 76 "/opt/topspin3.5pl7/exp/stan/nmr/lists/pp/user/cpXpdsd_2D.moha"

;----- Relaxation & reset parameters -----

# 1 "mc_line 79 file /opt/topspin3.5pl7/exp/stan/nmr/lists/pp/user/cpXpdsd_2D.moha exp.
start label for mc cmd."
2 MCWRK * 2 do:f2
LBLF1, MCWRK * 2
LBLST1, MCWRK
    MCREST
# 80 "/opt/topspin3.5pl7/exp/stan/nmr/lists/pp/user/cpXpdsd_2D.moha"

    2u pl5:f1 pl2:f2
    2u fq=cnst10:f1
    2u fq=cnst20:f2
    2u rpp10
;----- 90 on H -----
# 87 "/opt/topspin3.5pl7/exp/stan/nmr/lists/pp/user/cpXpdsd_2D.moha"
    (p2 pl2 ph1):f2

;----- H/X CP -----

if (l31 == 1)

```

```
{
(p15 pl5 ph2):f1 (p15:sp0 ph0):f2
}
# 96 "/opt/topspin3.5pl7/exp/stan/nmr/lists/pp/user/cpXpdsd_2D.moha"
if (l31 == 2)
{
(p15:sp1 ph2):f1 (p15 pl6 ph0):f2
}

;----- F1 dimension & decoupling -----

; 2u fq=0:f1 ; This line should be uncommented if cnst10 is non zero value
; 1u pl12:f2
0.5u cpds2:f2
d0
# 108 "/opt/topspin3.5pl7/exp/stan/nmr/lists/pp/user/cpXpdsd_2D.moha"
;----- PDS mixing time -----
0.5u do:f2
(p1 pl1 ph3):f1

# 125 "/opt/topspin3.5pl7/exp/stan/nmr/lists/pp/user/cpXpdsd_2D.moha"
5m ;short z filter
0.5u cpds4:f2
4 d5
(p10 pl10 ph10^):f1
d5
lo to 4 times l1
0.5u do:f2
5m

# 136 "/opt/topspin3.5pl7/exp/stan/nmr/lists/pp/user/cpXpdsd_2D.moha"
(p1 pl1 ph4):f1

;----- acquisition with decoupling -----

1u pl12:f2
# 142 "/opt/topspin3.5pl7/exp/stan/nmr/lists/pp/user/cpXpdsd_2D.moha"
go=2 ph31 cpds2:f2
# 1 "mc_line 143 file /opt/topspin3.5pl7/exp/stan/nmr/lists/pp/user/cpXpdsd_2D.moha exp.
mc cmd. in line"
MCWRK do:f2 wr #0 if #0 zd
```

```

"ph1loop+=1"
  "d0=d0orig + t1loop * in0 "
  "phval2 = (ph1loop % 4) * 90"
  MCWRK ip2 + phval2
lo to LBLF1 times 2
MCWRK

"t1loop+=1"
  "d0=d0orig + t1loop * in0 "
  "phval2 = (ph1loop % 4) * 90"
  MCWRK ip2 + phval2
lo to LBLST1 times ST1CNT
MCWRK
"t1loop=0"
"ph1loop=0"
MCWRK rf #0
lo to LBLAV times tdav
# 145 "/opt/topspin3.5pl7/exp/stan/nmr/lists/pp/user/cpXpdsd_2D.moha"

;----- 2D increments & write data -----

; 10m wr #0 if #0 zd
; 1m id0
; 1m ip2
; lo to 2 times td1
HaltAcqu, 1m
exit
# 155 "/opt/topspin3.5pl7/exp/stan/nmr/lists/pp/user/cpXpdsd_2D.moha"
;----- Phase cycling -----

ph0 = 0
ph1 = 1 1 1 1 3 3 3 3
ph2 = 0 1 ;try 0 2 and ph31 of 0 0 2 2 2 2 0 0
ph3 = 1 2 3 4
ph4 = 0 2
ph10 = 2 0 2 0 0 2 0 2 1 3 1 3 3 1 3 1

ph31= 0 2 2 0 2 0 0 2
# 168 "/opt/topspin3.5pl7/exp/stan/nmr/lists/pp/user/cpXpdsd_2D.moha"
;old cycle
;ph0 = 0
;ph1 = 1 1 1 1 3 3 3 3
;ph2 = 0 2 ;try 0 2 and ph31 of 0 0 2 2 2 2 0 0
;ph3 = 1 1 3 3

```

```
-----  
;ph4 = 0 2  
;ph10 = 2 0 2 0 0 2 0 2 1 3 1 3 3 1 3 1  
  
;ph31= 0 0 2 2 2 2 0 0  
  
;old phase cycle  
;ph0 = 0  
;ph1 = 1 1 1 1 1 1 1 1 3 3 3 3 3 3 3 3  
;ph2 = 0  
;ph3 = 1 1 1 1 3 3 3 3  
;ph4 = 0 1 2 3  
;ph10 = 2 0 2 0 0 2 0 2 1 3 1 3 3 1 3 1  
;ph31= 0 1 2 3 2 3 0 1 2 3 0 1 0 1 2 3  
# 187 "/opt/topspin3.5pl7/exp/stan/nmr/lists/pp/user/cpXpdsd_2D.moha"  
; Old phase cycling  
;ph0 = 0  
;ph1 = 1 1 1 1 3 3 3 3  
;ph2 = 0  
;ph3 = 1  
;ph4 = 3 0 1 2  
;ph31= 0 1 2 3 2 3 0 1  
  
;=====  
; END Pulse program  
;=====
```

6.7 Pulse program for 2D NCA/NCO experiments

```
# 1 "/opt/topspin3.5pl7/exp/stan/nmr/lists/pp/user/zTEDOR.ride"  
;zTEDOR  
;  
;version: 2.0 TS3 / 7/14/2011  
;  
;transverse echo double resonance experiment  
;Tested 12/06 in jos1206 on AV III console  
;updated and tested JOS 07/14/2011  
;  
;Reference:  
;C.P. Jaroniec, C. Filip, and R.G. Griffin, JACS 124, 2002, 10728-10742  
;  
;Avance III version  
;parameters:  
;d1 : recycle delay
```

```

;d31 : =1s/cnst31, 1 rotor period, to check correct cnst31 value
;p2 : X 180 degree pulse
;p3 : 90 degree 1H pulse at p12
;p12 : proton hard pulse power
;p5 : 90 pulse on Y channel
;p12 : 180 deg. pulse on the Y channel
;p15 : contact pulse
;cnst31 : must be set to the spinning speed (in Hz).
;spnam0 : file name for variable amplitude CP
;p11 : to drive HP-X transmitter (CP power)
;p13 : Y rf-power for pi pulse
;p111 : X rf-power for pi pulse
;p112 : 1H power for decoupling if not 13
;p113 : 1H power for decoupling if not 12
;p114 : rf-power for z-filter use f_nutation= f_rotation for recoupling of protons to 13C fast
quenching of transverse magnetization
;sp0 : rf-power for proton contact pulse
;cpdprg2 : decoupling sequence for REDOR
;pcpd2 : decoupling pulse width
;cpdprg2 : decoupling during recoupling block us cw13 or lgcw
;FnMODE: use States-TPPI, States or TPPI
;ZGOPTNS : -DsmallSW for rotor synchronization for spectral width in F1 < sample rotation
rate
;
;I9 : fraction of rotation rate for t1 increment for choice of smallSW else multiple of rotor
frequency for larger SW
;ns : =n*16 =n*32 with td=phase cycle
;
;
;$CLASS=Solids
;$DIM=2D
;$TYPE=cross polarisation
;$SUBTYPE=TEDOR
;$COMMENT=heteronuclear correlation

"d25=0.25s/cnst31-1u"
"d26=0.25s/cnst31-(p12/2)" ; one-quarter rotor cycle ...
"d27=0.25s/cnst31-(p1)"
"d28=0.25s/cnst31-5u"
"d29=0.75s/cnst31-(p2/2)"
"d31=1s/cnst31"
define pulse tauz
"tauz=l8*1s/cnst31-p1"

```

```

# 1 "/opt/topspin3.5pl7/exp/stan/nmr/lists/pp/user/trigg.incl" 1
;$COMMENT=definition of external trigger output, conn l pin 1
;$CLASS=Solids INCL
;$OWNER=nmrstu

# 57 "/opt/topspin3.5pl7/exp/stan/nmr/lists/pp/user/zTEDOR.ride" 2

"d0=1s/(l9*cnst31)"
"acqt0=0"
define delay t1incr
# 63 "/opt/topspin3.5pl7/exp/stan/nmr/lists/pp/user/zTEDOR.ride"
"l0=0"

# 72 "/opt/topspin3.5pl7/exp/stan/nmr/lists/pp/user/zTEDOR.ride"
define delay tau
"tau=1s*(2*l9-1)/(l9*cnst31)"
"l10=1"
"l11=l10 %l9"
"d2=(1s*(2*l9-l11)/(l9*cnst31))-p1-p5"
"t1incr=1s/(l9*cnst31)"
"in0=t1incr"
"inf1=in0"

define delay mix
"mix=4*2*l1/cnst31"

# 1 "mc_line 84 file /opt/topspin3.5pl7/exp/stan/nmr/lists/pp/user/zTEDOR.ride exp. def.
part of mc cmd. before ze"
; dimension 2D; AQ_mode (F1) States-TPPI
define delay MCWRK
define delay MCREST
define loopcounter ST1CNT
"ST1CNT = td1 / 2"
"MCREST = 30m - 30m"
"MCWRK = 0.200000*30m"

    dccorr
# 84 "/opt/topspin3.5pl7/exp/stan/nmr/lists/pp/user/zTEDOR.ride"
1 ze
# 1 "mc_line 84 file /opt/topspin3.5pl7/exp/stan/nmr/lists/pp/user/zTEDOR.ride exp. def. of
mc cmd. after ze"

```

```
LBLAV, MCWRK
# 85 "/opt/topspin3.5pl7/exp/stan/nmr/lists/pp/user/zTEDOR.ride"
  t1incr
  tau
  mix
d2
# 1 "mc_line 89 file /opt/topspin3.5pl7/exp/stan/nmr/lists/pp/user/zTEDOR.ride exp. start
label for mc cmd."
2 MCWRK
LBLSTS1, MCWRK * 3
LBLF1, MCWRK
  MCREST
# 90 "/opt/topspin3.5pl7/exp/stan/nmr/lists/pp/user/zTEDOR.ride"
  d1 do:f2
# 92 "/opt/topspin3.5pl7/exp/stan/nmr/lists/pp/user/zTEDOR.ride"
  "I11=I10 %I9"
  "d2=1s*(2*I9-I11)/(I9*cnst31)"

  10u pl1:f1           ;set power level to drive HP amplifier
  10u pl2:f2           ;set decoupler power
  10u pl3:f3

# 1 "/opt/topspin3.5pl7/exp/stan/nmr/lists/pp/user/p15_prot.incl" 1
;p15_prot.incl

; Test the rf on-time and duty cycle
;protect against too long contact time
;Test the rf on-time and duty cycle
;$COMMENT=protect against too long contact time
;$CLASS=Solids INCL
;$OWNER=nmrstu
1m
if "p15<10.1m" goto Passp15
print "contact time exceeds 10msec limit!"
goto HaltAcqu
Passp15, 1m
# 98 "/opt/topspin3.5pl7/exp/stan/nmr/lists/pp/user/zTEDOR.ride" 2

          ;make sure p15 does not exceed 10 msec
          ;let supervisor change this pulseprogram if
          ;more is needed

# 104 "/opt/topspin3.5pl7/exp/stan/nmr/lists/pp/user/zTEDOR.ride"
```

```

# 1 "/opt/topspin3.5pl7/exp/stan/nmr/lists/pp/user/aq_prot.incl" 1
;aq_prot.incl
; Test the rf on-time and duty cycle
;protect against too long acquisition time
;$COMMENT=protect against too long acquisition time
;$CLASS=Solids INCL
;$OWNER=nmrstu
1m
if "aq<50.1m" goto Passaq
print "acquisition time exceeds 50m limit!"
goto HaltAcqu
Passaq, 1m

# 106 "/opt/topspin3.5pl7/exp/stan/nmr/lists/pp/user/zTEDOR.ride" 2

;allows max. 50 msec acquisition time, supervisor
;may change to max. 1s at less than 5 % duty cycle
;and reduced decoupling field

1m rpp8 ; reset phase list ph8 ...
1m rpp9
1m rpp10
1m rpp11
6u setnmr3l28 \n 4u setnmr3^28 ;additional trigger available on HP router
p3:f2 ph1 ;90 degree proton pulse
0.3u
(p15 ph2):f1 (p15:sp0 ph0):f2 ;cross-polarization
1u cpds2:f2
d25 pl11:f1 ; tppm decoupling at pl12 if synchronized with
TPPM use special decoupling sequence
5 d26 ; several F3 pulses
...
(p12 ph8^):f3 ; ... at intervals of ...
d26 ; ... one-half rotor cycle
d26
(p12 ph8^):f3 ; ... at intervals of ...
d26 ; F1 pulse
d26 ; several F3 pulses
...
(p12 ph8^):f3 ; ... at intervals of ...
d26 ; ... at intervals of ...
d26 ; ... one-half rotor
cycle
(p12 ph8^):f3 ; ... at intervals of ...

```

```

d26 ; F1 pulse
lo to 5 times l1
d29
(p2 ph6):f1 ; ... at intervals of ...
d29 ; Hahn echo refocussing pulse on F1
6 d26 ; several F3 pulses
...
(p12 ph9^):f3 ; ... at intervals of ...
d26 ; ... at intervals of ...
d26 ; ... one-half rotor
cycle
(p12 ph9^):f3 ; ... at intervals of ...
d26 ;
d26 ; several F3 pulses
...
(p12 ph9^):f3 ; ... at intervals of ...
d26 ; ... at intervals of ...
d26 ; ... one-half rotor
cycle
(p12 ph9^):f3 ; ... at intervals of ...
d26 ; F1 pulse
lo to 6 times l1
d27
(p1 ph6):f1 (1u do):f2 ; end of integer rotor period
(tauz pl14 ph19):f2 ;Z-filter integer rotor period
(p5 ph6):f3 ; begin rotor period at beginning of pulse
if "l0==1"{
  "d0=in0"
}
if "l0>0"{
d0 cpds3:f2
}
(p5 ph3):f3 (1u do):f2
d2 cpds2:f2 ;for rotor synchronization
(p1 pl11 ph6):f1 ; rotor period done at end of p1!
1u
d25 pl11:f1 ; tppm decoupling at pl12
7 d26 ; several F3 pulses
...
(p12 ph10^):f3 ; ... at intervals of ...
d26 ; ... one-half rotor cycle
d26
(p12 ph10^):f3 ; ... at intervals of ...
d26

```

```

d26 ; several F3 pulses
...
(p12 ph10^):f3 ; ... at intervals of ...
d26 ; ... one-half rotor cycle
d26
(p12 ph10^):f3 ; ... at intervals of ...
d26
lo to 7 times l1
d29
(p2 ph6):f1 ; Hahn echo refocussing pulse
d29
8 d26 ; several F3 pulses
...
(p12 ph11^):f3 ; ... at intervals of ...
d26 ; ... one-half rotor cycle
d26
(p12 ph11^):f3 ; ... at intervals of ...
d26
d26 ; several F3 pulses
...
(p12 ph11^):f3 ; ... at intervals of ...
d26 ; ... one-half rotor cycle
d26
(p12 ph11^):f3 ; ... at intervals of ...
d26
lo to 8 times l1
d27 ; Hahn echo occurs about now
(p1 ph4):f1 (1u do):f2
(tauz pl14 ph19):f2
(p1 ph5):f1 (1u cpds3):f2
# 199 "/opt/topspin3.5pl7/exp/stan/nmr/lists/pp/user/zTEDOR.ride"
go=2 ph31
1m do:f2
# 1 "mc_line 201 file /opt/topspin3.5pl7/exp/stan/nmr/lists/pp/user/zTEDOR.ride exp. mc
cmd. in line"
MCWRK wr #0 if #0 zd ip3
lo to LBLSTS1 times 2
MCWRK id0 MCWRK iu10 MCWRK iu0
lo to LBLF1 times ST1CNT
MCWRK rf #0
lo to LBLAV times tdav
# 202 "/opt/topspin3.5pl7/exp/stan/nmr/lists/pp/user/zTEDOR.ride"

HaltAcqu, 1m

```

exit

```
# 207 "/opt/topspin3.5pl7/exp/stan/nmr/lists/pp/user/zTEDOR.ride"
ph1= 193*16 {3}*16
ph0= 0
ph2= 0
ph3= 0 2
ph4= 1 1 3 3
ph5= 0 0 0 0 1 1 1 1 2 2 2 2 3 3 3 3
ph6= 0
ph8= 0 1 0 1 1 0 1 0 2 3 2 3 3 2 3 2      ;xy16
ph9= 0 1 0 1 1 0 1 0 2 3 2 3 3 2 3 2
ph10= 0 1 0 1 1 0 1 0 2 3 2 3 3 2 3 2
ph11= 0 1 0 1 1 0 1 0 2 3 2 3 3 2 3 2
ph19= 0
ph31= 3 1 1 3 0 2 2 0
      1 3 3 1 2 0 0 2
      1 3 3 1 2 0 0 2
      3 1 1 3 0 2 2 0
```

6.8 Pulse program for 3D NCACX/NCOCX experiments

```
# 1 "/root/.topspin-BladeEpu/local_acqu/ppDirs/zTEDORcc2.land"
# 1 "<built-in>"
# 1 "<command-line>"
# 1 "/root/.topspin-BladeEpu/local_acqu/ppDirs/zTEDORcc2.land"
;zTEDOR
;
;version: 2.0 TS3 / 7/14/2011
;
;transverse echo double resonance experiment
;Tested 12/06 in jos1206 on AV III console
;updated and tested JOS 07/14/2011
;
;Reference:
;C.P. Jaroniec, C. Filip, and R.G. Griffin, JACS 124, 2002, 10728-10742
;
;Avance III version
;parameters:
;d1 : recycle delay
;d31 : =1s/cnst31, 1 rotor period, to check correct cnst31 value
;p2 : X 180 degree pulse
```

```
;p3 : 90 degree 1H pulse at p12
;p12 : proton hard pulse power
;p5 : 90 pulse on Y channel
;p6 : RDFR pi/2 pulse
;p12 : 180 deg. pulse on the Y channel
;p15 : contact pulse
;cnst31 : must be set to the spinning speed (in Hz).
;spnam0 : file name for variable amplitude CP
;p11 : to drive HP-X transmitter (CP power)
;p13 : Y rf-power for pi pulse
;p16 : carbon RFDR power level at p6
;p111 : X rf-power for pi pulse
;p112 : 1H power for decoupling if not 13
;p113 : 1H power for decoupling if not 12
;p114 :DARR field
;d29 : PDSM time
;p114 : rf-power for z-filter use f_nutation= f_rotation for recoupling of protons to 13C fast
quenching of transverse magnetization
;sp0 : rf-power for proton contact pulse
;cpdprg2 : decoupling sequence for REDOR
;pcpd2 : decoupling pulse width
;cpdprg2 : decoupling during recoupling block us cw13 or lgcw
;FnMODE: use States-TPPI, States or TPPI
;ZGOPTNS : -DsmallSW for rotor synchronization for spectral width in F1 < sample rotation
rate
;
;I9 : fraction of rotation rate for t1 increment for choice of smallSW else multiple of rotor
frequency for larger SW
;I2 : RFDR loop
;I1 : TEDOR loop
;I8 : z filter control
;ns : =n*16 =n*32 with td=phase cycle
;
;
;$CLASS=Solids
;$DIM=2D
;$TYPE=cross polarisation
;$SUBTYPE=TEDOR
;$COMMENT=heteronuclear correlation

"d25=0.25s/cnst31-1u"
"d26=0.25s/cnst31-(p12/2)" ; one-quarter rotor cycle ...
"d27=0.25s/cnst31-(p1)"
```

```

"d28=0.25s/cnst31-5u"
"d29=0.75s/cnst31-(p2/2)"
"d31=1s/cnst31"
define pulse tauz
"tauz=18*1s/cnst31-p1"
# 1 "/root/.topspin-BladeEpu/local_acqu/ppDirs/trigg.incl" 1
;trigg.incl
;version (16/09/08)
;
;$COMMENT=definition of external trigger output, conn l pin 1
;$CLASS=Solids INCL

# 13 "/root/.topspin-BladeEpu/local_acqu/ppDirs/trigg.incl"
;$ld: 6u setrtp0l6 \n          4u setrtp0^6.incl,v 1.8 2016/09/08 13:06:12 ber Exp $
# 65 "/root/.topspin-BladeEpu/local_acqu/ppDirs/zTEDORcc2.land" 2

"d0=0"
"acqt0=0"
define delay t1incr

"l0=0"
#ifdef smallSW
define delay tau
"tau=1s*19/cnst31"
"d2=1s/cnst31-p5-p1"
"t1incr=(1s*19)/(cnst31)"
"in0=t1incr"
"inf1=in0"
#else
;define delay tau
;"tau=1s*(2*19-1)/(19*cnst31)"
;"l10=1"
;"l11=l10 %19"
;"d2=(1s*(2*19-l11)/(19*cnst31))-p1-p5"
;"t1incr=1s/(19*cnst31)"
;"in0=t1incr"
;"inf1=in0"
#endif
"in10=inf2"
"d10=0"
define delay mix
"mix=4*2*11/cnst31"
# 94 "/root/.topspin-BladeEpu/local_acqu/ppDirs/zTEDORcc2.land"

```

```

define delay tau2
"tau2=0.5s/cnst31-p6"
;"d31=1s/cnst31" ;allow protection for misset l31
define delay mixrfrd
"mixrfrd=l2*d31"

# 1 "mc_line 101 file /root/.topspin-BladeEpu/local_acqu/ppDirs/zTEDORcc2.land exp. def.
part of mc cmd. before ze"
; dimension 3D; AQ_mode (F2) States-TPPI (F1) States-TPPI
define delay MCWRK
define delay MCREST
define delay d0orig
"d0orig=d0"
define delay d10orig
"d10orig=d10"
define loopcounter t2loop
"t2loop=0"
define loopcounter t1loop
"t1loop=0"
define loopcounter ph1loop
"ph1loop=0"
define loopcounter ph2loop
"ph2loop=0"
define loopcounter ST1CNT
"ST1CNT = trunc(td1 / 2)"
define loopcounter ST2CNT
"ST2CNT = trunc(td2 / 2)"
"MCREST = 30m - 30m"
"MCWRK = 0.071429*30m"
# 101 "/root/.topspin-BladeEpu/local_acqu/ppDirs/zTEDORcc2.land"
1 ze
# 1 "mc_line 101 file /root/.topspin-BladeEpu/local_acqu/ppDirs/zTEDORcc2.land exp. def.
of mc cmd. after ze"
LBLAV, MCWRK
    "d0=d0orig + t1loop * in0 "
    "phval3 = (ph1loop % 4) * -90"
    MCWRK ip3 + phval3
    "d10=d10orig + t2loop * in10 "
    "phval5 = (ph2loop % 4) * 90"
    MCWRK ip5 + phval5
# 102 "/root/.topspin-BladeEpu/local_acqu/ppDirs/zTEDORcc2.land"
t1incr
tau

```

```

mix
mixrfd
    tauz
d2
# 1 "mc_line 108 file /root/.topspin-BladeEpu/local_acqu/ppDirs/zTEDORcc2.land exp. start
label for mc cmd."
2 MCWRK * 3
LBLF2, MCWRK * 3
LBLST2, MCWRK * 4
LBLF1, MCWRK * 3
LBLST1, MCWRK
MCREST
# 109 "/root/.topspin-BladeEpu/local_acqu/ppDirs/zTEDORcc2.land"
d1 do:f2
;#ifndef smallSW
; "I11=I10 %I9"
; "d2=1s*(2*I9-I11)/(I9*cnst31)"
;#endif
    10u pl1:f1           ;set power level to drive HP amplifier
    10u pl2:f2           ;set decoupler power
    10u pl3:f3
# 1 "/root/.topspin-BladeEpu/local_acqu/ppDirs/p15_prot.incl" 1
;p15_prot.incl
;avance-version (13/01/29)
;Test the rf on-time and duty cycle
;protect against too long contact time
;Test the rf on-time and duty cycle
;
;$CLASS=Solids INCL
;$COMMENT=protect against too long contact time

1m
if "p15 < 10.1m" goto Passp15
2u
print "contact time exceeds 10msec limit!"
goto HaltAcqu
Passp15, 1m
# 20 "/root/.topspin-BladeEpu/local_acqu/ppDirs/p15_prot.incl"
;$Id: p15_prot.incl,v 1.8 2013/01/29 15:40:14 ber Exp $
# 118 "/root/.topspin-BladeEpu/local_acqu/ppDirs/zTEDORcc2.land" 2
    ;make sure p15 does not exceed 10 msec
    ;let supervisor change this pulseprogram if
    ;more is needed

```

```

# 1 "/root/.topspin-BladeEpu/local_acqu/ppDirs/aq_prot.incl" 1
;aq_prot.incl
;avance-version (13/01/28)
;Test the rf on-time and duty cycle
;protect against too long acquisition time

;$CLASS=Solids INCL
;$COMMENT=protect against too long acquisition time

1m
if "aq < 50.1m" goto Passaq
2u
print "acquisition time exceeds 50m limit!"
goto HaltAcqu
Passaq, 1m
# 16 "/root/.topspin-BladeEpu/local_acqu/ppDirs/aq_prot.incl"
;$Id: aq_prot.incl,v 1.8 2013/01/28 17:39:02 ber Exp $
# 126 "/root/.topspin-BladeEpu/local_acqu/ppDirs/zTEDORcc2.land" 2
;allows max. 50 msec acquisition time, supervisor
;may change to max. 1s at less than 5 % duty cycle
;and reduced decoupling field

1m rpp8 ; reset phase list ph8 ...
1m rpp9
1m rpp10
1m rpp11
6u setrtp0l6 \n 4u setrtp0^6 ;additional trigger available on
HP router
p3:f2 ph1 ;90 degree proton pulse
0.3u
(p15 ph2):f1 (p15:sp0 ph0):f2 ;cross-polarization
1u cpds2:f2
d25 pl11:f1 ; tppm decoupling at pl12 if synchronized with
TPPM use special decoupling sequence
5 d26 ; several F3 pulses
...
(p12 ph8^):f3 ; ... at intervals of ...
d26 ; ... one-half rotor cycle
d26
(p12 ph8^):f3 ; ... at intervals of ...
d26 ; F1 pulse

```

```

d26 ; several F3 pulses
...
(p12 ph8^):f3 ; ... at intervals of ...
d26 ; ... at intervals of ...
d26 ; ... one-half rotor
cycle
(p12 ph8^):f3 ; ... at intervals of ...
d26 ; F1 pulse
lo to 5 times l1
d29
(p2 ph6):f1 ; ... at intervals of ...
d29 ; Hahn echo refocussing pulse on F1
6 d26 ; several F3 pulses
...
(p12 ph9^):f3 ; ... at intervals of ...
d26 ; ... at intervals of ...
d26 ; ... one-half rotor
cycle
(p12 ph9^):f3 ; ... at intervals of ...
d26 ;
d26 ; several F3 pulses
...
(p12 ph9^):f3 ; ... at intervals of ...
d26 ; ... at intervals of ...
d26 ; ... one-half rotor
cycle
(p12 ph9^):f3 ; ... at intervals of ...
d26 ; F1 pulse
lo to 6 times l1
d27
(p1 ph6):f1 (1u do):f2 ; end of integer rotor period
(taus pl14 ph19):f2 ;Z-filter integer rotor period
(ralign (p5 ph6):f3 (0.5u cpds3):f2 ) ; begin rotor period at beginning of pulse

;if "l0==1"{
; "d0=in0"
; }
;if "l0>0"{
d0 ;cpds3:f2
; }
(p5 ph3):f3 (1u do):f2
d2 cpds2:f2 ;for rotor synchronization
(p1 pl11 ph6):f1 ; rotor period done at end of p1!
1u

```

d25 pl11:f1 ; tppm decoupling at pl12
 7 d26 ; several F3 pulses
 ...
 (p12 ph10[^]):f3 ; ... at intervals of ...
 d26 ; ... one-half rotor cycle
 d26
 (p12 ph10[^]):f3 ; ... at intervals of ...
 d26
 d26 ; several F3 pulses
 ...
 (p12 ph10[^]):f3 ; ... at intervals of ...
 d26 ; ... one-half rotor cycle
 d26
 (p12 ph10[^]):f3 ; ... at intervals of ...
 d26
 lo to 7 times l1
 d29
 (p2 ph6):f1 ; Hahn echo refocussing pulse
 d29
 8 d26 ; several F3 pulses
 ...
 (p12 ph11[^]):f3 ; ... at intervals of ...
 d26 ; ... one-half rotor cycle
 d26
 (p12 ph11[^]):f3 ; ... at intervals of ...
 d26
 d26 ; several F3 pulses
 ...
 (p12 ph11[^]):f3 ; ... at intervals of ...
 d26 ; ... one-half rotor cycle
 d26
 (p12 ph11[^]):f3 ; ... at intervals of ...
 d26
 lo to 8 times l1
 d27 ; Hahn echo occurs about now
 (p1 ph4):f1 (1u do):f2
 (tauz pl14 ph19):f2
 (p1 ph5):f1 (1u cpds3):f2
 ;carbon evolution
 d10
 (p1 ph7):f1 (0.5u do):f2
 (p29 pl14):f2
 3m
 1u cpds2:f2

```

9 tau2 ;mixing time with Gullion sequence
(p6*2 pl6 ph18^):f1
tau2 pl11:f1
lo to 9 times l2
1u do:f2
3m
(p1 ph0):f1 (1u cpds3):f2

go=2 ph31
1m do:f2
# 1 "mc_line 234 file /root/.topspin-BladeEpu/local_acqu/ppDirs/zTEDORcc2.land exp. mc
cmd. in line"
MCWRK wr #0 if #0 zd

"ph2loop+=1 "
"d0=d0orig + t1loop * in0 "
"phval3 = (ph1loop % 4) * -90"
MCWRK ip3 + phval3
"d10=d10orig + t2loop * in10 "
"phval5 = (ph2loop % 4) * 90"
MCWRK ip5 + phval5
lo to LBLF2 times 2
MCWRK

"t2loop+=1 "
"d0=d0orig + t1loop * in0 "
"phval3 = (ph1loop % 4) * -90"
MCWRK ip3 + phval3
"d10=d10orig + t2loop * in10 "
"phval5 = (ph2loop % 4) * 90"
MCWRK ip5 + phval5
lo to LBLST2 times ST2CNT
MCWRK
"t2loop=0"
"ph2loop=0"
MCWRK

"ph1loop+=1 "
"d0=d0orig + t1loop * in0 "
"phval3 = (ph1loop % 4) * -90"
MCWRK ip3 + phval3
"d10=d10orig + t2loop * in10 "
"phval5 = (ph2loop % 4) * 90"
MCWRK ip5 + phval5

```

lo to LBLF1 times 2
MCWRK

```
"t1loop+=1"
  "d0=d0orig + t1loop * in0 "
  "phval3 = (ph1loop % 4) * -90"
  MCWRK ip3 + phval3
  "d10=d10orig + t2loop * in10 "
  "phval5 = (ph2loop % 4) * 90"
  MCWRK ip5 + phval5
```

lo to LBLST1 times ST1CNT
MCWRK

```
"t1loop=0"
"ph1loop=0"
MCWRK rf #0
```

lo to LBLAV times tdav

```
# 237 "/root/.topspin-BladeEpu/local_acqu/ppDirs/zTEDORcc2.land"
# 239 "/root/.topspin-BladeEpu/local_acqu/ppDirs/zTEDORcc2.land"
HaltAcqu, 1m
exit
```

```
ph1= 1 1 1 1 3 3 3 3
ph0= 0
ph2= 0
ph3= 0 2
ph4= 1 1 3 3
ph5= 0 0 0 0 ;1 1 1 1 2 2 2 2 3 3 3 3
ph6= 0
ph7= 0 0 0 0 0 0 0 2 2 2 2 2 2 2 ;extended cycle
# 252 "/root/.topspin-BladeEpu/local_acqu/ppDirs/zTEDORcc2.land"
ph8= 0 1 0 1 1 0 1 0 2 3 2 3 3 2 3 2 ;xy16
ph9= 0 1 0 1 1 0 1 0 2 3 2 3 3 2 3 2
ph10= 0 1 0 1 1 0 1 0 2 3 2 3 3 2 3 2
ph11= 0 1 0 1 1 0 1 0 2 3 2 3 3 2 3 2
ph18= 0 1 0 1 1 0 1 0 2 3 2 3 3 2 3 2

ph19= 0
ph31= 1 3 3 1 3 1 1 3
      3 1 1 3 1 3 3 1
```

6.9 Pulse program for hCHHC experiment

```
# 1 "/opt/topspin3.5pl6/exp/stan/nmr/lists/pp/hChhC.cp"
;hChhC.cp

;version: 1.0/ TS3.2 /2013/06/17

;written for BioToolkit: JOS WTF 10.5.2013
;double-checked: VEDA SEWE July 2013
# 8 "/opt/topspin3.5pl6/exp/stan/nmr/lists/pp/hChhC.cp"
;2D long-range correlation experiment via Proton-Proton-through space mixing
;zero-quantum version

;Avance II / AVIII version
;Parameters:
;p1      : pulse width for C 90 at pl1
;p3      : pulse width for H 90 at pl2
;p15     : pulse width for first CP (HC, long: 500-2000 us)
;p21     : pulse width for N 90 at pl21
;p22     : pulse width for N 180 at pl21
;p44     : pulse width for second CP (CH, short: <500 us)
;p48     : pulse width for third CP (HC, short: <500 us)
;p11     : C pulse power
;p12     : H pulse power
;p112    : H dec power
;p121    : N pulse power
;sp40    : H HC CP power
;sp41    : C HC CP power
;sp44    : H power for second CP (CH)
;sp45    : C power for second CP (CH)
;sp48    : H power for third CP (HC)
;sp49    : C power for third CP (HC)
;d0      : incremented delay (t1)
;d1      : recycle delay; 1 to 5 times T1
;d9      : HH mixing time (short (less than 750 us); 300 us ~ 6 Angstroms)
;d30     : extra time for constant duty cycle
;pcpd2   : pulse length in decoupling sequence
;cpdprg2 : spinal64, swftppm, tppm etc. decoupling program
;spnam40 : H ramp use e.g. ramp.10070 for variable amplitude CP
;spnam41 : C ramp use e.g. square.100 for square pulse CP
;spnam44 : H ramp use e.g. ramp.10070 for variable amplitude CP
;spnam45 : C ramp use e.g. square.100 for square pulse CP
;spnam48 : H ramp use e.g. ramp.10070 for variable amplitude CP
;spnam49 : C ramp use e.g. square.100 for square pulse CP
;cnst30  : expected td1 for use in constant duty cycle (CDC)
;cnst31  : MAS rotation rate in Hz
```

```
-----

;inf1: 1/SW(C) = 2 * DW(C)
;in0 : = inf1
;in30: = inf1
;l0 : loopcounter for F1
;l1 : loopcounter for mixing time
;ZGOPTNS : -DCDC : for constant duty cycle
;      -DDP : direct C excitation
;      -DTC : probe in triple channel mode
;              or blank
;FnMODE: TPPI, States or States-TPPI
;ns: MIN. 4 (full:16)

# 57 "/opt/topspin3.5pl6/exp/stan/nmr/lists/pp/hChhC.cp"
#####
;#                #
;# CHHC                #
;# Lange, A.; Becker, S.; Seidel, K.; Pongs, O.; #
;# and Baldus, M. Angw. Chem. 2005, 44, 2089-92 #
;# Lange, A.; Seidel, K.; Verdier, L.; Luca, S.; #
;# and Baldus, M., JACS 2003, 125, 12640-48 #
;# Lange, A.; Luca, S.; and Baldus, M.; #
;# JACS 2002, 124, 9704-5 #
;#                #
#####

;$COMMENT=Transverse Proton Mixing
;$CLASS=BioSolids
;$DIM=2D
;$TYPE=Homonuclear
;$SUBTYPE=ZQ mixing
# 77 "/opt/topspin3.5pl6/exp/stan/nmr/lists/pp/hChhC.cp"
prosol relations=<biosolCHN>

# 1 "/opt/topspin3.5pl6/exp/stan/nmr/lists/pp/CHN_defs.incl" 1
;Define Frequencies and other common variables
;Use with Carbon (X-channel) Detection

# 5 "/opt/topspin3.5pl6/exp/stan/nmr/lists/pp/CHN_defs.incl"
;$COMMENT=Frequency and Timing definitions
;$CLASS=BioSolids INCL
;$DIM=
;$TYPE=Definitions
;$SUBTYPE=Carbon Detect
```

```
# 18 "/opt/topspin3.5pl6/exp/stan/nmr/lists/pp/CHN_defs.incl"
;$Id: CHN_defs.incl,v 1.1.2.2 2013/08/29 14:03:53 ber Exp $
# 79 "/opt/topspin3.5pl6/exp/stan/nmr/lists/pp/hChhC.cp" 2

                ; defines which channel corresponds to which nucleus
# 1 "/opt/topspin3.5pl6/exp/stan/nmr/lists/pp/trigg.incl" 1
;version (13/08/19)

;$COMMENT=definition of external trigger output, conn l pin 1
;$CLASS=Solids INCL
# 12 "/opt/topspin3.5pl6/exp/stan/nmr/lists/pp/trigg.incl"
;$Id: 6u setnmr3l28 \n 4u setnmr3^28.incl,v 1.6.2.1 2013/08/29 14:03:54 ber Exp $
# 81 "/opt/topspin3.5pl6/exp/stan/nmr/lists/pp/hChhC.cp" 2

                ; definition of external trigger output

# 1 "/opt/topspin3.5pl6/exp/stan/nmr/lists/pp/TauR_def.incl" 1
;TauR_def.incl
;version (13/08/21)
;Define different rotor period-dependent delays
# 6 "/opt/topspin3.5pl6/exp/stan/nmr/lists/pp/TauR_def.incl"
;$COMMENT=TauR definitions
;$CLASS=BioSolids INCL
;$TYPE=Rotor sync

;TauR : time for one rotor period
;TauRm2 : time for one rotor period - 2us
;TauRm4 : time for one rotor period - 4us
# 15 "/opt/topspin3.5pl6/exp/stan/nmr/lists/pp/TauR_def.incl"
;cnst31 : MAS rate in Hz

define delay TauR
  "TauR=1s/cnst31"

define delay TauRm2
  "TauRm2=1s/cnst31 - 2u"

define delay TauRm4
  "TauRm4=1s/cnst31 - 4u"
# 29 "/opt/topspin3.5pl6/exp/stan/nmr/lists/pp/TauR_def.incl"
```

```

;$Id: TauR_def.incl,v 1.1.2.2 2013/08/29 14:03:53 ber Exp $
# 84 "/opt/topspin3.5pl6/exp/stan/nmr/lists/pp/hChhC.cp" 2

        ; definition of rotor period dependent delays

# 88 "/opt/topspin3.5pl6/exp/stan/nmr/lists/pp/hChhC.cp"
;#####
;#      Define Mixing Parameters          #
;#####

"l1=d9/TauR"                ; TauR = time of one rotor period
define delay mixing
"mixing=(l1*TauR)"          ;mixing = d9

"acqt0=-1u"
# 98 "/opt/topspin3.5pl6/exp/stan/nmr/lists/pp/hChhC.cp"
"in0=inf1"                  ;#####
"d0=1u"                     ;# t1_init => 0, 0 #
"in30=inf1"                 ;#####
"l0=0"

define delay ONTIME        ;#####
define loopcounter T1evo   ;# Power Deposition Calcs #

# 110 "/opt/topspin3.5pl6/exp/stan/nmr/lists/pp/hChhC.cp"
;#####
;$EXTERN                    ;# python insertion point #
;#####

# 1 "mc_line 114 file /opt/topspin3.5pl6/exp/stan/nmr/lists/pp/hChhC.cp exp. def. part of
mc cmd. before ze"
; dimension 2D; AQ_mode (F1) States-TPPI
define delay MCWRK
define delay MCREST
define delay d0orig
"d0orig=d0"
define delay d30orig
"d30orig=d30"
define loopcounter l0orig
"l0orig=l0"
define loopcounter t1loop
"t1loop=0"
define loopcounter ph1loop
"ph1loop=0"

```

```

define loopcounter ST1CNT
"ST1CNT = td1 / 2"
"MCREST = 30m - 30m"
"MCWRK = 0.200000*30m"

    dccorr
# 114 "/opt/topspin3.5pl6/exp/stan/nmr/lists/pp/hChhC.cp"
Prepare, ze
# 1 "mc_line 114 file /opt/topspin3.5pl6/exp/stan/nmr/lists/pp/hChhC.cp exp. def. of mc
cmd. after ze"
LBLAV, MCWRK
    "d0=d0orig + t1loop * in0 "
    "d30=d30orig - t1loop * in30 "
    "phval2 = (ph1loop % 4) * 90"
    MCWRK ip2 + phval2
    "l0 = l0orig + t1loop * 1"

# 115 "/opt/topspin3.5pl6/exp/stan/nmr/lists/pp/hChhC.cp"

"d30=d30/2"
# 118 "/opt/topspin3.5pl6/exp/stan/nmr/lists/pp/hChhC.cp"
"ONTIME=aq+d0+d30+p15+p44+p48"

#####
;#          Protections: Pre-Check          #
#####

# 1 "/opt/topspin3.5pl6/exp/stan/nmr/lists/pp/TauR_prot.incl" 1
;TauR_prot.incl
# 3 "/opt/topspin3.5pl6/exp/stan/nmr/lists/pp/TauR_prot.incl"
; Test that the MAS rate is set
; 400 us TauR is allowed (2.5kHz spinning)

;$COMMENT=Protection for MAS not set
;$CLASS=Solids PROT

# 10 "/opt/topspin3.5pl6/exp/stan/nmr/lists/pp/TauR_prot.incl"
if "TauR<400.1u" goto PassTauR
1u
print "Spinning frequency (cnst31) not set, or too low"
goto HaltAcqu
PassTauR, 1m

```

```
# 18 "/opt/topspin3.5pl6/exp/stan/nmr/lists/pp/TauR_prot.incl"
;$Id: TauR_prot.incl,v 1.1.2.2 2013/08/29 14:03:53 ber Exp $
# 124 "/opt/topspin3.5pl6/exp/stan/nmr/lists/pp/hChhC.cp" 2

                ;min. spinning 2.5 kHz
# 1 "/opt/topspin3.5pl6/exp/stan/nmr/lists/pp/acq_prot.incl" 1
;aq_prot.incl

; Test the rf on-time during Aquisition (aq)
; 50ms is allowed
# 6 "/opt/topspin3.5pl6/exp/stan/nmr/lists/pp/acq_prot.incl"
;$COMMENT=Protection against long acquisition time
;$CLASS=Solids PROT

if "aq<50.1m" goto Passaq
1u
print "Acquisition time exceeds 50 ms limit!"
goto HaltAcqu
Passaq, 1m
# 18 "/opt/topspin3.5pl6/exp/stan/nmr/lists/pp/acq_prot.incl"
;$Id: acq_prot.incl,v 1.1.2.2 2013/08/29 14:03:54 ber Exp $
# 126 "/opt/topspin3.5pl6/exp/stan/nmr/lists/pp/hChhC.cp" 2

                ;Max. 50 ms acquisition time
# 1 "/opt/topspin3.5pl6/exp/stan/nmr/lists/pp/HHmix_prot.incl" 1
;f2-f2 mixing protection file

; Test the rf on-time for the HH-mixing in CHHC/NHHC (d9)
; more than 750 us are inefficient
# 6 "/opt/topspin3.5pl6/exp/stan/nmr/lists/pp/HHmix_prot.incl"
;$COMMENT=Protection against long f2-f2 mixing time
;$CLASS=BioSolids PROT

if "d9<500.1u" goto PassdHH
1u
print "Mixing time d9 exceeds 750 us limit!"
goto HaltAcqu
PassdHH, 1m
# 18 "/opt/topspin3.5pl6/exp/stan/nmr/lists/pp/HHmix_prot.incl"
;$Id: HHmix_prot.incl,v 1.1.2.2 2013/08/29 14:03:53 ber Exp $
# 128 "/opt/topspin3.5pl6/exp/stan/nmr/lists/pp/hChhC.cp" 2
```

```

; d9 max. 750 us
# 1 "/opt/topspin3.5pl6/exp/stan/nmr/lists/pp/p15bio_prot.incl" 1
;p15_prot.incl

; Test the rf on-time for HC CP
; 10ms is maximum
# 6 "/opt/topspin3.5pl6/exp/stan/nmr/lists/pp/p15bio_prot.incl"
;$COMMENT=Protection against long HC CP time
;$CLASS=BioSolids PROT

if "p15<10.1m" goto Passp15
1u
print "HC CP time p15 exceeds 10 ms limit!"
goto HaltAcqu
Passp15, 1m
# 18 "/opt/topspin3.5pl6/exp/stan/nmr/lists/pp/p15bio_prot.incl"
;$Id: p15bio_prot.incl,v 1.1.2.2 2013/08/29 14:03:54 ber Exp $
# 130 "/opt/topspin3.5pl6/exp/stan/nmr/lists/pp/hChhC.cp" 2

; p15 max. 10 ms
# 1 "/opt/topspin3.5pl6/exp/stan/nmr/lists/pp/p44bio_prot.incl" 1
;p44bio_prot.incl

; Test the rf on-time for the second CP in an hChhC.cp
; 10ms is maximum
# 6 "/opt/topspin3.5pl6/exp/stan/nmr/lists/pp/p44bio_prot.incl"
;$COMMENT=Protection against long CP time
;$CLASS=BioSolids PROT

if "p44<10.1m" goto Passp44
1u
print "Second CP time p44 exceeds 10 msec limit!"
goto HaltAcqu
Passp44, 1m
# 18 "/opt/topspin3.5pl6/exp/stan/nmr/lists/pp/p44bio_prot.incl"
;$Id: p44bio_prot.incl,v 1.1.2.2 2013/08/29 14:03:54 ber Exp $
# 132 "/opt/topspin3.5pl6/exp/stan/nmr/lists/pp/hChhC.cp" 2

; p44 max. 10 ms
# 1 "/opt/topspin3.5pl6/exp/stan/nmr/lists/pp/p48bio_prot.incl" 1
;p48bio_prot.incl
```

```
-----

; Test the rf on-time for the third CP in an hXhhC.cp
; 10ms is maximum
# 6 "/opt/topspin3.5pl6/exp/stan/nmr/lists/pp/p48bio_prot.incl"
;$COMMENT=Protection against long CP time
;$CLASS=BioSolids PROT

if "p48<10.1m" goto Passp48
1u
print "Third CP time p48 exceeds 10 msec limit!"
goto HaltAcqu
Passp48, 1m
# 18 "/opt/topspin3.5pl6/exp/stan/nmr/lists/pp/p48bio_prot.incl"
;$ld: p48bio_prot.incl,v 1.1.2.2 2013/08/29 14:03:54 ber Exp $
# 134 "/opt/topspin3.5pl6/exp/stan/nmr/lists/pp/hChhC.cp" 2

                ;p48 max. 10 ms
# 1 "/opt/topspin3.5pl6/exp/stan/nmr/lists/pp/t1_prot.incl" 1
;t1_prot.incl

; List of Protections for t1 evolution
# 5 "/opt/topspin3.5pl6/exp/stan/nmr/lists/pp/t1_prot.incl"
;$COMMENT=t1 Protections
;$CLASS=BioSolids INCL

;#####
;# Protections for #
;# t1 evolution #
;#####
# 15 "/opt/topspin3.5pl6/exp/stan/nmr/lists/pp/t1_prot.incl"
if "d30<25m" goto Passd30
1u
print "final t1 evolution (d30) too large. Reduce inf1, td1, or cnst30"
goto HaltAcqu
Passd30, 1m

if "d0<25m" goto PrePassd0
1u
print "initial t1 evolution (d0) too large. Reduce inf1"
goto HaltAcqu
PrePassd0, 1m

# 29 "/opt/topspin3.5pl6/exp/stan/nmr/lists/pp/t1_prot.incl"
```

```
-----
;$Id: t1_prot.incl,v 1.1.2.2 2013/08/29 14:03:54 ber Exp $
# 136 "/opt/topspin3.5pl6/exp/stan/nmr/lists/pp/hChhC.cp" 2

                ;check t1 evolution time
# 1 "/opt/topspin3.5pl6/exp/stan/nmr/lists/pp/ONTIME_prot.incl" 1
;OnTime_prot.incl

; Check the total RF on-time
; 150ms is maximum
# 6 "/opt/topspin3.5pl6/exp/stan/nmr/lists/pp/ONTIME_prot.incl"
;$COMMENT=Protection against long decoupling time
;$CLASS=BioSolids PROT

if "ONTIME<150ms" goto PassONTIME
1u
print "The total RF ON-time exceeds 150 ms"
goto HaltAcqu
PassONTIME, 1m
# 18 "/opt/topspin3.5pl6/exp/stan/nmr/lists/pp/ONTIME_prot.incl"
;$Id: ONTIME_prot.incl,v 1.1.2.2 2013/08/29 14:03:53 ber Exp $
# 138 "/opt/topspin3.5pl6/exp/stan/nmr/lists/pp/hChhC.cp" 2

                ;total RF deposition restriction

#####
;#      Start of Active Pulse Program      #
#####
# 1 "mc_line 145 file /opt/topspin3.5pl6/exp/stan/nmr/lists/pp/hChhC.cp exp. start label for
mc cmd."
Start, MCWRK * 2 do:f2
LBLF1, MCWRK * 2
LBLST1, MCWRK
MCREST
# 146 "/opt/topspin3.5pl6/exp/stan/nmr/lists/pp/hChhC.cp"
# 146 "/opt/topspin3.5pl6/exp/stan/nmr/lists/pp/hChhC.cp"
d1

6u setnmr3|28 \n 4u setnmr3^28
1u fq=0.0:f2                ;set 1H on resonance

#####
;#      Cross/Direct Polarization      #
#####
```

```
-----

# 158 "/opt/topspin3.5pl6/exp/stan/nmr/lists/pp/hChhC.cp"
(p3 pl2 ph1):f2
(p15:sp41 ph2):f1 (p15:sp40 ph0):f2

#####
;#          t1 evolution          #
#####

(0.5u pl12):f2
# 179 "/opt/topspin3.5pl6/exp/stan/nmr/lists/pp/hChhC.cp"
# 180 "/opt/topspin3.5pl6/exp/stan/nmr/lists/pp/hChhC.cp"

if "l0>0"
{
  "d51=d0-2u"

  0.5u cpds2:f2
  d51
  0.5u do:f2
}
# 191 "/opt/topspin3.5pl6/exp/stan/nmr/lists/pp/hChhC.cp"
#####
;#          CP to f2; Mix; CP to f1    #
#####

(p44:sp45 ph3):f1 (p44:sp44 ph4):f2

(lalign (p1 pl1 ph9):f1 (p3 pl2 ph5):f2) ;store magn. along Z

mixing
# 201 "/opt/topspin3.5pl6/exp/stan/nmr/lists/pp/hChhC.cp"
(p3 pl2 ph6):f2          ; readout
(p48:sp49 ph8):f1 (p48:sp48 ph7):f2

#####
;#          Acquisition          #
#####

(0.5u pl12):f2
0.5u cpds2:f2
# 211 "/opt/topspin3.5pl6/exp/stan/nmr/lists/pp/hChhC.cp"
gosc ph31          ;start ADC with ph31 signal routing
```

```

# 217 "/opt/topspin3.5pl6/exp/stan/nmr/lists/pp/hChhC.cp"
1m do:f2                ;decoupler off
lo to Start times ns

# 1 "mc_line 220 file /opt/topspin3.5pl6/exp/stan/nmr/lists/pp/hChhC.cp exp. mc cmd. in
line"
MCWRK wr #0 if #0 zd

"ph1loop+=1"
"d0=d0orig + t1loop * in0 "
"d30=d30orig - t1loop * in30 "
"phval2 = (ph1loop % 4) * 90"
MCWRK ip2 + phval2
"I0 = I0orig + t1loop * 1 "

lo to LBLF1 times 2
MCWRK

"t1loop+=1"
"d0=d0orig + t1loop * in0 "
"d30=d30orig - t1loop * in30 "
"phval2 = (ph1loop % 4) * 90"
MCWRK ip2 + phval2
"I0 = I0orig + t1loop * 1 "

lo to LBLST1 times ST1CNT
MCWRK
"t1loop=0"
"ph1loop=0"
MCWRK rf #0
lo to LBLAV times tdav
# 222 "/opt/topspin3.5pl6/exp/stan/nmr/lists/pp/hChhC.cp"

HaltAcqu, 1m
exit
# 226 "/opt/topspin3.5pl6/exp/stan/nmr/lists/pp/hChhC.cp"
;#####
;#          Phase Cycle          #
;#####

ph0= 0                ; f2 CP spin lock during first cp
ph1= {{1}*8}^2       ; f2 hard pulse

```

```

ph2= 0 ; f1 CP spin lock during first cp
ph3= 0 0 2 2 ; f1 CP spin lock during second cp
ph4= 1 ; f2 CP spin lock during second cp
ph5= 0 ; f2 hard pulse for Z-filter
ph6= 0 2 ; f2 hard pulse for readout
ph7= 1 ; f2 CP spin lock during third cp
ph8= {{0}*4}^2 ; f1 CP spin lock during third cp
ph9= 1 ; f1 hard pulse for Z-filter

ph20= 0 ; f3 90 hard pulse
ph21= 1 ; f3 180 pulse
# 244 "/opt/topspin3.5pl6/exp/stan/nmr/lists/pp/hChhC.cp"
ph31= {{{2 0}^2}^2}^2 ; receiver

```

```
#####
```

```

# 250 "/opt/topspin3.5pl6/exp/stan/nmr/lists/pp/hChhC.cp"
;$ld: hChhC.cp,v 1.1.2.4 2014/02/11 14:42:32 ber Exp $

```

6.10 Pulse program for hNHHC experiments

```

# 1 "/opt/topspin3.5pl6/exp/stan/nmr/lists/pp/user/NHHCzf.land"
;fixed inversion of 15N dim -lba 6/2017
;XHHY.crmn NHHC-type experiment with Y/X decoupling during t1/t2
;written by AL&GP&SL 9.12.2008
;modified by land from NHHC.ebm 6.2017
;p3 : proton 90 at power level pl2
;p2 : proton Pi/2
;p15 : long contact time at pl1 (f3) and sp20 (f2)
;p16 : short contact time at pl1 (f3) and sp20 (f2)
;p15 : X power level during contact
;sp20 : proton power level during first CP
;sp21 : proton power level during second CP
;p17 : short contact time at pl4 (f1) and sp0 (f2)
;p14 : thrid CP (Y power level during contact)
;sp0 : proton power level during third CP
;p12 : decoupling power level (if not pl13)
;p13 : special decoupling power level
;p16 WALTZ 15N decoupling power
;p1 13C power level for pulses
;p3 15N hard pulse
;p7 15N hard pulse
;p2 13C Pi/2

```

```
;d8 : mixing time
;d1 : recycle delay
;d21 : z filter time (no 1H power)
;cnst21 : on resonance, usually = 0
;pcpd2 : pulse length in decoupling sequence
;cpdprg2 : cw, tppm (at pl12), or lgs, cwlg. cwlg (LG-decoupling)
;spnam0 : use e.g. ramp.100 for variable amplitude CP
;here pl13 is used instead of pl12

# 1 "/opt/topspin3.5pl6/exp/stan/nmr/lists/pp/Avancesolids.incl" 1
;Avancesolids.incl
; for TCU3
;
;version 1 28.2.2001, written by HF
;      4.4.2006, complemented by Ste

;$CLASS=Solids INCL
;$COMMENT=definitions for setrtp and setnmr

;switch between 1H or 19F output (H amplifier)
# 14 "/opt/topspin3.5pl6/exp/stan/nmr/lists/pp/Avancesolids.incl"
;gating pulse for RX, ADC and HPPR auto mode

# 18 "/opt/topspin3.5pl6/exp/stan/nmr/lists/pp/Avancesolids.incl"
;explicit blanking of preamp, receiver, adc, not implemented yet

# 26 "/opt/topspin3.5pl6/exp/stan/nmr/lists/pp/Avancesolids.incl"
;generate dwell clock

;turn dwell clock on/off
# 32 "/opt/topspin3.5pl6/exp/stan/nmr/lists/pp/Avancesolids.incl"
;

# 36 "/opt/topspin3.5pl6/exp/stan/nmr/lists/pp/Avancesolids.incl"
;define data sampling for WAHUA type experiments, samples analogue or digitally for d9,
closes receiver

# 40 "/opt/topspin3.5pl6/exp/stan/nmr/lists/pp/Avancesolids.incl"
```

;explicit transmitter blanking, not supported yet

;NCO switching, to be implemented

;\$id: \$

33 "/opt/topspin3.5pl6/exp/stan/nmr/lists/pp/user/NHHCzf.land" 2

35 "/opt/topspin3.5pl6/exp/stan/nmr/lists/pp/user/NHHCzf.land"

;**#ifdef** fslg

;**#include** <lgcalc.incl>

;cnst20 : RF field achieved at pl13

;cnst21 : on resonance, usually = 0

;cnst22 : positive LG offset

;cnst23 : negative LG offset

;cnst24 : additional LG-offset

;**#endif**

;cnst11 : to adjust t=0 for acquisition, if digmod = baseopt

"acqt0=1u*cnst11 "

"d0=0"

"in0=inf1 "

1 "mc_line 49 file /opt/topspin3.5pl6/exp/stan/nmr/lists/pp/user/NHHCzf.land exp. def.
part of mc cmd. before ze"

; dimension 2D; AQ_mode (F1) States-TPPI

define delay MCWRK

define delay MCREST

define delay d0orig

"d0orig=d0"

define loopcounter t1loop

"t1loop=0"

define loopcounter ph1loop

"ph1loop=0"

define loopcounter ST1CNT

"ST1CNT = td1 / 2"

"MCREST = d1 - 100m"

"MCWRK = 0.200000*100m"

 dccorr

49 "/opt/topspin3.5pl6/exp/stan/nmr/lists/pp/user/NHHCzf.land"

1 ze

1 "mc_line 49 file /opt/topspin3.5pl6/exp/stan/nmr/lists/pp/user/NHHCzf.land exp. def. of
mc cmd. after ze"

LBLAV, MCWRK

 "d0=d0orig + t1loop * in0 "

```

"phval12 = (ph1loop % 4) * -90"
MCWRK ip12 + phval12
# 50 "/opt/topspin3.5pl6/exp/stan/nmr/lists/pp/user/NHHCzf.land"
# 1 "mc_line 51 file /opt/topspin3.5pl6/exp/stan/nmr/lists/pp/user/NHHCzf.land exp. start
label for mc cmd."
2 MCWRK * 2 do:f2
LBLF1, MCWRK * 2
LBLST1, MCWRK
MCREST
# 52 "/opt/topspin3.5pl6/exp/stan/nmr/lists/pp/user/NHHCzf.land"
# 52 "/opt/topspin3.5pl6/exp/stan/nmr/lists/pp/user/NHHCzf.land"
;1m do:f3
1u pl1:f1 pl2:f2 pl3:f3
# 1 "/opt/topspin3.5pl6/exp/stan/nmr/lists/pp/p15_prot.incl" 1
;p15_prot.incl
;avance-version (13/01/29)
;Test the rf on-time and duty cycle
;protect against too long contact time
;Test the rf on-time and duty cycle
;
;$CLASS=Solids INCL
;$COMMENT=protect against too long contact time

1m
if "p15 < 10.1m" goto Passp15
2u
print "contact time exceeds 10msec limit!"
goto HaltAcqu
Passp15, 1m
# 20 "/opt/topspin3.5pl6/exp/stan/nmr/lists/pp/p15_prot.incl"
;$ld: p15_prot.incl,v 1.8 2013/01/29 15:40:14 ber Exp $
# 54 "/opt/topspin3.5pl6/exp/stan/nmr/lists/pp/user/NHHCzf.land" 2

;make sure p15 does not exceed 10 msec
;let supervisor change this pulseprogram if
;more is needed

;#ifndef 1
;disable protection file for long acquisition change decoupling power
!!! or you risk probe damage
;if you set the label 1 (ZGOPTNS -Dlacq), the protection is disabled

# 1 "/opt/topspin3.5pl6/exp/stan/nmr/lists/pp/aq_prot.incl" 1
;aq_prot.incl

```

```
-----
;avance-version (13/01/28)
;Test the rf on-time and duty cycle
;protect against too long acquisition time
# 6 "/opt/topspin3.5pl6/exp/stan/nmr/lists/pp/aq_prot.incl"
;$CLASS=Solids INCL
;$COMMENT=protect against too long acquisition time

1m
if "aq < 50.1m" goto Passaq
2u
print "acquisition time exceeds 50m limit!"
goto HaltAcqu
Passaq, 1m

;$ld: aq_prot.incl,v 1.8 2013/01/28 17:39:02 ber Exp $
# 62 "/opt/topspin3.5pl6/exp/stan/nmr/lists/pp/user/NHHCzf.land" 2
# 63 "/opt/topspin3.5pl6/exp/stan/nmr/lists/pp/user/NHHCzf.land"
        ;allows max. 50 msec acquisition time, supervisor
        ;may change to max. 1s at less than 5 % duty cycle
        ;and reduced decoupling field
;#endif

1u fq=cnst21:f2
(p3 ph1 pl2):f2 ;(ralign (p3 ph1 pl2):f2 (p7 ph13 pl3):f3)
(p15 ph2 pl5):f3 (p15:sp20 ph10):f2 ;1H to 15N long contact pulse with square or ramp
(p7 ph11 pl3):f3
;add shaped 180 pulse for selective seq.
d21 ;z filter
1u cpds2:f2
(p7 ph12 pl3):f3
;(center (d0) (p2*2 pl1 ph0):f1) ;13C refocusing pulse during t1
    d0
0.5u do:f2
(p16 pl5 ph3):f3 (p16:sp21 ph4):f2 ;15N to 1H short contact pulse with square or ramp
(p3 ph5 pl2):f2 ;1H flip-back pulse
d8
;    1u fq=cnst22:f2 ; mixing time
(p3 ph6 pl2):f2 ;1H 90 degree pulse
(p17 pl4 ph7):f1 (p17:sp0 ph8):f2 ;1H to 13C short contact pulse with square or ramp

1u cpds2:f2 ; 1u cpds3:f3 ;use cpdprg3=waltz16
go=2 ph31
1u do:f2 ; do:f3
```

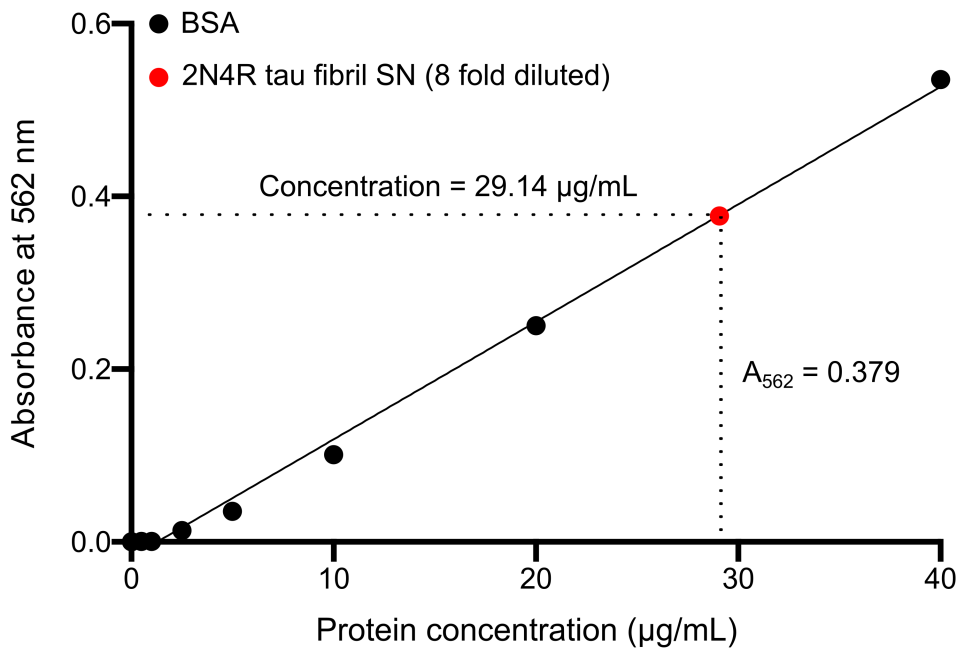
```
# 1 "mc_line 89 file /opt/topspin3.5pl6/exp/stan/nmr/lists/pp/user/NHHCzf.land exp. mc
cmd. in line"
MCWRK wr #0 if #0 zd

"ph1loop+=1"
  "d0=d0orig + t1loop * in0 "
  "phval12 = (ph1loop % 4) * -90"
  MCWRK ip12 + phval12
lo to LBLF1 times 2
MCWRK

"t1loop+=1"
  "d0=d0orig + t1loop * in0 "
  "phval12 = (ph1loop % 4) * -90"
  MCWRK ip12 + phval12
lo to LBLST1 times ST1CNT
MCWRK
"t1loop=0"
"ph1loop=0"
MCWRK rf #0
lo to LBLAV times tdav
# 90 "/opt/topspin3.5pl6/exp/stan/nmr/lists/pp/user/NHHCzf.land"
HaltAcqu, 1m          ;jump address for protection files
exit                  ;quit

ph0= 0
ph1= 1
ph2= 0
ph3=0 1
ph4={0}*4 {2}*4
ph5=1
ph6={0}*8 {2}*8
ph7={0}*16 {2}*16
ph8=1
ph10= 0
ph11= 1
ph12= 1 0 3 2
;ph13=1
ph31= 0 2 2 0 2 0 0 2
      2 0 0 2 0 2 2 0
      2 0 0 2 0 2 2 0
      0 2 2 0 2 0 0 2
```

6.11 Bicinchoninic acid assay of 2N4R tau



Concentration of 2N4R tau before aggregation = 1.146 mg/mL

Concentration of 2N4R tau in SN = $(29.14 \times 8) \mu\text{g/mL} = 0.233 \text{ mg/mL}$

~ 80 % 2N4R tau aggregated

Figure 6-2 BCA assay of 2N4R tau

Determination of the concentration of 2N4R tau present in the supernatant (SN; red dot; 8-fold dilution) after aggregation in the absence of heparin. Concentrations were determined using the BCA assay. Absorbance values, which were detected for BSA standard solutions with known concentrations, are shown in black

6.12 2D hCH spectra of specifically labeled heparin-free 2N4R tau fibrils

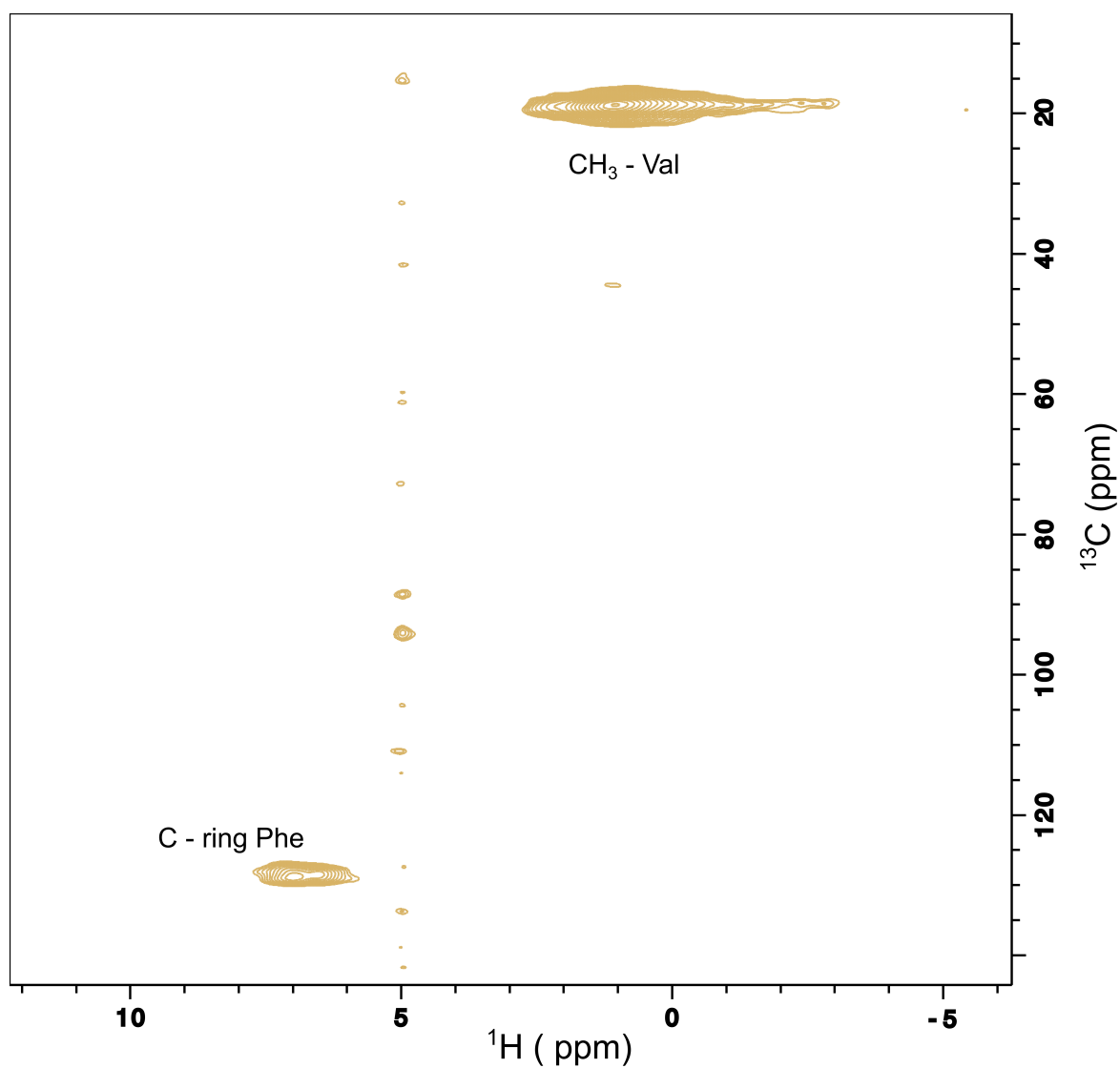


Figure 6-3 2D hCH spectra of heparin-free fibrils of $^{13}\text{C}_\gamma$ valine, ^{13}C -ring phenylalanine-labeled 2N4R tau

6.13 Electrostatic surface potential of heparin-induced 2N4R tau fibrils

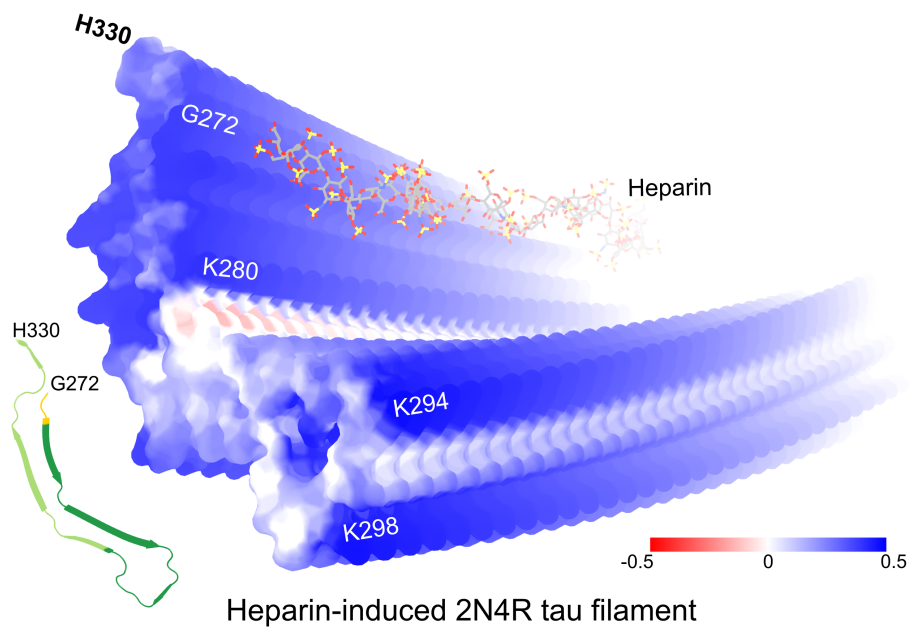


Figure 6-4 Electrostatic surface potential of the heparin-induced 2N4R tau fibrils (snake form; PDB code: 6QJH).

Positively and negatively charged residues are shown in blue and red, respectively. A molecule of heparin is displayed to illustrate the presence of heparin on the surface of the fibril.

Co-factor-free aggregation of tau into seeding-competent RNA-sequestering amyloid fibrils

Pijush Chakraborty ¹, Gwladys Rivière¹, Shu Liu², Alain Ibáñez de Opakua¹, Riza Dervişoğlu ³, Alina Hebestreit², Loren B. Andreas ³, Ina M. Vorberg ^{2,4} & Markus Zweckstetter ^{1,3}✉

Pathological aggregation of the protein tau into insoluble aggregates is a hallmark of neurodegenerative diseases. The emergence of disease-specific tau aggregate structures termed tau strains, however, remains elusive. Here we show that full-length tau protein can be aggregated in the absence of co-factors into seeding-competent amyloid fibrils that sequester RNA. Using a combination of solid-state NMR spectroscopy and biochemical experiments we demonstrate that the co-factor-free amyloid fibrils of tau have a rigid core that is similar in size and location to the rigid core of tau fibrils purified from the brain of patients with corticobasal degeneration. In addition, we demonstrate that the N-terminal 30 residues of tau are immobilized during fibril formation, in agreement with the presence of an N-terminal epitope that is specifically detected by antibodies in pathological tau. Experiments in vitro and in biosensor cells further established that co-factor-free tau fibrils efficiently seed tau aggregation, while binding studies with different RNAs show that the co-factor-free tau fibrils strongly sequester RNA. Taken together the study provides a critical advance to reveal the molecular factors that guide aggregation towards disease-specific tau strains.

¹German Center for Neurodegenerative Diseases (DZNE), Göttingen, Germany. ²German Center for Neurodegenerative Diseases (DZNE), Bonn, Germany. ³Department for NMR-based Structural Biology, Max Planck Institute for Biophysical Chemistry, Göttingen, Germany. ⁴Rheinische Friedrich-Wilhelms-Universität, Bonn, Germany. ✉email: Markus.Zweckstetter@dzne.de

Pathological aggregation of the microtubule-binding protein tau (Fig. 1a) into amyloid fibrils is a hallmark of different neurodegenerative diseases collectively termed tauopathies¹. To date, tau amyloid structures associated with four different tauopathies (Alzheimer's disease, Chronic traumatic encephalopathy, Corticobasal degeneration (CBD; Fig. 1b) and Pick's disease) have been determined^{2–6}. Strikingly, structures are homogeneous within one disease, but significantly different between different diseases, suggesting a critical interplay between the amyloid structure, the nature of the disease and its propagation. The distinct aggregate structures, termed amyloid “strains”, can induce aggregation of tau in cellula and recapitulate pathological phenotypes when injected into animals⁷. So far, the emergence of such tau amyloid strains remains elusive, and the factors that drive tau aggregation towards a well-defined strain are unknown.

Recombinant tau monomers can efficiently form fibrils in vitro but only in the presence of negatively charged co-factors such as heparin^{8,9}. The biological relevance of co-factor-induced fibrillization as an in vitro model of tau aggregation has, however, been

questioned¹⁰. Indeed, cryo-electron microscopy (cryoEM) of heparin-induced fibrils of the longest isoform of tau (2N4R tau; Fig. 1a) demonstrated that the heparin-induced fibrils differ structurally from the tau filaments extracted from human patient brain (Fig. 1b, c)¹⁰. Another major drawback of the heparin-based in vitro fibrillization assay is the high negative charge of heparin: heparin-induced tau fibrillization has been extensively used to search for small molecules as tau aggregation inhibitors^{11,12}, potentially generating false hits due to electrostatic interactions between the small molecules and heparin.

Here we describe an approach to convert full-length tau protein into amyloid fibrils in the absence of heparin or other negatively charged co-factors. Using a combination of biochemical experiments and NMR spectroscopy we then provide evidence that the co-factor-free tau fibrils have structural properties that largely differ from those of heparin-induced tau fibrils. In addition, we show that the tau fibrils aggregated in the absence of heparin display certain properties of amyloid fibrils from patient material, including a similar size and location of the fibrillar core,

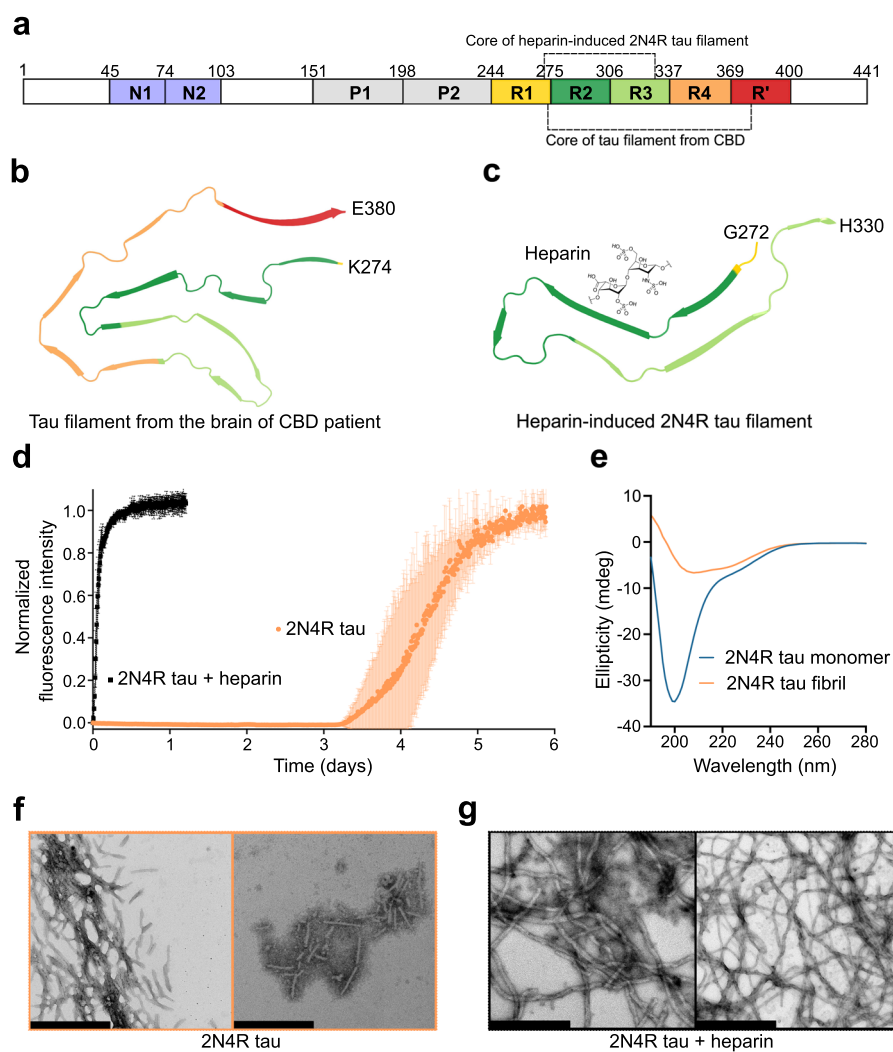


Fig. 1 Amyloid fibrils of tau without co-factors. **a** Schematic representation of the domain organization of 2N4R tau. N1 and N2 are two inserts subject to alternative splicing, P1 and P2 mark the proline-rich regions, and R1–R' are pseudo-repeats that bind to microtubules. Tau fibril cores from CBD-brain and heparin-induced 2N4R fibrils are marked by dashed lines (see also **(b, c)**). **b** CryoEM structure of tau filament (type 1) extracted from the brain of a patient with CBD (PDB code: 6TJO). **c** CryoEM structure of heparin-induced 2N4R tau fibrils (snake form; PDB code: 6QJH). A molecule of heparin is displayed to illustrate that these fibrils are formed in the presence of heparin. **d** Aggregation kinetics of 25 μ M 2N4R tau with (black) and without (orange) heparin. Data are presented as mean \pm standard deviation of $n = 3$ independent samples. **e** Circular dichroism spectra of 2N4R tau monomer and heparin-free fibrils. **f, g** Negative-stain electron micrographs of 2N4R fibrils aggregated without heparin (**f**) or with heparin (**g**). Scale bar, 500 nm. Similar micrographs have been observed for both 2N4R fibrils aggregated in presence/absence of heparin with ten independently aggregated samples.

a change in the molecular properties of the N-terminal antibody binding epitope and the strong and specific sequestration of RNA.

Results

Full-length tau fibrillizes without co-factors. To achieve tau fibrillization in the absence of co-factors, we incubated 25 μ M 2N4R tau at 37 °C in 25 mM HEPES, 10 mM KCl, 5 mM MgCl₂, 3 mM TCEP, 0.01% NaN₃, pH 7.2, buffer with polytetrafluoroethylene beads. To trigger aggregation, double orbital shaking at an interval of every 10 min was applied. Thioflavin-T was used to monitor the aggregation kinetics. 2N4R tau started aggregating after 3 days in the absence of heparin as compared to very rapid aggregation in presence of heparin (Fig. 1d). After about 6 days the ThT fluorescence saturated in the absence of heparin, indicating that heparin-free fibrillization of 2N4R was complete (Fig. 1d). The time-dependent ThT fluorescence of heparin-free tau aggregation displayed the typical sigmoidal kinetics of nucleation-dependent protein aggregation (Fig. 1d). By measuring the concentration of the monomeric protein left after reaching ThT saturation, we found that ~80% of 2N4R tau was aggregated (Supplementary Fig. 1).

To gain first insights into the structure of the aggregated 2N4R tau, we recorded circular dichroism (CD) spectra and negative-stain electron microscopy (EM) images. According to CD, monomeric tau prior to aggregation displays a spectrum (Fig. 1e), which is characteristic for intrinsically disordered proteins such as tau^{13,14}. In contrast, the CD spectrum of the heparin-free 2N4R tau fibrils obtained after 6 days of aggregation (Fig. 1e) is typical for amyloid fibrils comprised of a β -structure-rich core and flexible tails. Quantification of the CD spectrum estimated the β -structure content as ~39%.

In the case of heparin-induced tau aggregation, it is known that this results in long tau fibrils that form an almost net-like arrangement on EM grids (Fig. 1g)^{15,16}. In contrast, the 2N4R tau fibrils formed in the absence of heparin (but otherwise using the identical protocol, i.e., the same buffer, the same polytetrafluoroethylene beads and the same shaking procedure) are short and do not display an extended network on the EM grid (Fig. 1f). The overall morphological properties of tau fibrils obtained without and with heparin are thus very different (Fig. 1f, g).

Protease-resistant core of heparin-free tau fibrils. To obtain direct information about the fibrillar core, 2N4R fibrils were digested by trypsin to remove the fuzzy coat (Fig. 2a), followed by pelleting down the protease-resistant material through ultracentrifugation. SDS-PAGE gel analysis indicated a much longer core for 2N4R tau fibrils as compared to heparin-induced fibrils (Fig. 2b). The short trypsin-resistant core of heparin-induced fibrils is in agreement with previous data¹⁶.

To further analyze the rigid core of the fibrils, we determined the sequence of the tau bands observed in SDS-PAGE by mass spectrometry. For heparin-induced fibrils, we detected a large number of peptides from residues ~260 to ~340 (Fig. 2c; black; Supplementary Fig. 2), consistent with structural analysis by cryoEM (Fig. 1c)¹⁰. For 2N4R fibrils, we detected a large number of peptides from residue ~280 to ~400 (Fig. 2c, orange; Supplementary Fig. 3). In addition, a few peptides for the C-terminal tail were detected, most probably because trypsin cuts the protein carboxy-terminally of K/R residues and there are only a few target residues (K395, R406, K438) for trypsin in this region.

To get more precise information about the protease-resistant core of the heparin-free 2N4R fibrils, especially to get more resolution at the C-terminus, we repeated the experiments with pronase. Pronase is a mixture of several endo- and exoproteases

that can digest a protein into individual amino acids. 2N4R fibrils were digested by pronase and the resistant fibril core was pelleted down by ultracentrifugation. After excising the pronase-resistant band with trypsin, we detected peptides up to residue 379 (Supplementary Fig. 4).

Rigidification of the N-terminal epitope of pathological tau.

Next, we aggregated uniformly ¹³C/¹⁵N-labeled 2N4R tau both in the absence and presence of heparin and recorded ¹H-¹⁵N Inesensitive nuclei enhanced by polarization transfer (INEPT) spectra under conditions of magic angle spinning (Fig. 2d and Supplementary Fig. 5). INEPT experiments use scalar coupling for polarization transfer, thereby detecting only the highly dynamic residues in solid samples, i.e., the fuzzy coat in the case of tau fibrils (Fig. 2a, d). Residue-specific analysis of the INEPT spectra revealed a complete loss of signal from residues ~270 to ~400 in the case of 2N4R fibrils (Fig. 2e), in agreement with mass spectrometry analysis (Fig. 2c). In the case of heparin-induced fibrils, no INEPT signals were detected for residues ~260 to ~330. Because cryoEM resolves only the very rigid residues in cross- β -structure at high resolution and has reported additional unidentified electron density in tau fibrils, the analysis suggests that in vitro-generated 2N4R fibrils, but not heparin-induced fibrils, have a similar core length as tau fibrils purified from CBD patient brain (residues ~274 to ~380 were resolved at high resolution; PDB code: 6TJO; marked in light blue in Fig. 2e).

The NMR analysis, however, provided further insights into the key regions of tau aggregation. Not only residues ~270 to ~400 were broadened beyond detection in the case of the heparin-free 2N4R tau fibrils, but also the amino-terminal 30 residues (Fig. 2e; marked in pink). This is most likely because of a dynamic interaction of the N-terminus of tau with the cross- β -structure core¹⁷. The immobilization of the N-terminal 30 residues provides a structural basis for the specificity of antibodies that specifically detect pathological tau¹⁸ and require two discontinuous epitopes located in the repeat region (residues 313–322) and at the N-terminus (residues 1–18)¹⁸.

Solid-state NMR of the fibrillar core.

Next, we probed the rigid core of the 2N4R tau fibrils. To this end, ¹³C-¹³C correlations were recorded using cross-polarization solid-state NMR experiments (Fig. 3a). In agreement with mass spectrometry and the INEPT-based NMR analysis (Fig. 2), the ¹³C-¹³C spectrum of 2N4R fibrils contained many more signals when compared to the spectrum of heparin-induced fibrils (Fig. 3a). This was particularly evident from the C β region of serine and threonine residues (Fig. 3a), indicating that more serine and threonine residues are located in the core of 2N4R fibrils (Fig. 3b, c). In addition, only one broad cross-peak was observed in the threonine C γ region of the heparin-induced fibrils, while about six cross peaks were present in the case of the 2N4R fibrils (Fig. 3a, selected zoom). Because only rigid residues are detected in the cross-polarization NMR experiments, the number of observed threonine cross peaks is consistent with the fibrillar core of 2N4R fibrils derived from mass spectrometry and INEPT-based NMR experiments (Fig. 3b, c).

To further characterize the 2N4R fibrils, we recorded 2D NCA as well as 3D NCACX and 3D NCOX experiments. Due to strong signal overlap, however, only a few residues in the fibril core could be identified (Fig. 3d–f). This included the residue stretch from G303 to V306 (Fig. 3d–f) that is part of the cross- β -structure core of tau fibrils purified from a CBD patient (Fig. 1b). Isolated peaks in the 2D RFDR and 2D NCA spectra of the heparin-free 2N4R tau fibrils show ¹³C and ¹⁵N line widths of

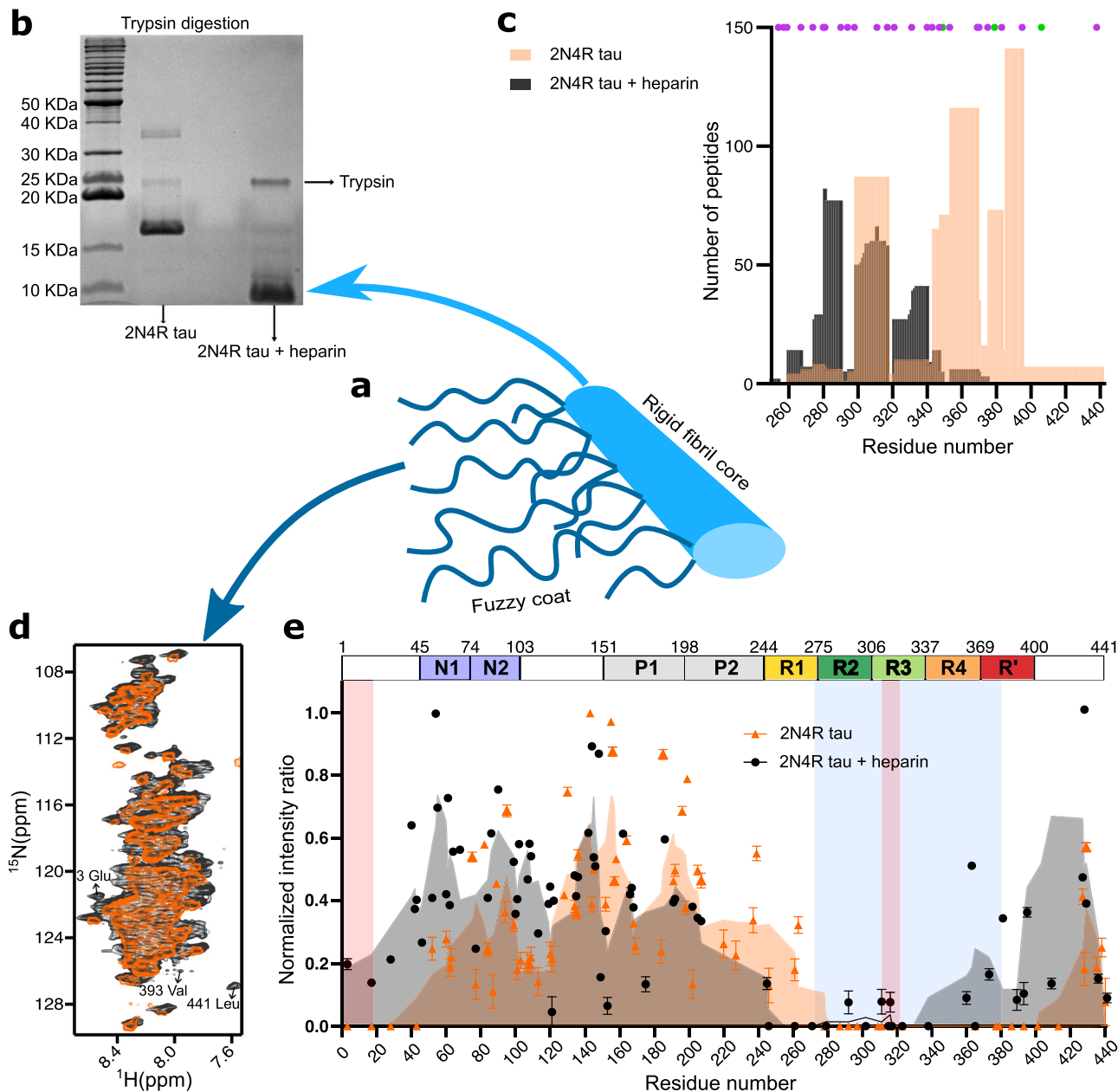


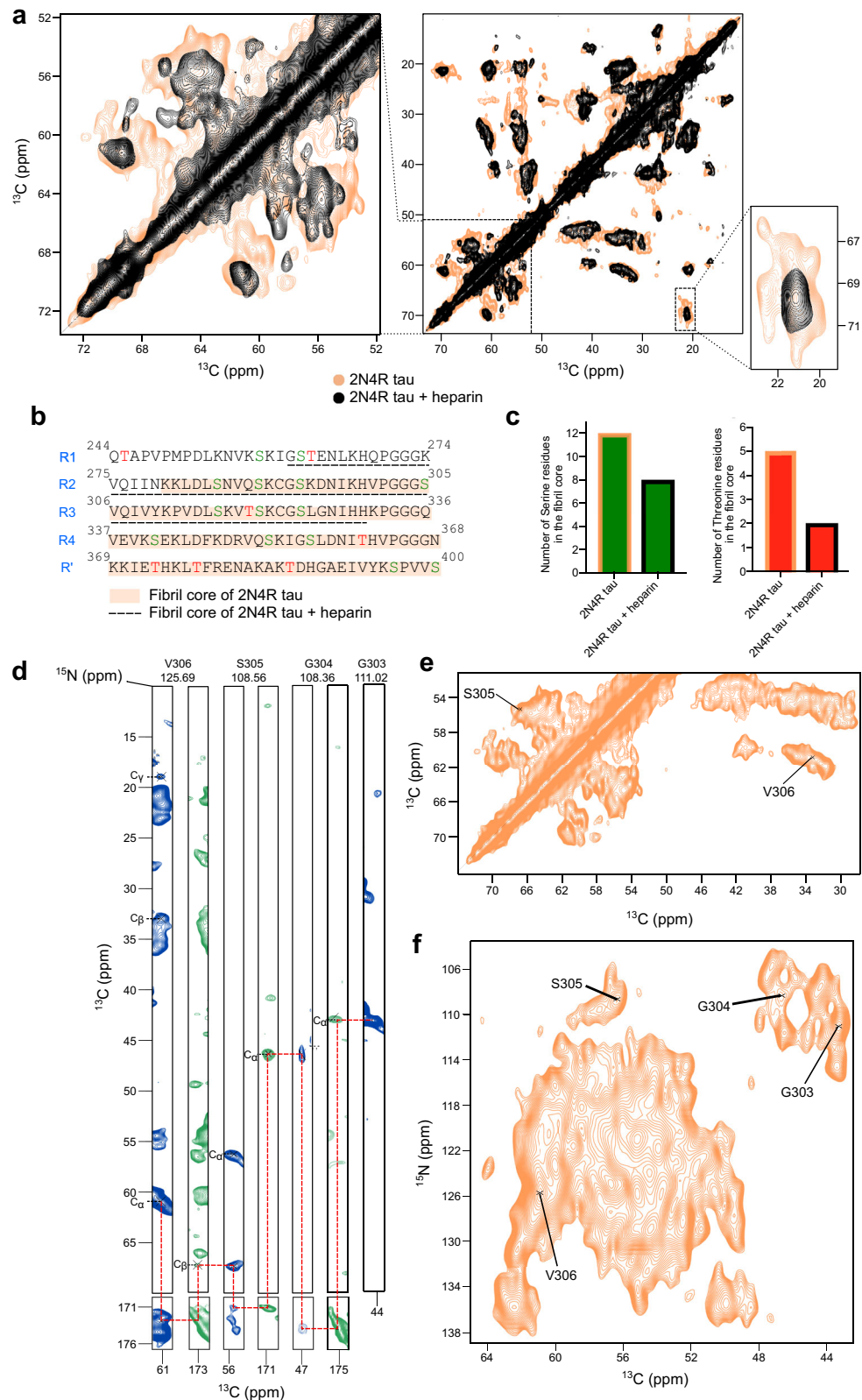
Fig. 2 Heparin-free tau fibrils have an extended core and an immobile N-terminal antibody-binding epitope. **a** Cartoon representation of the rigid core and dynamic (termed fuzzy) coat of tau fibrils. **b** SDS-PAGE gel of trypsin-digested tau fibrils formed in the absence or presence of heparin. The trypsin band is indicated. The result was reproducible for three independently performed experiments. **c** Number of peptides detected from the enzymatic digestion of the tau bands observed in SDS-PAGE in **(a)**. The position of lysine and arginine residues of 2N4R tau are marked with purple and green dots, respectively. **d** Superposition of ^1H - ^{15}N INEPT spectra of 2N4R tau fibrils aggregated in the absence (orange) and presence (black) of heparin. **e** Intensity ratio plot of 2N4R tau fibrils aggregated in the absence (orange) and presence (black) of heparin. The intensity ratio was calculated by dividing the signal intensity of each residue in the fibril state by the monomeric state. The error of the intensity ratio for each residue was calculated from the signal-to-noise ratio of the cross peaks in the spectra. The rigid cross- β -sheet core of the tau fibril extracted from a CBD patient brain (PDB code: 6TJO) is marked in light blue. The two discontinuous epitopes (residues 1–18 and residues 313–322) of antibodies that specifically detect pathological tau¹⁸ are marked by red boxes.

0.6–0.8 ppm and 0.9–1.1 ppm, respectively, indicating structural homogeneity of the rigid core.

To gain further insight into the structural properties of 2N4R tau fibrils, we aggregated selectively labeled ($^{13}\text{C}_\gamma$ valine, ^{13}C -ring phenylalanine, ^{15}N histidine) 2N4R tau in the absence of heparin. 2D hCH and 2D hNH cross-polarization spectra demonstrated that the protein is ^{13}C labeled only at the C_γ of valine and the ring carbons of phenylalanine, and ^{15}N -labeled at the backbone and side chain of histidine residues (Fig. 4a; Supplementary Fig. 6).

We then recorded Dynamic Nuclear Polarization (DNP)-enhanced solid-state NMR spectra in order to achieve maximum sensitivity. We used TEMTriPol-1^{19,20} and observed a 12-fold DNP enhancement of the signal (Fig. 4b).

Next, DNP-enhanced 2D hCHHC spectra with 200 μs and 400 μs mixing were measured. The chosen mixing times will result in cross peaks between two ^{13}C atoms that are about $\leq 4 \text{ \AA}$ and $\leq 6 \text{ \AA}$ apart, respectively²¹. In the spectra displayed in Fig. 4c, two cross peaks between the C_γ of valine and the ring carbons of



phenylalanine are present. The cross peaks are detected both below and above the diagonal (Fig. 4c), in agreement with the expected symmetric magnetization transfer. The presence of the two cross peaks suggests that the side chains of one or two valine residues are in close spatial proximity to the side chain of a phenylalanine residue. We also recorded DNP-enhanced 2D hNHC spectra with 200 μ s mixing and observed a cross peak between the 15 N-ring of

histidine and 13 C $_{\gamma}$ of valine (Fig. 4d), indicating that the aromatic ring of a histidine is in proximity (~ 4 Å) to the side chain of a valine residue in the structure of 2N4R fibrils.

The 2N4R tau sequence contains three phenylalanine residues, but only two (F346 and F378) are located in the rigid/semi-rigid core of 2N4R tau fibrils, which comprises residues ~ 270 to ~ 380 (Fig. 2). In the cryoEM structure of ex vivo CBD fibrils, F346

Fig. 3 Solid-state NMR of the core of heparin-free tau fibrils. **a** ^{13}C - ^{13}C RFDR spectra of 2N4R tau fibrils (middle panel), which were aggregated without (orange) or with heparin (black). The C_β region of serine and threonine residues is highlighted on the left, the C_γ region of threonine to the right. **b** Amino acid sequence of the repeat region of 2N4R tau. Serine residues are colored in green, threonine residues in red. The core of heparin-free 2N4R tau fibrils is highlighted in orange. The fibrillar core of heparin-induced 2N4R tau fibrils is underlined with black dashed lines. **c** Number of serine and threonine residues in the core of 2N4R tau fibrils that were formed in the absence or presence of heparin (according to **b**). **d**, Strips from 3D NCACX (blue) and 3D NCOCX (green) spectra of heparin-free 2N4R tau fibrils, illustrating the sequential assignment of residues. **e** Selected region of the ^{13}C - ^{13}C RFDR spectrum of heparin-free 2N4R tau fibrils, indicating the assignment of the cross peaks of residues S305 and V306. **f** 2D NCA spectrum of heparin-free 2N4R tau fibrils, indicating the assignment of the cross peaks of residues 303-306 (based on **d**).

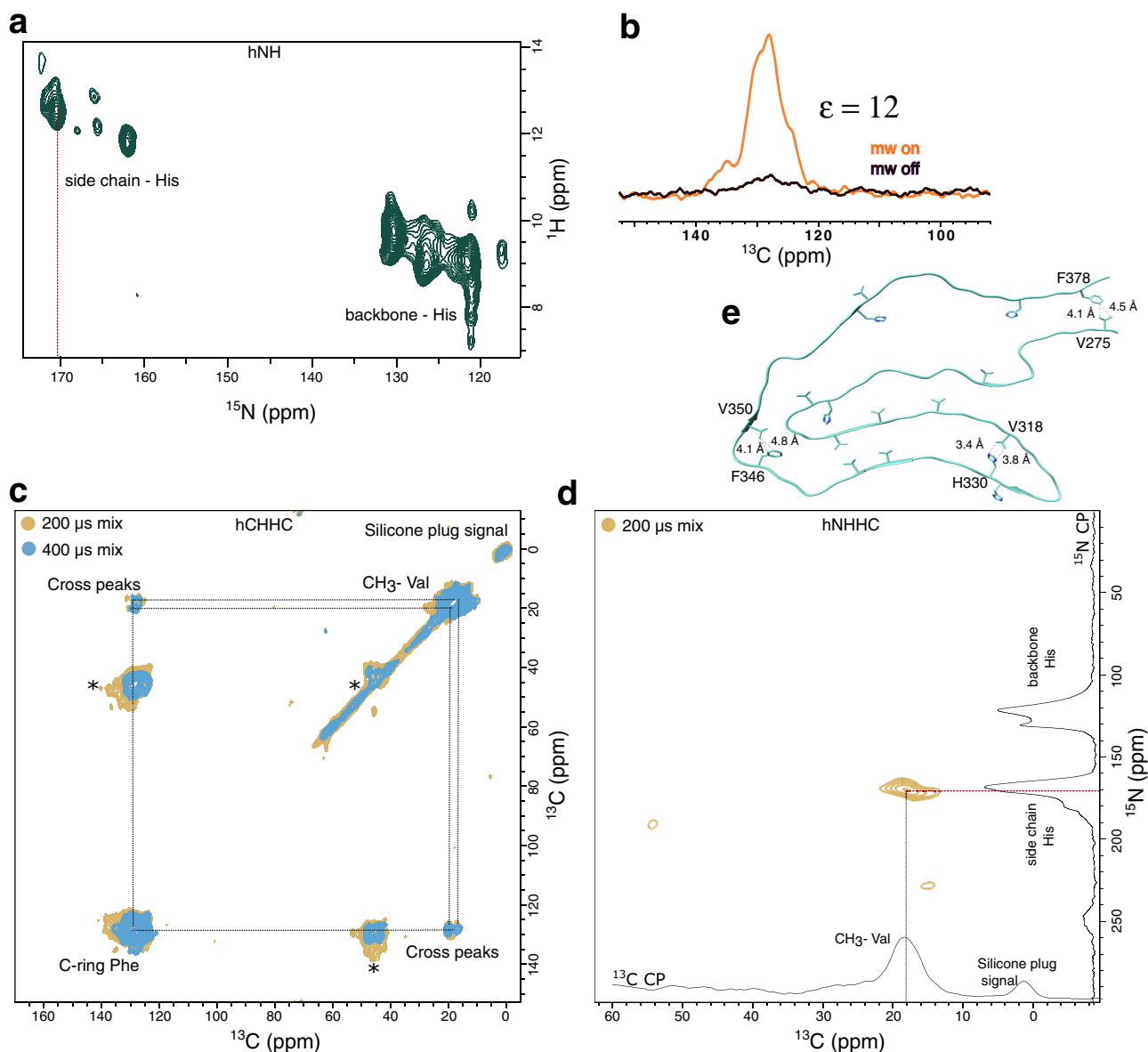


Fig. 4 Residue type-specific contacts within the core of heparin-free 2N4R tau fibrils. **a** Proton-detected ^1H - ^{15}N correlation solid-state NMR spectrum of heparin-free fibrils of 2N4R tau selectively labeled with ^{15}N Histidine (and at the $^{13}\text{C}_\gamma$ of valine and the ^{13}C -ring of phenylalanine). The spectrum was recorded at room temperature at a NMR spectrometer with 850 MHz ^1H frequency using 55 kHz magic angle spinning (MAS) frequency. **b** Comparison of the ^{13}C NMR signal of phenylalanine (ring carbons) when the microwave is turned on (orange) or off (black). The signal enhancement (ϵ) is displayed. Spectra shown in **(b-d)** were recorded at a temperature of 100 K at a NMR spectrometer with 600 MHz ^1H frequency using 12.5 kHz MAS spinning. **c** Superposition of DNP-enhanced 2D hCHHC spectra of selectively labeled ($^{13}\text{C}_\gamma$ valine, ^{13}C -ring phenylalanine, ^{15}N histidine) heparin-free 2N4R tau fibrils with 200 μs (yellow) and 400 μs (sky blue) mixing time. Spinning side bands are labeled with *. **d** DNP-enhanced 2D hNHHC spectrum of selectively labeled ($^{13}\text{C}_\gamma$ valine, ^{13}C -ring phenylalanine, ^{15}N histidine) heparin-free 2N4R tau fibrils. **e** Location of valine, phenylalanine and histidine residues within the core structure of the tau filament (type 1) extracted from the brain of a patient with CBD (PDB code: 6TJO). Short-range distances between valine and phenylalanine, and histidine and valine are marked.

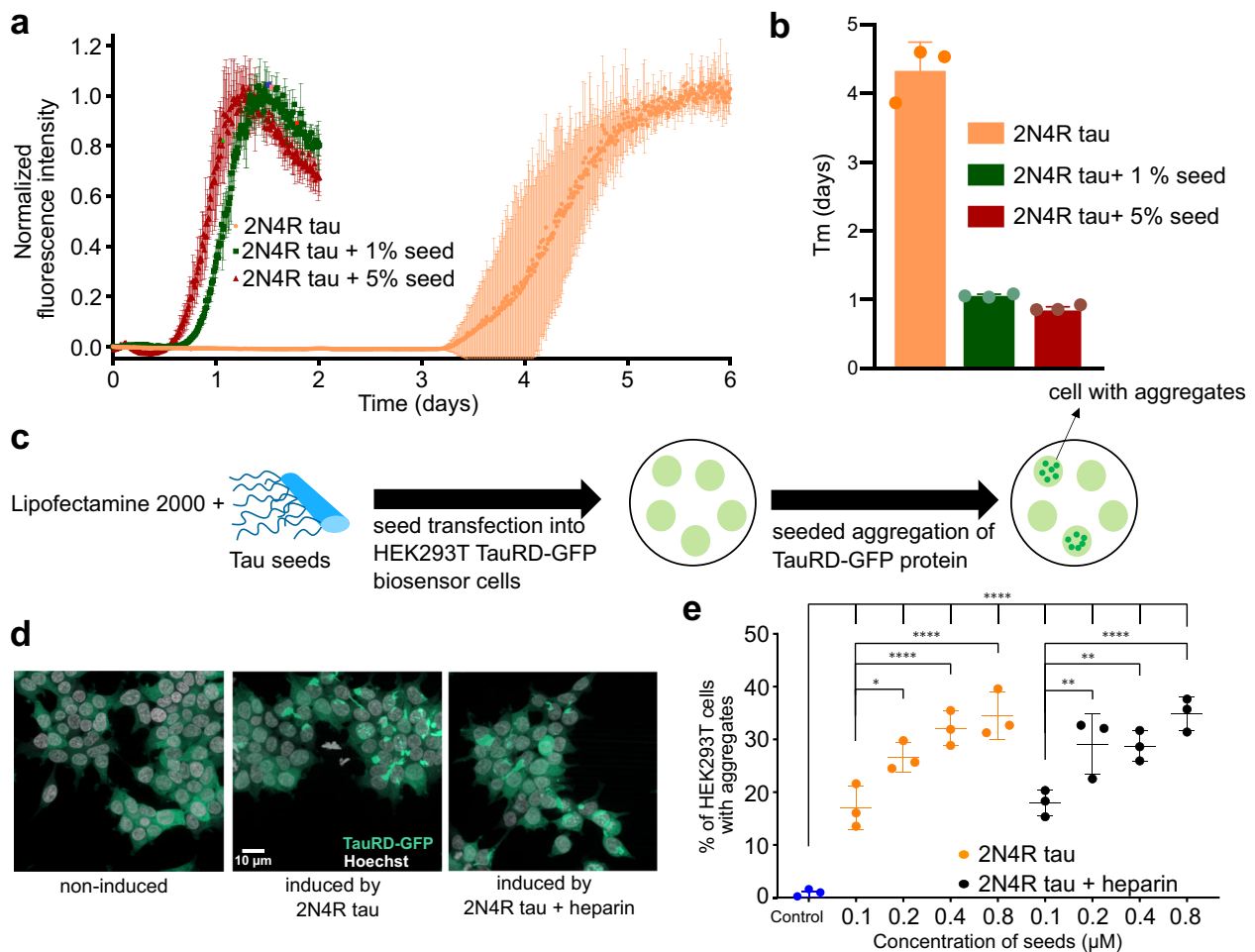


Fig. 5 Seeding activity of heparin-free tau fibrils. **a** Aggregation kinetics of 25 μM 2N4R tau in the absence (orange) and presence of 1% (green) and 5% (red) tau seeds generated without heparin. Data are presented as mean \pm standard deviation of $n = 3$ independent samples. **b** Half-time (T_m) of aggregation of 2N4R tau in the absence (orange) and presence of 1% (green), 5% (red) tau seeds (see **a**). Data are presented as mean \pm standard deviation of $n = 3$ independent samples. **c** Schematic representation of the process of seeding of tau aggregation in biosensor cells. **d** TauRD-GFP puncta in HEK293T biosensor cells²³, expressing the tau repeat domain carrying the mutations P301L and V337M, induced by 2N4R tau seeds, which were formed either in the absence (left) or presence of heparin (right). The result was reproducible for three independently performed experiments. **e** Comparison of the efficiency of 2N4R tau seeding in tau biosensor cells. Fibrils were generated by aggregating 2N4R tau in the absence (orange) or presence (black) of heparin. Different concentrations of seeds (0.1–0.8 μM) were used to induce TauRD-GFP puncta. The statistical analysis between the % of HEK293T cells with puncta induced by each concentration of seeds in the absence/presence of heparin was performed by one-way ANOVA analysis. Fibrils of different concentrations were independently transfected $n = 3$ times. Error bars represent the standard deviation of three independent experiments. Four stars represent $p < 0.0001$, two stars represents $p \leq 0.0021$, one star represents $p = 0.0296$.

contacts V350, and F378 contacts V275 (Fig. 4e). The two phenylalanine-valine cross peaks observed in the spectra of 2N4R fibrils might thus arise from these structure-specific contacts. In addition, there is only a single close contact between the aromatic ring of a histidine (H330) and the C_γ of valine (V318) in the structure of CBD fibrils (Fig. 4e). This could correspond to the observed His(^{15}N -ring)/V($^{13}\text{C}_\gamma$) cross peak in 2N4R fibrils (Fig. 4d).

Seeding of tau fibrillization in vitro and in cells. Tau pathology in the brain follows a “prion-like” behavior with transneuronal propagation of tau aggregates from one brain region to another⁷. A critical process in tau spreading is the ability of tau aggregates to seed fibrillization of monomeric tau. In order to study the in vitro seeding efficiency of 2N4R fibrils, 1% and 5% seeds (w/w) of 2N4R fibrils were added to the monomeric protein. The addition of seeds decreased the half-time of aggregation four times (Fig. 5a, b), confirming the seeding activity of 2N4R fibrils.

Next, we performed an in-cell seeding experiment using tau biosensor cells (Fig. 5c)^{22,23}. Four different concentrations (0.1, 0.2, 0.4, and 0.8 μM) of seeds of 2N4R fibrils, as well as heparin-induced fibrils, were used to induce aggregation. The 2N4R fibril seeds efficiently induced TauRD-GFP puncta in a concentration-dependent manner (Fig. 5d, e).

Heparin-free tau fibrils strongly bind RNA. Tau aggregates in human patient brains are extensively decorated with RNA²⁴, consistent with the positively charged surface seen in the cryoEM structure of CBD fibrils (Fig. 6a). To investigate the interaction of 2N4R fibrils with RNA, we added polyU, polyA or tRNA to the fibrils and incubated the samples for 1.5 h in the aggregation assay buffer (10 mM KCl, 25 mM HEPES, 5 mM MgCl_2 , 3 mM TCEP, pH 7.2) followed by centrifugation to separate the pellet and supernatant (Fig. 6b). In these conditions, 2N4R tau fibrils were found to interact strongly with all three RNAs as detected by the presence of ~82% polyU, ~80% polyA and ~93% tRNA in the

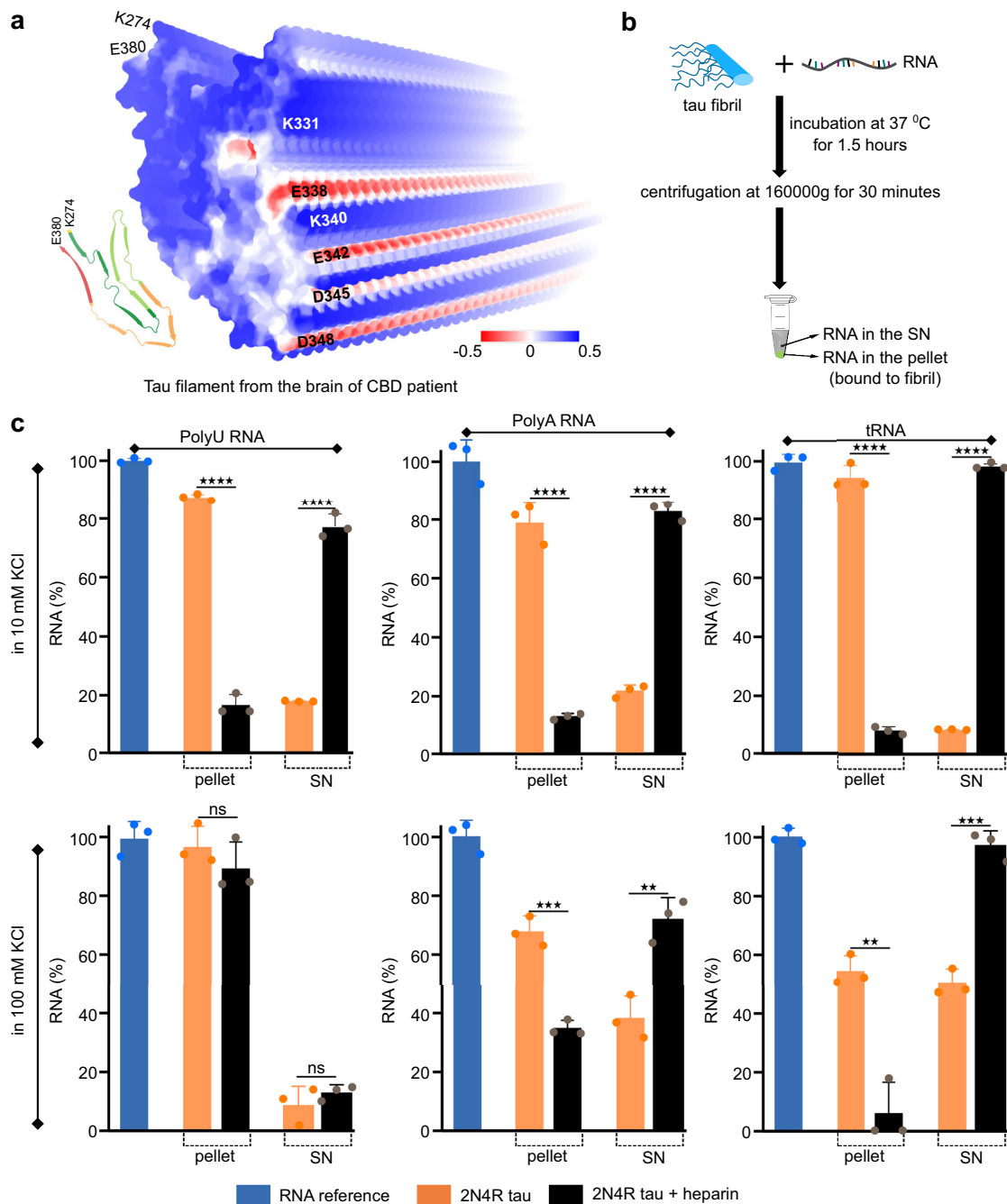


Fig. 6 Heparin-free tau fibrils strongly bind RNA. **a** Electrostatic surface potential of the tau filament extracted from a CBD patient (PDB code: 6TJO). Positively and negatively charged residues are shown in blue and red, respectively. **b** Schematic representation of the protocol to determine the binding of RNA to tau fibrils. **c** Quantitative analysis of the binding of polyU, polyA and tRNA to tau fibrils aggregated without (orange) or with heparin (black) in the aggregation assay buffer (10 mM KCl, 25 mM HEPES, 5 mM MgCl₂, 3 mM TCEP, pH 7.2) or at increased ionic strength (100 mM KCl, 25 mM HEPES, 5 mM MgCl₂, 3 mM TCEP, pH 7.2). The amount of RNA in the pellet represents the % of RNA bound to the fibril and the amount of RNA in the supernatant (SN) represents the % of unbound RNA. The statistical analysis between the % of RNA bound to heparin-free and heparin-induced tau fibrils was performed by Welch's *t* test. Four stars represent $p < 0.0001$, three stars represents $p < 0.0002$, two stars represents $p < 0.0021$. Data are represented as mean values of $n = 3$ independent experiments. Error bars represent the standard deviation of three independent experiments.

pellet (Fig. 6c). In contrast, only ~18% polyU, ~15% polyA and ~7% tRNA were found in the pellets of the heparin-induced fibrils (Fig. 6c) suggesting very weak affinity of all three RNAs to the heparin-induced fibrils in the aggregation assay buffer.

In order to investigate the fibril interaction of the three RNAs at higher ionic strength, we repeated the experiments in a buffer with increased KCl concentration (100 mM KCl). At this higher ionic strength, the 2N4R tau fibrils, which were aggregated in

the absence of heparin, interacted with all three RNAs (Fig. 6c). Comparison of the amount of RNA in the pellets further suggested that polyU binds most efficiently to the fibrils (Fig. 6c). In the case of the heparin-induced 2N4R tau fibrils, ~90% polyU, ~35% polyA and ~6% tRNA was detected in the pellet. The heparin-induced fibrils thus bind to polyU in 100 mM KCl, but hardly interact in this condition with tRNA (Fig. 6c).

Discussion

Increasing evidence indicates that the structure of tau fibrils differs between distinct neurodegenerative diseases. This suggests that molecular pathology based on tau fibril structure might not only help to stratify patient groups but also to develop personalized medicines to treat these devastating diseases. At the same time, we currently do not know why the structure of tau fibrils is different in different diseases and which molecular factors drive tau into disease-specific amyloid fibril structures. Insight into these questions, however, are likely to be critical for the design and development of therapeutics that work in different tauopathies.

A major bottleneck towards this goal was the high solubility of tau. Thus, a major step forward was when it was shown that tau can efficiently be fibrillized in the presence of negatively charged co-factors^{8,9}. A particular effective co-factor is heparin, which was therefore widely used to study the molecular mechanisms of tau aggregation. The aggregation of tau can further be accelerated when shorter constructs comprising the repeat region are used, potentially combined with genetic mutations^{25–27}. Comparison of the cryo-EM structure of heparin-induced tau fibrils and tau fibrils purified from patient brain, however, showed that the structure of heparin-induced tau fibrils differs strongly from those derived from patients²⁸. This questioned the results of a huge amount of studies that used heparin-induced aggregation in order to gain insight into the molecular factors that drive tau aggregation. In addition, we are still left with the situation that we know about the presence of disease-specific tau strains, but do not know what causes the formation of these strains.

In the current study, we made an important advance towards a better understanding of the molecular factors that drive tau aggregation: we showed that the full-length tau protein can be aggregated into amyloid fibrils in the absence of heparin or other co-factors (Fig. 1). We further showed that the co-factor-free tau fibrils differ drastically in their structure and molecular properties from heparin-induced fibrils (Figs. 2–6). Solid-state NMR spectroscopy in combination with biochemical experiments revealed that the rigid/semi-rigid core of the heparin-free tau fibrils is formed by the tau residues ~270 to ~380, i.e., a similar size and location of the fibril core region as in tau fibrils purified from a CBD patient brain (Figs. 2, 3). However, the similarity in the size and location of the fibril core region does not guarantee that the heparin-free 2N4R tau fibrils prepared *in vitro* and the tau fibrils purified from CBD patient brain have an identical structure. *In vivo* tau exists in an environment rich in co-factors and also undergoes post-translational modifications including phosphorylation, ubiquitination and acetylation^{29,30}. The structure of the *in vitro* aggregated 2N4R tau fibrils therefore might differ in the presence of co-factors (e.g., RNA, polyphosphate) in the aggregation reaction or when post-translationally modified tau is used. Consistent with this hypothesis, the fibrillar cores of tau filaments from AD and CBD display distinct patterns of acetylation, phosphorylation, trimethylation and ubiquitination⁵. Using the protocol of *in vitro* self-aggregation of tau, the effect of different post-translational modifications and co-factors can now be studied. In contrast, heparin is likely to largely override the impact of PTMs and other co-factors (especially when these co-factors are used at low concentrations) due to its very high negative charge.

Our study further provides single-residue evidence for the contribution of the N-terminal region of tau to pathological aggregation. The broadening of the NMR signals of the N-terminal 30 residues indicates that the corresponding residues lose their mobility during aggregation (Fig. 2). Taking further into account that conformation-specific antibodies such as Alz50 and MC1 specifically detect pathological tau in brain tissue, but require two discontinuous epitopes, one located in the repeat region (residues 313–322) and the other at the N-terminus

(residues 1–18)¹⁸, suggests that the N-terminal residues of tau bind to the cross- β -structure of the fibrils and thereby generates the pathology-specific recognition motif. Currently, we do not know if part of the N-terminal epitope folds into β -structure as part of this process. The interaction, however, might be more transient when compared to the interactions that stabilize the fibrillar core, because the N-terminal region of tau was so far not detected in cryo-EM studies of tau fibrils (despite its importance for antibody binding).

A potential mechanism for the connection between tau fibril structure and specific diseases could be related to differences in the interactions that each tau fibril structure has with proteins and nucleic acids. In this study, we probed the interaction of the heparin-free 2N4R fibrils with three different RNAs (polyU, polyA, tRNA) (Fig. 6). PolyU is mainly disordered and it's able to engage in both hydrophobic (through the nitrogen bases) and electrostatic interactions (through the negatively charged phosphate backbone). PolyA is known to have partial secondary structure in the presence of Mg^{2+} ³¹. PolyA can thus engage in some hydrophobic interactions but less efficiently than polyU. tRNA, on the other hand, has a distinct secondary structure and is unable to engage in hydrophobic interactions through its bases, because the bases are hidden inside the structure. tRNA thus mainly interacts electrostatically through its negatively charged phosphate backbone.

We observed that at low ionic strength, the heparin-free 2N4R fibrils strongly interact with all three RNAs (polyU, polyA and tRNA) (Fig. 6c). At increased ionic strength, the interaction gradually weakens from polyU to polyA and to tRNA (Fig. 6c). In contrast the heparin-induced 2N4R tau fibrils were found to interact very weakly with the three RNAs at low ionic strength, but strongly bound to polyU at higher ionic strength (Fig. 6c). In addition, a weaker interaction of the heparin-induced 2N4R tau fibrils was observed with polyA, and very little interaction with tRNA at higher ionic strength (Fig. 6c). These results can be attributed to differences in the surface charge of the two fibril types and differences in the dominating interactions at low and high ionic strength: at low ionic strength electrostatic interactions dominate, while at higher ionic strength hydrophobic interactions come into play.

The surface of the heparin-free 2N4R fibril is mostly positively charged (shown in blue, Fig. 6a) with some patches of uncharged hydrophobic residues (shown in white, Fig. 6a) giving it the possibility to interact both electrostatically and hydrophobically with different RNAs. At low ionic strength, all three RNAs (polyU, polyA and tRNA) electrostatically interact with the heparin-free 2N4R tau fibrils resulting in comparable amounts of bound RNA (Fig. 6c). At higher ionic strength, hydrophobic interactions play a bigger role and the amount of bound RNA gradually decreases from polyU to polyA and to tRNA (hydrophobic interaction strength of polyU > polyA > tRNA). In contrast, heparin-induced tau fibrils (Supplementary Fig. 7) show weak affinity for RNA at low ionic strength where electrostatic repulsion between negatively charged RNA and the negatively charged heparin is strong. At higher ionic strength, this repulsion is attenuated and hydrophobic interactions between polyU and the surface of the fibrils result in binding of polyU, but not tRNA, to the heparin-induced fibrils. The combined data suggest that the binding of RNAs depends both on the structure of the RNA and the surface electrostatic properties of different tau conformers.

Taken together our study provides an important step to reveal the connection between tau fibril structure and neuronal toxicity. In combination with high-resolution structure determination by cryo-electron microscopy and solid-state NMR spectroscopy, it sets the basis for future work to investigate the impact of post-translational modifications, one of the potential factors

determining different tau strains⁵, on the three-dimensional structure of tau amyloid fibrils. Our study thus can help to elucidate the still enigmatic molecular causes that guide aggregation towards disease-specific tau strains.

Methods

Protein preparation. Unlabeled and ¹³C/¹⁵N-labeled 2N4R tau (hTau40, Uniprot ID 10636-8, 441 residues) were expressed in *Escherichia coli* strain BL21(DE3) from a pNG2 vector (a derivative of pET-3a, Merck-Novagen, Darmstadt) in presence of ampicillin. In case of unlabeled protein, cells were grown in 1–10 L LB and induced with 0.5 mM IPTG at OD₆₀₀ of 0.8–0.9. To obtain ¹³C/¹⁵N-labeled protein, cells were grown in LB until an OD₆₀₀ of 0.6–0.8 was reached, then centrifuged at low speed, washed with M9 salts (Na₂HPO₄, KH₂PO₄ and NaCl) and resuspended in minimal medium M9 supplemented with 1 g/L ¹⁵NH₄Cl as the only nitrogen source, 4 g/L ¹³C glucose as carbon source, and induced with 0.5 mM IPTG.

To obtain specifically (¹³C_γ valine, ¹³C-ring phenylalanine, ¹⁵N histidine) labeled 2N4R tau, cells were grown in LB until an OD₆₀₀ of 0.6–0.8 was reached, then centrifuged at low speed, washed with M9 salts (Na₂HPO₄, KH₂PO₄ and NaCl) and resuspended in M9 minimal medium supplemented with 0.125 g/L of L-phenylalanine (ring-¹³C₆, 99%) (CLM-1055, Cambridge Isotope Laboratories), 0.15 g/L of L-valine (dimethyl-¹³C₂, 99%) (CLM-9217-PK, Cambridge Isotope Laboratories), 0.125 g/L of L-histidine (¹⁵N₃, 98%) (NLM-1513 Cambridge Isotope Laboratories). To minimize scrambling, all other amino acid types were added in unlabeled form: 0.50 g/L alanine, 0.40 g/L arginine, 0.40 g/L aspartic acid, 0.05 g/L cysteine, 0.40 g/L glutamine, 0.65 g/L glutamic acid, 0.55 g/L glycine, 0.23 g/L isoleucine, 0.23 g/L leucine, 0.42 g/L lysine hydrochloride, 0.25 g/L methionine, 0.10 g/L proline, 2.10 g/L serine, 0.23 g/L threonine and 0.17 g/L tyrosine, as well as 0.50 g/L adenine, 0.65 g/L guanosine, 0.20 g/L thymine, 0.50 g/L uracil and 0.20 g/L cytosine³².

After induction with 0.5 mM IPTG, the bacterial cells were harvested by centrifugation and the cell pellets were resuspended in lysis buffer (20 mM MES pH 6.8, 1 mM EGTA, 2 mM DTT) complemented with protease inhibitor mixture, 0.2 mM MgCl₂, lysozyme and DNase I. Subsequently, cells were disrupted with a French pressure cell press (in ice cold conditions to avoid protein degradation). In the next step, NaCl was added to a final concentration of 500 mM and lysates were boiled for 20 min. Denatured proteins were removed by ultracentrifugation with 127,000 g at 4 °C for 30 min. The supernatant was dialyzed overnight at 4 °C against dialysis buffer A (20 mM MES pH 6.8, 1 mM EDTA, 2 mM DTT, 0.1 mM PMSF, 50 mM NaCl) to remove salt. The following day, the sample was filtered and applied onto an equilibrated ion exchange chromatography column and the weakly bound proteins were washed out with buffer A. Tau protein was eluted with a linear gradient of 60% final concentration of buffer B (20 mM MES pH 6.8, 1 M NaCl, 1 mM EDTA, 2 mM DTT, 0.1 mM PMSF). Protein samples were concentrated by ultrafiltration (5 kDa Vivaspin, Sartorius) and purified by reverse phase chromatography using a preparative C4 column (Vydac 214 TP, 5 μm, 8 × 250 mm). The purified protein was lyophilized and re-dissolved in the aggregation assay buffer.

Aggregation assays. Aggregation of 25 μM 2N4R tau was performed in 25 mM HEPES, 10 mM KCl, 5 mM MgCl₂, 3 mM TCEP, 0.01% Na₂S₂O₈, pH 7.2 buffer (aggregation assay buffer). One tablet of protease inhibitor (complete, EDTA-free, Sigma Aldrich) was added to 100 mL aggregation assay buffer. The buffer was filtered through a 0.2 μm filter to remove bacterial contamination. Thioflavin T (ThT) was added to the protein at a final concentration of 50 μM to monitor aggregation kinetics. A total of 100 μL of 25 μM 2N4R tau protein with 50 μM ThT was pipetted in a well of 96 well plate (Greiner Bio-one, microplate, 96 well, PS, F-bottom, Chimney well, μClear, black, non-binding, item no - 655906) with 3 polytetrafluoroethylene beads of 2.45 mm per well. The aggregation assay was performed at 37 °C in a Tecan spark plate reader with double orbital shaking (shaking duration — 1 min, shaking amplitude — 6 mm, shaking frequency — 54 rpm) at an interval of 10 min. An excitation filter at a wavelength of 430 nm with an excitation bandwidth of 35 nm was used to excite ThT. The emission wavelength was set to 485 nm with a bandwidth of 20 nm (manual gain — 40, number of flashes — 30, integration time — 40 μs). The Z-position was calibrated using an empty well before starting each experiment. ThT fluorescence data were collected using Tecan Spark control software (v 2.2). The analysis of the aggregation data was performed using Graphpad PRISM (v 9) software.

Heparin-induced fibrillization of 25 μM 2N4R tau was achieved using the same protocol described above, but 6.25 μM heparin was added to 25 μM protein.

Electron microscopy. A total of 30 μL of aggregated 2N4R tau sample was centrifuged at 20,000 g for 15 min in an Eppendorf centrifuge 5424. The supernatant was removed, and the pellet was resuspended in 25 μL aggregation assay buffer. KCl was added to the redissolved aggregated sample to a final concentration of 500 mM and a final volume of 30 μL to neutralize the surface charges of the fibril. The heparin-induced fibril sample was directly imaged by transmission electron microscopy (TEM) after the aggregation. Aggregated samples were adsorbed onto carbon-coated copper grids and stained by 1% uranyl acetate solution and imaged

by CM 120 transmission electron microscope (FEI, Eindhoven, The Netherlands). Pictures were taken with a Tietz F416 CMOS camera (TVIPS, Gauting, Germany).

Circular dichroism. Ten μL of 25 μM 2N4R fibril were centrifuged at 20,000 g for 15 min in an Eppendorf centrifuge 5424. The supernatant was removed, and the pellet was resuspended in 50 μL of distilled water. The 2N4R tau monomer was also diluted to a final concentration of 5 μM in 50 μL of distilled water. Both the fibril and the monomer samples were transferred to a 0.02 cm pathlength cuvette. CD data were collected from 190 to 280 nm using a Chirascan-plus qCD spectrometer (Applied Photophysics, UK) at 25 °C, 1.5 s per point in 1 nm steps. The datasets were averaged from 10 repeated measurements. Spectra were baseline-corrected and smoothed with a window size of six. CDNN software v 2 (Chirascan, Applied Photophysics, UK) was used to analyze the CD spectrum of the heparin-free 2N4R tau fibrils.

Trypsin digestion. Fifty μL of 0.9 mg/mL 2N4R fibril (aggregated in either the absence or presence of heparin) and 0.45 mg/mL of trypsin (T8003, Sigma-Aldrich) were incubated in the aggregation assay buffer for 30 min with 1400 rpm in a thermomixer (Eppendorf) at 37 °C. The trypsin-resistant fibril core was pelleted down by centrifugation at 160,000 g for 30 min at 4 °C using a Beckman Coulter Optima MAX-XP ultracentrifuge. The supernatant was discarded and the pellet was dissolved in 10 μL of aggregation assay buffer followed by loading onto a 15% SDS PAGE gel.

Pronase digestion. Fifty μL of 0.8 mg/mL 2N4R fibrils (aggregated in the absence of heparin) and 0.4 mg/mL of pronase from *Streptomyces griseus* (53702, Merck-millipore) were incubated in the aggregation assay buffer in a thermomixer (Eppendorf) for 30 min at 37 °C. The pronase-resistant fibril core was pelleted down by centrifugation at 160,000 g for 30 min at 4 °C using a Beckman Coulter Optima MAX-XP ultracentrifuge. The supernatant was discarded and the pellet was dissolved in 10 μL of aggregation assay buffer followed by loading onto a 15% SDS PAGE gel.

In-gel digestion and extraction of peptides for mass spectrometry. The respective bands from the SDS-PAGE gels were carefully cut and kept in an Eppendorf tube. To wash the gel pieces, 150 μL of water was added and incubated for 5 min at 26 °C with 1050 rpm shaking in a thermomixer. The gel pieces were spun down and the liquid was removed using thin tips (the same washing protocol was used in all subsequent steps with different solvents). The gel pieces were washed again with 150 μL acetonitrile. After washing, the gel pieces were dried for 5 min using a SpeedVacc vacuum centrifuge. To reduce disulfide bridges, 100 μL of 10 mM DTT was added to the gel pieces and incubated for 50 min at 56 °C followed by centrifugation and removal of liquid. The gel pieces were washed again with 150 μL of acetonitrile. To alkylate reduced cysteine residues, 100 μL of 55 mM iodoacetamide were added and incubated for 20 min at 26 °C with 1050 rpm shaking followed by centrifugation and removal of liquid. Subsequently, the gel pieces were washed with 150 μL of 100 mM NH₄HCO₃, and then twice with 150 μL of acetonitrile and dried for 10 min in a vacuum centrifuge. The gel pieces were rehydrated at 4 °C for 45 min by addition of small amounts (2–5 μL) of digestion buffer 1 (12.5 μg/mL trypsin, 42 mM NH₄HCO₃, 4 mM CaCl₂). The samples were checked after every 15 min and more buffer was added in case the liquid was completely absorbed by the gel pieces. Twenty μL of digestion buffer 2 (42 mM NH₄HCO₃, 4 mM CaCl₂) were added to cover the gel pieces and incubated overnight at 37 °C.

To extract the peptides, 15 μL water was added to the digest and incubated for 15 min at 37 °C with 1050 rpm shaking followed by spinning down the gel pieces. Fifty μL acetonitrile was added to the entire mixture and incubated for 15 min at 37 °C with 1050 rpm shaking. The gel pieces were spun down and the supernatant (SN1) containing the extracted peptides was collected. Thirty μL of 5% (v/v) formic acid was added to the gel pieces and incubated for 15 min at 37 °C with 1050 rpm shaking followed by spinning down. Again 50 μL acetonitrile were added to the entire mixture and incubated for 15 min at 37 °C with 1050 rpm shaking. The gel pieces were spun down and the supernatant (SN2) containing the extracted peptides was collected. Both supernatants (SN1 & SN2) containing the extracted peptides were pooled together and evaporated in the SpeedVacc vacuum centrifuge. The dried peptides were resuspended in 5% acetonitrile and 0.1% formic acid and analyzed using an Orbitrap Fusion Tribrid (Thermo Fischer Scientific) instrument.

NMR spectroscopy. The ¹H-¹⁵N HSQC spectrum of 25 μM 2N4R tau monomer in the aggregation assay buffer was acquired at 278 K on an Avance III 900 MHz spectrometer (Bruker) using a 5 mM HCN Cryoprobe. The chemical shift assignments of 2N4R tau is available¹³.

¹³C/¹⁵N-labeled 2N4R tau was aggregated either in the absence or presence of heparin using the protocol described above, but without ThT. Approximately 30 mg of fibrils were packed into 3.2 mm MAS rotors by ultracentrifugation. Solid-state NMR experiments were acquired at 265 K on a Avance-III 850 MHz spectrometer (Bruker) using a 3.2 mm HCN probe, and a Avance-III 950 MHz spectrometer (Bruker) using a 3.2 mm HCN probe. MAS frequency for all

measurements was 17 kHz. Two-dimensional ^1H - ^{15}N INEPT experiments of both fibril samples were recorded with 32 scans per point (ns), and indirect acquisition times $\text{td1} = 48$ ms, $\text{td2} = 50$ ms. ^{13}C - ^{13}C radio frequency-drive recoupling (RFDR) experiments were recorded with $\text{ns} = 64$, $\text{td1} = 21.5$ ms, $\text{td2} = 15$ ms, $\text{Tmix} = 1.882$ ms. The final ^{13}C - ^{13}C RFDR spectra are the sum of 11 datasets. The 2D NCA/NCX experiment of the heparin-free 2N4R fibrils was recorded using a TEDOR sequence with $\text{ns} = 64$, $\text{td1} = 21.5$ ms, $\text{td2} = 75.5$ ms. 3D NCACX and NCOCX spectra of heparin-free 2N4R fibrils were recorded using a TEDOR pulse sequence with $\text{ns} = 8$, $\text{td1} = 21.7$ ms, $\text{td2} = 4.72$ ms, $\text{td3} = 5.9$ ms. The final 3D NCACX and NCOCX spectra used for analysis are the sum of nine experiments each. Spectra were processed using the Topspin 3.6.2 (Bruker) and analyzed using CCPNMR 2.4.2³³.

Signals in the ^1H - ^{15}N INEPT spectra were assigned by transferring the resonance assignment of the 2N4R tau monomer. Intensity ratios were calculated by dividing the signal intensity observed for each residue in the ^1H - ^{15}N INEPT spectrum of the fibril sample by the signal intensity observed in the ^1H - ^{15}N HSQC spectrum of the monomeric protein. The residue with the highest intensity ratio was normalized to 1. The average line connecting residues was calculated by smoothing using a 2nd order polynomial function with a window size of four.

DNP-enhanced solid-state NMR spectra were recorded for heparin-free fibrils of 2N4R labeled with $^{13}\text{C}_2$ (methyl) Val, and $^{13}\text{C}_6$ (ring) Phe and $^{15}\text{N}_3$ His using a commercial Bruker DNP spectrometer system with a sweepable cryo-magnet of 14.1 ± 0.1 T ($\sim 600 \pm 5$ MHz ^1H frequency) and 395 GHz gyrotron for the microwaves, operating at 100 K with the Bruker 3.2 mm LT-MAS HCN probe and an Avance III HD spectrometer. 2N4R tau sample was prepared for MAS DNP NMR as follows: the 2N4R tau fibril pellet was mixed with 10 μL of the stock 10 mM TEMTriPol-1^{19,20} in DNP juice (60:30:10 by volume ^{12}C -glycerol- d_8 : D_2O : H_2O). The excess solution was removed by ultracentrifugation at 24,000 rpm for 1 h with a Beckman Coulter SW32-Ti rotor (k-Factor 204). After removal of the excess solution, the sample was homogenized with a non-stick stainless steel needle tool. The TEMTriPol-1 final concentration was estimated at 3 mM. The sample was packed into a 3.2 mm Bruker zirconia MAS rotor with a vespel drive cap and spun at a frequency of 12.5 kHz. The 90° hard pulses were, respectively, 2.5, 3.5 and 6 μs for ^1H , ^{13}C and ^{15}N . The ^1H - ^{13}C and ^{13}C - ^1H cross-polarization (CP) conditions were met with 75 kHz for ^{13}C and a ramp from 90 to 100 kHz for ^1H and a duration of 700 μs (^1H to ^{13}C CP) or 350 μs (^{13}C to ^1H CP). The ^1H - ^{15}N and ^{15}N - ^1H CP conditions were met with 30 kHz ^{15}N radiofrequency (RF) and 46–45 kHz linear ramp for ^1H RF with a duration of 350 μs (^1H - ^{15}N) and 370 μs (^{15}N - ^1H). The interscan delay was 2.5 s. The magnetic field was calibrated to an internal standard, the ^{13}C resonance of the silicone plug (polydimethylsiloxane) used for DNP sample packing, which was set to be at 1.6 ppm on the TMS scale³⁴. With these NMR settings, 2D hCHHC at 200 μs and 400 μs H-H mixing times were acquired for 2 days, and hNHHC at 200 μs H-H mixing time for 3 days²¹.

Seeding of 2N4R tau aggregation. For in vitro seeding experiments, 2N4R tau fibrils, which had been generated in the absence of heparin according to the protocol described above, were used as seed. One percent (w/w) and 5% (w/w) seeds were added to 25 μM monomeric 2N4R tau in the aggregation assay buffer. Prior to addition, the seeds were sonicated for 2 min at 37 °C in a water bath. The same protocol was used for aggregation, as described above. The in vitro measurements were performed with three independently prepared samples.

Biosensor cell line HEK293T TauRD-GFP were generated²³ to assess the seeding activity of fibrils in cellula. These cells were engineered to stably express the human tau repeat domain (RD; amino acids 243–375) with point mutations P301L/V337M and an carboxyterminal GFP-tag connected through an 18-amino acid flexible linker (EFCRRYRGPGIHRSPTA) (thereafter termed TauRD-GFP³⁵). HEK293T TauRD-GFP cells were seeded on 384 well plates. Next day, tau fibrils were mixed with lipofectamine 2000 and added to the cells at different concentrations. Prior to addition, the fibrils were sonicated for 6 min at 10% power. After 3 days, cells were fixed and nuclei were stained with Hoechst. Images were taken with an automated confocal microscope (CellVoyager 6000) and automated image analysis was performed to calculate total Tau-GFP cell numbers and cells containing Tau-GFP aggregates²³. Please note that automatic image analysis of aggregates takes into account local fluorescence intensity increase, resulting in low background levels of positives due to condensed cell bodies. Cell measurements were performed with three independent transfections at different concentrations per fibril type.

RNA binding assay. A total of 10 $\mu\text{g}/\text{mL}$ of yeast tRNA (AM7119, Thermo Fischer Scientific) poly(A) (P9403, Sigma-Aldrich) or poly(U) (P9528, Sigma-Aldrich) were added to 100 μL of 5 μM 2N4R fibrils either in the aggregation assay buffer (10 mM KCl, 25 mM HEPES, 5 mM MgCl_2 , 3 mM TCEP, pH 7.2) or in the same buffer but at increased ionic strength (100 mM KCl, 25 mM HEPES, 5 mM MgCl_2 , 3 mM TCEP, pH 7.2). The fibril/RNA-mixture was incubated at 37 °C with 550 rpm shaking for 1.5 h in a Thermomixer (Eppendorf, Thermomixer comfort). After the incubation, the fibril/RNA-mixture was centrifuged at 160,000 g at 37 °C for 30 min in an ultracentrifuge (Optima MAX-XP, Beckman Coulter). The supernatant was removed and the pellet was resuspended in 100 μL of aggregation assay buffer with 2% SDS. The concentration of RNA in the supernatant and the pellet

(resuspended) was calculated using a Nanodrop 2000 spectrophotometer (Thermo Fischer Scientific). Spectra were baseline corrected using the buffer as reference. The concentrations of polyU, polyA and tRNA were calculated from a sample of 10 $\mu\text{g}/\text{mL}$ RNA in 100 μL of buffer. Measurements were performed with three independently prepared samples in each case.

Bicinchoninic acid assay. The concentration of 2N4R tau in the supernatant after aggregation (in the absence of heparin) was determined using the micro-bicinchoninic acid (BCA) assay kit (23235, Thermo Fischer Scientific). The microplate procedure (linear working range of 2–40 $\mu\text{g}/\text{mL}$) as described in the instruction manual provided by the manufacturer was used to perform the experiment.

Electrostatic surface potential. The electrostatic surface potential of the tau filament (type 1) extracted from the brain of a patient with CBD (PDB code: 6TJO) and the heparin-induced 2N4R tau fibrils (snake form; PDB code: 6QJH) was displayed using the coulombic surface coloring tool in UCSF Chimera³⁶ (v 1.14.0). The dielectric constant of water ($\epsilon = 78.4$) was used; the distance from the surface (d) was set to 1.4 Å. The minimum value for the number of colors was set to -0.5 kcal/mol* e and the maximum value was set to 0.5 kcal/mol* e .

Reporting summary. Further information on experimental design is available in the Nature Research Reporting Summary linked to this paper.

Acknowledgements

We thank the mass spectrometry facility of the Max Planck Institute for Biophysical Chemistry (MPIBPC) for mass spec data, and the EM facility of MPIBPC for electron micrographs and the chemical synthesis facility of MPIBPC for preparation of the TEMTriPol-1 radical. M.Z. was supported by the European Research Council (ERC) under the EU Horizon 2020 research and innovation program (grant agreement No. 787679).

Author contributions

P.C. conducted aggregation assays, biochemical analysis, RNA binding studies and NMR experiments; G.R. recorded solid-state NMR spectra including DNP experiments; S.L. and A.H. performed biosensor cell experiments; R.D. recorded DNP NMR experiments; A.I.O. supported biophysical analysis; L.A. supervised solid-state NMR experiments; I.M. V. supervised biosensor cell experiments; P.C. and M.Z. designed the project and wrote the paper.

Funding

Open Access funding enabled and organized by Projekt DEAL.

Competing interests

The authors declare no competing interests.

Data availability

All relevant data are available from the corresponding author upon reasonable request. Source data are provided with this paper. All the PDB codes (6TJO, 6QJH) cited in this paper are available in the protein data bank web server.

Received: 11 December 2020; Accepted: 16 June 2021;

Published online: 09 July 2021

References

- Wang, Y. & Mandelkow, E. Tau in physiology and pathology. *Nat. Rev. Neurosci.* **17**, 5–21 (2016).
- Fitzpatrick, A. W. P. et al. Cryo-EM structures of tau filaments from Alzheimer's disease. *Nature* **547**, 185–190 (2017).
- Falcon, B. et al. Novel tau filament fold in chronic traumatic encephalopathy encloses hydrophobic molecules. *Nature* **568**, 420–423 (2019).
- Zhang, W. et al. Novel tau filament fold in corticobasal degeneration. *Nature* **580**, 283–287 (2020).
- Arakhamia, T. et al. Posttranslational modifications mediate the structural diversity of tauopathy strains. *Cell* **180**, 633–644 (2020).
- Falcon, B. et al. Structures of filaments from Pick's disease reveal a novel tau protein fold. *Nature* **561**, 137–140 (2018).
- Clavaguera, F., Tolnay, M. & Goedert, M. The Prion-like behavior of assembled tau in transgenic mice. *Cold Spring Harb. Perspect. Med.* **7**, a024372 (2017).

8. Goedert, M. et al. Assembly of microtubule-associated protein tau into Alzheimer-like filaments induced by sulphated glycosaminoglycans. *Nature* **383**, 550–553 (1996).
9. Friedhoff, P., Schneider, A., Mandelkow, E. M. & Mandelkow, E. Rapid assembly of Alzheimer-like paired helical filaments from microtubule-associated protein tau monitored by fluorescence in solution. *Biochemistry* **37**, 10223–10230 (1998).
10. Zhang, W. et al. Heparin-induced tau filaments are polymorphic and differ from those in Alzheimer's and Pick's diseases. *Elife* **8**, e43584 (2019).
11. Lo Cascio, F. et al. Modulating disease-relevant tau oligomeric strains by small molecules. *J. Biol. Chem.* **295**, 14807–14825 (2020).
12. Bulic, B. et al. Development of tau aggregation inhibitors for Alzheimer's disease. *Angew. Chem. Int. Ed. Engl.* **48**, 1740–1752 (2009).
13. Mukrasch, M. D. et al. Structural polymorphism of 441-residue tau at single residue resolution. *PLoS Biol.* **7**, e34 (2009).
14. Weingarten, M. D., Lockwood, A. H., Hwo, S. Y. & Kirschner, M. W. A protein factor essential for microtubule assembly. *Proc. Natl Acad. Sci. U.S.A.* **72**, 1858–1862 (1975).
15. Xu, S., Brunden, K. R., Trojanowski, J. Q. & Lee, V. M. Characterization of tau fibrillization in vitro. *Alzheimers Dement.* **6**, 110–117 (2010).
16. Dregni, A. J. et al. In vitro 0N4R tau fibrils contain a monomorphic beta-sheet core enclosed by dynamically heterogeneous fuzzy coat segments. *Proc. Natl Acad. Sci. U.S.A.* **116**, 16357–16366 (2019).
17. Bibow, S. et al. The dynamic structure of filamentous tau. *Angew. Chem. Int. Ed. Engl.* **50**, 11520–11524 (2011).
18. Jicha, G. A., Bowser, R., Kazam, I. G. & Davies, P. Alz-50 and MC-1, a new monoclonal antibody raised to paired helical filaments, recognize conformational epitopes on recombinant tau. *J. Neurosci. Res.* **48**, 128–132 (1997).
19. Mentink-Vigier, F. et al. Efficient cross-effect dynamic nuclear polarization without depolarization in high-resolution MAS NMR. *Chem. Sci.* **8**, 8150–8163 (2017).
20. Mathies, G. et al. Efficient dynamic nuclear polarization at 800 MHz/527 GHz with Trityl-Nitroxide Biradicals. *Angew. Chem. Int. Ed.* **54**, 11770–11774 (2015).
21. Lange, A., Luca, S. & Baldus, M. Structural constraints from proton-mediated rare-spin correlation spectroscopy in rotating solids. *J. Am. Chem. Soc.* **124**, 9704–9705 (2002).
22. Holmes, B. B. et al. Proteopathic tau seeding predicts tauopathy in vivo. *Proc. Natl Acad. Sci. U.S.A.* **111**, E4376–E4385 (2014).
23. Liu, S. et al. Highly efficient intercellular spreading of protein misfolding mediated by viral ligand - receptor interactions. *bioRxiv*, <https://doi.org/10.1101/2020.06.26.173070> (2020).
24. Ginsberg, S. D., Crino, P. B., Lee, V. M., Eberwine, J. H. & Trojanowski, J. Q. Sequestration of RNA in Alzheimer's disease neurofibrillary tangles and senile plaques. *Ann. Neurol.* **41**, 200–209 (1997).
25. Xiang, S. et al. A two-component adhesive: tau fibrils arise from a combination of a well-defined motif and conformationally flexible interactions. *J. Am. Chem. Soc.* **139**, 2639–2646 (2017).
26. Daebel, V. et al. Beta-sheet core of tau paired helical filaments revealed by solid-state NMR. *J. Am. Chem. Soc.* **134**, 13982–13989 (2012).
27. von Bergen, M. et al. Mutations of tau protein in frontotemporal dementia promote aggregation of paired helical filaments by enhancing local beta-structure. *J. Biol. Chem.* **276**, 48165–48174 (2001).
28. Scheres, S. H., Zhang, W., Falcon, B. & Goedert, M. Cryo-EM structures of tau filaments. *Curr. Opin. Struct. Biol.* **64**, 17–25 (2020).
29. Wickramasinghe, S. P. et al. Polyphosphate initiates tau aggregation through intra- and intermolecular scaffolding. *Biophys. J.* **117**, 717–728 (2019).
30. Li, D. & Liu, C. Hierarchical chemical determination of amyloid polymorphs in neurodegenerative disease. *Nat. Chem. Biol.* **17**, 237–245 (2021).
31. Tang, T. T. L. & Passmore, L. A. Recognition of Poly(A) RNA through its intrinsic helical structure. *Cold Spring Harb. Symp. Quant. Biol.* **84**, 21–30 (2019).
32. Muchmore, D. C., McIntosh, L. P., Russell, C. B., Anderson, D. E. & Dahlquist, F. W. Expression and nitrogen-15 labeling of proteins for proton and nitrogen-15 nuclear magnetic resonance. *Methods Enzymol.* **177**, 44–73 (1989).
33. Vranken, W. F. et al. The CCPN data model for NMR spectroscopy: development of a software pipeline. *Proteins* **59**, 687–696 (2005).
34. Birkefeld, A. B., Bertermann, R., Eckert, H. & Pfeleiderer, B. Liquid- and solid-state high-resolution NMR methods for the investigation of aging processes of silicone breast implants. *Biomaterials* **24**, 35–46 (2003).
35. Woerman, A. L. et al. Tau prions from Alzheimer's disease and chronic traumatic encephalopathy patients propagate in cultured cells. *Proc. Natl Acad. Sci. U.S.A.* **113**, E8187–E8196 (2016).
36. Pettersen, E. F. et al. UCSF Chimera—a visualization system for exploratory research and analysis. *J. Comput. Chem.* **25**, 1605–1612 (2004).

Additional information

Supplementary information The online version contains supplementary material available at <https://doi.org/10.1038/s41467-021-24362-8>.

Correspondence and requests for materials should be addressed to M.Z.

Peer review information *Nature Communications* thanks Kwang Hun Lim, Abhinav Nath and the other, anonymous, reviewer(s) for their contribution to the peer review of this work. Peer reviewer reports are available.

Reprints and permission information is available at <http://www.nature.com/reprints>

Publisher's note Springer Nature remains neutral with regard to jurisdictional claims in published maps and institutional affiliations.



Open Access This article is licensed under a Creative Commons Attribution 4.0 International License, which permits use, sharing, adaptation, distribution and reproduction in any medium or format, as long as you give appropriate credit to the original author(s) and the source, provide a link to the Creative Commons license, and indicate if changes were made. The images or other third party material in this article are included in the article's Creative Commons license, unless indicated otherwise in a credit line to the material. If material is not included in the article's Creative Commons license and your intended use is not permitted by statutory regulation or exceeds the permitted use, you will need to obtain permission directly from the copyright holder. To view a copy of this license, visit <http://creativecommons.org/licenses/by/4.0/>.

© The Author(s) 2021

Pijush Chakraborty

Zimmermann str. 13, 37075, Göttingen
DOB – 7th December 1993
pijush.chakraborty@dzne.de

Experience

Doctoral Researcher, German Center for Neurodegenerative Diseases (DZNE) Göttingen

January 2018 - Present

Scientific employee/Pre-doctoral fellow, University Medical Center Göttingen (UMG)

August 2017 – December 2017

Education

Master of Science (M.Sc.) in Chemistry

Indian Institute of Technology (IIT) Bhubaneswar, Bhubaneswar, India

July 2015 – June 2017

Bachelor of Science (B.Sc.) with Honours in Chemistry

University of Calcutta, Kolkata, India

July 2012 – June 2015

Publications

Oroz J., Chang B. J., Wysoczanski P., Lee C., Pérez-Lara Á., Chakraborty P., Hofele R. V., Baker J. D., Blair L. J., Biernat J., Urlaub H., Mandelkow E., Dickey C. A., & Zweckstetter, M.

Structure and pro-toxic mechanism of the human Hsp90/PPIase/Tau complex.

Nat Commun 9, 4532 (2018)

Chakraborty P., Rivière G., Liu S., Ibáñez de Opakua A., Dervişoğlu R., Hebestreit A., Andreas L. B., Vorberg I. M., & Zweckstetter M.

Co-factor-free aggregation of tau into seeding-competent RNA-sequestering amyloid fibrils

Nat Commun 12, 4231 (2021)

Achievements

- Recipient of IIT Bhubaneswar's 'Institute Silver Medal' for obtaining highest Cumulative Grade Point (CGPA = 9.64/10) amongst the students graduating with Master of Science Degree in Chemistry in the academic year 2016-2017
- Recipient of IIT Bhubaneswar's 'Project Proficiency Award' for the best thesis work amongst the students graduating with Master of Science Degree in Chemistry in the academic year 2016-2017
- Selected for INSPIRE fellowship 2017, funded by Department of Science & Technology, Government of India, for pursuing doctoral studies in India
- Qualified Joint Admission Test (JAM 2015) for admission to M.Sc. at IITs with All India Rank (AIR) of 216.
- Recipient of the INSPIRE scholarship (2012 to 2017) funded by Department of Science & Technology, Government of India, for being amongst the top 1 % students appeared in intermediate exam.